TECHNISCHE UNIVERSITÄT MÜNCHEN

Lehrstuhl für Nachrichtentechnik

Optimization of Wavelength Division Multiplexed Optical Communication Systems at 100 Gb/s Using Multilevel Phase Modulation and Direct Detection

Oscar Cristóbal Gaete Jamett

Vollständiger Abdruck der von der Fakultät für Elektrotechnik und Informationstechnik der Technischen Universität München zur Erlangung des akademischen Grades eines

Doktor-Ingenieurs

genehmigten Dissertation.

Vorsitzender: Univ.-Prof. Dr.-Ing. habil., Dr.h.c. A.W. Koch
Prüfer der Dissertation: 1. Univ.-Prof. Dr.-Ing. N. Hanik
                         2. Assoc. Prof. Dr.ir. H. de Waardt
                            Technische Universiteit Eindhoven, Niederlande.

Die Dissertation wurde am 17.06.2013 bei der Technischen Universität München eingereicht und durch die Fakultät für Elektrotechnik und Informationstechnik am 04.03.2014 angenommen.

Preface

This thesis was written during my time as a researcher and teaching assistant at the Institute for Communications Engineering of the Technische Universität München and as an external researcher at Nokia-Siemens Network GmbH (NSN), within the collaboration framework of the European project "100-Gbit/s Carrier-Grade Ethernet Transport Technologies" (100-GET).

I would like to thank my doctoral supervisor Professor Norbert Hanik for giving me the opportunity to work towards my doctoral degree under his guidance, and to Bernhard Spinnler and Harald Rohde at NSN for setting up this project. Their advice and constant support were essential in developing the ideas behind this work. I am also grateful to Professor Huug de Waardt for acting as second supervisor.

Many people contributed to making these past years enjoyable. I am thankful to my former colleagues of the Optical Communications Group at LNT: Leonardo Coelho, Bernhard Göbel, Stephan Hellerbrand and Florian Breyer for the innumerable inspiring discussions, for their help with technical problems and in general for the great time at the Institute. Also to my former fellow doctoral students at NSN: Mohammad Alfiad, Beril Innan, Susmita Adhikari, Maxim Kushnerov, Dirk van den Borne and Sander Jansen, I am grateful for having had the chance to work and collaborate with them. I especially enjoyed our many trips abroad.

I am also in debt to Professor William Shieh for having given me the chance to visit and work in his group at The University of Melbourne. I had a memorable time there.

Finally, a big thanks goes to my family in Chile for their love and encouragement, which I feel strongly in spite of the distance. And to my family in Germany for their love and support throughout all these years. Last but not least, thanks to Barbara for her endless love, care and patience. Undoubtedly, this work would not have been possible without her in my life.

München, June 2013   Oscar Gaete

Contents

Abstract

This thesis investigates the performance limits of phase modulated and direct detected WDM systems at 55.5 and 111 Gb/s with 50 GHz channel spacing. Particularly, we are interested in identifying the parameters of the optical link that maximize the performance of a certain transmission format and subsequently analyze different modulation schemes and link configurations at their optimum operation points. For this purpose, a novel optimization algorithm is proposed and extensively used for determining the optimum parameters of the investigated scenarios.

Firstly, different "flavors" of DQPSK at 55.5 Gb/s are compared, such as return and non-return-to-zero pulse shapes using single and dual-carrier implementations. Secondly, we introduce optical DQPSK transmission using Nyquist pulses as a way of minimizing the spectral occupancy of the signals. By means of spectral shaping we attempt to increase the tolerance of the Nyquist signals to transmission impairments. And finally, the transmission of 111 Gb/s encoding 3 bits per transmitted symbol is investigated. Because of the broad spectrum of the signals and small channel separation, transmission suffers from strong performance penalties due to WDM cross-talk and narrow-band filtering. We justify using ASK-DQPSK as the modulation format for such scenario.

Transmission performance is quantified by means of simulations, which assess robustness to narrow-band filtering, dispersion and non-linear tolerance, and propagation in non-dispersion and dispersion managed links. The optimum dispersion map parameters, launch powers and an estimation of the maximum transmission distance are given for each of the considered transmission formats.

1

Introduction

Up until a few years ago, optical communication systems primarily employed on-off keying (OOK) as the modulation format of choice. In such systems the transmitted data is conveyed in the intensity of the optical carrier. Presently, the majority of the worldwide installed optical fiber networks use OOK at 10 Gb/s and wavelength division multiplexing (WDM) with channel separation of 50 GHz [Tel10], resulting in a spectral efficiency of only 0.2 b/s/Hz. The steady increase in capacity requirements for the present and future optical network has opened the way to more advanced and spectrally efficient modulation formats, where not only the amplitude of the optical carrier is modulated but also the frequency, phase and polarization state of the carrier can be used to transmit information.

In the past decade, interest in optical phase modulation re-emerged[1] due to a number of advantages over OOK for systems with data rates of more than 10 Gb/s. For example, binary phase shift keying (PSK) has an inherent ∼3 dB advantage in receiver sensitivity compared to OOK. This is due to the bigger separation of its constellation points, for the same transmitted power. Without considering nonlinearities this advantage would directly translate into doubling of the maximum transmission distance. Additionally, phase modulated signals are expected to be more tolerant than OOK signals against nonlinear effects. This results from the fact that the optical power in PSK is more evenly distributed in time than in OOK: Power is present in every bit slot for PSK, which effectively reduces bit-pattern-dependent nonlinear effects; and the optical peak power is 3 dB lower for PSK than for OOK for the same average optical power [GW05]. All these advantages have led phase modulation to be the format of choice for the second

---

[1]Optical systems using phase-shift keying were extensively studied in the late 1980s and early 1990s mainly for single-span fiber-optic systems using coherent detection, as well as in free space optical communication systems, where the sensitivity advantage of phase modulation could be exploited. With the introduction of optical amplifiers, interest in phase modulation and coherent detection declined.

generation of 40 Gb/s systems[2] [Inf12]. In such systems direct detection is still used at the receiver side, mainly due to its straightforward implementation compared to more advanced coherent technologies.

The "mobile revolution" we have experienced in the last couple of years, characterized by ubiquitous broadband connectivity and driven by wireless technologies such as Wi-fi, UMTS/HSPA and LTE[3], has brought a significant increase in the capacity requirements for the existing and future optical networks. It has been envisioned for such advanced networks to operate at 100 Gb/s bit rate per wavelength channel, delivering a spectral efficiency of 2 b/s/Hz. At such high data rates, the bandwidth of binary PSK signals is so broad that strong performance penalties due to WDM cross-talk and to optical filtering are unavoidable. For this reason, multilevel modulation formats must be employed in such transmission scenarios. For example, quadrature phase-shift keying (QPSK) retains the abovementioned advantages of PSK over OOK and, by using four phase states, conveys two bits per symbol effectively reducing the symbol rate and the spectral occupancy of the optical signals.

Nevertheless, the spectral occupancy of QPSK signals at 100 Gb/s is still too high for WDM systems using 50 GHz of channel separation. With this respect, polarization division multiplexing (PDM) has proven an attractive alternative. In PDM the two polarization states of the optical carrier are used to transmit signals with only half of the total data rate. The two tributaries are multiplexed using linear, but orthogonal states of polarization (SOP) [vdB08]. They can be separated at the receiver side using a polarization beam splitter (PBS) aligned with the incoming signal's SOP. If direct detection is employed, a feedback loop must be used to control the alignment of the PBS [WBO+09], since the SOP of the signal changes randomly during propagation.

Still, the high symbol rate of QPSK at 25 GS/s per polarization greatly impacts the tolerance to detrimental propagation effects, resulting in reduced transmission distances. With this regard, and in the advents of ultra fast analog-to-digital converters [Inf12], optical coherent detection using digital signal processing has positioned itself as a key enabling technology for increasing the overall performance of an optical transmission link. By mixing the incoming optical signal with a laser of similar optical frequency at the receiver side, the full optical field (amplitude and phase) can be recovered. Not only the receiver sensitivity is improved compared to direct detection, but subsequent digital processing is able to compensate for all linear (and some nonlinear) detrimental effects that the signal experiences before, during and after propagation such as chromatic and polarization mode dispersion, transmitter IQ imbalance, PBS misalignment, etc.

Digital coherent detection is an important step towards increasing the capacity and reducing the costs of core networks that require to transmit large amounts of data over the longest possible distances (> 1000 km). On the other hand, and mainly due to their straightforward implementation, lower power consumption, and thus reduced costs,

---

[2]The first generation was based on duobinary modulation.
[3]Wi-Fi is the wireless network technology based on the IEEE 802.11 standard [IEEa]. UMTS/HSPA and LTE are cellular technologies standardized by the 3GPP group [3GP].

direct detection systems at 100 Gb/s remain an attractive solution in scenarios where capacity is required but transmission distances are shorter like, for example, regional and metropolitan networks, which are typically composed of 300 to 1000 km long point-to-point links.

This thesis investigates the performance limits of phase modulated and direct detected WDM systems at 50 and 100 Gb/s with 50 GHz channel spacing. Particularly, we are firstly interested in identifying the parameters of the optical link that maximize the performance of a certain transmission format. In this way, we are able to analyze different modulation schemes and transmission configurations at their optimum operation points and thus, provide a fair comparison between them.

The thesis is organized as follows:

Chapter 2 introduces the theoretical foundations of the models used in this thesis. Starting with Maxwell's equations, the conditions for single-mode transmission are reviewed and the scalar nonlinear Schroedinger equation (NLSE) is derived. The NLSE is used throughout this thesis to describe and simulate the propagation of the optical signals within the fiber. Subsequently, the most important linear and nonlinear effects to which the optical signals are exposed during propagation are discussed. Analytical and numerical solutions of the NLSE are presented.

Chapter 3 is divided into three main parts. The first part mentions the most important elements that compose the optical transmission systems considered in this thesis. In the second part the criteria for the optimum design of such systems are reviewed. Special relevance is given to the design of dispersion maps. The third part is dedicated to the proper evaluation of the performance of an optical communication link. Firstly, the theory of pseudo-random sequences is briefly reviewed. Secondly, a semi-analytical method for the evaluation of the bit-error rate is described. Finally, the mathematical algorithm used in this thesis for the global optimization of the investigated systems is introduced.

Using the models and tools described in chapters 2 and 3, **chapter 4** investigates the performance limits of directly detected WDM transmission systems using differential QPSK (DQPSK) at 50 Gb/s. Firstly, a fundamental explanation of DQPSK in optical communication systems is provided focusing in transmitter and receiver structures, spectral characteristics and demodulation properties. Secondly, different "flavors" of DQPSK are compared, such as return and non-return-to-zero pulse shapes, dual-carrier implementation and stereo multiplexing. Finally, the propagation of WDM signals after 1040 km with optimum dispersion maps is thoroughly analyzed and maximum transmission distances are estimated. The optimum link parameters are identified and the robustness of each transmission format with respect to variations in the dispersion map is assessed. Additionally, in appendix D, an original mathematical framework is introduced that proves helpful in analyzing direct detected frequency division multiplexed signals. It is used to generalize stereo multiplexing for a higher number of sub-carriers.

In **chapter 5**, we introduce optical DQPSK transmission using Nyquist pulses as a way of minimizing the spectral occupancy of the signals. By means of spectral shaping

we attempt to increase the tolerance of the Nyquist signals to transmission impairments. Finally we use the same propagation scenarios as in chapter 4 in order to assess the performance of Nyquist pulses and compare them to the more classic (non) return-to-zero pulses (NRZ and RZ).

Chapter 6 investigates the transmission of 100 Gb/s signals encoding 3 bits per transmitted symbol. This scenario is radically different to the ones considered in chapters 4 and 5, because of the broad spectrum of the signals and small channel separation, which translates into strong performance penalties due to WDM cross-talk and narrow-band filtering. Firstly, we justify using ASK-DQPSK as the modulation format for such scenario. Then, a thorough description of the transmitter and receiver architectures is given. As in the previous chapters, the performance of the transmission format is assessed emphasizing the difference between (N)RZ and Nyquist pulses.

Finally, **chapter 7** summarizes the main contributions of this thesis and proposes possible directions for future research.

Some parts of this thesis have been already published in the following conference proceedings [GCS$^+$08, GCS$^+$09, CGS$^+$09, GCS$^+$10, GHC$^+$10, GCSH10a, GCSH10b, CGS$^+$10, GJC$^+$11, GCSH11, AKJ$^+$12] and journal papers [CGH09, GCS12, AJK$^+$13].

Notes on general premises used throughout this thesis:

The following premises are taken as basis throughout this thesis:

▷ 100 Gb/s is the *net* data rate of interest considered throughout this thesis. As in most communication system, there is an overhead added to the information payload that includes redundancy bits for error correction procedures. The standard error correction used in today's installed 10 and 40 Gb/s systems uses Reed-Solomon codes RS(255, 239) with 7% overhead, which is able correct bit-error rates of up to 2.2×10^{-3} [ITU09]. Additionally, it is envisioned for future generation optical networks to use the Ethernet networking standard [IEEb] which adds an extra 4% overhead. Thus, 111 Gb/s is the gross data rate of the signals investigated in the following chapters.

▷ In chapters 4 and 5, it is assumed that polarization division multiplexing is used and, therefore, the data rate of the DQPSK signals is 55.5 Gb/s. However, polarization effects are not taken into account in the simulations, which only focus on the nonlinear interaction of the optical signals along propagation. Polarization effects are discussed in more detail in chapter 2.8.1.

▷ When simulating WDM transmission, seven uncorrelated co-polarized optical signals are considered. The channel separation is 50 GHz and the wavelength of the center channel is 1550.52 nm, which corresponds to channel H33 of the International Telecommunication Union (ITU) 50 GHz WDM grid [ITU02]. The performance evaluations always refer to the center channel. Channel H33 is simulated as well in single-channel scenarios.

Table 1.1: Fiber parameters

		SSMF	DCF	
Attenuation	α	0.23	0.50	dB/km
Dispersion	D	16.6	-103.4	ps/nm/km
Slope	S	0.058	-0.200	ps/nm^2/km
Nonlinearity	γ	1.52	5.27	1/W/km

▷ The fibers used to model the pre- and post-compensation stages are considered non-attenuating and linear. In this way, the results presented in the following chapters are independent of the technology used to manipulate the waveform before and after propagation. Standard single-mode fiber and dispersion compensating fiber with the parameters shown in Table 1.1 are considered for all simulations carried out in this thesis. EDFAs have a noise figure of 6 dB.

2

Propagation of Light in Optical Fibers

In this chapter, the theory that sustains the models used in this thesis is reviewed. Starting with the Maxwell's equations, the nonlinear Schroedinger equation (NLSE) is derived. The NLSE governs the propagation of light in single-mode fibers and is extensively used in the simulations carried out in this thesis. Subsequently, the most important linear and nonlinear effects to which the optical signals are exposed during propagation are discussed. Analytical and numerical solutions to the NLSE are described at the end of the chapter.

2.1   The general wave equation

The propagation of light in the optical fiber, as any electromagnetic phenomena, can be described by Maxwell's equations:

$$\nabla \times \mathbf{E} = \frac{\partial \mathbf{B}}{\partial t}, \tag{2.1}$$

$$\nabla \times \mathbf{H} = \mathbf{J} + \frac{\partial \mathbf{D}}{\partial t}, \tag{2.2}$$

$$\nabla \cdot \mathbf{B} = 0, \tag{2.3}$$

$$\nabla \cdot \mathbf{D} = \rho_f, \tag{2.4}$$

where $\mathbf{E}$ is the electric field vector, $\mathbf{H}$ is the magnetic field vector and $\mathbf{D}$ and $\mathbf{B}$ are their respective flux densities. Since the optical fiber is a nonconductive medium without free charges, the electric current density vector $\mathbf{J}$ and the electric charge density ρ_f equal zero.

The flux densities relate to the field vectors through the material equations:

$$\mathbf{D} = \varepsilon_0 \mathbf{E} + \mathbf{P}, \tag{2.5}$$

$$\mathbf{B} = \mu_0 \mathbf{H} + \mathbf{M}, \tag{2.6}$$

where ε_0 and μ_0 are the free space permittivity and permeability, respectively. $\mathbf{P}$ is the electric material polarization and $\mathbf{M}$ is the magnetic material polarization that, for nonmagnetic media such as optical fibers, equals zero.

By taking the curl of (2.1) and using (2.2), (2.5) and (2.6) we obtain

$$\nabla \times \nabla \times \mathbf{E} = -\frac{1}{c^2} \frac{\partial^2 \mathbf{E}}{\partial t^2} - \mu_0 \frac{\partial^2 \mathbf{P}}{\partial t^2}, \tag{2.7}$$

where $c = 1/\sqrt{\varepsilon_0 \mu_0}$ is the speed of light in free space.

Equation (2.7) describes the temporal and spatial evolution of the electrical field propagating along the optical fiber and is known as the *general wave equation* [Agr02].

2.2   Material polarization

An external electric field applied to a nonconductive material leads the atoms of the material to react by creating dipole moments, which in turn, serve as a source of electromagnetic radiation [Sch04]. The field created as a consequence of the internal charge distribution superimposes with the external applied field and propagates along the fiber. This interaction between light and material is accounted in (2.7) through the material polarization vector $\mathbf{P}$.

In general $\mathbf{P}$ depends nonlinerly on $\mathbf{E}$ and can be written as a power series [Han95]

$$\mathbf{P}(\mathbf{r}, t) = \mathbf{P}^{(1)}(\mathbf{r}, t) + \mathbf{P}^{(2)}(\mathbf{r}, t) + \mathbf{P}^{(3)}(\mathbf{r}, t) + \dots, \tag{2.8}$$

where $\mathbf{r} = (x \ y \ z)^{\mathrm{T}}$ is the spatial vector with cartesian components.

$\mathbf{P}^{(n)}(\mathbf{r}, t)$ is related to $\mathbf{E}(\mathbf{r}, t)$ through the nth order susceptibility $\boldsymbol{\chi}^{(n)}(t)$ so that (2.8) can be written:

$$
\begin{aligned}
\mathbf{P}(\mathbf{r}, t) = {} & \varepsilon_0 \int_0^\infty \boldsymbol{\chi}^{(1)}(t - \tau_1) \cdot \mathbf{E}(\mathbf{r}, \tau_1) \, \mathrm{d}\tau_1 \\
& + \varepsilon_0 \iint_0^\infty \boldsymbol{\chi}^{(2)}(t - \tau_1, t - \tau_2) : \mathbf{E}(\mathbf{r}, \tau_1)\mathbf{E}(\mathbf{r}, \tau_2) \, \mathrm{d}\tau_1 \, \mathrm{d}\tau_2 \\
& + \varepsilon_0 \iiint_0^\infty \boldsymbol{\chi}^{(3)}(t - \tau_1, t - \tau_2, t - \tau_3) \vdots \mathbf{E}(\mathbf{r}, \tau_1)\mathbf{E}(\mathbf{r}, \tau_2)\mathbf{E}(\mathbf{r}, \tau_3) \, \mathrm{d}\tau_1 \, \mathrm{d}\tau_2 \, \mathrm{d}\tau_3 \dots
\end{aligned}
\tag{2.9}
$$

The susceptibility is a measure of the *polarizability* of the material. In optical fibers, due to the inversion symmetry of the silicon molecules, even-order $\boldsymbol{\chi}^{(n)}(t)$ are zero. The

fifth and higher order susceptibilities are small and can be neglected for the power range used in optical communication systems [Hel77]. As a result, only the linear and cubic polarizations are the dominant contributions to the evolution of the electric field in the fiber.

2.2.1 Linear material polarization

The linear susceptibility $\boldsymbol{\chi}^{(1)}$ is a second rank tensor with frequency-dependent complex elements, that relates the linear polarization with the strength of the electric field by the linear term in (2.9). This relationship can be written in the frequency domain in matrix form as

$$\tilde{\mathbf{P}}^{(1)}(\mathbf{r}, \omega) = \varepsilon_0 \tilde{\boldsymbol{\chi}}^{(1)}(\omega) \cdot \tilde{\mathbf{E}}(\mathbf{r}, \omega). \tag{2.10}$$

Equivalently, each component of the linear material polarization can be expressed in summation form as

$$\tilde{P}_k^{(1)}(\mathbf{r}, \omega) = \varepsilon_0 \sum_l \tilde{\chi}_{kl}^{(1)}(\omega) \tilde{E}_l(\mathbf{r}, \omega), \tag{2.11}$$

where

$$\tilde{\chi}_{kl}^{(1)}(\omega) = \int_{-\infty}^{\infty} \chi_{kl}^{(1)}(t) e^{-j\omega t} \, \mathrm{d}t \tag{2.12}$$

are the Fourier-transformed elements of $\boldsymbol{\chi}^{(1)}(t)$ and $k, l \in \{x, y, z\}$.

The first-order material susceptibility gives origin to all linear fiber effects. These can be separated from each other by expressing $\boldsymbol{\chi}^{(1)}$ through the relative permittivity tensor of the material

$$\varepsilon_r = \mathbf{I}_3 + \boldsymbol{\chi}^{(1)}, \tag{2.13}$$

where $\mathbf{I}_3$ is the 3×3 identity matrix . Concordantly, the elements of $\boldsymbol{\chi}^{(1)}$ can be expressed as

$$\chi_{kl}^{(1)} = (\varepsilon_{r,r} - j\varepsilon_{r,i} - 1)\, \delta_{kl} + \Delta\varepsilon_{r,kl}, \tag{2.14}$$

where δ_{kl} is the Kronecker delta function with $\delta_{kl} = 1$ when $k = l$ and $\delta_{kl} = 0$ otherwise.

The term $\varepsilon_{r,r}$ relates to the refractive index of the material by $\varepsilon_{r,r} = n^2(\mathbf{r}, \omega)$. Its frequency dependence causes the effect of *material dispersion* that contributes the greatest to *chromatic dispersion*. The imaginary part of $\chi_{kl}^{(1)}$ is associated with the linear attenuation of the fiber, and due to the homogeneity of the fiber in a large scale, it can be considered independent of the spatial coordinates. $\Delta\varepsilon_{r,kl}$ models birefringence and mode coupling that, ultimately, lead to the effect of *polarization mode dispersion*. *Polarization dependent loss* can also be modeled if $\Delta\varepsilon_{r,kl}$ is allowed to have an imaginary part. All of these effects cause the performance of a communication system to detriment and will be treated in more detail later in this chapter.

In the derivations of this chapter, and in most of this thesis, the waveguide will be considered perfectly cylindrical and isotropic, i.e., its optical properties at each point are

independent of the direction along which the electrical field is applied. Therefore, $\Delta\varepsilon_{r,kl}$ is always zero and $\chi_{xx}^{(1)} = \chi_{yy}^{(1)} = \chi_{zz}^{(1)}$. Following this assumption, (2.10) can be written as

$$\tilde{\mathbf{P}}^{(1)}(\mathbf{r},\omega) = \varepsilon_0 \; \tilde{\chi}_{xx}^{(1)}(\omega) \cdot \tilde{\mathbf{E}}(\mathbf{r},\omega). \tag{2.15}$$

2.2.2   Nonlinear material polarization

The most relevant nonlinear effects that detriment the performance of an optical communication link originate from the third-order susceptibility $\boldsymbol{\chi}^{(3)}$. Most notably, its real part is responsible for the dependance of the refractive index on the intensity of the applied electric field, generally known as the *Kerr effect*. This effect leads to degradations through self-phase modulation, cross-phase modulation and four-wave mixing, all of which will be described more thoroughly later in this chapter.

$\boldsymbol{\chi}^{(3)}$ is a fourth rank tensor with 81 frequency-dependent complex elements, that relate the cubic material polarization vector with the electric field by the last term in (2.9). Conveniently, significant simplifications occur if *Raman effects* are neglected by considering the nonlinear response of the fiber *instantaneous*. This is true for the frequency range and channel separation in which dense wavelength division multiplexing systems operate [Goe10]. Following these assumptions, the cubic material polarization can be written as

$$\mathbf{P}^{(3)}(\mathbf{r},t) = \varepsilon_0\boldsymbol{\chi}^{(3)} \vdots \mathbf{E}(\mathbf{r},t)\mathbf{E}(\mathbf{r},t)\mathbf{E}(\mathbf{r},t), \tag{2.16}$$

where the elements $\boldsymbol{\chi}^{(3)}$ are supposed real and constant.

Equivalently, each component of $\mathbf{P}^{(3)}$ can be expressed in summation form as

$$P_k^{(3)}(\mathbf{r},t) = \varepsilon_0 \sum_{lmn} \chi_{klmn}^{(3)} E_l(\mathbf{r},t) E_m(\mathbf{r},t) E_n(\mathbf{r},t), \tag{2.17}$$

where $k,l,m,n \in \{x,y,z\}$.

Due to material symmetries in the fiber, 21 elements of $\boldsymbol{\chi}^{(3)}$ are non-zero of which only three are independent [Boy08]. In consequence, each element of $\boldsymbol{\chi}^{(3)}$ can be written as

$$\chi_{klmn}^{(3)} = \chi_{xxyy}^{(3)}\delta_{kl}\delta_{mn} + \chi_{xyxy}^{(3)}\delta_{km}\delta_{ln} + \chi_{xyyx}^{(3)}\delta_{kn}\delta_{lm}. \tag{2.18}$$

Inserting (2.18) into (2.17) we get that

$$\begin{aligned} P_k^{(3)}(\mathbf{r},t) &= \varepsilon_0 \sum_l \chi_{xxyy}^{(3)} E_k E_l E_l + \chi_{xyxy}^{(3)} E_l E_k E_l + \chi_{xyyx}^{(3)} E_l E_l E_k \\ &= \varepsilon_0 \sum_l \left(\chi_{xxyy}^{(3)} + \chi_{xyxy}^{(3)} + \chi_{xyyx}^{(3)} \right) E_k E_l^2, \end{aligned} \tag{2.19}$$

where for simplicity of notation the time and space dependence of $\mathbf{P}^{(3)}$ and $\mathbf{E}$ was dropped.

Finally, noting from (2.18) that $\chi^{(3)}_{xxxx} = \chi^{(3)}_{xxyy} + \chi^{(3)}_{xyxy} + \chi^{(3)}_{xyyx}$, an expression for the cubic material polarization is obtained:

$$P^{(3)}_k(\mathbf{r}, t) = \varepsilon_0 \chi^{(3)}_{xxxx} \sum_l E_k(\mathbf{r}, t) E^2_l(\mathbf{r}, t). \tag{2.20}$$

For example, consider a real horizontally polarized optical field propagating in the z direccion

$$\mathbf{E}(\mathbf{r}, t) = \hat{\mathbf{x}} \cdot \Re\{E_x(\mathbf{r}, t)\} = \hat{\mathbf{x}} \cdot \left(\tfrac{1}{2} E_x(\mathbf{r}, t) + \tfrac{1}{2} E^*_x(\mathbf{r}, t) \right), \tag{2.21}$$

where $E_x(\mathbf{r}, t) = \underline{E}_x(\mathbf{r}, t) e^{j\omega_c t}$ and $\underline{E}_x(\mathbf{r}, t)$ is the complex slowly varying amplitude of the field oscillating at the carrier frequency ω_c. The induced cubic material polarization is then obtained by inserting (2.21) into (2.20) and is given by

$$\begin{aligned} P^{(3)}_x(\mathbf{r}, t) &= \varepsilon_0 \chi^{(3)}_{xxxx} \left(\tfrac{1}{2} \underline{E}_x(\mathbf{r}, t) e^{j\omega_c t} + \tfrac{1}{2} \underline{E}^*_x(\mathbf{r}, t) e^{-j\omega_c t} \right)^3 \\ &= \varepsilon_0 \chi^{(3)}_{xxxx} \left(\tfrac{1}{8} \underline{E}^3_x(\mathbf{r}, t) e^{j3\omega_c t} + \tfrac{3}{8} |\underline{E}_x(\mathbf{r}, t)|^2 \underline{E}_x(\mathbf{r}, t) e^{j\omega_c t} + \text{c.c.} \right) \\ &= \tfrac{3}{8} \varepsilon_0 \chi^{(3)}_{xxxx} |E_x(\mathbf{r}, t)|^2 E_x(\mathbf{r}, t) + \text{c.c.} \end{aligned} \tag{2.22}$$

where the term "c.c." stands for complex conjugate.

In deriving (2.22), the term oscillating at the third harmonic frequency of ω_c is not phase-matched and is generally negligible [Agr01].

Equation (2.22) and its frequency domain representation will be useful in chapter 2.4 when describing the nonlinear propagation of optical signals. Its Fourier transform can be written using a double convolution integral, and is given by

$$\tilde{P}^{(3)}_x(\mathbf{r}, \omega) = \tfrac{3}{8} \varepsilon_0 \chi^{(3)}_{xxxx} \iint_{-\infty}^{\infty} E_x(\mathbf{r}, \omega_p) E^*_x(\mathbf{r}, \omega_q) E_x(\mathbf{r}, \omega - \omega_p + \omega_q) \, d\omega_p \, d\omega_q + \text{c.c.} \tag{2.23}$$

2.3 Fiber modes and single-mode condition

A fiber mode refers to a specific solution of the general wave equation with the property that its spatial distribution does not change with propagation. For a given transversal profile of the refractive index and frequency ω_c, the number of modes supported by the fiber and their respective modal distribution and propagation constants can be calculated [Agr01]. In the following section, the guiding properties of a single-mode fiber with step-index profile are derived.

When discussing fiber modes, it is accustomed to observe that the main contribution to the material polarization comes from $\varepsilon_{r,r}$, therefore, nonlinear effects and losses are neglected at first and added later as perturbative terms.

By applying the Fourier transform to (2.7) and inserting (2.15) we obtain

$$\nabla \times \nabla \times \tilde{\mathbf{E}} = \tilde{\varepsilon}_r(\mathbf{r}, \omega) \cdot k_0^2 \tilde{\mathbf{E}}, \tag{2.24}$$
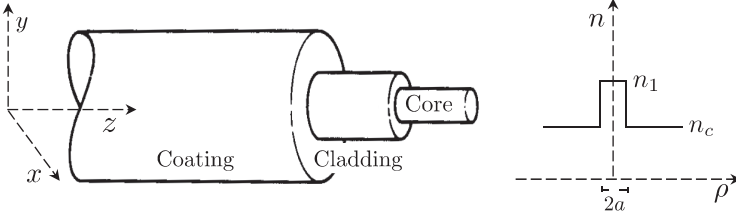
Figure 2.1: Schematic of a step-index fiber structure and index profile. A circular core with refractive index n_1 is surrounded by a cladding with index $n_c < n_1$. A plastic coating encapsulates the fiber.

where $k_0 = \omega/c$ is the free space wave number and $\tilde{\varepsilon}_r(\mathbf{r}, \omega) = 1 + \tilde{\chi}_{xx}^{(1)}(\omega)$ is the scalar version of the relative permittivity tensor defined in (2.13). For fibers with low losses and small birefringence $\tilde{\varepsilon}_r(\mathbf{r}, \omega) \approx n^2(\mathbf{r}, \omega)$.

Further simplifications can be made to (2.24). In a step-index fiber (see Fig. 2.1) the refractive index is independent of the spatial coordinates in the fiber's core and cladding implying that the gradient of the index is zero, i.e., $\nabla n = 0$, and consequently, using (2.4), (2.5) and (2.15), that $\nabla \cdot \mathbf{E} = 0$. This is used in the identity

$$\nabla \times \nabla \times \tilde{\mathbf{E}} = \nabla(\nabla \cdot \tilde{\mathbf{E}}) - \nabla^2\tilde{\mathbf{E}} = -\nabla^2\tilde{\mathbf{E}} \tag{2.25}$$

to obtain the *homogeneous wave equation* in the frequency domain [Agr02]

$$\nabla^2\tilde{\mathbf{E}} + n^2(\omega)k_0^2\tilde{\mathbf{E}} = 0, \tag{2.26}$$

whose analytical solution represents the spatial distribution of a finite number of guided modes. To take advantage of the cylindrical symmetry of the fiber, (2.26) is written in the cylindrical coordinates ρ, ϕ and z as

$$\frac{\partial^2\tilde{\mathbf{E}}}{\partial\rho^2} + \frac{1}{\rho}\frac{\partial\tilde{\mathbf{E}}}{\partial\rho} + \frac{1}{\rho^2}\frac{\partial^2\tilde{\mathbf{E}}}{\partial\phi^2} + \frac{\partial^2\tilde{\mathbf{E}}}{\partial z^2} + n^2(\omega)k_0^2\tilde{\mathbf{E}} = 0, \tag{2.27}$$

where the refractive index is of the form

$$n = \begin{cases} n_1 & , \rho \leq a \\ n_c & , \rho > a. \end{cases} \tag{2.28}$$

A similar equation can be stated for $\tilde{\mathbf{H}}$. From all 6 components of the electric and the magnetic fields, only two are independent. It is customary to solve for $\tilde{E}_z$ and $\tilde{H}_z$, and obtain $\tilde{E}_\rho$, $\tilde{E}_\phi$, $\tilde{H}_\rho$ and $\tilde{H}_\phi$ in terms of them.

Equation (2.27) can be easily solved for the z component using separation of variables, resulting in the following general solution [Kei91, Agr01]:

$$\tilde{E}_z = E_0(\omega)F(\rho)e^{jm\phi}e^{-j\beta z}, \tag{2.29}$$

where β represents the frequency dependent propagation constant of the field; m is a constant that, due to the periodic nature of the field in ϕ, is restricted to be an integer value; $E_0(\omega)$ is the field's amplitude and $F(\rho)$ represents the transverse distribution of the field inside the fiber.

By inserting (2.29) into (2.27) we get

$$\frac{\mathrm{d}^2 F(\rho)}{\mathrm{d}\rho^2} + \frac{1}{\rho}\frac{\mathrm{d}F(\rho)}{\mathrm{d}\rho} + \left(n^2 k_0^2 - \beta^2 - \frac{m^2}{\rho^2}\right) F(\rho) = 0. \tag{2.30}$$

For simplicity of notation, the frequency dependence of the refractive index and of the propagation constant has been dropped and is implicitly understood for the rest of this section. Equation (2.30) is the well-known Bessel's differential equation whose general solution for core and cladding can be written as [Agr02]:

$$F(\rho) = \begin{cases} C_1 J_m(p\rho) + C_2 N_m(p\rho) & , \rho \leq a \\ C_3 K_m(q\rho) + C_4 I_m(q\rho) & , \rho > a, \end{cases} \tag{2.31}$$

where J_m is the Bessel function, N_m is the Neumann function and I_m and K_m are the modified Bessel functions of the first and second kind, respectively[1]. C_i with $i = 1, 2, 3, 4$ are constants that must be determined by the boundary conditions. The parameters p and q are defined by

$$p^2 = n_1^2 k_0^2 - \beta^2, \tag{2.32}$$
$$q^2 = \beta^2 - n_c^2 k_0^2. \tag{2.33}$$

Observe that because p and q are always positive, the values that β can take are restricted to $k_c \leq \beta \leq k_1$, where $k_1 = n_1 k_0$ and $k_c = n_c k_0$ are the wave numbers of the core and the cladding respectively. Due to the singularity of $N_m(p\rho)$ at $\rho = 0$, for a meaningful solution C_2 must be zero. Additionally, the optical field should vanish at $\rho \to \infty$ in the cladding and that happens only if $C_4 = 0$. E_0 in (2.29) is then absorbed by C_1 and C_3 which form $\hat{A}$ and $\hat{B}$, so that the solution of (2.27) can be written as

$$\tilde{E}_z = \begin{cases} \hat{A}(\omega) J_m(p\rho) e^{jm\phi} e^{-j\beta z} & , \rho \leq a \\ \hat{B}(\omega) K_m(q\rho) e^{jm\phi} e^{-j\beta z} & , \rho > a. \end{cases} \tag{2.34}$$

As it was previously mentioned, $\tilde{\mathbf{H}}$ also satisfies (2.27), and thus, the same method can be used to obtain H_z, that derives in the same solution, albeit with different normalization functions:

$$\tilde{H}_z = \begin{cases} \hat{C}(\omega) J_m(p\rho) e^{jm\phi} e^{-j\beta z} & , \rho \leq a \\ \hat{D}(\omega) K_m(q\rho) e^{jm\phi} e^{-j\beta z} & , \rho > a. \end{cases} \tag{2.35}$$

The other four components of the electric and magnetic fields can be expressed in terms of E_z and H_z by using Maxwell's equations (2.1)-(2.4) in the frequency domain with

---

[1]See appendix A for a definition of the abovementioned mathematical functions.

cylindrical coordinates. After some algebraic detail we obtain for the core region:

$$\tilde{E}_\rho = -\frac{j}{p^2}\left(\beta\frac{\partial\tilde{E}_z}{\partial\rho} + \mu_0\frac{\omega}{\rho}\frac{\partial\tilde{H}_z}{\partial\phi}\right), \tag{2.36}$$

$$\tilde{E}_\phi = -\frac{j}{p^2}\left(\frac{\beta}{\rho}\frac{\partial\tilde{E}_z}{\partial\phi} - \mu_0\omega\frac{\partial\tilde{H}_z}{\partial\rho}\right), \tag{2.37}$$

$$\tilde{H}_\rho = -\frac{j}{p^2}\left(\beta\frac{\partial\tilde{H}_z}{\partial\rho} - \varepsilon_0 n_1^2\frac{\omega}{\rho}\frac{\partial\tilde{E}_z}{\partial\phi}\right), \tag{2.38}$$

$$\tilde{H}_\phi = -\frac{j}{p^2}\left(\frac{\beta}{\rho}\frac{\partial\tilde{H}_z}{\partial\phi} + \varepsilon_0 n_1^2\omega\frac{\partial\tilde{E}_z}{\partial\rho}\right). \tag{2.39}$$

The same expressions can be used for the cladding region after replacing p^2 by q^2 and n_1 by n_c. $\hat{A}$, $\hat{B}$, $\hat{C}$ and $\hat{D}$ can be obtained by applying boundary conditions at $\rho = a$, conditioning the tangential components of $\mathbf{E}$ and $\mathbf{H}$ to be continuous between the core and the cladding regions. Therefore, a set of four homogeneous equations is obtained whose solution is nontrivial only if the determinant of the coefficient matrix is zero. This leads to the eigenvalue equation:

$$\left(\frac{1}{p}\frac{J_m'(pa)}{J_m(pa)} + \frac{1}{q}\frac{K_m'(qa)}{K_m(qa)}\right)\left(\frac{n_1^2}{p}\frac{J_m'(pa)}{J_m(pa)} + \frac{n_c^2}{q}\frac{K_m'(qa)}{K_m(qa)}\right) = \left(\frac{m\beta}{a}\right)^2\left(\frac{1}{p^2} + \frac{1}{q^2}\right)^2, \tag{2.40}$$

where the prime symbol represents derivation with respect to the argument.

Due to the oscillatory nature of J_m, (2.40) has multiple solutions of β for every value of m. Each of these solutions represent the propagation constant of one specific mode supported by the fiber. The nth solution of a certain value of m is designated HE_{mn} or EH_{mn} depending on whether H_z or E_z dominates. When $m = 0$, HE_{0n} and EH_{0n} are also denoted TE_{0n} and TM_{0n} respectively, since they correspond to transverse electric ($H_z = 0$) and transverse magnetic ($E_z = 0$) modes of propagation.

Figure 2.2 shows the effective index, defined by $\bar{n} = \beta/k_0$ versus the normalized frequency defined as $V = k_0 a\sqrt{n_1^2 - n_c^2}$. The single-mode condition is determined by the value of V at which the TE_{01} and TM_{01} reach cut-off. It can be obtained by setting $m = 0$ in (2.40) and $\bar{n} = n_c$ or, equivalently, $q = 0$. As a result, the cut-off condition for both modes is given by $J_0(V) = 0$. The smallest value of V that sets the Bessel function to zero is $V = 2.405$. A fiber designed such that $V < 2.405$ supports only the fundamental mode HE_{11}.

In single-mode fibers where $n_1 - n_c \ll 1$, the axial components E_z and H_z are small and either E_x or E_y dominates. These fibers are usually called *weakly guiding* fibers. In such case, the HE_{11} is approximately linearly polarized and sometimes denoted as LP_{01}. At the same time, the fiber supports a second linearly polarized mode in the orthogonal direction. It is, therefore, possible to express these linearly polarized modes propagating along the fiber as

$$\tilde{\mathbf{E}}(\mathbf{r},\omega) = \hat{\mathbf{x}}\cdot\underline{\tilde{E}}_x(\omega)F(x,y)e^{-j\beta_x(\omega)z} + \hat{\mathbf{y}}\cdot\underline{\tilde{E}}_y(\omega)F(x,y)e^{-j\beta_y(\omega)z}, \tag{2.41}$$
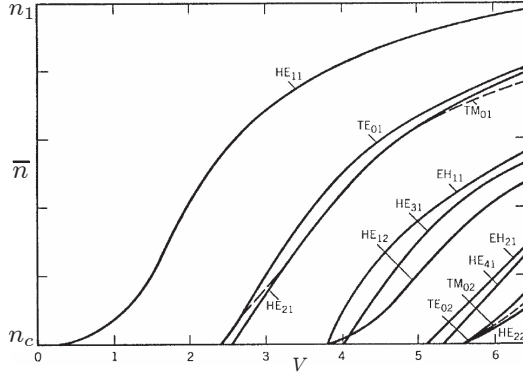
Figure 2.2: Effective index $\overline{n}$ vs. normalized frequency V for a few fiber modes (After [Agr02]). When $V < 2.405$ only a single mode propagates through the fiber.

where the modal distribution is found to be [Agr01]

$$F(x,y) = \begin{cases} J_0(p\rho) & , \rho \leq a \\ \sqrt{a/\rho}J_0(pa)e^{-q(\rho-a)} & , \rho > a, \end{cases} \tag{2.42}$$

and $\rho = \sqrt{x^2 + y^2}$. For practical reasons, the modal distribution is often approximated by a Gaussian distribution of the form

$$F(x,y) \approx e^{-(x^2+y^2)/r_{\text{eff}}^2}, \tag{2.43}$$

where r_{eff} is a frequency dependent fitting parameter.

For ideal fibers with perfectly cylindrical core of uniform diameter the propagation constants of the two orthogonal modes are equal, i.e., $\beta_x = \beta_y$. However, this does not happen in real single-mode fibers as they exhibit considerable variation in the shape of the core along the fiber, either because of fabrication issues or because of nonuniform mechanical stress applied to it. For these reasons, fibers acquire birefringence that is not constant along its length but changes randomly, leading to the effect of polarization-mode dispersion.

2.4 Nonlinear wave propagation

For the practical analysis of the propagation of light in single-mode fibers, a simplified equation known as the nonlinear Schroedinger equation (NLSE) is derived from the more general wave equation (2.7). The propagation of an optical signal through a nonbirefringent fiber will be modeled. It is assumed that the frequency bandwidth of the signal is much smaller than the carrier frequency at which it propagates. Raman effects are neglected.

Consider a horizontally polarized, real modulated optical field of the form

$$\mathbf{E}(\mathbf{r}, t) = \hat{\mathbf{x}} \cdot \Re\{E_x(\mathbf{r}, t)\} = \hat{\mathbf{x}} \cdot \left(\tfrac{1}{2}E_x(\mathbf{r}, t) + \tfrac{1}{2}E_x^*(\mathbf{r}, t)\right), \tag{2.44}$$

The evolution of $E_x(\mathbf{r}, t)$ along the single-mode fiber is governed by the NLSE. In order to derive it, it is more convenient to work in the frequency domain. This is, however, not straightforward because of the intensity dependance of $\mathbf{P}$. One approach is to assume that $\mathbf{P}^{(3)}$ is a small perturbation to $\mathbf{P}$ and that it varies instantly with $\mathbf{E}$ [Agr01]. Consequently, for a birefringent fiber, the x-component of the nonlinear polarization can be approximated by

$$\tilde{P}_x^{(3)}(\mathbf{r}, \omega) \approx \varepsilon_0 \varepsilon_{\mathrm{NL}} \cdot \Re\{\tilde{E}_x(\mathbf{r}, \omega)\}. \tag{2.45}$$

where $\varepsilon_{\mathrm{NL}}$ represents a first-order perturbation constant.

Using (2.15), (2.25) and (2.45), equation (2.7) can be written in the Fourier domain for the positive frequencies of (2.44) as [Agr01]

$$\nabla^2 \tilde{E}_x(\mathbf{r}, \omega) + \hat{\varepsilon}_r k_0^2 \tilde{E}_x(\mathbf{r}, \omega) = 0, \tag{2.46}$$

where $\hat{\varepsilon}_r = \tilde{\varepsilon}_{r,r} - j\tilde{\varepsilon}_{r,i} + \varepsilon_{\mathrm{NL}}$. An additional equation similar to (2.46) is obtained for the negative frequency content of $\mathbf{E}$, however, it does not provide any new information and therefore, it will not be used in the following analysis.

Similar to the procedure shown in chapter 2.3, equation (2.46) can be solved by the method of separation of variables by assuming a solution of the form

$$\tilde{E}_x(\mathbf{r}, \omega) = \tilde{S}(z, \omega - \omega_c)F(x, y)e^{-j\beta_0 z}, \tag{2.47}$$

where

$$\tilde{S}(z, \omega - \omega_c) = \int_{-\infty}^{\infty} S(z, t)e^{-j(\omega - \omega_c)t}\, \mathrm{d}t. \tag{2.48}$$

$S(z, t)$ is the complex slowly-varying amplitude of the modulated field oscillating at the carrier frequency ω_c with propagation constant $\beta_0 = \beta(\omega_c)$. Observe that, in contrast to the amplitude term in (2.29), the amplitude in (2.47) is z-dependent due to the perturbative effect of the nonlinearities and the losses.

Inserting (2.47) into (2.46) and recalling that $\varepsilon_{r,r} = n^2$, we obtain

$$\left(\frac{\partial^2 F}{\partial x^2} + \frac{\partial^2 F}{\partial y^2} + n^2 k_0^2 F\right)\tilde{S} = -\left(\frac{\partial^2 \tilde{S}}{\partial z^2} - 2j\beta_0\frac{\partial \tilde{S}}{\partial z} - \beta_0^2\tilde{S} - j\tilde{\varepsilon}_{r,i}k_0^2\tilde{S} + \varepsilon_{\mathrm{NL}}k_0^2\tilde{S}\right)F, \tag{2.49}$$

where the space and time/frequency dependance of the variables has been dropped for a compact notation. The separation of (2.49) is valid if we assume that the perturbative effect of $\varepsilon_{\mathrm{NL}}$ is small and does not affect the modal distribution F. With these assumptions, for equation (2.49) to hold, both sides must be equal to $\kappa(\omega)\tilde{S}F$, where $\kappa(\omega)$ is a separation constant that is independent of F or $\tilde{S}$. Thus, two equations are obtained:

$$\frac{\partial^2 F}{\partial x^2} + \frac{\partial^2 F}{\partial y^2} + \left(n^2 k_0^2 - \kappa(\omega)\right) F = 0 \tag{2.50}$$

and

$$\frac{\partial^2 \tilde{S}}{\partial z^2} - 2j\beta_0 \frac{\partial \tilde{S}}{\partial z} + \left(\kappa(\omega) - \beta_0^2\right) \tilde{S} = j\tilde{\varepsilon}_{r,i} k_0^2 \tilde{S} - \varepsilon_{\mathrm{NL}} k_0^2 \tilde{S}. \tag{2.51}$$

Equation (2.50) is equivalent to (2.30) for single-mode fibers ($m = 0$). Its solution represents the modal distribution obtained in (2.42). Observe that the separation constant has a physical meaning: it relates to the frequency-dependent propagation constant by $\kappa(\omega) = \beta^2(\omega)$.

Some simplifications can be made to (2.51). Because the perturbed field's amplitude varies very slowly compared to the light's wave oscillations, the term involving the second derivative with respect to z can be neglected. This is usually referred to as the *slowly-varying wave* approximation [Han95]. In addition, it is valid to approximate $\beta^2(\omega) - \beta_0^2 \approx 2\beta_0 \left(\beta(\omega) - \beta_0\right)$. Consequently, (2.51) can be written as

$$\frac{\partial \tilde{S}}{\partial z} + j \left(\beta(\omega) - \beta_0\right) \tilde{S} = -\frac{\alpha(\omega)}{2} \tilde{S} - \frac{j}{2} \frac{k_0^2}{\beta_0} \varepsilon_{\mathrm{NL}} \tilde{S}, \tag{2.52}$$

where the attenuation coefficient $\alpha(\omega) = k_0^2 \varepsilon_{r,i}/\beta_0$ was introduced.

Since the bandwidth of $S(z,t)$ is significantly smaller than the carrier frequency $f_c = \frac{\omega_c}{2\pi}$ that is in the order of hundreds of THz, several simplifications can be made to (2.52). Firstly,

$$\frac{k_0^2}{\beta_0} \approx \frac{\omega_c^2}{\beta_0 c^2} \tag{2.53}$$

and $\alpha(\omega) \approx \alpha(\omega_c)$. Furthermore, $\beta(\omega)$ can be expanded in a Taylor series around the carrier frequency such that

$$\beta(\omega) = \beta_0 + \beta_1 \cdot (\omega - \omega_c) + \tfrac{1}{2}\beta_2 \cdot (\omega - \omega_c)^2 + \tfrac{1}{6}\beta_3 \cdot (\omega - \omega_c)^3 + \dots, \tag{2.54}$$

with $\beta_m = \frac{\partial^m \beta(\omega)}{\partial \omega^m}\big|_{\omega=\omega_c}$. Higher order terms are negligible under the abovementioned assumption. The cubic term can be neglected in many practical cases as well, however, it must be included when the signal propagates near the zero-dispersion wavelength, i.e., when $\beta_2 \approx 0$. With this approximations (2.52) can be written as

$$\frac{\partial \tilde{S}}{\partial z} + j \left(\beta_1 \cdot (\omega - \omega_c) + \tfrac{1}{2}\beta_2 \cdot (\omega - \omega_c)^2\right) \tilde{S} = -\frac{\alpha(\omega_c)}{2} \tilde{S} - \frac{j}{2} \frac{k_0^2}{\beta_0} \varepsilon_{\mathrm{NL}} \tilde{S}, \tag{2.55}$$

The term $\varepsilon_{\mathrm{NL}} \tilde{S}$ in the right-hand side of (2.55) can be expanded by inserting (2.47) into equations (2.45) and (2.23), which yields

$$\frac{\partial \tilde{S}}{\partial z} + j \left(\beta_1 \cdot \omega' + \tfrac{1}{2}\beta_2 \cdot \omega'^2\right) \tilde{S} = -\frac{\alpha(\omega_c)}{2} \tilde{S} -$$
$$j\frac{3}{8} \frac{\omega_c^2}{\beta_0 c^2} \chi_{xxxx}^{(3)} |F|^2 \iint_{-\infty}^{\infty} \tilde{S}(\omega_p') \tilde{S}^*(\omega_q') \tilde{S}(\omega' - \omega_p' + \omega_q') \, \mathrm{d}\omega_p' \, \mathrm{d}\omega_q', \tag{2.56}$$

where the tilde sign indicates translation in angular frequency, i.e., $\omega' = \omega - \omega_c$.

Applying the inverse Fourier transform to (2.56) results in the NLSE:

$$\frac{\partial S}{\partial z} + \beta_1 \frac{\partial S}{\partial t} - \frac{1}{2} j \beta_2 \frac{\partial^2 S}{\partial t^2} = -\frac{1}{2} \alpha(\omega_c) S - j \frac{3}{8} \frac{\omega_c^2}{c^2} \frac{\chi_{xxxx}^{(3)}}{\beta_0} |F|^2 |S|^2 S. \tag{2.57}$$

It is usually more convenient to describe the electromagnetic wave in terms of its power P. For this purpose we define a normalized signal $A(z,t) = \sqrt{P} \cdot S(z,t)$, such that $|A|^2 = P$. The power is defined as the product between the temporal mean value of the wave's intensity and the area within it propagates, i.e., $P = \iint I \, \mathrm{d}x \, \mathrm{d}y$. The intensity I of an electromagnetic wave of the form of (2.44) is given by [Sch04]

$$I = \frac{1}{2Z_f} |E_x(\mathbf{r}, t)|^2, \tag{2.58}$$

where Z_f is the impedance of the medium, that relates to the free space impedance Z_0 by $Z_f = Z_0/n$. Using (2.47), (2.58) and calculating the power, we obtain the normalized signal

$$A(z,t) = S(z,t) \sqrt{\frac{1}{2Z_f} \iint |F(x,y)|^2 \, \mathrm{d}x \, \mathrm{d}y}. \tag{2.59}$$

Using (2.59), equation (2.57) can be written as

$$\frac{\partial A}{\partial z} + \beta_1 \frac{\partial A}{\partial t} - \frac{1}{2} j \beta_2 \frac{\partial^2 A}{\partial t'^2} = -\frac{\alpha(\omega_c)}{2} A - j \frac{3}{8} \frac{\omega_c^2}{c^2} \frac{\chi_{xxxx}^{(3)}}{\beta_0} \frac{2 Z_f |F|^2}{\iint |F|^2 \, \mathrm{d}x \, \mathrm{d}y} |A|^2 A. \tag{2.60}$$

Equation (2.60) can be further simplified by reducing the model to that of an equivalent plane wave propagating within an effective area. For this purpose it is multiplied by the transversal field distribution $|F|^2$ and integrated over the whole cross-section. The resulting equation is written as

$$\frac{\partial A}{\partial z} + \beta_1 \frac{\partial A}{\partial t} - \frac{1}{2} j \beta_2 \frac{\partial^2 A}{\partial t'^2} = -\frac{\alpha(\omega_c)}{2} A - j\gamma |A|^2 A. \tag{2.61}$$

where

$$\gamma = \frac{3}{4} \frac{\omega_c^2}{c^2} \frac{\tilde{\chi}_{xxxx}^{(3)}}{\beta_0} \frac{Z_f}{A_{\text{eff}}} = \frac{\omega_c}{c A_{\text{eff}}} \cdot \underbrace{\frac{3 Z_0 \tilde{\chi}_{xxxx}^{(3)}}{4 n_1^2}}_{n_2} \tag{2.62}$$

is the *nonlinear coefficient* that is proportional to the *nonlinear index coefficient* n_2; and A_{eff} corresponds to the *effective mode area* [Agr01] defined as

$$A_{\text{eff}} = \frac{\left(\iint |F(x,y)|^2 \, \mathrm{d}x \, \mathrm{d}y \right)^2}{\iint |F(x,y)|^4 \, \mathrm{d}x \, \mathrm{d}y}. \tag{2.63}$$

If the Gaussian approximation (2.43) is used, equation (2.63) becomes $A_{\text{eff}} = \pi \cdot r_{\text{eff}}^2$. In obtaining γ the approximation $\beta_0 \approx \frac{\omega_c}{c} n_1$ was used. Observe that, in practice, different types of fibers are characterized by the nonlinear parameters γ, n_2 and A_{eff}.

An additional simplification occurs in (2.61) by substituting

$$t' = t - z/v_g = t - \beta_1 z, \tag{2.64}$$

which is equivalent to observe the signal propagation relative to a reference frame moving through the fiber with the same speed as the signal's group velocity v_g. Using (2.64) in (2.61) yields

$$\frac{\partial A(z,t')}{\partial z} - \frac{1}{2} j \beta_2 \frac{\partial^2 A(z,t')}{\partial t'^2} = -\frac{\alpha(\omega_c)}{2} A(z,t') - j\gamma |A(z,t')|^2 A(z,t'). \tag{2.65}$$

The time variable t' is usually called the *local time*. From this point forward, the prime sign will be dropped and the use of local time is implicitly understood.

Equation (2.65) can be solved analytically only in particular cases, when either attenuation, dispersion or nonlinearities are neglected. In general, a close form solution does not exist and numerical simulations are commonly used to model the evolution of the optical signal along the fiber.

2.5 Length scales and propagation regimes

In analyzing the interaction between the linear and non linear effects that impact the evolution of an optical pulse along the fiber, it is useful to define characteristic lengths in order to identify various propagation regimes. Two length scales that give insights about the dominance of dispersion over nonlinearities or viceversa are the *dispersion length*

$$L_{\text{D}} = \frac{T_0}{\beta_2} \tag{2.66}$$

and the *nonlinear length*

$$L_{\text{NL}} = \frac{1}{\gamma P}, \tag{2.67}$$

where T_0 is the pulse duration and P is the average signal power. The NLSE can be written as a function of L_{D} and L_{NL} by means of the substitutions [Agr02]

$$A(z,t) = a(z,t) e^{-\frac{\alpha}{2}z} \sqrt{P} \tag{2.68}$$

and

$$\tau = \frac{t}{T_0}, \tag{2.69}$$

where $a(z,t)$ represents a dimensionless unattenuated optical signal and τ is a normalized time variable. Using equations (2.68) and (2.69) the NLSE (2.65) can be written as

$$\frac{\partial a(z,\tau)}{\partial z} - j\frac{1}{2L_{\text{D}}} \text{sgn}(\beta_2) \frac{\partial^2 a(z,\tau)}{\partial \tau^2} = -j\gamma \frac{e^{-\alpha z}}{L_{\text{NL}}} |a(z,\tau)|^2 a(z,\tau). \tag{2.70}$$

The dispersion term in (2.70) is negligible for long dispersion lengths, i.e., from (2.66), when either the pulse width is broad or the fiber dispersion is small. The nonlinear term in (2.70) is negligible for long nonlinear lengths; from (2.67) this occurs when the nonlinear parameter γ is small or when the average signal power is low. Generally, four propagation regimes can be recognized for a fiber of length L [Sch04]:

▷ If $L \ll L_{\mathrm{D}}$ and $L \gtrsim L_{\mathrm{NL}}$ dispersion plays a minor role and nonlinearities dominate. This is generally the situation for a system with a low bit rate such as 2.5 Gb/s or less.

▷ If $L \gtrsim L_{\mathrm{D}}$ and $L \gtrsim L_{\mathrm{NL}}$ both dispersion and nonlinearities have a strong impact on the signal and their interaction must be considered. This is the typical situation for 10 Gb/s systems operating over standard single-mode fiber (SSMF). This regime is beneficial for the generation of solitons (see ch. 2.9) and accordingly, it is sometimes referred to as *soliton regime* [Xia08].

▷ When $L \gtrsim L_{\mathrm{D}}$ and $L \ll L_{\mathrm{NL}}$ dispersion is the dominant effect and nonlinearities can be treated in a perturbative manner. If $L_{\mathrm{D}} \ll L_{\mathrm{NL}}$, large pulse spreading occurs through dispersion, reducing the high peak power of individual pulses and, therefore, limiting the effect of nonlinearities. This is usually referred to as *pseudo-linear regime of propagation* [MM99, STM+98] since, similar to linear transmission, the optimum residual dispersion for single-channel transmission is around 0 ps/nm. This situation is generally met in optical systems with high bit rate, i.e., 40 Gb/s and beyond.

▷ If $L \ll L_{\mathrm{D}}$ and $L \ll L_{\mathrm{NL}}$ neither dispersion nor nonlinearities have a strong impact on the propagation of the signal.

2.6   Propagation of WDM signals

In wavelength-division multiplexed (WDM) systems, the available bandwidth of the fiber is used to propagate a comb of independently modulated optical signals at different optical frequencies. Usually the spacing between dense WDM (DWDM) signals is equal and can go from 100 GHz down to 50 GHz. The NLSE, derived in the previous section for a single-channel case, can also be used to analyse the evolution of several optical signals co-propagating along the fiber. This is done by assuming that the input field to an optical fiber composed of K multiplexed signals is of the form

$$A(z,t) = \sum_{k=1}^{K} U_k(z,t) e^{j\Delta\omega_k t}, \tag{2.71}$$

where U_k is the slowly varying envelope of the signal in channel k and $\Delta\omega_k = \omega_k - \omega_c$ is the difference between the central frequency of channel k and the frequency of the center channel of the WDM comb.

The simulation of the propagation of such a signal along the fiber is usually referred to as the *total field* approach. By using (2.71) as input to the NLSE, all linear[2] and nonlinear (Kerr) interactions between the WDM signals are accounted for. However, because of the great bandwidth of the input signal, simulations using the total field can take considerable effort. Firstly, a great number of points per symbol must be used to comply with the Nyquist-Shannon sampling theorem [Sha49]. Furthermore, because of nonlinear effects, new frequencies are created along propagation that enlarge the spectrum and, in turn, increase the requirements for the simulation's temporal resolution.

Secondly, as it will be discussed in the following section, the number of iteration steps of the numerical algorithm used to solve the NLSE is directly proportional to the maximum instantaneous power of the signal, which tends to remain high in the case of a total field approach. In the single-channel case, spikes in the instantaneous power occur due to overlap of neighboring pulses. However, their amplitude decrease monotonically with distance. By contrast, due to pulses from different channels rapidly passing through each other, the peak power of the multi-channel system presents spikes irregularly distributed along the propagation length that do not necessarily decrease monotonically in amplitude [SHZM03]. This translates into notoriously smaller steps when simulating multi-channel in comparison to single-channel systems.

Due to the mentioned reasons, it is of interest to obtain a separate propagation equation for each WDM channel. This is usually referred to as the *coupled equations* approach. Moreover, additional insights can be gained regarding the nonlinear interaction between WDM channels when deriving the coupled system of equations. For this purpose, it is more convenient to analyze the linear and nonlinear parts of the NLSE separately. Observe that, since the signals in the WDM comb experience *walk-off*, i.e., each one propagates with a different group velocity, it is not appropriate to use (2.65) as a starting point but (2.61) instead.

Consider the linear part of (2.61) written in the frequency domain as

$$\frac{\partial \tilde{A}(z,\omega)}{\partial z} = -\frac{\alpha(\omega_c)}{2}\tilde{A}(z,\omega) - j\hat{\beta}(\omega)\tilde{A}(z,\omega), \qquad (2.72)$$

where

$$\tilde{A}(z,\omega) = \sum_k \tilde{U}_k(z,\omega - \Delta\omega_k) \qquad (2.73)$$

is the Fourier transform of $A(z,t)$, $k = 1, 2, \ldots, K$ and

$$\hat{\beta}(\omega) = \beta_1 \cdot \omega + \tfrac{1}{2}\beta_2 \cdot \omega^2 + \tfrac{1}{6}\beta_3 \cdot \omega^3 + \cdots . \qquad (2.74)$$

Inserting (2.73) into (2.72) and applying the superposition principle, we get a set of linear equations, each describing one WDM channel, written as

$$\frac{\partial \tilde{U}_k(z,\omega)}{\partial z} = -\frac{\alpha(\omega_c)}{2}\tilde{U}_k(z,\omega) - j\hat{\beta}^{(k)}(\omega)\tilde{U}_k(z,\omega), \qquad (2.75)$$

---

[2]Observe that the NLSE derived in chapter 2.4 models nonbirefringent fibers, and therefore polarization effects are excluded from the linear interactions which are accounted for by using the total field approach.

with $\hat{\beta}^{(k)}(\omega) = \beta_1^{(k)} \cdot \omega + \frac{1}{2}\beta_2^{(k)} \cdot \omega^2 + \frac{1}{6}\beta_3^{(k)} \cdot \omega^3 + \cdots$ and $\beta_m^{(k)} = \frac{\partial^m \beta(\omega)}{\partial \omega^m}\big|_{\omega=\omega_k}$. The values that β_m^k take for each WDM channel will be discussed in detail in chapter 3.2.2. Observe that $\alpha(\omega_k) \approx \alpha(\omega_c)$ was assumed. This is true for the wavelength range of modern DWDM systems.

Now, consider the nonlinear part of (2.61) written in the time domain as

$$\frac{\partial A(z,t)}{\partial z} = -j\gamma |A(z,t)|^2 A(z,t). \tag{2.76}$$

Using the identity $|A(z,t)|^2 = A(z,t)A^*(z,t)$ and inserting (2.71) into (2.76) we obtain

$$\sum_k \frac{\partial U_k}{\partial z} e^{j\Delta\omega_k t} = -j\gamma \sum_l \sum_m \sum_n U_l U_m U_n^* e^{j(\Delta\omega_l + \Delta\omega_m - \Delta\omega_n)t}, \tag{2.77}$$

where the spatial and temporal dependence has been dropped for a compact notation. Equation (2.77) is not directly separable under the superposition principle because of the terms that fall outside of the bandwidth of $A(z,t)$ and that cannot be associated with any frequency ω_k, i.e., $\omega_k \neq \omega_l + \omega_m - \omega_n$. Fortunately, such terms are usually of small energy for pseudo-linear systems and can be neglected [Agr01]. With this assumption, (2.77) is written as a coupled system of equations

$$\frac{\partial U_k}{\partial z} = -j\gamma_k \sum_{\substack{l,m,n \\ \omega_l+\omega_m-\omega_n=\omega_k}} U_l U_m U_n^*, \tag{2.78}$$

where $\gamma_k = \gamma(\omega_k)$. From (2.62) it follows that $\gamma_k = \gamma_r \lambda_r / \lambda_k$, where γ_r is a reference value of the nonlinear coefficient at a wavelength λ_r and λ_k is the wavelength of the kth channel.

Note that each WDM signal propagates with a different propagation constant, therefore, the appropriate phase shift must be added when writing the equations of each WDM channel. This is done by substituting

$$U_k(z,t) = A_k(z,t)e^{-j\beta_0^{(k)}z}. \tag{2.79}$$

Merging the nonlinear part (2.78) with the linear part (2.75) written in the time domain, we obtain the following set of coupled equations:

$$\frac{\partial A_k}{\partial z} + \beta_1^{(k)}\frac{\partial A_k}{\partial t} - \frac{1}{2}j\beta_2^{(k)}\frac{\partial^2 A_k}{\partial t^2} = -\frac{\alpha}{2}A_k - j\gamma_k \sum_{\substack{l,m,n \\ \omega_l+\omega_m-\omega_n=\omega_k}} A_l A_m A_n^* e^{-j\Delta\beta_{lmn}z}, \tag{2.80}$$

where $\Delta\beta_{lmn} = \beta_0^{(l)} + \beta_0^{(m)} - \beta_0^{(n)} - \beta_0^{(k)}$ is called the *phase matching* coefficient.

Different inter-channel nonlinear effects can be identified in (2.80) by varying the indices l, m and n. Self-phase modulation (SPM) in each WDM signal is accounted for by the term given by $\omega_l = \omega_m = \omega_n = \omega_k$. Cross-phase modulation (XPM) occurs when $(\omega_l = \omega_n) \neq (\omega_m = \omega_k)$, or when $(\omega_l = \omega_k) \neq (\omega_n = \omega_m)$. Note that SPM and XPM are always

phase-matched, i.e., the phase matching coefficient is always zero. The set $\mathcal{L}$ of all other combinations of l, m and n give raise to four-wave mixing (FWM). By expressing all these effects explicitly in (2.80), we obtain

$$\frac{\partial A_k}{\partial z} = - \underbrace{\frac{\alpha}{2}A_k}_{\text{attenuation}} - \underbrace{\beta_1^{(k)}\frac{\partial A_k}{\partial t}}_{\text{walk-off}} + \underbrace{\frac{1}{2}j\beta_2^{(k)}\frac{\partial^2 A_k}{\partial t^2}}_{\text{chromatic dispersion}}$$

$$- \underbrace{j\gamma_k|A_k|^2 A_k}_{\text{SPM}}$$

$$- j\gamma_k \cdot 2 \underbrace{\sum_{l \neq k}|A_l|^2 A_k}_{\text{XPM}}$$

$$- j\gamma_k \underbrace{\sum_{l,m,n \in \mathcal{L}} A_l A_m A_n^* e^{-j\Delta\beta_{lmn}}}_{\text{FWM}} . \tag{2.81}$$

FWM is responsible for energy transfer between WDM channels, and its strength decreases with channel separation. It is, however, effectively suppressed by the phase mismatch in WDM systems caused by chromatic dispersion. This is not true if fibers with a low value of dispersion are used, e.g., dispersion shifted fibers.

Because XPM is always phase matched its strength, in principle, does not vary with channel separation. Furthermore, from (2.81) it appears that the impact of XPM between two channels is twice as large as that of SPM. However, the walk-off that the two channels experience causes an averaging effect that reduces the strength of XPM [KK97a]. Thus, the detrimental effect of XPM decreases when channel separation increases.

If the propagation of all channels is taken relative to the center channel, then (2.64) can be used in (2.81). In the absence of FWM the coupled equations can be written as

$$\frac{\partial A_k}{\partial z} + \left(\beta_1^{(k)} - \beta_1\right)\frac{\partial A_k}{\partial t} - \frac{1}{2}j\beta_2^{(k)}\frac{\partial^2 A_k}{\partial t^2} = -\frac{\alpha}{2}A_k - j\gamma_k\left(|A_k|^2 + 2\sum_{l \neq k}|A_l|^2\right)A_k. \tag{2.82}$$

As it will be shown later in this chapter, equation (2.82), in contrast to (2.81), can be easily solved with numeric algorithms. However, (2.82) should not be used if the channel separation relative to the bandwidth of the signals is small, as it does not take into consideration the spectrum overlap of neighboring channels and it neglects FWM. If channel separation is small, the total field approach given by (2.65) should be used instead.

2.7 Inter- and intra-channel nonlinear effects

The nonlinear effects of SPM, XPM and FWM are accounted for by the nonlinear term in the NLSE (2.65). They are defined in the frequency domain by the interaction between

four discrete frequencies propagating through the fiber. In the context of WDM, XPM and FWM effects are usually referred to as *inter-channel* effects and describe the interaction between all signals in the WDM comb. On the other hand, the nonlinear effect of a WDM signal onto itself, labeled SPM in equation (2.81), comprises all nonlinear interactions of the spectral components of the signal through the *intra-channel* processes of SPM, XPM and FWM. In this context, they are usually referred to as ISPM, IXPM and IFWM [Agr02, EMR99].

The intra-channel effects are usually analyzed in the time domain by modeling the interaction between the pulses of a signal in a way similar to the derivation of the WDM coupled equations in chapter 2.6. Consider the signal $A(z,t)$ composed of a train of K pulses p_k of duration T_0:

$$A(z,t) = \sum_{k=1}^{K} p_k(z, t - kT_0). \tag{2.83}$$

Inserting (2.83) into the NLSE (2.65), we obtain

$$\sum_k \left(\frac{\partial p_k}{\partial z} - \frac{1}{2} j\beta_2 \frac{\partial^2 p_k}{\partial t^2} + \frac{\alpha}{2} p_k \right) = -j\gamma_k \sum_{l,m,n} p_l p_m p_n^*, \tag{2.84}$$

where $k, l, m, n = 1, 2, \ldots, K$. The triple sum at the right side of (2.84) includes all intra-channel nonlinear effects. ISPM occurs when $l = m = n$. When dispersion is high, due to the broadening of the pulse and the consequent reduction in peak power, ISPM is considerably reduced. The term responsible for IXPM correspond to $l = m \neq n$ and $l \neq m = n$. Even though IXPM affects only the phase of each pulse, this phase shift is time dependent and, therefore, affects the carrier frequency of the pulse. The resulting frequency chirp leads to time jitter through fiber dispersion [MCS00]. The remaining terms that do not correspond to ISPM and IXPM give origin to IFWM. Intra-channel FWM is a nonlinear process where energy transfer between pulses can take place. For example, in intensity modulated systems using on-off keying, it can create new pulses in bit slots that represent 0's and contain no pulse initially. Such IFWM-generated pulses are usually referred to as *ghost* or *shadow pulses* and lead to additional errors if their amplitude becomes substantial [EMR99].

The dominance of inter- or intra-channel effects in a transmission system is in general dependent on the system design. For example, in the pseudo-linear regime, where signal dispersion is kept high along propagation, the spreading of pulses belonging to different WDM channels produces an averaging effect that reduces the inter-channel nonlinear effects considerably [Agr02]. However, at the same time, the interaction between pulses of the same channel produces intra-channel nonlinear effects that dominate and limit the system performance. Quite the opposite occurs when dispersion is tightly controlled as, for example, in dispersion-managed soliton systems, where inter-channel effects dominate and seriously impair the performance of the transmission system [DDKB04].

2.8 Other propagation effects

A handful of fiber effects were not taken into account in the derivation of the NLSE and are not considered in the rest of the thesis. Polarization effects may be the most important ones since they produce dispersion-induced inter-symbol interference and, at the same time, affect the strength of the Kerr nonlinearities. The implications of not considering these effects in the results of this thesis are subsequently addressed. Finally, nonlinear phase noise and nonlinear scattering processes are briefly described.

2.8.1 Polarization effects

As discussed in chapter 2.3, two orthogonal fundamental modes are able to propagate in a single-mode fiber. In deriving the NLSE, ideal fibers with perfectly cylindrical core of uniform diameter were assumed such that both modes have identical propagation properties. In practice, however, this does not occur and the modes propagate with different velocities and exchange power along the way. This is referred to as *birefringence* and *mode coupling*, respectively. When a pulse excites both polarization components of the fundamental mode it becomes broader as the two components disperse along the fiber due to their different group velocities. In a short piece of fiber of length L, where birefringence can be considered constant, the broadening can be estimated from the time delay $\Delta\tau$ between the two polarization components during propagation of the pulse. The time delay $\Delta\tau$ is usually referred to as *differential group delay* (DGD) and is given by

$$\Delta\tau = L|\beta_{1,x} - \beta_{1,y}|. \tag{2.85}$$

However, for real fibers, the birefringence changes randomly over time, frequency and fiber length because of change in the shape of the core due to fabrication imperfections, mechanical stress applied to the fiber, temperature changes, etc. As a result, *polarization mode dispersion* (PMD) arises as a stochastic process where the DGD value is not constant but changes randomly.

The expected DGD value is referred to as the *PMD value* $\mathcal{E}\{\Delta\tau\}$ and is related to the DGD as $\mathcal{E}\{\Delta\tau\} = \overline{\Delta\tau}$, where $\overline{\Delta\tau}$ represents the mean DGD value. It has been shown that the probability density function for the DGD follows a Maxwellian distribution [KK97a]. In a good approximation, in long fibers the PMD value increases with the square root of the transmission distance, i.e., $\mathcal{E}\{\Delta\tau\} = D_{\mathrm{PMD}}\sqrt{L}$, where D_{PMD} is called the *PMD coefficient* with units of ps/$\sqrt{\mathrm{km}}$. The PMD coefficient is a measure of the quality of the fiber and it varies from $\sim$0.5 ps/$\sqrt{\mathrm{km}}$ for old fibers, to less than 0.1 ps/$\sqrt{\mathrm{km}}$ for new ones.

The impact of PMD scales with the symbol rate and becomes a limiting factor for lightwave systems designed to operate over long distances at high data rates [Agr02]. In such scenarios, and specially when using old fibers with high PMD coefficient, some kind of PMD compensation scheme must be employed [vdB08]. It has been shown in [CGS+10] that, regarding maximum transmission distance, PMD becomes the limiting effect in systems using DPSK and DQPSK with symbol rates above 40 GSym/s.

Additionally, changes in the light polarization due to mode coupling lead to a continuous power exchange between the light wave's orthogonal components, directly influencing the strength of fiber nonlinearities. In [Han95, Goe10] it is shown that the varying polarization state of the propagating field has an averaging effect on the cubic susceptibility $\chi_{xxxx}^{(3)}$. This leads to an effective nonlinear parameter γ_{eff} that varies between $\sim \frac{8}{9}\gamma$ and $\sim \frac{2}{3}\gamma$, depending if the frequency spacing of the interacting waves is small or large, respectively.

Furthermore, the impact of inter-channel nonlinearities is dependent on the relative polarization states of the WDM signals. For example, consider the nonlinear induced material polarization at a frequency ω_1 produced by two real signals propagating at frequencies ω_1 and ω_2. Firstly, let the two signals be co-polarized linearly in the x direction so they can be written as

$$\mathbf{E}_{\parallel}(\mathbf{r}, t) = \hat{\mathbf{x}} \cdot (E_1(\mathbf{r}, t) + E_2(\mathbf{r}, t)) . \tag{2.86}$$

The resulting x-component of the cubic polarization vector oscillating with frequency ω_1 is obtained by inserting (2.86) into (2.20) and can be written as

$$P_{x,\parallel}^{(3)} = \frac{3}{8}\varepsilon_0 \chi_{xxxx}^{(3)} \left(|E_1|^2 E_1 + 2|E_2|^2 E_1 \right) + \text{c.c.} \tag{2.87}$$

The first and second terms at the right side of (2.87) are responsible for SPM and XPM, respectively. The spatial and time dependence of the variables has been dropped for readability. Now, for comparison, let the two signals be perpendicularly polarized linearly in the x and y directions so they can be written as

$$\mathbf{E}_{\perp}(\mathbf{r}, t) = \hat{\mathbf{x}} \cdot E_1(\mathbf{r}, t) + \hat{\mathbf{y}} \cdot E_2(\mathbf{r}, t). \tag{2.88}$$

The resulting x-component of the cubic polarization at ω_1 yields

$$P_{x,\perp}^{(3)} = \frac{3}{8}\varepsilon_0 \chi_{xxxx}^{(3)} \left(|E_1|^2 E_1 + \frac{2}{3}|E_2|^2 E_1 \right) + \text{c.c.} \tag{2.89}$$

Clearly, in the perpendicular case, the impact of XPM is only one third compared to the parallel case. This fact is used in *polarization-interleaved* WDM transmission systems [ZLL$^+$01], where adjacent channels are polarized orthogonally to each other in order to reduce the penalty associated with inter-channel XPM. In classic WDM systems, however, the real impact of XPM varies according to the relative polarization state of the channels. Similarly for the impact of FWM, the strength of the resulting newly generated wave depends on the polarization of the other three interacting waves [Sch04].

Because in the evaluation of WDM systems all channels are considered to be co-polarized, the results presented in the following chapters may slightly overestimate the impact of nonlinearities. More detailed information on the influence of polarization on the nonlinear propagation of signals in fiber-optic systems can be found in [Han95, Coe10, Goe10, Agr01, MMW97] and [MM06].

2.8.2   Nonlinear phase noise

Nonlinear phase noise (NPN), also known as the Gordon-Mollenauer effect after [GM90], results from the nonlinear interaction between the optical signal and the noise produced by the optical amplifiers (see ch. 3). The power fluctuations induced by the noise onto the signal are transformed to phase noise through interaction with the Kerr effect. It is, therefore, of importance only for modulation formats that encode the information in the phase of the optical carrier.

Several methods have been proposed to mitigate the impact of NPN, including optical phase conjugation [LK97b, JvdBM$^+$05] and semiconductor optical amplifiers based regeneration [GSD$^+$06]. In [HK04a] it has been shown that the variance of the NPN can be reduced by a factor of four by using a compensator which rotates the received phase proportional to the received optical power. This results into doubling the transmission distance for systems limited by NPN.

The variance of phase fluctuations decreases as the dispersive effects become more dominant [Kum05]. Since dispersion causes the pulses to spread, peak pulse power is reduced, therefore, averaging out the nonlinear phase contribution. Moreover, the impairing effect of NPN is indirectly related to the data rate. Transmission systems with higher bit rates require lower amounts of accumulated noise along the link to deliver a certain bit-error rate, compared to system using lower bit rate. Consequently, the power of the noise in such systems is not large enough to make a significant contribution to the total nonlinear phase shift and thus, NPN is not the limiting effect. For example in [CGS$^+$10], it was shown that regarding transmission distance, NPN is the limiting effect distance for DPSK and DQPSK systems when symbol rates were below 40 and 30 GSym/s, respectively.

In this thesis, due to the relatively high symbol rate of the considered modulation formats, it is assumed that the effect of NPN on the system performance can be neglected. A more detailed description of the evaluation of the impact of NPN in phase modulated systems can be found in [CMG$^+$09, CGS$^+$10] and [Coe10].

2.8.3   Nonlinear scattering effects

Apart from the Kerr based nonlinearities, two nonlinear scattering effects can take place that may impair fiber-optic transmission systems, namely stimulated Raman scattering and stimulated Brillouin scattering. They manifest themselves as an intensity dependent attenuation of the optical signals.

Stimulated Raman scattering

Stimulated Raman scattering (SRS) is an interaction of the photons of an optical signal with the molecular vibrations of the transmission medium [Isl04]. Its effect on the pulse propagation is accounted for by the imaginary part of the cubic susceptibility in chapter 2.2.2. Observe that it was not considered in the derivation of the NLSE. Fundamentally, SRS occurs when a photon is incident on a molecule of the transmission fiber's

silica, and part of its energy is absorbed. The resulted scattered photon is of lower energy and thus, of lower frequency than the incident one. This happens to a very small fraction of the incident photons and under particular circumstances [Agr01].

In fiber-optic transmission systems, SRS must be considered for systems with high number of WDM channels. When co-propagating signals are present within the Raman bandwidth, SRS can cause a power transfer from shorter to longer wavelengths channels resulting in unwanted crosstalk. The efficiency of the power transfer through SRS is dependent on wavelength and can take place for channels placed up to 125 nm apart [Isl04]. Its peak is at a frequency separation of ∼13.2 THz. This takes effect only for high optical powers greater than 500 mW [Sei10]. Above this threshold, the amplification scales exponentially with the power of the shorter wavelength. This effect is used intentionally to create Raman amplifiers.

In this thesis, since the bandwidth of the analyzed WDM signals is relatively small compared to the Raman bandwidth, and since the total power is below the Raman threshold, SRS is not considered.

Stimulated Brillouin scattering

Stimulated Brillouin scattering (SBS), similarly to SRS, results from the nonlinear interaction of an incident photon with the transmission medium, however, it is not described by the cubic susceptibility tensor. SBS occurs when a pump wave generates acoustic waves in the medium through the process of *electrostriction* [Boy08]. The acoustic wave, in turn, modulates the refractive index of the medium effectively creating a moving reflection grating. The grating scatters the pump light through *Bragg diffraction* and downshifts it in frequency due to the Doppler effect associated with the acoustic velocity of the moving grating [Agr01].

In communication systems employing modulation formats with a strong optical carrier, e.g., on-off-keying, SBS limits the maximum power that can be launched into the fiber. The gain of SBS has a narrow bandwidth of around 20 MHz [Jan06]. Therefore, the generation of SBS is significantly reduced by spreading the energy of the carrier signal over a wider bandwidth. For modulation formats without a strong carrier, like those analyzed in this thesis, SBS can be neglected.

2.9   Solutions of the nonlinear Schroedinger equation

The NLSE (2.65) derived in the previous sections is a powerful model for understanding the propagation of light in the fiber and it is used extensively in order to simulate and characterize the transmission systems investigated in this thesis. In the following section some important analytical solutions of the NLSE are shown followed by a description of the numerical algorithm generally used to solve it.

2.9.1 Analytical solutions of the NLSE

Close form solutions of the Equation (2.65) exist only in special cases where nonlinearities, chromatic dispersion or attenuation are neglected.

If nonlinearities are neglected ($\gamma = 0$), the NLSE can be written as

$$\frac{\partial A(z,t)}{\partial z} = \frac{1}{2} j\beta_2 \frac{\partial^2 A(z,t)}{\partial t^2} - \frac{1}{2}\alpha(\omega_c)A(z,t), \qquad (2.90)$$

whose solution can be directly written in the frequency domain as

$$\tilde{A}(z,\omega) = \tilde{A}(0,\omega) \cdot \exp\left(-\frac{\alpha}{2}z - j\frac{\beta_2}{2}\omega^2 z\right). \qquad (2.91)$$

The term containing β_2 in (2.91) produces dispersion of the group velocity of the signal. This is usually referred to as *group velocity dispersion* (GVD) and is responsible of inter-symbol interference (ISI).

If dispersion is neglected ($\beta_2 = 0$), the NLSE can be written as:

$$\frac{\partial A(z,t)}{\partial z} = -j\gamma|A(z,t)|^2 A(z,t) - \frac{1}{2}\alpha(\omega_c)A(z,t). \qquad (2.92)$$

with the time domain solution written as

$$A(z,t) = A(0,t) \cdot \exp\left(-\frac{\alpha}{2}z - j\gamma|A(0,t)|^2 L_{\text{eff}}\right), \qquad (2.93)$$

where the effective length L_{eff} is defined as $L_{\text{eff}} = (1 - e^{-\alpha z})/\alpha$. The nonlinear term gives rise to an intensity dependent phase shift, whereas the amplitude of the signal is unchanged.

A noteworthy solution of the NLSE is obtained when attenuation is neglected. If the anomalous dispersion regime is considered ($\beta_2 < 0$), it is possible to obtain a solution of the NLSE where the nonlinear chirp ideally cancels the broadening of a pulse caused by dispersion, resulting in undistorted pulse propagation. Such a solution of the NLSE is called a *soliton*. In order to obtain the waveform description of a soliton of peak power P_{sol}, it is useful to normalize (2.65) using $\zeta = \frac{z|\beta_2|}{T_0^2}$, $\tau = \frac{t}{T_0}$ and

$$u(z,t) = A(z,t)\sqrt{\frac{T_0^2 \gamma P_{\text{sol}}}{|\beta_2|}}, \qquad (2.94)$$

where T_0 is a measure of the pulse width. The normalized NLSE with zero attenuation and anomalous dispersion is, therefore, written as [KA03]

$$\frac{\partial u}{\partial \zeta} + \frac{1}{2}j\frac{\partial^2 u}{\partial \tau^2} = -j|u|^2 u. \qquad (2.95)$$

Equation (2.95) is solved by the method of separation of variables, assuming a solution of the form $u(\zeta, \tau) = v(\tau)e^{j\phi(\zeta)}$. By doing the substitution in (2.95) we obtain

$$\frac{\partial \phi}{\partial \zeta} = -\frac{1}{2v}\frac{\partial^2 v}{\partial \tau^2} + v^2. \tag{2.96}$$

Equation (2.96) is separable, i.e., the right and the left sides must be equal to a constant value K, so that $\phi(\zeta) = K \cdot \zeta$ and

$$\frac{\partial^2 v}{\partial \tau^2} = 2v \cdot (K - v^2). \tag{2.97}$$

This equation can be solved by multiplying it with $2\frac{\partial v}{\partial \tau}$ and integrating over τ. Subsequently, boundary conditions are applied so that v and $\frac{\partial v}{\partial \tau}$ vanish for $|\tau| \to \infty$; and $v = 1$ and $\frac{\partial v}{\partial \tau} = 0$ for $\tau = 0$ which, in sum, yields $K = \frac{1}{2}$. The resulting equation is then easily integrated to give a solution of the form $v(\tau) = \text{sech}(\tau)$, where the hyperbolic secant function is defined as $\text{sech}(\tau) = 2/(e^{\tau} + e^{-\tau})$. The solution of (2.95) is then

$$u(\zeta, \tau) = \text{sech}(\tau)e^{j\frac{\zeta}{2}}. \tag{2.98}$$

The power of the soliton can be derived from (2.98) and the normalization variables ζ, τ and u used to obtain (2.95). It results in a peak power $P_{\text{sol}} = \frac{|\beta_2|}{T_0^2 \gamma}$. The parameter T_0 is related to the full width, half maximum T_{FWHM} of the soliton by $T_{\text{FWHM}} = 2T_0 \ln(1 + \sqrt{2})$ [KA03]. Observe that shorter soliton pulses need higher power in order to exist, compared to pulses with longer duration. Alternatively, highly nonlinear fibers require less power for solitons to form and propagate.

In general Equation (2.95) has infinite solutions called *higher-order solitons*, that in contrast to the *fundamental soliton* obtained in (2.98), do change their amplitude while propagating but return periodically to their original shape. Higher-order solitons can be analytically obtained from (2.95) using the method of *inverse scattering* [KA03]. Using inverse scattering, even soliton solutions for the normal dispersion regime ($\beta_2 > 0$) can be found. They are referred to as *dark solitons* because they appear as dark dips in a uniformly lightened background.

The soliton solution is the optimum pulse shape to be used in an optical communication system, as it does not change its shape while propagating. Unfortunately, the departure from the ideal conditions assumed in (2.95), e.g., attenuation, strongly impact in the complexity of soliton systems regarding practical implementation. A less complex alternative has prevailed in the realization of high capacity optical communication systems: periodic dispersion management. By using fibers with opposite dispersion with respect to the standard single-mode fiber, it is possible to counteract the pulse broadening caused by dispersion. By carefully choosing the parameters of such a system, detrimental non linear effects can be minimized so that a soliton-like transmission is achieved, i.e., the transmitted pulse arrives undistorted at the receiver side. The design and optimization of such systems is introduced in chapter 3 and is developed extensively in this thesis.

2.9.2 The split-step Fourier method

As it was previously mentioned, Equation (2.65) does not have a closed-form solution if attenuation, dispersion and nonlinearities are all taken into account. However, efficient numeric algorithms exist that allow the evaluation of the propagation of an optical signal of arbitrary shape along the fiber. The most commonly used algorithm is the *split-step Fourier* (SSF) method .

The idea is to divide the total fiber length in multiple segments of length dz and assume that linear and nonlinear effects act separately, so they can be evaluated using (2.91) and (2.93) (see Fig. 2.3). The output signal is then the sum of all individual segments where the SSF algorithm is applied. Therefore, equation (2.65) can be written as

$$\frac{\partial A(z,t)}{\partial z} = \left(\hat{D}(t) + \hat{N}(z,t) \right) A(z,t), \tag{2.99}$$

where the linear and nonlinear operators are respectively defined as

$$\hat{D}(t) = -\frac{\alpha}{2} + \frac{1}{2} j \beta_2 \frac{\partial^2}{\partial t^2} \tag{2.100}$$

and

$$\hat{N}(z,t) = -j\gamma |A(z,t)|^2. \tag{2.101}$$

The linear operator $\hat{D}$ is usually evaluated in the frequency domain, whereas $\hat{N}$ is directly evaluated in the time domain. To improve accuracy, the nonlinear operator is placed in the middle between two linear operators acting over segments of length $dz/2$. This is usually referred to as the *symmetric* SSF. Consequently, (2.99) is solved as follows:

$$\frac{\partial A}{\partial z} = \left(\hat{D} + \hat{N} \right) A$$

$$\int \frac{\partial A}{A} = \int \left(\frac{1}{2}\hat{D} + \hat{N} + \frac{1}{2}\hat{D} \right) \partial z$$

$$\ln(A) = \int \left(\frac{1}{2}\hat{D} + \hat{N} + \frac{1}{2}\hat{D} \right) \partial z$$

$$A(z+dz,t) \approx \mathfrak{F}^{-1}\left\{ \exp\left(\frac{dz}{2}\hat{D}(\omega) \right) \cdot \mathfrak{F}\left\{ \exp\left(\int_z^{z+dz} \hat{N}(z',t)\,dz' \right) \cdot \right.$$

$$\left. \mathfrak{F}^{-1}\left\{ \exp\left(\frac{dz}{2}\hat{D}(\omega) \right) \cdot \mathfrak{F}\{A(z,t)\} \right\} \right\} \right\}. \tag{2.102}$$

In (2.102), $\mathfrak{F}$ and $\mathfrak{F}^{-1}$ represent the direct and inverse Fourier transforms, respectively, the linear operator $\hat{D}$ is evaluated in the frequency domain as $\hat{D}(\omega) = -\frac{1}{2}\alpha - \frac{1}{2}j\beta_2\omega^2$ and the integral term can be evaluated using the trapezoidal approximation

$$\int_z^{z+dz} \hat{N}(z',t)\,dz' \approx \frac{dz}{2}\left(\hat{N}(z+dz,t) + \hat{N}(z,t) \right). \tag{2.103}$$
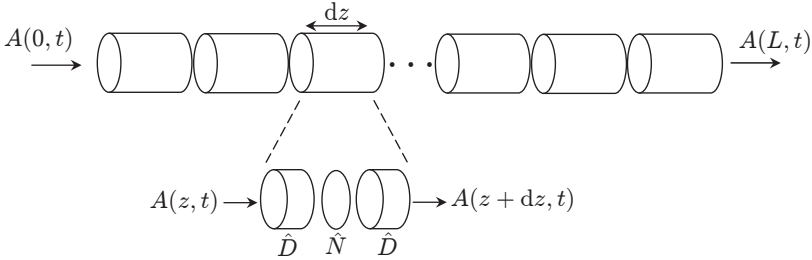
Figure 2.3: Symmetric split-step Fourier method.

Because $\hat{N}(z + \mathrm{d}z, t)$ depends on the unknown $A(z + \mathrm{d}z, t)$, an iterative procedure must be used to evaluate (2.103) until a certain tolerated error is achieved.

The SSF method can also be used if the WDM coupled equations (2.82) are to be solved. In such case the linear and nonlinear operators for the kth channel are written as

$$\hat{D}_k(t) = -\frac{\alpha}{2} - \left(\beta_1^{(k)} - \beta_1\right)\frac{\partial}{\partial t} + \frac{1}{2}j\beta_2^{(k)}\frac{\partial^2}{\partial t^2} \tag{2.104}$$

and

$$\hat{N}_k(z, t) = -j\gamma_k\left(|A_k(z, t)|^2 + 2\sum_{l \neq k}|A_l(z, t)|^2\right). \tag{2.105}$$

Subsequently (2.102) is evaluated for each channel. Observe that now, $\hat{N}_k(z + \mathrm{d}z, t)$ in (2.103) depends on all the unknown channels $A_k(z + \mathrm{d}z, t)$. Algorithm 2.1 summarizes the implementation of the SSF for both single-channel and total field ($k = 1$); and for the coupled equations ($k > 1$).

Since the linear and nonlinear operators do not commute, the solution in (2.102) is an approximation to the exact solution of the NLSE. It can be shown that the global error accumulated over a fiber span is bounded by $\mathrm{d}z^2$ [SHZM03]. Therefore, the step-size $\mathrm{d}z$ plays an important role in the accuracy and in the numerical efficiency of the algorithm. There are a multitude of criteria to select the optimum distribution of the step-size and, in general, it depends on the particular optical system to be analyzed.

If dispersion is the dominant effect in the link and nonlinearities play a second role, the step size can be determined with the *walk-off* method. This method is particularly useful in WDM systems in which the channels cover a broad spectrum and pulses in different channels move through each other very quickly. The step size is chosen so that in a single step two pulses in the two edge channels shift with respect to each other by a time which is a specified fraction of the pulse width. In this way, all collisions between pulses in different channels can be resolved. The step size is, therefore, constant and function of the largest group velocity difference between channels. It is given by

$$\mathrm{d}z = \frac{C \cdot T_0}{|D_{\mathrm{f}}\lambda_{\mathrm{f}} - D_{\mathrm{l}}\lambda_{\mathrm{l}}|}, \tag{2.106}$$

Algorithm 2.1 Symmetrized split-step Fourier method

$\epsilon = 10^{-12}, \phi_{\mathrm{NL}}^{\max} = 2.5 \cdot 10^{-3}, C = 0.5, z = 0$

$\mathrm{d}z^{\max} = C \cdot T_0/(|D_{\mathrm{f}}\lambda_{\mathrm{f}} - D_{\mathrm{l}}\lambda_{\mathrm{l}}|)$

for $k = 1 \to K$ **do**

$\quad \hat{D}_k = -\frac{1}{2}\alpha + j(\beta_1^{(k)} - \beta_1)\omega - \frac{1}{2}j\beta_2^{(k)}\omega^2$

end for

while $z < L$ **do**

$\quad$ **for** $k = 1 \to K$ **do**

$\quad\quad P_k^{\max} = \max_t \left(|A_k|^2\right)$

$\quad\quad \mathrm{d}z_k = \phi_{\mathrm{NL}}^{\max}/(\gamma_k P_k^{\max})$

$\quad$ **end for**

$\quad \mathrm{d}z = \min_k(\mathrm{d}z_k, \mathrm{d}z^{\max}), z = z + \mathrm{d}z$

$\quad$ **if** $z > L$ **then**

$\quad\quad \mathrm{d}z = L - (z - \mathrm{d}z), z = L$

$\quad$ **end if**

$\quad$ **for** $k = 1 \to K$ **do**

$\quad\quad A_k^{\mathrm{L_1}} = \mathfrak{F}^{-1}\left\{\exp\left(\frac{\mathrm{d}z}{2}\hat{D}_k\right) \cdot \mathfrak{F}\{A_k\}\right\}$

$\quad$ **end for**

$\quad$ **for** $k = 1 \to K$ **do**

$\quad\quad \hat{N}'_k = -j\gamma_k \left(|A_k^{\mathrm{L_1}}|^2 + 2\sum_{l \neq k}|A_l^{\mathrm{L_1}}|^2\right)$

$\quad\quad A_k^{\mathrm{NL_1}} = A_k^{\mathrm{L_1}} \cdot \exp\left(\mathrm{d}z \hat{N}'_k\right)$

$\quad\quad A_k^{\mathrm{NL_1}} = \mathfrak{F}^{-1}\left\{\exp\left(\frac{\mathrm{d}z}{2}\hat{D}_k\right) \cdot \mathfrak{F}\{A_k^{\mathrm{NL_1}}\}\right\}$

$\quad\quad \mathrm{err}_k = 1$

$\quad$ **end for**

$\quad$ **while** $\max_k(\mathrm{err}_k) > \epsilon$ **do**

$\quad\quad$ **for** $k = 1 \to K$ **do**

$\quad\quad\quad \hat{N}''_k = -j\gamma_k \left(|A_k^{\mathrm{NL_1}}|^2 + 2\sum_{l \neq k}|A_l^{\mathrm{NL_1}}|^2\right)$

$\quad\quad\quad A_k^{\mathrm{NL_2}} = A_k^{\mathrm{L_1}} \cdot \exp\left(\mathrm{d}z \cdot \frac{1}{2}\left(\hat{N}''_k + \hat{N}'_k\right)\right)$

$\quad\quad\quad A_k^{\mathrm{NL_2}} = \mathfrak{F}^{-1}\left\{\exp\left(\frac{\mathrm{d}z}{2}\hat{D}_k\right) \cdot \mathfrak{F}\{A_k^{\mathrm{NL_2}}\}\right\}$

$\quad\quad\quad \mathrm{err}_k = \max_t \left(|A_k^{\mathrm{NL_1}} - A_k^{\mathrm{NL_2}}|^2/|A_k^{\mathrm{NL_1}}|^2\right)$

$\quad\quad\quad A_k^{\mathrm{NL_1}} = A_k^{\mathrm{NL_2}}$

$\quad\quad$ **end for**

$\quad$ **end while**

$\quad A_k = A_k^{\mathrm{NL_2}}$

end while

---

where D_f and D_l are the dispersion coefficients (see ch. 3.2.2) corresponding to the first and last wavelengths λ_f and λ_l of the WDM comb, T_0 is the pulse duration and $C \in \,]0, 1]$. The walk-off method can also be used for single-channel transmission by choosing λ_f and λ_l at the two edges of the signals spectrum.

One inconvenience of using a constant step size is that it is prone to produce numerical artifacts. It has been shown [For97, Fra99] that, since four-wave mixing is a resonance effect, the power of the four-wave mixing products can be greatly overestimated by a constant step size method. If XPM and SPM are neglected, equation (2.81) can be solved to obtain the power of the FWM products and its frequency dependent efficiency η [SBW87]. Considering the interaction of four optical frequencies in a comb of WDM signals along a piece of fiber of length L, the FWM efficiency can be written as

$$\eta = \frac{\alpha^2}{\alpha^2 + \Delta\beta^2} \left(1 + \frac{4e^{-\alpha L} \cdot \sin^2(\Delta\beta L)}{(1 - e^{-\alpha L})^2} \right), \tag{2.107}$$

where $\Delta\beta = 4\pi^2 \beta_2 \Delta f$ is the phase-matching coefficient in the presence of only chromatic dispersion and Δf is the frequency separation between the spectral lines in Hertz.

In [BCC+00], an analytical expression for the FWM efficiency altered by the SSF method was obtained. The FWM efficiency at the end of a fiber span of length L subdivided into K generic sections of length $\mathrm{d}z_n$ is

$$\eta' = \frac{1}{(1 - e^{-\alpha L})^2} \left| \sum_{n=1}^{K} \varrho_n e^{j\phi_n} \right|^2 \tag{2.108}$$

where $\varrho_n = \left(1 - e^{-\alpha \, \mathrm{d}z_n} \right) \exp\left(-\alpha \sum_{i=1}^{n-1} \mathrm{d}z_i \right)$ and $\phi_n = -\Delta\beta \sum_{i=1}^{n} \mathrm{d}z_i$.

Figure 2.4a depicts η and η' when using the walk-off method for a typical scenario. The altered FWM efficiency follows the theoretical value for small frequency separation. Still, it starts to grow again, presenting several peaks at different frequencies. Whatever optical power is at those spectral distances from a carrier, acts like an unrealistic pump for spurious tones. It is possible to choose the step size so that the first peak of η' falls outside the simulation bandwidth, yet, this results in prohibitively small steps. Bosco et al. propose in [BCC+00] to use a logarithmic distribution for the step size to effectively suppress these numerical artifacts. However, it is shown in [SHZM03] that this method performs rather poorly in terms of accuracy for both single- and multi-channel transmission.

If nonlinearities play an important role in the system, the *nonlinear phase rotation* (NLPR) method is commonly used. In this method, a variable step-size is used that is inversely proportional to the instantaneous power of the signal. An upper bound on $\mathrm{d}z$ can be obtained by limiting the nonlinear phase increment of the operator $\hat{N}$ to a maximum value ϕ_{NL}^{max}. Consequently, the step-size can be written as

$$\mathrm{d}z = \frac{\phi_{NL}^{max}}{\gamma \cdot \max_t \left(|A(z, t)|^2 \right)}. \tag{2.109}$$
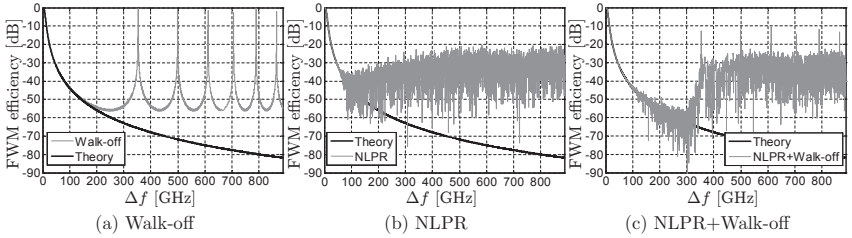
Figure 2.4: FWM efficiency vs. channel spacing for a common transmission scenario with parameters: $L = 80$ km, $\beta_2 = -21.1$ ps^2/km, $\alpha = 0.23$ dB/km resulting in d$z \approx 60$ m for the Walk-off method; average power of 0 dBm, $\gamma = 1.53$ 1/W/km and $\phi_{\mathrm{NL}}^{\max} = 2.5 \cdot 10^{-3}$ are used for the NLPR method.

Usually $\phi_{\mathrm{NL}}^{\max}$ ranges from 10^{-3} to 10^{-2} to keep the global error small. The altered FWM efficiency using the NLPR method is plotted in Fig. 2.4b. Now, the efficiency follows the theoretical value until approximately $1/K$ and departs randomly afterwards, maintaining this value as statistical average. By using the nonlinear rotation method, the peaks in η' are not present anymore and the SSF artifacts are effectively suppressed.

An upper limit in the step size derived from the NLPR method should be imposed and determined by the walk-off method such that the collisions between pulses in different frequencies can always be resolved. In such case, the altered FWM efficiency appears random and has peaks, albeit of smaller amplitude compared to the peaks of the walk-off method (see Fig. 2.4c).

A comparison between the three methods for the propagation of a WDM comb of 7 signals is shown in Fig 2.5, where the total number of steps vs. the length of a piece of fiber is plotted. For 80 km of fiber and 0 dBm per channel, simulation of the total field with the NLPR method requires 932 steps; with the walk-off method: 1327 steps; and with the combined method: 1622 steps. Observe that for the abovementioned signal power, the NLPR method is successful in resolving pulse collisions in WDM transmission only for fiber lengths shorter than ~ 20 km.

Recall that the number of steps is directly proportional to the simulation time. In Fig 2.5 the number of steps required to simulate propagation of a single channel is also shown for comparison. Using the NLPR method, the SSF method requires only 107 steps. Assuming that the length of the vector representing the total field is equal to the length of vectors representing individual channels, in this example WDM simulation using the coupled equations would take $\sim 7 \times 107$ steps (=749), which translates into a $\sim 54\%$ reduction in simulation time compared to simulating the total field using the NLPR + Walk-off method. This reduction is even larger when considering that vectors representing the total field of a WDM comb usually require a larger number of samples than the vectors representing the individual channels.
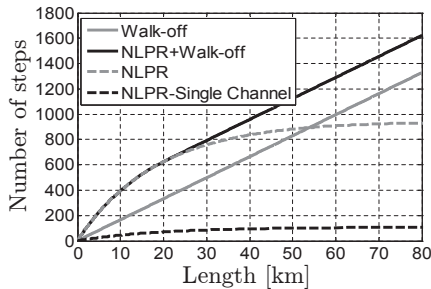
Figure 2.5: Number of steps vs. length for different step-size distributions. Parameters are the same as in Fig. 2.4.

2.10   Summary

In this chapter, the theory of propagation of light in single-mode fibers was thoroughly reviewed. In summary, the main points of this chapter are the following:

▷ Starting with Maxwell's equations, the condition for single-mode propagation was derived: fibers with normalized frequency $V < 2.405$ propagate a single mode per polarization. With the assumption that the fiber is isotropic, the scalar NLSE was derived. The NLSE governs the propagation of light in single-mode fibers and models a handful of effects that the optical signals experience during propagation.

▷ A system of coupled NLSE was also derived, which is useful in the analysis of the interaction between co-propagating WDM signals. It is pointed out that the model does not account for linear cross-talk between the signals and that it is valid only when FWM can be neglected. The coupled system of equations is also useful in order to reduce the simulation time of WDM systems.

▷ The NLSE used in this thesis effectively models attenuation, chromatic dispersion and Kerr nonlinear effects. Polarization effects are not included. Since random polarization rotations reduce the cubic susceptibility to an effective value, and additionally decreases the effect of XPM, the nonlinear penalties presented in this thesis can be regarded as worst-case scenario.

▷ Nonlinear phase noise and polarization mode dispersion are not considered in the derived models. Still, they should not be the limiting factors for the symbol rates investigated in this thesis (assuming that fibers with low PMD coefficient are used). Nonlinear scattering effects are also not considered in the derivation of the NLSE since they are not relevant for the considered power range and modulation formats.

▷ Characteristic lengths were defined and shown to determine the regime of propagation that the optical signals experience. Most of the systems investigated in this thesis fall into the pseudo-linear regime of propagation.

▷ The analytical solutions of the NLSE were presented. They show that chromatic dispersion produces a frequency dependent group velocity dispersion which leads to pulse broadening and, consequently, to inter-symbol interference. Kerr nonlinear effects produce a power dependent phase shift which by itself does not cause signal distortion in intensity modulated systems. In the presence of dispersion though, it does lead to waveform distortion unless the power and shape of the pulses is such that dispersion and nonlinear effects balance each other. Such pulses are referred to as solitons and were shown to exist in the absence of attenuation.

▷ The split-step Fourier (SSF) method was reviewed. This algorithm is used to solve the NLSE numerically. It was shown that the step size is an important parameter that influences the running time and the accuracy of the simulation. The walk-off method is a common selection criterion for the step size. Its advantage is that it allows to successfully resolve all pulse collisions between different WDM signals. On the other hand, since it is a constant step size method, it overestimates the efficiency of FWM. The nonlinear phase rotation method is another common selection criterion. The step size is not constant and so the FWM efficiency is not overestimated. But it is not successful in resolving all pulse collisions. A combination of both methods is the correct approach.

3

Fiber-Optic Transmission Systems

This chapter is divided in three main parts: The first part is devoted to describe the most important elements that compose the optical transmission systems considered in this thesis. In the second part, the criteria for the optimum design of such systems are reviewed. Special relevance is given to the design of dispersion maps, which play an important role in minimizing the detrimental effect of nonlinearities. The third part of this chapter is dedicated to the proper evaluation of the performance of an optical communication link. Firstly, the theory of pseudo-random sequences is briefly reviewed. The impact of the length and the order of the sequences on the evaluation of the bit-error rate (BER) is also addressed. Secondly, a semi-analytical method for the evaluation of the BER is described. Finally, a mathematical algorithm for the global optimization of the performance of a system is introduced.

3.1   System components

The following section outlines the most important components of the transmission systems considered in this thesis. All components described here serve as the building blocks of the optical link. However, carefully-designed systems must account for the restrictions imposed by these components, as their transmission characteristics or deviation from ideal behavior may cause loss in the performance of the system, for example, due to nonlinearities, noise and bandwidth limitations.

3.1.1   Optical sources

Most of the transmission systems based on single-mode fiber use semiconductor lasers[1] as light sources. In semiconductor lasers, the atoms of the direct band-gap semiconductor material are taken to an excited state by absorbing energy from an externally pumped electrical current. They return eventually to their normal ground state and emit light in the process. Light emission can occur through two fundamental processes known as *spontaneous* and *stimulated emission*. The later is the dominant process in lasers. Stimulated emission occurs when an already existing photon causes the decay of an atom from the excited to the ground state, generating a second photon that matches the original photon in energy (frequency), phase, direction and polarization state. Thus a narrow beam of coherent light is generated and used as the optical carrier.

Ideally, the carrier is a light-wave with constant amplitude, frequency and phase, that translates into zero laser spectral line-width. However, the process of spontaneous emission takes place along with stimulated emission, causing fluctuations in the intensity and the phase of the signal which subsequently, results in broadening of the signal's spectral width.

The normalized electrical field of an optical carrier without intensity fluctuations can be written in complex notation as

$$\mathbf{E}(t) = \sqrt{P} \cdot e^{j(2\pi f_c t + \varphi(t))} \cdot \mathbf{e}, \tag{3.1}$$

where P and f_c are the power and frequency of the optical carrier respectively, and $\mathbf{e}$ is the polarization-state vector. The random variation of the phase $\varphi(t)$ is denominated *laser phase noise* and is caused by spontaneously emitted photons that do not match the phase of the photons generated by stimulated emission. The evolution of the phase in a time interval $\mathrm{d}t$ can be modeled as a random-walk process of the form

$$\varphi(t + \mathrm{d}t) = \varphi(t) + \Delta\varphi, \tag{3.2}$$

where the phase change $\Delta\varphi$ is a normally distributed random variable with zero mean and variance σ_{PN}^2 given by

$$\sigma_{\mathrm{PN}}^2 = 2\pi\Delta\nu|\mathrm{d}t|, \tag{3.3}$$

where $\Delta\nu$ corresponds to the laser linewidth defined as the full-width at half-maximum bandwidth of the Lorentzian-shaped power spectral density of the optical field.

The requirements on the laser linewidth depend on the data rate and the modulation format used to transmit data. For DQPSK systems it has been shown [Sei10] that a laser linewidth to data rate ratio of $\sim 2 \cdot 10^{-3}$ results in a penalty of 3 dB irrespective of the pulse shape used for transmission. For systems at 55.5 Gb/s this translates into a laser linewidth tolerance of more than 100 MHz. Commercially available *distributed feedback lasers* (DFB) have linewidths in the order of 1-3 MHz [FNM+04], whereas *external cavity lasers* (ECL) can have linewidths as low as 100 kHz [JMST09]. Therefore, phase noise is not of concern for the systems investigated in this thesis.

---

[1]The term "laser" originated as an acronym for Light Amplification by Stimulated Emission of Radiation.

(a) Dual-drive MZM

(b) MZM transfer function
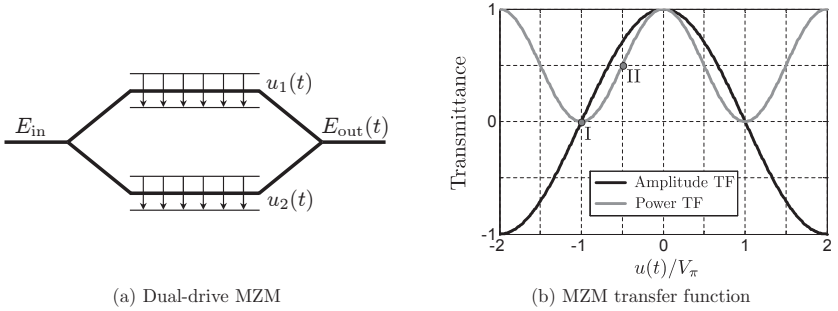
Figure 3.1: Structure of a dual-drive Mach-Zehnder Modulator and its transfer function (TF) in push-pull configuration. The transition point (I) and quadrature point (II) of the nonlinear transfer function are shown.

3.1.2 Optical modulation

Optical modulation is the process by which data, conveyed in an electrical signal, is converted into an optical signal with the same information. One technique is the direct modulation of the electrical current that drives a semiconductor laser. Direct modulation is a simple and cost-effective technique, since it does not require any additional optical component. However, the lasers modulation bandwidth is limited and high speed modulation introduces unwanted frequency chirp. At bit rates of 5 Gb/s or higher, the frequency chirp becomes large enough, that direct modulation of semiconductor lasers is rarely used [Agr02]. Instead, external modulators are used to modulate the continuous wave (CW) output of a laser.

The most widely used device for external modulation is the *Mach-Zehnder modulator* (MZM), schematically depicted in Figure 3.1a. In a MZM, CW light with amplitude E_{in} is split equally (ideally) into two branches. A waveguide material that exhibits strong electro-optical effect is used, such as LiNbO$_3$. The refractive index of the waveguide material is changed by means of the applied voltages $u_1(t)$ and $u_2(t)$ in each branch respectively, therefore, producing a phase shift in the optical field. If no voltage is applied, the optical field in the two branches experience equal phase shift and interfere constructively. If different voltages are applied to the arms of the MZM, constructive interference no longer occurs, and the intensity of the light at the output of the MZM is reduced proportionally to the phase difference between the two arms. When the phase difference between the arms is π, destructive interference occurs and no light is transmitted.

According to the Pockels effect, the phase shift experienced by the light in each branch due to the change in refractive index varies linearly with the applied voltage $u(t)$ and can be written as $\Delta\varphi = \pi\frac{u(t)}{2V_\pi}$, where V_π denotes the drive voltage necessary to produce a phase shift of π between the two branches. Typical values for V_π range between 3 to 6

Volts. If the extinction ratio is assumed infinite and insertion loss is not considered, the complex envelope of the light at the output of the MZM can be written as

$$E_{\text{out}}(t) = E_{\text{in}} \cdot \cos \left(\pi \frac{u_1(t) - u_2(t)}{4\,V_\pi} \right) \cdot e^{j\alpha_c \pi \frac{u_1(t) - u_2(t)}{4\,V_\pi}}, \tag{3.4}$$

where $\alpha_c = \frac{u_1(t) + u_2(t)}{u_1(t) - u_2(t)}$ is the linear frequency chirp parameter.

Chirp-free modulation can be obtained if the MZM is driven in *push-pull* configuration, by setting $-u_1(t) = u_2(t) = u(t)$, resulting in the transfer function

$$\frac{E_{\text{out}}(t)}{E_{\text{in}}} = \cos \left(\pi \frac{u(t)}{2\,V_\pi} \right). \tag{3.5}$$

Intensity modulation is obtained by biasing the MZM at its quadrature point, i.e., when the power transfer function $P_{\text{out}}(t)/P_{\text{in}} = (E_{\text{out}}(t)/E_{\text{in}})^2$ equals 0.5 or equivalently, when $u(t) = \pm V_\pi/2$, whereas amplitude and binary phase modulation are achieved by biasing at the transition point, i.e., $E_{\text{out}}(t)/E_{\text{in}} = 0$ or equivalently, when $u(t) = \pm V_\pi$. The MZM has a nonlinear transfer function (see Fig. 3.1b), however, it can be regarded as a linear amplitude modulator around $\pm V_\pi$ if the modulation voltage is small and the saturation region is avoided.

In principle, arbitrary complex optical waveforms can be generated using a dual-drive MZM. Nevertheless, in practice, optical IQ modulator are used. They consist of two parallel MZM in push-pull configuration that are used for the signal's in-phase and quadrature components respectively, and a phase modulator that confers a phase shift of $\pi/2$ to the output of the quadrature branch. The resulting transfer function can be written as

$$\frac{E_{\text{out}}(t)}{E_{\text{in}}} = \frac{1}{2} \left(\cos \left(\pi \frac{u_I(t)}{2\,V_\pi} \right) + j \cdot \cos \left(\pi \frac{u_Q(t)}{2\,V_\pi} \right) \right). \tag{3.6}$$

Mach-Zehnder modulators are particulary suitable for long-haul transmission of high data rates as they can have modulation bandwidths as high as 100 GHz [Nog07], high extinction ratio (>20 dB), low insertion loss (~4 dB) and are nearly wavelength independent [vdB08]. In this thesis, MZM are regarded as ideal devices, albeit, with nonlinear transfer function.

3.1.3 Optical amplification

In spite of the low attenuation of standard single-mode optical fibers (see ch. 3.2.1), transmission systems with distances of over 100 km require the use of optical amplification. Furthermore, the actual realization of WDM long-haul transmission systems is based on the periodic concatenation of transmission spans composed of fiber and optical amplifiers that are capable of compensating for the loss suffered by all WDM channels simultaneously.

Most systems employ lumped erbium-doped fiber amplifiers (EDFAs) in which losses accumulated over 60 to 80 km of fiber lengths are compensated using short lengths of erbium-doped fibers [Agr02]. In EDFAs, the erbium ions (Er^{3+}) are excited to a higher energy state by means of a pump wave at a certain wavelength, usually 980 nm or 1480 nm, so that the incoming optical signal at around 1550 nm is coherently amplified by stimulated emission.

Unfortunately, spontaneous emission of photons also occurs, leading to the generation of an incoherent optical flux around the signal's wavelength that becomes amplified upon propagation along the doped fiber, a process known as *amplified spontaneous emission* (ASE). ASE is the main source of noise in optically amplified lightwave communication systems. The noise can be modeled as complex additive white Gaussian noise (AWGN), with single-sided power spectral density (PSD) per polarization given by [GWL63]:

$$\Phi_{\mathrm{ASE}} = hf_c(G-1)n_{\mathrm{sp}}, \tag{3.7}$$

where h is Planck's constant, f_c is the signal frequency and G is the amplifier's gain. The *spontaneous emission factor* n_{sp} is related to the erbium ion population in the ground state and in the higher states, such that when total population inversion is ideally achieved $n_{\mathrm{sp}} = 1$. In general this does not occur and $n_{\mathrm{sp}} > 1$.

Since the spontaneous emission factor is not directly measurable, the *noise figure* parameter F_n is used to characterize the optical amplifier. It is defined, in analogy to electronic amplifiers, as the quotient between the electrical signal-to-noise ratio of a photodetected electrical signal before and after optical amplification. For an ideal photodetector with unit quantum efficiency, no dark current and only limited by shot noise, the calculated noise figure reads [Agr04]

$$F_n = 2n_{\mathrm{sp}}\frac{G-1}{G} + \frac{1}{G}. \tag{3.8}$$

In the high-gain limit ($G \gg 1$) the noise figure approaches $F_n = 2n_{\mathrm{sp}}$. This indicates that even an ideal amplifier with $n_{\mathrm{sp}} = 1$ has a noise figure of 3 dB. For most practical amplifiers, F_n exceeds 3 dB and can be as large as 6 to 8 dB [Agr02]. The wavelength of the pump laser has a direct impact on the noise figure. Laser pumps in the 980 nm region achieve population inversion more efficiently, which in turn, effectively lowers the noise figure of the amplifier. On the other hand, a laser pump at 1480 nm guarantees higher output power, but with a consequent detriment on the noise-related characteristics of the amplifier [KL02].

Inserting (3.8) into (3.7) and assuming $G \gg 1$, we obtain

$$\Phi_{\mathrm{ASE}} = \frac{1}{2}hf_cGF_n. \tag{3.9}$$

In general, the gain of the EDFA depends on multiple parameters such as power and wavelength of both signal and pump, as well as the length of the erbium doped fiber. In the praxis, however, EDFAs can be regarded as devices with configurable gain or configurable output optical power, that is independent of the signal wavelength within a

certain frequency band. Furthermore, since the gain dynamics of the EDFAs are rather slow, its gain responds to the average incident power and is, therefore, transparent to variable data rates and modulation formats [KK97b]. Another important characteristic of EDFAs is their low dependence on light polarization [DBDB02].

Other optical amplification technologies include Raman amplification and parametric amplification that rely on the nonlinear effects of stimulated Raman scattering and four-wave mixing in an optical fiber, respectively; and semiconductor optical amplifiers, that amplify the signal using a semiconductor material and an electrical pump. Although attractive due to their low noise figure and high bandwidth, Raman amplifiers are not yet commercially successful since they have important drawbacks compared to EDFAs. The most important one is that the pump power required by Raman amplifiers is significantly higher than the power required in EDFAs [vdB08]. Semiconductor amplifiers and parametric amplifiers are found mostly in optical signal processing applications [Agr02]. Only EDFAs will be considered in this thesis.

3.1.4   Photodetection

Photodetection is the process by which an optical signal is converted to an electrical signal. A photodetector is usually composed of a photodiode and a receiver electronic circuit. The current I_{out} generated by the photodiode is proportional to the incident optical power, i.e.,

$$I_{\text{out}}(t) = R \cdot |E_{\text{in}}(t)|^2, \tag{3.10}$$

where E_{in} is the incident normalized optical field in units of $\sqrt{\text{W}}$, as defined in (3.1); and R is the photodiode's *responsivity* (in A/W). The responsivity is proportional to the *quantum efficiency* of the photodiode, defined as the quotient between the electron generation rate and the photon incident rate.

Due to the particle nature of light, photodetection causes shot noise. Additionally, the receiver electronic circuit produces thermal noise. Both noises can be neglected in the analysis of optically amplified lightwave systems, in which ASE noise dominates. Photodetectors are considered ideal devices in this thesis, i.e., without any bandwidth limitation and $R = 1$ A/W.

3.1.5   Optical couplers

Optical couplers are used to split or combine optical signals as shown in the directional coupler depicted in Figure 3.2. Directional couplers are four port devices where the incident light in two ports is divided into two output ports according to the power splitting ratio κ. For all optical couplers used in this thesis $\kappa = \frac{1}{2}$.

Optical Y-junctions can also be regarded as four ports directional couplers with either only one input port when used as a power divider, or only one output port when used as a power combiner, in which case the other port acts as the output of a *radiation mode*, effectively modeling the inherent 3 dB power loss of optical combiners [INS82].
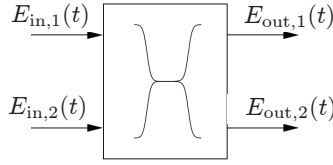
Figure 3.2: Optical coupler.

The transfer function of an optical coupler can be written as [Agr04]

$$
\begin{pmatrix} E_{\text{in},1}(t) \\ E_{\text{in},2}(t) \end{pmatrix} = \begin{pmatrix} \sqrt{\kappa} & j\sqrt{1-\kappa} \\ j\sqrt{1-\kappa} & \sqrt{\kappa} \end{pmatrix} \begin{pmatrix} E_{\text{out},1}(t) \\ E_{\text{out},2}(t) \end{pmatrix}. \tag{3.11}
$$

3.1.6 Optical and electrical filters

Optical filters are used in WDM systems mainly for multiplexing, demultiplexing and noise filtering. Most systems employ filters based on fiber Bragg gratings, Fabry-Perót interferometers or arrayed waveguide gratings [Agr02]. Their low pass equivalent transfer function can be modeled as a Gaussian function of order n_o given by

$$
H_o(f) = \exp\left(-\ln(\sqrt{2})\left(\frac{2f}{B_o}\right)^{2n_o}\right), \tag{3.12}
$$

where B_o is the two-sided 3 dB bandwidth.

Electrical filtering occurs naturally due to the bandwidth limitation of optoelectronic components such as lasers, modulators and photodetectors. Also, electrical filters can be used intentionally in digital transmitters as image rejection filters after digital-to-analog conversion. At the receiver side, electrical filters are used in order to further filter noise after photodetection.

Electrical filters are usually modeled as low-pass Bessel filters since they can be physically implemented, exhibit a linear phase response and an excellent step response with minimal overshoot and ringing [Sei10]. In this thesis, 5$^{\text{th}}$ order Bessel filters are used with normalized transfer function given by

$$
H_e(s) = \frac{945}{s^5 + 15s^4 + 105s^3 + 420s^2 + 945s + 945}, \tag{3.13}
$$

where $s = j\frac{Kf}{B_e}$, B_e is the one-sided 3 dB bandwidth and $K = 2.42741070215263$ is the 3 dB normalization constant.

3.2   Link design

As detailed in chapter 2, the propagation of light in the fiber is exposed to several detrimental effects of linear and nonlinear nature. In the following section, the proper design of a link will be discussed such that the most important impairments can be effectively minimized.

3.2.1   Fiber loss management

Fiber loss

Since optical receivers need a minimum optical power for error-free detection, fiber loss imposes a fundamental limit on the maximum reach of a transmission link. In equation (2.65), fiber loss is accounted for by the fiber attenuation coefficient α, measured in units of km^{-1}. If dispersion and nonlinear effects are not considered in (2.65), the propagation equation reduces to

$$\frac{\partial A(z,t)}{\partial z} = -\frac{1}{2}\alpha(\omega_c)A(z,t), \tag{3.14}$$

whose solution yields

$$A(z,t) = A(0,t)e^{-\frac{\alpha(\omega_c)}{2}z}. \tag{3.15}$$

In terms of the instantaneous power $P(z,t)$ of the signals, and recalling that $P = |A|^2$, equation (3.15) is equivalent to

$$P(z,t) = P(0,t)e^{-\alpha(\omega_c)z}. \tag{3.16}$$

Equation (3.16) shows that due to fiber loss, the power of the signals decreases exponentially along the fiber.

Observe that conventionally, the attenuation coefficient is expressed in units of dB/km by

$$\alpha_{\mathrm{dB}} = \frac{10}{\ln(10)}\alpha \approx 4.343\alpha. \tag{3.17}$$

Figure 3.3 shows the typical attenuation of the standard single-mode fiber (SSMF) as a function of the wavelength and frequency of the optical carrier, with a minimum of 0.2 dB/km at around 1550 nm. The two fundamental loss mechanisms that govern the loss profile of an optical fiber are shown as well: Rayleigh scattering and infrared absorption. Rayleigh scattering results from local microscopic fluctuations in the material density that lead to small variations of the refractive index on a scale smaller than the optical wavelength λ [Agr02]. The Rayleigh scattering varies as λ^{-4} and is the dominant loss mechanism at 1550 nm. Infrared absorption dominates for large wavelengths (> 1650 nm). It is caused by vibrational resonances of the optical signal with the silica molecules of the fiber. The peak in Fig. 3.3 results from the presence of impurities in the fiber, specifically, due to absorption caused by water vapor ions (OH$^-$). This is not a
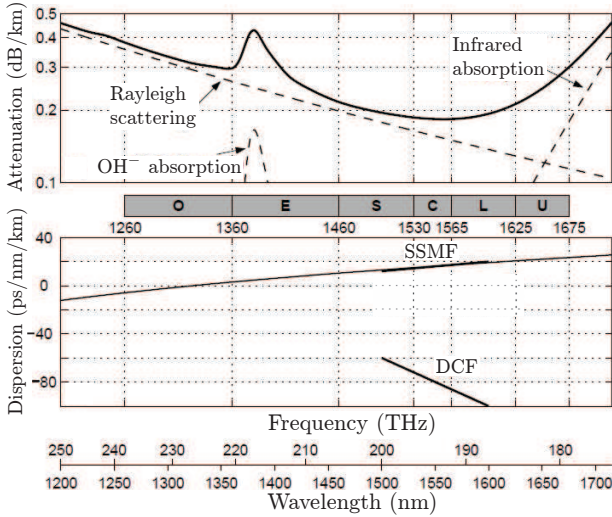
Figure 3.3: Fiber attenuation and chromatic dispersion profile. The linear approximations for the dispersion of SSMF and DCF are depicted as well (adapted from [Ran05]).

fundamental loss mechanism and can be eliminated by reducing the concentration of OH in the manufacturing process [TSGS00].

In order to establish a general framework for fiber-optic transmission systems, the telecommunication section of the International Telecommunication Union (ITU-T) defined six standard bands for transmission using single-mode fiber [Int03]. They are depicted in Fig. 3.3. Most commercial systems employ the conventional band (C-band), from 1530 nm to 1565 nm, where the fiber loss is the lowest. If more bandwidth is required, transmission can take place in the long (L) or in the short (S) wavelength bands. The extended (E) and the ultra-long wavelength (U) bands are of less interest due to their relative high attenuation. The original band (O) was used in early long-haul transmission systems and is used nowadays almost exclusively for the client interface in the access networks [Jan06]. This thesis focuses on transmission in the C-band.

Loss compensation and optical signal-to-noise ratio

As discussed in chapter 3.1.3, fiber loss is compensated by periodic optical amplification. In turn, this adds ASE noise to the optical signal. In such a system, the total noise power accumulated at the end of the link is the sum of the noise powers produced by each amplifier along the link. When all N spans have equal length L_{span} and the EDFAs

compensate exactly for the loss in one span, the one-sided ASE noise PSD becomes

$$\Phi_{\text{ASE}}^{\text{total}} = \frac{1}{2}hf_c GF_n N = \frac{1}{2}hf_c e^{\alpha L_{\text{span}}} F_n \frac{L_{\text{total}}}{L_{\text{span}}}. \tag{3.18}$$

Since the noise is a stochastic process, its total power per polarization at the end of a link can be calculated by integrating, in the frequency domain, the response of the receiver optical filter to a random input signal. In general, the noise power is given by

$$P_{\text{ASE}} = \int_{-\infty}^{\infty} |H_o(f)|^2 \Phi_{\text{ASE}}^{\text{total}} \, \mathrm{d}f. \tag{3.19}$$

where $H_o(f)$ is the low-pass equivalent transfer function of the receiver optical filter. Since the ASE noise is white, equation (3.19) is equivalent to

$$P_{\text{ASE}} = \Phi_{\text{ASE}}^{\text{total}} B_{o,\text{eff}}. \tag{3.20}$$

where $B_{o,\text{eff}} = \int_{-\infty}^{\infty} |H_o(f)|^2$ is defined as the effective optical filter bandwidth. It is customary, however, to compare the power of the ASE noise and the power of the optical signal *before* the receiver optical filter by means of a reference bandwidth $B_{o,\text{ref}}$ usually set to 12.5 GHz. The optical signal-to-noise ratio (OSNR) is consequently defined as

$$\text{OSNR} = \frac{P}{P_{\text{ASE}}} = \frac{P}{2\Phi_{\text{ASE}}^{\text{total}} B_{o,\text{ref}}}, \tag{3.21}$$

where P is the average signal power. The factor 2 in (3.21) accounts for the noise power in both polarizations.

The optimum span length to produce the minimum ASE noise is found by setting $\partial \Phi_{\text{ASE}}^{\text{total}} / \partial L_{\text{span}} = 0$ in (3.18), which yields $L_{\text{span}}^{\text{opt}} = \alpha^{-1}$. For SSMF with $\alpha_{\text{dB}} = 0.2$ dB/km this results in $L_{\text{span}}^{\text{opt}} \approx 21$ km. This is, however, not practical from a cost point of view. Following the ITU-T recommendations for terrestrial networks [Int98], span lengths of 80 km are considered in this thesis. An estimation of the degradation of the OSNR due to the use of non-optimal span lengths can be obtained by computing the ratio between $\Phi_{\text{ASE}}^{\text{total}}$ for a link with optimum span length and for one with an arbitrary span length. For a link composed of SSMF and EDFAs with spans of 80 km in length, the OSNR is 6 dB less than if using spans of optimum length. The fact that OSNR can be increased by spacing EDFAs closer together is used in ultra long-haul transmission systems that have to bridge transoceanic distances.

3.2.2   Dispersion management

Chromatic dispersion

Chromatic dispersion (CD) is the phenomenon by which different frequency components of an optical signal travel with different group velocities along the single-mode fiber. There are two kinds of contribution to CD: material and waveguide dispersion. Material

dispersion originates from the frequency dependance of the refractive index (see ch. 2.2), and it is the dominant contribution to CD in the C-band. Waveguide dispersion is caused by the dependence on wavelength of the power distribution between core and cladding. Its contribution to CD depends on fiber parameters such as core radius and the difference in refractive index between core and cladding.

The effect of the dispersion on modulated signals can be described by considering the propagation constant and its Taylor series expansion around the carrier frequency ω_c. Recalling (2.54):

$$\beta(\omega) = \beta_0 + \beta_1 \cdot (\omega - \omega_c) + \tfrac{1}{2}\beta_2 \cdot (\omega - \omega_c)^2 + \tfrac{1}{6}\beta_3 \cdot (\omega - \omega_c)^3 + \dots, \tag{3.22}$$

with

$$\beta_m = \left.\frac{\partial^m \beta(\omega)}{\partial \omega^m}\right|_{\omega=\omega_c}. \tag{3.23}$$

In (3.22), β_0 in km^{-1} results in a constant phase shift and β_1 in ps/km leads to a constant group delay, or group velocity $v_g = 1/\beta_1$. Neither β_0 nor β_1 induce any signal distortions. β_2 in ps^2/km and β_3 in ps^3/km represent the group velocity dispersion (GVD) and dispersion slope, respectively. They induce a frequency dependent group delay and, therefore, lead to signal distortion.

In practice, it is more common to use the *dispersion parameter* D in ps/nm/km which characterizes the change in group delay per unit distance [Agr02]. It is related to β_2 by

$$D = \frac{\partial \beta_1}{\partial \lambda} = -\frac{2\pi c}{\lambda^2}\beta_2. \tag{3.24}$$

The wavelength dependency of D in SSMF is shown in Fig. 3.3. It can be approximated around a reference wavelength λ_r by the linear function

$$D(\lambda) = D_r + S_r \cdot (\lambda - \lambda_r) \tag{3.25}$$

where $D_r = D(\lambda_r)$. The reference *slope parameter* $S_r = S(\lambda_r)$, in ps/nm^2/km, is defined as

$$S(\lambda_r) = \left.\frac{\partial D}{\partial \lambda}\right|_{\lambda=\lambda_r} = \frac{4\pi c}{\lambda_r^3}\beta_2 + \left(\frac{2\pi c}{\lambda_r^2}\right)^2 \beta_3. \tag{3.26}$$

Equations (3.24)-(3.26) can be used to calculate the values of $\beta_1^{(k)}$, $\beta_2^{(k)}$ and $\beta_3^{(k)}$ introduced in (2.75) which are used to model the propagation of WDM signals with the system of coupled NLSEs (see equation (2.82)). Observe that $\beta_m^{(0)} = \beta_m$. According to (3.24), the value of β_1 is obtained by integrating (3.25), which can be used to obtain

$$\left(\beta_1^{(k)} - \beta_1\right) = \left(D_r - S_r\lambda_r\right)\left(\lambda_k - \lambda_r\right) + \frac{S_r}{2}\left(\lambda_k^2 - \lambda_r^2\right), \tag{3.27}$$

where λ_k is the wavelength of the kth channel. $\beta_2^{(k)}$ is obtained by directly inserting (3.24) in (3.25) resulting in

$$\beta_2^{(k)} = -\frac{\lambda_k^2}{2\pi c}\left(D_r + S_r \cdot (\lambda_k - \lambda_r)\right). \tag{3.28}$$
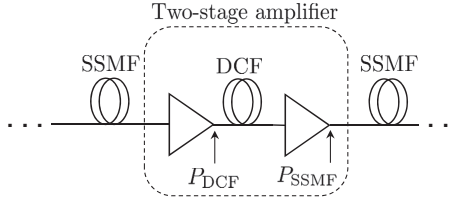
Figure 3.4: Schematic of in-line dispersion compensation with DCF and two-stage amplifier.

Since dispersion was approximated using a linear function, the slope is constant for all channels and, therefore, $\beta_3^{(k)} = \beta_3$, $\forall k$. Combining (3.28) and (3.26) we obtain

$$\beta_3^{(k)} = \frac{\lambda_r^3}{(2\pi c)^2} \left(2D_r + \lambda_r S_r\right). \tag{3.29}$$

The dispersion parameter for SSMF varies between $D = 15 - 18$ ps/nm/km in the C-band. The dispersion slope is typically $S = 0.06$ ps/nm²/km. The zero dispersion wavelength is present near 1320 nm [Neu88], and corresponds to the wavelength where both material dispersion and waveguide dispersion have the same magnitude, but opposite signs.

The waveguide dispersion can be manipulated by modifying the refractive index profile of the fiber. This can be used to produce fibers with negative dispersion parameter in the C-band, which are referred to as *dispersion compensating fibers* (DCF) and are widely used in fiber-optic transmission systems to compensate for chromatic dispersion. The approximate wavelength dependance of D in DCFs is shown in Fig. 3.3.

Dispersion compensation

In long-haul transmission systems with data rates over 2.5 Gb/s the accumulated dispersion must be compensated for. Many different methods have been proposed to compensate for CD such as dispersion compensating fibers (DCFs) [GNWK+05], dispersion managed cables [BMM+04], fiber Bragg gratings [Que87], electronic pre-distortion [KA85] and optical phase conjugation [YFP79]. Most commercial transmission links to date, however, are realized using DCF modules for in-line dispersion compensation as shown in Fig. 3.4. Its main advantage is the possibility to compensate simultaneously the dispersion of multiple WDM channels. Modern DCF modules can be designed to be *sloped-matched*, i.e., the slope of the DCF is inverse and equal in magnitude to the slope of the transmission fiber.

Due to the relatively high attenuation of the DCF (~ 0.5 dB/km) and the high complexity of cable installation, DCFs are not used as transmission fiber but coiled around a spool for *discrete* dispersion compensation. Usually a two-stage EDFA structure with mid-stage access for the DCF is used for compensating the loss of the DCF. In such configuration, the input power into the DCF (P_{DCF}) is an important design parameter. Because of
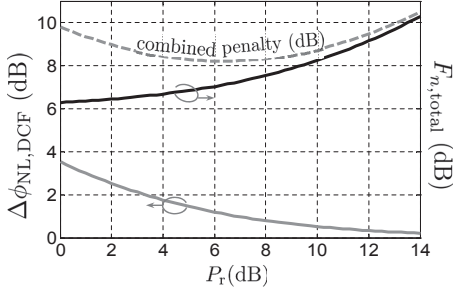
Figure 3.5: DCF-induced penalty as a function of the SSMF-DCF power ratio P_r. Parameters for the SSMF and DCF are those shown in Table 1.1. The compensation ratio is 1 and the noise figure of the amplifiers is 6 dB.

the higher nonlinear coefficient of the DCF ($\gamma =\sim$ 3-6 $W^{-1}km^{-1}$) than that of the SSMF ($\gamma =\sim$ 1.3-1.6 $W^{-1}km^{-1}$), the input power into the DCF is usually chosen several decibels lower than that of the SSMF in order to reduce de DCF-induced nonlinearities.

A figure of merit for the nonlinearities induced by the fiber is the *nonlinear phase-shift* which is defined as

$$\phi_{NL} = \gamma L_{eff} P, \tag{3.30}$$

where P is the power of the optical signal. Recall that the effective length L_{eff} is defined as $L_{eff} = (1 - e^{-\alpha z})/\alpha$. Consequently, the DCF-induced increase in the total nonlinear phase-shift can be written as [vdB08]

$$\Delta\phi_{NL,DCF} = \frac{\phi_{NL,SSMF} + \phi_{NL,DCF}}{\phi_{NL,SSMF}} = 1 + \frac{\gamma_{DCF} \cdot L_{eff}^{DCF}}{\gamma_{DCF} \cdot L_{eff}^{SSMF} \cdot P_r}, \tag{3.31}$$

where $P_r = P_{SSMF}/P_{DCF}$ is the power ratio. Clearly from (3.31), when the power ratio between SSMF and DCF increases, the DCF-induced contribution to the total nonlinear phase shift shrinks.

On the other hand, the power ratio influences the amount of noise produced by the two-stage amplifier, therefore, modifying the accumulated OSNR at the end of the link. The total noise figure of a two-stage amplifier can be calculated using Friis's formula [GNWK+05]

$$F_{n,total} = F_{n,1} + \frac{e^{\alpha_{DCF}L_{DCF}} \cdot F_{n,2} - 1}{e^{\alpha_{SSMF}L_{SSMF}}/P_r}, \tag{3.32}$$

where $F_{n,1}$ and $F_{n,2}$ are the respective noise figures of the two-stage amplifier. Evidently, from (3.32), the total noise figure increases when P_r increases. This suggests that there exists an optimum power ratio that balance the nonlinear effects and noise contributions of the DCF. Figure 3.5 depicts equations (3.31) and (3.32) as a function of P_r. The combined penalty suggest an optimum power ratio of 6.5 dB. This is, however, a very simplified

analysis, since the effective penalty associated with the DCF-induced nonlinear effects is dependent on variables other than just ϕ_{NL} such as local dispersion, modulation format, pulse shape, etc. An important goal of this thesis is to identify the optimum power difference between SSMF and DCF, for different modulation formats and transmission scenarios.

3.2.3   Design of dispersion maps

There are several ways of compensating for dispersion using DCFs. Compensation can take place either at the transmitter or receiver side, or periodically along the link. In the absence of nonlinear effects it is not important which scheme is used, as long as the accumulated dispersion at the end of the link is zero. In this scenario, the performance would only be limited by the OSNR degradation induced by the ASE noise and, in principle, such a link could be made arbitrarily long only by increasing the input optical power. However, for long-haul transmission, nonlinearities are the limiting effect regarding maximum transmission distance. Because the strength of the nonlinear effects is dependent on the time-waveform of the optical signal, different dispersion-compensation schemes will lead to different system performances, i.e., the local dispersion determines the impact of the nonlinear effects.

The course of dispersion along a transmission link can be visualized using a *dispersion map*. Figure 3.6 shows the dispersion maps for non-dispersion managed (NDM) and dispersion-managed (DM) links. In the former case, compensation is realized at the receiver and/or at the transmitter side and the system performance is determined by the set of parameters $\mathcal{S}_{\text{NDM}} = \{P_{\text{SSMF}}, \mathcal{D}_{\text{pre}}, \mathcal{D}_{\text{pos}}\}$, where $\mathcal{D}_{\text{pre}}$ and $\mathcal{D}_{\text{pos}}$ are the amount of pre-compensation and post-compensation, respectively. In DM links, the performance of the link is determined by the set of parameters $\mathcal{S}_{\text{DM}} = \{P_{\text{SSMF}}, P_{\text{DCF}}, \mathcal{D}_{\text{pre}}, \mathcal{D}_{\text{res}}, \mathcal{D}_{\text{acc}}\}$, where $\mathcal{D}_{\text{res}}$ is the residual dispersion per span and $\mathcal{D}_{\text{acc}}$ is the total accumulated dispersion at the end of the link. The parameters $\mathcal{D}_{\text{pos}}$ and $\mathcal{D}_{\text{acc}}$ can be used indistinctively by noting that, for NDM links, they relate by $\mathcal{D}_{\text{acc}} = \mathcal{D}_{\text{pos}} + \mathcal{D}_{\text{pre}} + N \cdot L_{\text{SSMF}} D_{\text{SSMF}}$. Similarly, for DM links, they relate by $\mathcal{D}_{\text{acc}} = \mathcal{D}_{\text{pos}} + \mathcal{D}_{\text{pre}} + N \cdot \mathcal{D}_{\text{res}}$.

Pre-compensation is used in order to *prechirp* the pulses such that their path-averaged width, over the effective length of a fiber section, is minimized. This results in less overlapping of neighboring pulses in the high-power segments of the transmission sections and thus, reduces the distortions due to intra-channel nonlinearities.

The residual dispersion per span is usually chosen different than zero in order to change the amount of CD at the beginning of each subsequent span. This averages out the interaction between the nonlinear phase shift and chromatic dispersion, as the signal's waveform is slightly different in each of the following sections. Additionally, it has been shown [KSS97] that XPM is greatly reduced if $\mathcal{D}_{\text{res}} \neq 0$, since the walk-off between WDM channels slightly changes between subsequent spans, hence, producing an averaging effect.

Many engineering design rules have been developed that relate the amount of pre-compensation with the residual dispersion per span, e.g., [KTMB00, FABH02, BSO08].
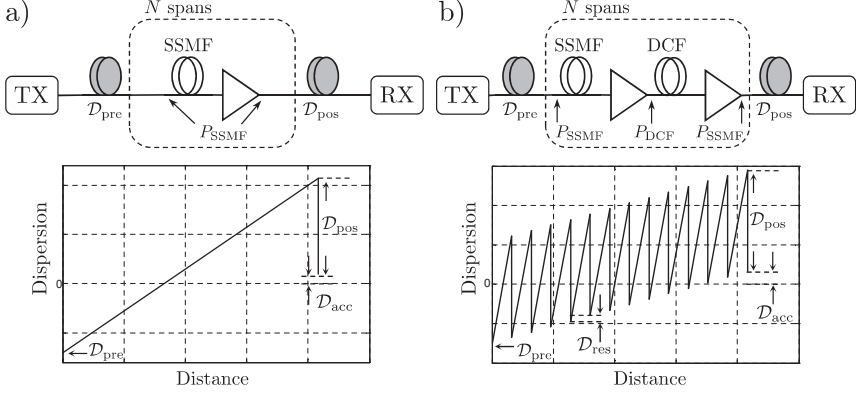
Figure 3.6: Dispersion compensation schemes with dispersion maps. a) Non-dispersion-managed links. b) Dispersion-managed links. Dispersion maps are not to scale.

They are based on the idea that an optimized pre-compensation minimizes the average broadening of the pulses in the high power segments of the link, while making the dispersion map symmetric with respect to the zero dispersion point where, in turn, the pulse width reaches its minimum. This translates into the well-known *straight-line rule* where the pre-compensation value is chosen such that [KTMB00]

$$\mathcal{D}_{\text{pre}} = \frac{D_{\text{SSMF}}}{\alpha_{\text{SSMF}}} \log\left(\frac{e^{-\alpha_{\text{SSMF}}L_{\text{SSMF}}}+1}{2}\right) - \frac{N}{2}\mathcal{D}_{\text{res}}. \tag{3.33}$$

In [Coe10], the straight-line rule was further refined by taking into consideration the nonlinear phase-shift induced by the DCFs. The resulting pre-compensation can be written as

$$\mathcal{D}_{\text{pre}} = -D_{\text{SSMF}} \cdot z_a - \frac{N}{2}\mathcal{D}_{\text{res}}, \tag{3.34}$$

where the length z_a is written as

$$z_a = -\frac{1}{\alpha_{\text{SSMF}}} \log\left(\frac{e^{-\alpha_{\text{SSMF}}L_{\text{SSMF}}}+1}{2} + \frac{\gamma_{\text{DCF}}P_{\text{DCF}}\alpha_{\text{SSMF}}}{2\gamma_{\text{SSMF}}P_{\text{SSMF}}\alpha_{\text{DCF}}}\left(1 + e^{-\alpha_{\text{DCF}}L_{\text{DCF}}} - 2e^{-\alpha_{\text{SSMF}}z_b}\right)\right), \tag{3.35}$$

and

$$z_b = \frac{D_{\text{SSMF}}}{D_{\text{DCF}}}(z_a - L_{\text{SSMF}}) + L_{\text{SSMF}}. \tag{3.36}$$

Observe that when $\gamma_{\text{DCF}} = 0$, equations (3.33) and (3.34) are equivalent. The straight-line rule will be discussed further in the next section when estimating the maximum transmission reach of a system.

Finally, $\mathcal{D}_{\text{pos}}$ is used to compensate for the remaining dispersion accumulated along the link. Since the nonlinear and the dispersion-induced phase-shift have opposite signs

when $D > 0$, a certain amount of accumulated dispersion ($\mathcal{D}_\text{acc}$) can be left uncompensated in order to partially reduce the net effect of SPM [EFS$^+$00]. This is specially effective in 10 Gb/s systems [BBB99]. On the other hand, when propagation falls under the pseudo-linear regime the optimum value of $\mathcal{D}_\text{acc}$ is close to zero. The extensive simulations conducted in [FB00] for pseudo-linear systems show that the optimum $\mathcal{D}_\text{acc}$ depends linearly on the nonlinear phase shift ϕ_NL and does not seem to be influenced by the shape of the dispersion map. These results suggest that it is possible to optimize $\mathcal{S}_\text{DM} = \{P_\text{SSMF}, P_\text{DCF}, \mathcal{D}_\text{pre}, \mathcal{D}_\text{res}\}$ for a fixed $\mathcal{D}_\text{acc}$, e.g., equal to zero, and then use $\mathcal{D}_\text{pos}$ as a fine-tuning parameter to further maximize the performance of the link.

Observe that in the rest of this thesis, the fibers used to model the pre- and post-compensation stages are considered non-attenuating and linear. In this way, the results presented in the following chapters are independent on the technology used to manipulate the waveform before and after propagation.

The optimization of dispersion maps and input powers for WDM systems is subject of intense research and has been reported in many theoretical and experimental studies, e.g., [Car99, SMKT00, vdBJK$^+$06]. Since there is no known analytical closed-form function that relates, for example, BER or maximum transmission distance with $\mathcal{S}$, the global optimization of an optical communication link must rely on very time-consuming simulations, usually involving grid searches, where all possible combinations of parameters are simulated and the one that performs the best is chosen as the optimum one. An alternative is to apply mathematical optimization algorithms as proposed in [GCS$^+$08, CGH09]. This is thoroughly described in the next section and applied extensively in the following chapters.

3.2.4   Maximum transmission distance

The maximum transmission distance is defined as the maximum number of spans N_max at which the OSNR margin is still positive, i.e, the accumulated OSNR is greater than or equal to the required OSNR for a certain target BER. Usually, it is obtained by means of a grid search, e.g., [HEG$^+$04], where all possible combinations of a set of parameters are simulated in order to find the one that delivers the longest transmission distance. Observe that this method requires that, for *each* combination of parameters, the maximum number of concatenated spans must be found.

An alternative method uses the nonlinear phase-shift (NLPS) criterion [ABF02]. It assumes that, in DM links, the nonlinear signal distortion depends *only* on the total amount of nonlinear phase-shift $\phi_\text{NL}^\text{total}$, given that the dispersion map is chosen according to the straight-line rule, i.e., (3.33) or (3.34). In other words, the required OSNR remains constant with N, provided that $\phi_\text{NL}^\text{total}$, $\mathcal{D}_\text{pre}$ and $\mathcal{D}_\text{acc}$ remain constant as well, and that $\mathcal{D}_\text{res}$ varies according to the straight-line rule. Several studies have shown the validity of the nonlinear phase shift criterion in SPM-limited systems, e.g, [ABF02, Vor07, CGS$^+$10].

The NLPS criterion can be used to estimate the maximum transmission distance of DM links as follows: Simulations are carried out in order to find the set of parameters $\mathcal{S}_\text{DM}^\text{opt}$

Algorithm 3.1 Maximum number of spans with NLPS criterion

$P_{\text{SSMF}}^*, P_{\text{DCF}}^*, \mathcal{D}_{\text{pre}}^*, \mathcal{D}_{\text{res}}^*, \text{OSNR}_{\text{req}}^*, \text{OSNR}_{\text{acc}}^*$: optimum parameters for N^* spans
$P_{\text{r}} = P_{\text{SSMF}}^*/P_{\text{DCF}}^*$
$\Delta N = 0$
$\text{OSNR}_{\text{acc}}' = \text{OSNR}_{\text{acc}}^*$
while $\text{OSNR}_{\text{acc}}' > \text{OSNR}_{\text{req}}^*$ **do**
    $\Delta N = \Delta N + 1$
    Estimate $\mathcal{D}_{\text{res}}'$ in (3.33) with $\mathcal{D}_{\text{pre}} = \mathcal{D}_{\text{pre}}^*$ and $N = N^* + \Delta N$
    Calculate L_{DCF}' in (3.40) with $\mathcal{D}_{\text{res}} = \mathcal{D}_{\text{res}}'$
    $L_{\text{DCF}}'' = \infty$
    while $|L_{\text{DCF}}'' - L_{\text{DCF}}'| > 10^{-4}$ **do**
        $L_{\text{DCF}}'' = L_{\text{DCF}}'$
        Numerically obtain z_a in (3.35) with $L_{\text{DCF}} = L_{\text{DCF}}'$
        Calculate $\mathcal{D}_{\text{res}}'$ in (3.34) with $\mathcal{D}_{\text{pre}} = \mathcal{D}_{\text{pre}}^*$ and $N = N^* + \Delta N$
        Calculate L_{DCF}' in (3.40) with $\mathcal{D}_{\text{res}} = \mathcal{D}_{\text{res}}'$
    end while
    Calculate $L_{\text{eff}}'^{\text{DCF}}$ with L_{DCF}'
    From (3.37) $P_{\text{SSMF}}' = P_{\text{SSMF}}^* \frac{N^*}{N^* + \Delta N} \left(\frac{\gamma_{\text{SSMF}} L_{\text{eff}}^{\text{SSMF}} + \gamma_{\text{DCF}} L_{\text{eff}}^{*\text{DCF}}/P_{\text{r}}}{\gamma_{\text{SSMF}} L_{\text{eff}}^{\text{SSMF}} + \gamma_{\text{DCF}} L_{\text{eff}}'^{\text{DCF}}/P_{\text{r}}} \right)$
    Calculate $\text{OSNR}_{\text{acc}}'$ in (3.38) and (3.39) with $P_{\text{SSMF}} = P_{\text{SSMF}}'$ and $L_{\text{DCF}} = L_{\text{DCF}}'$
end while
$N_{\max} = N^* + \Delta N - 1$

---

that maximizes the OSNR margin after an arbitrary number spans N; thus obtaining, at the same time, the required OSNR (OSNR_{req}) for a certain *maximum total nonlinear phase shift* defined as

$$\phi_{\text{NL,max}}^{\text{total}} = N \cdot \left(\gamma_{\text{SSMF}} L_{\text{eff}}^{\text{SSMF}} P_{\text{SSMF}} + \gamma_{\text{DCF}} L_{\text{eff}}^{\text{DCF}} P_{\text{DCF}} \right). \quad (3.37)$$

Equation (3.37) considers the pre- and post compensation stages linear. If $\phi_{\text{NL,max}}^{\text{total}}$ does not change with N, the OSNR_{req} remains constant and, therefore, it is possible to estimate the maximum transmission distance by finding the number of sections $N_{\max}$ at which the accumulated OSNR (OSNR_{acc}) is equal to the OSNR_{req}. In calculating the OSNR_{acc} for subsequent number of spans, the ratio $P_{\text{r}} = P_{\text{SSMF}}/P_{\text{DCF}}$ is kept constant; P_{SSMF} is varied according to N so that $\phi_{\text{NL,max}}^{\text{total}}$ remains constant; and $\mathcal{D}_{\text{res}}$ is varied according to N so that $\mathcal{D}_{\text{pre}}$ remains constant by means of the straight-line rule.

Observe that OSNR_{acc} for the DM link shown in Fig. 3.6b can be analytically calculated according to (3.21) as

$$\text{OSNR}_{\text{acc}} = \frac{P_{\text{SSMF}}}{2\Phi_{\text{ASE}}^{\text{total}} B_{o,\text{ref}}}, \quad (3.38)$$

where the total PSD of the ASE noise is given by

$$\Phi_{\text{ASE}}^{\text{total}} = \frac{1}{2} h f_c F_n N \left(e^{\alpha_{\text{SSMF}} L_{\text{SSMF}}} + P_{\text{r}} \cdot e^{\alpha_{\text{DCF}} L_{\text{DCF}}} \right). \quad (3.39)$$

In (3.39), the attenuation of the pre-and post-compensation stages are not considered and it is assumed that all EDFAs have the same noise figure. The length of the DCFs vary according to the number of sections used to calculate the OSNR_{acc} since it depends on $\mathcal{D}_{\text{res}}$ and this one, in turn, varies with N by means of the straight-line rule. The DCF length is given by

$$L_{\text{DCF}} = \frac{D_{\text{SSMF}} L_{\text{SSMF}}}{D_{\text{DCF}}} \left(1 - \frac{\mathcal{D}_{\text{res}}}{D_{\text{SSMF}} L_{\text{SSMF}}} \right). \tag{3.40}$$

The term in brackets in (3.40) is usually referred to as the *compensation ratio* [HEG+04]. The procedure used to determine N_{max} given $\mathcal{S}_{\text{DM}}^{\text{opt}}$ and OSNR_{req} based on the NLPS criterion is summarized in algorithm 3.1.

This method will be used later in this thesis to estimate the maximum transmission distance of several formats. Observe that the NLPS criterion resorts in carrying out a grid search only over a single number of spans. This is, however, still very time-consuming. Chapter 3.3.3 presents a mathematical algorithm that allows to find the optimum set of parameters in a small number of iterations, so that a grid search is no longer needed.

3.3   System simulation aspects

Computer simulations are a cost-effective way of estimating the overall performance of a transmission system before its actual implementation. In this section, relevant aspects of the simulations conducted in this thesis are discussed. It covers the proper choice of test sequences, the detection statistics and estimation of the bit-error rate and the description of an algorithm for the global optimization of a transmission link.

3.3.1   Pseudo-random sequences and electrical signal generation

The evaluation of a communication system begins with the choice of a proper *test sequence* that correctly models the nature of the data to be transmitted. In digital systems, the data can be modeled as a random binary sequence of statistically independent ones and zeros with equal probability of occurrence. *Pseudo-random* binary sequences are, however, used in the praxis because of their reproducibility.

A pseudo-random sequence is a periodic sequence with an autocorrelation function that resembles the autocorrelation function of a true random sequence over one period [JB00]. A 2^r-ary sequence can be generated using a linear feedback shift register (LFSR) (Fig. 3.7) and is usually represented by a *generator polynomial* in x over the finite field $\text{GF}(2^r)$

$$G(x) = c_{n_s} x^{n_s} + c_{n_s-1} x^{n_s-1} + c_{n_s-2} x^{n_s-2} + \cdots + c_2 x^2 + c_1 x + c_0, \tag{3.41}$$

where the maximum degree n_s corresponds to the number of registers in the LFSR.

An output sequence has the maximum possible period $N_{\text{seq}} = (2^r)^{n_s} - 1$ if $G(x)$ is a *primitive* polynomial over $\text{GF}(2^r)$. In such case, the output sequence contains all n_s-bit patterns except the all-zero, and is usually referred to as *m-sequence*. By adding a 0 digit to the output sequence at a place where there are $n_s - 1$ zeros a *De Bruijn*
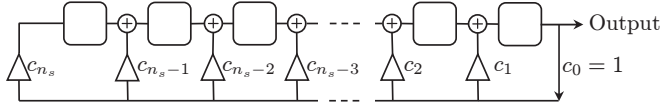
Figure 3.7: Galois implementation of a linear feedback shift register.

sequence is obtained, which contains all possible n_s bit patterns and has a period of $(2^r)^{n_s}$. Table B.1 in appendix B shows primitive polynomials in $GF(2^r)$ for different r and n_s. Alternatively, multilevel pseudo-random m-sequences can be generated by manipulating (shifting and decimating) a binary m-sequence of degree $n_s \cdot r$, hence, avoiding the complex implementation of arithmetic operations in higher-order finite fields [Gol67]. Moreover, high-speed m-sequences can be implemented by time-multiplexing the output sequences of several low-speed *parallel* LFSRs, as described in [Gue90].

It has been repeatedly shown, e.g.,[WEG$^+$04, SOB07], that in systems limited by intra-channel nonlinearities, the symbol pattern length n_s plays a critical role in correctly assessing the transmission impairments. In [WEG$^+$04], for example, a rule for the minimum pattern length is obtained by looking at the number of pulses that, due to dispersion, interact at the high power segments of the link. The rule predicts a scaling of n_s with the square of the symbol rate. Alternatively, in [SOB07] a rule is derived for dispersion managed systems using "optimized" dispersion maps., i.e., dispersion maps that follow the straight-line rule. It results in n_s to scale linearly with the symbol rate.

In [GAB10], the impact of the length of the sequences in NDM links was studied, where a high number of pulses interact with each other due to big amounts of accumulated dispersion. It concludes that pseudo-random sequences much shorter than the required by the abovementioned rules can be sufficient for an accurate estimation of the BER. Furthermore, it shows that even shorter truly random sequences may also be adequate for a correct assessment of the performance of the system.

Systems employing binary modulation formats are habitually evaluated using pseudo-random binary sequences (PRBSs), i.e., $r = 1$. If multilevel modulation is employed ($r > 1$), it is usual to multiplex r PRBSs with a cyclic shift between them for decorrelation. The resulting sequence, however, may fail to emulate all possible inter-symbol interactions thus, leading to underestimate the penalty associated with nonlinearities. As shown in [SX07, vdBKdWG07, RBF09], the use of multilevel pseudo-random sequences is necessary, in order to properly model the quality impairments of a transmission system subject to nonlinear and dispersive effects. Following the recommendations of [SX07], multilevel pseudo-random sequences of at least 4096 symbols are used in this thesis when characterizing the nonlinear propagation of an optical signal.

The pseudo-random sequences are imprinted in electrical signals that subsequently drive the optical modulators. In this thesis, in order to properly model the non-zero rise and fall times of the electrical signals, the ith output binary sequence of the bit-pattern generator

is modeled as a train of non-return-to-zero, (NRZ) raised-cosine pulses given by [HK04b]

$$b_i(t) = \sum_{k=1}^{(2^r)^{n_s}} d_{i,k} \cdot g(t - kT_0),$$ (3.42)

where $d_{i,k} \in \{0,1\}$, T_0 is the symbol duration and

$$g(t) = \begin{cases} 1 & , & \frac{T_0}{2}(1 - \beta_r) > |t| \\ \frac{1}{2} - \frac{1}{2}\sin\left(\frac{\pi}{\beta_r T_0}(|t| - \frac{T_0}{2})\right) & , & \frac{T_0}{2}(1 - \beta_r) \leq |t| \leq \frac{T_0}{2}(1 + \beta_r) \\ 0 & , & |t| > \frac{T_0}{2}(1 + \beta_r), \end{cases}$$ (3.43)

where $0 \leq \beta_r \leq 1$ is the roll-off factor.

3.3.2 Detection statistics and evaluation of the bit-error rate

The bit-error rate (BER) is considered the most significant criterion for performance characterization in digital transmission systems. Other figures of merit like required OSNR or maximum transmission distance are usually defined for a certain target BER.

A common approach to the determination of the BER in optical systems resorts in *Monte Carlo simulations*, where the propagation of a test sequence through the investigated system is simulated and the bit errors are counted after detection. This method has the advantage of being generally applicable to any arbitrary system while considering all deterministic and stochastic degradation effects [Sei10]. On the other hand, the accuracy of the estimated BER strongly depends on the length of the test pattern. As a rule of thumb, at least 10/BER bits should be simulated in order to have a confident interval of 95% on the estimated BER [Jer84]. This makes the computational effort of estimating very low BER ($< 10^{-6}$) prohibitively high.

An alternative to Monte Carlo simulations is to estimate the BER by directly looking at the probability density function (PDF) of the received signal. The BER is estimated by integrating over the PDF, without having to simulate long runs of bits. Conventional methods usually approximate the PDF of the photo-detected signal to a Gaussian distribution. This is relatively accurate in OOK systems but it does not work well in directly detected phase-modulated systems [BP04, GW05]. This is because the beating between signal and noise, caused by the squaring function of the photo-detection, is a nonstationary random process. As a result, the PDFs of each bit look different.

The exact detection statistics can be obtained by means of a semianalytic simulation method based on the principle of Karhunen-Loéve-like series expansions., i.e., on finding a set of orthonormal basis functions that make the expanded noise components Gaussian and statistically independent [GW05]. The following analysis is based largely on the work of [For00], [GW05] and [Coe10] .

Consider an arbitrary optical system as depicted in Fig. 3.8. The goal is to accurately estimate the BER of a signal of arbitrary waveform impaired by additive, Gaussian, white
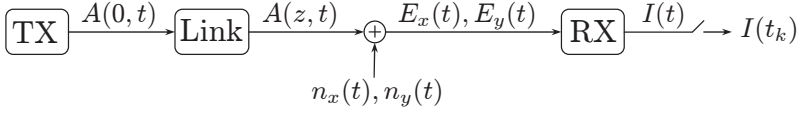
Figure 3.8: Block diagram for signal transmission. Observe that $A(z,t)$ is polarized in the x-direction only, whereas the Gaussian noise is polarized in both x- and y-directions.

optical noise (AWGN). In this model the nonlinear interaction between the signal and the noise is neglected, i.e., nonlinear phase noise is not considered; and the signal is linearly polarized along the (arbitrarily chosen) x-axis. For this system, given a certain decision threshold γ_{th} and a sampling time offset t_{s}, the overall BER of a sequence composed of N_{seq} pulses of duration T_0 can be written as

$$\text{BER}(\gamma_{\text{th}}, t_{\text{s}}) = \frac{1}{N_{\text{seq}}} \sum_{k=1}^{N_{\text{seq}}} \mathcal{P}_b(e_k|\{a_{0,k}\}), \tag{3.44}$$

where $\mathcal{P}_b(e_k|\{a_{0,k}\})$ represents the probability of an error e_k at the sampling time $t_k = t_{\text{s}} + kT_0$, conditional upon the information sequence $\{a_{0,k}\}$, and is given by

$$\mathcal{P}_b(e_k|\{a_{0,k}\}) = \begin{cases} \mathcal{P}(I(t_k) < \gamma_{\text{th}}) & , a_{0,k} = 1 \\ \mathcal{P}(I(t_k) > \gamma_{\text{th}}) & , a_{0,k} = 0, \end{cases} \tag{3.45}$$

where $I(t_k)$ is the received output decision variable as shown in Fig. 3.8. The probabilities at the right side of (3.45) can be computed using p_{Y_k}, that represents the PDF of $Y_k = I(t_k)$, by means of

$$\mathcal{P}(I(t_k) < \gamma_{\text{th}}) = \int_{-\infty}^{\gamma_{\text{th}}} p_{Y_k}(y)\mathrm{d}y, \tag{3.46}$$

$$\mathcal{P}(I(t_k) > \gamma_{\text{th}}) = \int_{\gamma_{\text{th}}}^{\infty} p_{Y_k}(y)\mathrm{d}y. \tag{3.47}$$

In order to obtain to PDFs to insert in (3.46) and (3.47), the decision variable can be written as

$$I(t_k) = I_x(t_k) + I_y(t_k), \tag{3.48}$$

where

$$I_{(x,y)}(t_k) = \iint_{-\infty}^{\infty} \tilde{E}_{(x,y)}^*(f_2) K(f_1, f_2) \tilde{E}_{(x,y)}(f_1) e^{j2\pi t_k(f_1-f_2)} \mathrm{d}f_1 \mathrm{d}f_2. \tag{3.49}$$

In (3.49), $\tilde{E}_x(f)$ and $\tilde{E}_y(f)$ represent the Fourier transforms of $E_x(t) = A(t) + n_x(t)$ and $E_y(t) = n_y(t)$, respectively (the spatial dependence of the electrical fields has been dropped for readability). The noises $n_x(t)$ and $n_y(t)$ are complex random variables such that $n_x, n_y \sim \mathcal{N}(0, 2\sigma_n^2)$, where $\sigma_n^2 = \frac{1}{2}\Phi_{\text{ASE}}^{\text{total}} B_{o,\text{ref}}$ is the variance of their real and imaginary parts over a certain reference bandwidth $B_{o,\text{ref}}$. The Hermitian kernel function $K(f_1, f_2)$ depends exclusively on the receiver structure. In the next chapters, $K(f_1, f_2)$ will be derived explicitly for each modulation format considered in this thesis.

For numerical convenience, (3.49) can be written as a double summation within the discrete fourier transform grid, so that (3.48) yields:

$$I(t_k) = \sum_{m=1}^{2M} \sum_{l=1}^{2M} e_{x,m}^* K_{ml} e_{x,l} + \sum_{m=1}^{2M} \sum_{l=1}^{2M} e_{y,m}^* K_{ml} e_{y,l}, \tag{3.50}$$

where $2M$ is the total number of samples and $e_{x,m}, e_{y,m}$ and K_{ml} are defined as

$$e_{x,m} = \tilde{E}_x(f_m) e^{j2\pi f_m t_k} \sqrt{\Delta f}, \tag{3.51}$$

$$e_{y,m} = \tilde{E}_y(f_m) e^{j2\pi f_m t_k} \sqrt{\Delta f}, \tag{3.52}$$

$$K_{ml} = K(f_m, f_l) \Delta f, \tag{3.53}$$

where $\Delta f = 1/(N_{\text{seq}} T_0)$ is the spacing between adjacent frequency points[2] and $f_m = (m - M - 1)\Delta f$. In turn the signal and noise parts of the fields can be written explicitly as $e_{x,m} = e_{s,m} + e_{n_x,m}$ and $e_{y,m} = e_{n_y,m}$ where

$$e_{s,m} = \tilde{A}(f_m) e^{j2\pi f_m t_k} \sqrt{\Delta f}, \tag{3.54}$$

$$e_{n_x,m} = \tilde{n}_x(f_m) e^{j2\pi f_m t_k} \sqrt{\Delta f}, \tag{3.55}$$

$$e_{n_y,m} = \tilde{n}_y(f_m) e^{j2\pi f_m t_k} \sqrt{\Delta f}. \tag{3.56}$$

Equation (3.50) can be written in matrix form as

$$I(t_k) = \mathbf{e}_x^{\text{H}} \mathbf{K} \mathbf{e}_x + \mathbf{e}_y^{\text{H}} \mathbf{K} \mathbf{e}_y, \tag{3.57}$$

where $\mathbf{e}_x = \mathbf{e}_s + \mathbf{e}_{n_x} = (e_{x,1}, e_{x,2}, \cdots, e_{x,2M})^{\text{T}}$, $\mathbf{e}_y = \mathbf{e}_{n_y} = (e_{y,1}, e_{y,2}, \cdots, e_{y,2M})^{\text{T}}$ and $\mathbf{K}$ is the square $2M \times 2M$ matrix whose $(m,l)^{\text{th}}$ element equals K_{ml}. The *eigendecomposition* of the Hermitian matrix yields $\mathbf{K} = \mathbf{Q}^{\text{H}} \mathbf{\Lambda} \mathbf{Q}$, where $\mathbf{Q}$ is the square $2M \times 2M$ matrix whose i^{th} column is the eigenvector $\mathbf{q}_i$ of $\mathbf{K}$ and $\mathbf{\Lambda}$ is the diagonal matrix whose diagonal elements are the corresponding real eigenvalues λ_i. Consequently, equation (3.57) can be rewritten as

$$
\begin{aligned}
I(t_k) &= & \mathbf{e}_x^{\text{H}} \mathbf{K} \mathbf{e}_x & + & \mathbf{e}_y^{\text{H}} \mathbf{K} \mathbf{e}_y & \\
&= & \mathbf{e}_x^{\text{H}} \mathbf{Q}^{\text{H}} \mathbf{\Lambda} \mathbf{Q} \mathbf{e}_x & + & \mathbf{e}_y^{\text{H}} \mathbf{Q}^{\text{H}} \mathbf{\Lambda} \mathbf{Q} \mathbf{e}_y & \\
&= & (\mathbf{s} + \mathbf{n}_x)^{\text{H}} \mathbf{\Lambda} (\mathbf{s} + \mathbf{n}_x) & + & \mathbf{n}_y^{\text{H}} \mathbf{\Lambda} \mathbf{n}_y & \\
&= & \underbrace{\sum_{i=1}^{2M} \lambda_i |s_i(t_k) + n_{x,i}(t_k)|^2}_{\text{noncentral}-\mathcal{X}^2} & + & \underbrace{\sum_{i=1}^{2M} \lambda_i |n_{y,i}(t_k)|^2}_{\text{central}-\mathcal{X}^2}, &
\end{aligned}
\tag{3.58}
$$

where $\mathbf{s} = \mathbf{Q} \mathbf{e}_s$ is a column vector with deterministic elements $s_i(t_k) = \mathbf{q}_i^{\text{H}} \mathbf{e}_s$; whereas $\mathbf{n}_x = \mathbf{Q} \mathbf{e}_{n_x}$ and $\mathbf{n}_y = \mathbf{Q} \mathbf{e}_{n_y}$ are column vectors with statistically independent random

---

[2]Evaluating the PDFs of all symbols at once is computationally intensive, since it requires to take the 2M-points DFT of the discrete version of $A(z,t)$, sampled at intervals $\Delta t = N_{\text{seq}} T_0/(2M)$. Observe that the total number of points $2M$ is chosen to be high enough to ensure that the Nyquist-Shannon [Sha49] sampling theorem is fulfilled. However, in practice, it can be assumed that only a small fraction of the signal around the kth symbol is relevant for the decision at each sampling instant. Hence, when evaluating the PDF of each symbol, it is sufficient to consider only a subsequence of length $N_{\text{sym}} \ll N_{\text{seq}}$ around it, provided that N_{sym} is long enough such that all ISI effects over the kth symbol are taken into account.

elements $n_{x,i}(t_k) = \mathbf{q}_i^{\mathrm{H}} \mathbf{e}_{n_x}$ and $n_{y,i}(t_k) = \mathbf{q}_i^{\mathrm{H}} \mathbf{e}_{n_y}$, respectively. It can be shown, e.g., in [Coe10], that $n_{x,i}(t_k)$ and $n_{y,i}(t_k)$ are zero-mean complex Gaussian random variables with independent real and imaginary components, each with variance $\sigma_n^2 = \frac{1}{2}\Phi_{\mathrm{ASE}}^{\mathrm{total}}\Delta f$.

Thus, the decision variable $I(t_k)$ can be represented as a weighted sum of magnitude-squared, complex Gaussian random variables of nonzero and zero mean, that result in random variables obeying noncentral-$\mathcal{X}^2$ and central-$\mathcal{X}^2$ distributions, respectively; and whose individual moment generating functions (MGFs) are well known [Sal78]. Since the terms making up the sum in (3.58) are statistically independent, the total MGF is the product of the individual MGFs and is given by [For00]

$$\Psi_{I(t_k)}(\xi) = \prod_{i=1}^{2M} \frac{\exp\left(\frac{\lambda_i |s_i(t_k)|^2 \xi}{1 - 2\lambda_i \sigma_n^2 \xi}\right)}{\left(1 - 2\lambda_i \sigma_n^2 \xi\right)^2}. \tag{3.59}$$

The PDFs in (3.46) and (3.47) are obtained from the total MGF in (3.59) by its conjugate complex inverse Laplace transform, and the consequent integral is solved numerically using the *saddle-point integration* method [Arf85]. Alternatively, the resulting probabilities in (3.46) and (3.47) can be approximated with high accuracy by the *saddle-point approximation* method [Hel78, Coe10] which yields

$$\mathcal{P}(I(t_k) \gtrless \gamma_{\mathrm{th}}) \approx \pm \frac{\exp\left(\Theta(\xi_0^{\pm})\right)}{\sqrt{2\pi \partial_\xi^2 \Theta(\xi_0^{\pm})}}, \tag{3.60}$$

where ∂_ξ^2 denotes a second order partial derivative with respect to ξ, evaluated at $\xi_0^{\pm}$, and $\Theta(\xi)$ is the function defined as

$$\Theta(\xi) = \ln(\Psi_{I(t_k)}(\xi)) - \ln(\xi) - \xi\gamma_{\mathrm{th}}. \tag{3.61}$$

The values ξ_0^{+} and ξ_0^{-} correspond to the positive and negative roots of the equation $\partial_\xi \Theta(\xi) = 0$, respectively. They can be calculated numerically as shown, for example, in [Coe10].

Finally, the mean and variance of $I(t_k)$ are given by [For00]

$$\mathcal{E}\{I(t_k)\} = \sum_{i=1}^{2M} \lambda_i \left(4\sigma_n^2 + |s_i(t_k)|^2\right) \tag{3.62}$$

$$\mathrm{Var}\{I(t_k)\} = \sum_{i=1}^{2M} 8\lambda_i^2 \sigma_n^2 \left(\sigma_n^2 + |s_i(t_k)|^2\right). \tag{3.63}$$

The method described in this section will be used extensively throughout the remaining chapters, in order to accurately evaluate the BERs and, subsequently, the performance of the analyzed transmission systems.

3.3.3   Global optimization of optical communication systems

Optimization addresses the problem of finding the set of parameters that leads to the best performance of the system. For example, dispersion map, filter bandwidths and launch powers can be varied in order to optimize the receiver power sensitivity, the OSNR or the transmission distance. In doing so, the usual approach is to carry out a grid search, in other words, to simulate every possible combination of parameters and choose the one that gives the best result. However, due to the long transmission distances and the extremely large bandwidth of the signals, the simultaneous optimization of several parameters often translates into prohibitive simulation times. In such scenarios advanced optimization algorithms prove to be an attractive alternative to the conventional grid search.

A suitable algorithm for the optimization of an optical communication link must posses certain characteristics: Since the objective function to be maximized[3] is unknown, the algorithm must resort on simulations; and because each simulation is extremely expensive in terms of computational time, the algorithm needs to converge to the desired solution using as few iterations as possible. Additionally, it should avoid getting trapped into local maxima by performing a *global* search.

The optimization of an optical communication link using an algorithm that fulfills the aforementioned requirements was first introduced in [GCS+08, CGH09]. It relies on modeling the unknown objective function as if it was generated by a normally distributed random process, i.e., a random walk [Kus62], and uses *Bayesian inference* to find the next set of parameters that will most probably improve the currently best solution [Kus63].

Formally, we are concerned with the problem of finding $\boldsymbol{x}^* \in \mathcal{S}$ such that $f(\boldsymbol{x}^*) \geq f(\boldsymbol{x}), \forall \boldsymbol{x} \in \mathcal{S}$, where $\mathcal{S}$ is the search space, that is a compact subset of $\mathbb{R}^d$. The objective function $f : \mathcal{S} \to \mathbb{R}$ is defined as an unknown continuous function and $\boldsymbol{x} = (x_1 x_2 \cdots x_d)^{\mathrm{T}}$ is the vector of parameters to optimize. If the elements of $\boldsymbol{x}$ are lower and upper bounded, the search space forms a hypercube of $N_{\mathrm{b}} = 2^d$ vertices in $\mathbb{R}^d$. Alternatively, the search space can be entirely defined by the convex hull formed by any N_{b} points, where $N_{\mathrm{b}} \geq d+1$.

Initially, the algorithm simulates the vertices of the search space, then it divides it into disjoint sub-regions. These sub-regions are obtained by using the *Delaunay triangulation* [Eld92], where each of their $d + 1$ vertices corresponds to a simulated point. Geometrically, each sub-region is a simplex (triangle for $d = 2$ or tetrahedron for $d = 3$). As a result, $f(\boldsymbol{x})$ is approximated over a bounded space by a set of simplexes.

In [Kus62], it was shown that the expected value of a one-dimensional unknown function $f(t)$, conditioned on all of the measurements taken, is a piecewise linear approximation of $f(t)$ itself, and that the conditional variance of the approximation is quadratic between the observation points [Stu88]. [Eld92] extends this results to higher-dimensional random walks. Consequently, each point $\boldsymbol{x}$ in the kth simplex $\mathcal{S}_k$ can be characterized with respect to its vertices by a mean $\mu_{f,k}(\boldsymbol{x}) = \mathcal{E}\{f(\boldsymbol{x})\}$ and a variance $\sigma_{f,k}^2(\boldsymbol{x}) = \mathcal{E}\{(f(\boldsymbol{x}) - \mu_{f,k}(\boldsymbol{x}))^2\}$.

---

[3]In this work, the algorithm is used for *maximization* of an objective function f, but note that there is no difference in maximizing f or minimizing $-f$.

Since the unknown objective function $f(\boldsymbol{x})$ is modeled as a sample function of a normally distributed random process, the probability that $\boldsymbol{x}$ improves the currently best solution $\boldsymbol{x}^*$ can be analytically calculated and written as

$$\mathcal{P}_k(f(\boldsymbol{x}) > f(\boldsymbol{x}^*) + \varepsilon_i) = 1 - \Phi\left(\frac{f(\boldsymbol{x}^*) + \varepsilon_i - \mu_{f,k}(\boldsymbol{x})}{\sigma_{f,k}(\boldsymbol{x})}\right), \qquad (3.64)$$

where $\Phi(\cdot)$ is the normal cumulative distribution function [AS64] and ε_i is a positive real number at the iteration i.

The mean and variance are given by

$$\mu_{f,k}(\boldsymbol{x}) = \mathbf{a}_k^{\mathrm{T}} \cdot \begin{pmatrix} \boldsymbol{x} \\ 1 \end{pmatrix}, \qquad (3.65)$$

$$\sigma_{f,k}^2(\boldsymbol{x}) = \begin{pmatrix} \boldsymbol{x} & 1 \end{pmatrix} \cdot \mathbf{C}_k \cdot \begin{pmatrix} \boldsymbol{x} \\ 1 \end{pmatrix}, \qquad (3.66)$$

where $\mathbf{a}_k$ is a $(d+1) \times 1$ vector and $\mathbf{C}_k$ is a $(d+1) \times (d+1)$ symmetrical matrix of unknown elements. They can be calculated as follows: the $d + 1$ vertices $\boldsymbol{x}_v$ of $\mathcal{S}_k$ are sufficient to calculate the elements of $\mathbf{a}_k$, since $\mu_{f,k}(\boldsymbol{x}_v) = f(\boldsymbol{x}_v)$. Equivalently, $\sigma_{f,k}^2(\boldsymbol{x}_v) = 0$, providing $d + 1$ conditions for calculating $\mathbf{C}_k$. The additional conditions are obtained at the midpoints $\boldsymbol{x}_{\mathrm{m}}$ of the $\frac{1}{2}(d^2 + d)$ edges of $\mathcal{S}_k$ by

$$\sigma_{f,k}^2(\boldsymbol{x}_{\mathrm{m}}) = \eta_i \cdot \|\boldsymbol{x}_p - \boldsymbol{x}_q\|, \qquad (3.67)$$

where $\|\boldsymbol{x}_p - \boldsymbol{x}_q\|$ is the Euclidean distance between the vertices $\boldsymbol{x}_p$ and $\boldsymbol{x}_q$ and η_i is the mean square variation in $f(\boldsymbol{x})$ as $\boldsymbol{x}$ changes, at the ith iteration.

The algorithm searches within $\mathcal{S}_k$ the point $\boldsymbol{x}_k$ with the highest probability of improvement according to (3.64). For this purpose, it does not need to directly calculate the probabilities but, since $\Phi(\cdot)$ is increasingly monotonic and, to avoid calculating the square root of the variance, only requires to find the point that minimizes the square of its argument, i.e.,

$$\boldsymbol{x}_k = \arg\max\{\mathcal{P}_k\} = \arg\min\{D_k^2(\boldsymbol{x})\}, \qquad (3.68)$$

where

$$D_k^2(\boldsymbol{x}) = \frac{(f(\boldsymbol{x}^*) + \varepsilon_i - \mu_{f,k}(\boldsymbol{x}))^2}{\sigma_{f,k}^2(\boldsymbol{x})} \qquad (3.69)$$

Since $D_k^2(\boldsymbol{x})$ is a convex function, there is only one point $\boldsymbol{x}_k$ where $\mathcal{P}_k$ is maximum. Observe that $\boldsymbol{x}_k$ is independent of η_i, which can be arbitrarily chosen at each iteration or numerically estimated, as explained later in this section. Finally, the point $\boldsymbol{x}_k$ with the highest probability of improvement $\mathcal{P}_k$ among all simplexes is the chose of parameters for the next simulation.

Observe that the global convergence of the global optimization algorithm (GOA) is guaranteed since, by minimizing $D_k^2(\boldsymbol{x})$, it balances the search in regions close to $f(\boldsymbol{x}^*)$ where the mean is maximum, and unexplored regions of the search space where the

(a)

(b)
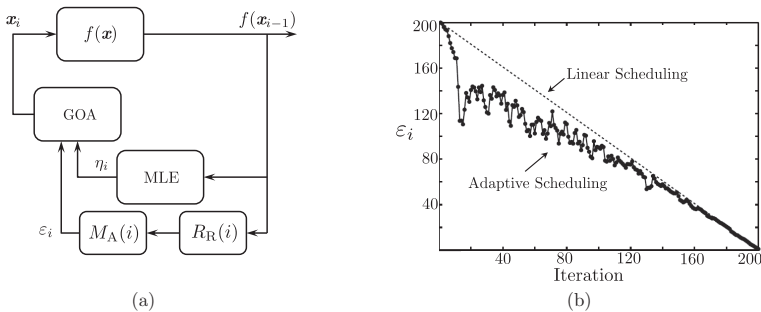
Figure 3.9: (a) Block diagram of the optimization procedure and (b) scheduling of ε_i .

variance is maximum. However, the algorithm has no feedback regarding if it is spending "too much time" searching near the current optimum, or whether its selections are indeed finding what it "expects" to find at each new iteration. Additionally, the algorithm relies on the normal distribution of the objective function at each point. Functions with this property would tend to have similar excursions above and below the mean of the function rather than, for example, functions with positive excursions and a floor, e.g., the maximum number of concatenated spans in a link. Therefore, using the normal distribution assumes functions that may not be representative of typical functions that are encountered in optical communication systems.

Both of the aforementioned drawbacks can be avoided, as proposed by [Per89], using the *rank transformation*. Ranking the objective function evaluations allows the algorithm to be unaffected by the location and scale of the function. All calculations described before can be performed on the ranked objective function evaluations rather than on the actual evaluations themselves and the statistical method's validity no longer depends on the normality of the data. Moreover, the search will give equivalent results for any monotonic transformation of the objective function, e.g., when optimizing receiver sensitivity, either in units of mW or dBm. By setting a predetermined number of iterations N_i, the number of function evaluations at the end of the optimization procedure will be $N_b + N_i$. Hence, after iteration $i - 1$, a vector with the function evaluations can be defined as $\mathbf{f} = (f(\boldsymbol{x}_1) \quad f(\boldsymbol{x}_2) \cdots f(\boldsymbol{x}_{N_b}) \cdots f(\boldsymbol{x}_{N_b+i-1}))^{\mathrm{T}}$, where $f(\boldsymbol{x}_{N_b+i-1})$ is the function evaluation at the iteration $i - 1$. Ranking the vector $\mathbf{f}$ results in another vector $\mathbf{f}_r$ of the same size, where each element is a natural number between 1 and $N_b + i - 1$. The next set of input parameters $\boldsymbol{x}_i$ is obtained by using $\mathbf{f}_r$ and the set of simplexes.

Furthermore, using the rank transformation allows for adaptive scheduling of search mode, i.e., to automatically balance the time the algorithm spends searching globally and locally by adjusting ε_i in each iteration. High values of ε_i will make the search global, while low values local. By linearly scheduling $\varepsilon_i = N_i - i + 1$, the algorithm first explores the search space sparsely, then it focusses on regions of interest and finally refines the search until $\varepsilon_i = 1$. The optimum time for the search to spend in global mode, i.e., the

---

Algorithm 3.2 Global optimization algorithm

$i = 1$

Simulate the N_b boundary points $\rightarrow$ **f**

$\boldsymbol{x}^* = \arg\max\{\mathbf{f}\}$

while $i < N_i$ **do**

    Rank all simulated points $\rightarrow$ $\mathbf{f}_r$

    Estimate η_i in (3.67) using (3.72)

    Calculate ε_i with (3.73)

    while $k <$ Number of simplexes **do**

        Calculate $\mu_{f,k}(\boldsymbol{x})$ and $\sigma^2_{f,k}(\boldsymbol{x})$ using (3.65) and (3.66)

        Find $\boldsymbol{x}_k$ that minimizes $D^2_k(\boldsymbol{x})$ using a grid search or an external local optimization

        procedure

        Calculate $\mathcal{P}_k$ with (3.64)

    end while

    For the simplex with maximum $\mathcal{P}_k$: $\boldsymbol{x}_i = \boldsymbol{x}_k$ and $\mathcal{P}_i = \mathcal{P}_k$

    Evaluate $f(\boldsymbol{x}_i)$

    if $f(\boldsymbol{x}_i) > f(\boldsymbol{x}^*)$ **then** $\boldsymbol{x}^* = \boldsymbol{x}_i$ **end if**

    $i = i + 1$

end while

Display $\boldsymbol{x}^*$ and $f(\boldsymbol{x}^*)$

---

slope of the linear scheduling function, can be set automatically by including a feedback loop for ε_i [Per89], as shown in Fig. 3.9a. Based on M previous iterations, ε_i can be set according to the following equations:

$$R_R(i) = \frac{\mathbf{f}_r(N_b + i - 1) - 1}{N_b + i - 2} \tag{3.70}$$

$$M_A(i) = \begin{cases} \frac{1}{i}\sum_{j=1}^{i} R_R(i - j + 1) & , M \leq i \\ \frac{1}{M}\sum_{j=1}^{M} R_R(i - j + 1) & , M > i \end{cases} \tag{3.71}$$

$$\varepsilon_i = (N_i - i) \cdot M_A(i) + 1, \tag{3.72}$$

where R_R is defined as the *rank ratio* and M_A is a moving average to statistically forecast the next rank ratio. $R_R(1)$ is defined as 1, $R_R(i)$ is equal 1, if $\mathbf{f}_r(N_b + i - 1) = N_b + i - 1$ and 0, if $\mathbf{f}_r(N_b + i - 1) = 1$. Consequently, ε_i will be near unity, if many new minima have been found and near $N_i - i + 1$, if many new maxima have been found. Fig. 3.9b depicts an example of adaptive versus linear scheduling of ε_i.

Finally, by estimating the actual variance of the objective function, i.e., η_i in (3.67), the probability of finding a new optimum with an extra simulation can be calculated and also used as termination criterion or a measure of confidence on how successful the search has already been. The maximum likelihood estimator (MLE) of the parameter η_i at the iteration i is given by [Stu88]

$$\hat{\eta}_i = \frac{1}{\binom{N_t}{2}} \sum_{p=1}^{N_t-1} \sum_{q=p+1}^{N_t-p} \frac{(\mathbf{f}_r(p) - \mathbf{f}_r(q))^2}{\|\boldsymbol{x}_p - \boldsymbol{x}_q\|}, \tag{3.73}$$

where $N_t = N_b + i - 1$ is the total number of simulated points at iteration i. The probability that the next simulation will improve the currently best result can be calculated using (3.64) and (3.73).

The described global optimization algorithm (GOA) is summarized in Algorithm 3.2. In [CGH09], its performance has been compared against state-of-the-art global optimization algorithms over a standard set of test functions, delivering excellent performance in terms of the number of iterations needed for convergence to the global optimum of the test functions. The algorithm is used widely in the rest of this thesis for the optimization of the transmission link parameters, as previously discussed in chapter 3.2.3.

3.4   Summary

In the first part of this chapter, the most important elements that compose the optical communication systems investigated in this thesis were described. The second part reviewed the most important criteria in the design of a link. The third part was concerned with three relevant simulation aspects for the correct evaluation of the system performance: pseudo-random sequences, BER estimation and system optimization. In summary, the main points are the following:

▷ Lasers are the preferred optical sources since they are able to generate almost monochromatic coherent light. The process by which coherent light is generated is called stimulated emission. Spontaneous emission also occurs but at a much lower rate. Nevertheless, it produces phase and intensity fluctuations. Modern lasers have very low values of phase fluctuations, also known as phase noise, that do not affect the performance of the differentially encoded modulation formats investigated in this thesis. Intensity fluctuations were not considered.

▷ Direct modulation of the optical sources is straightforward and cost-effective but, at high data rates, it leads to performance degradation due to the limited bandwidth of the lasers and induced chirping of the signals. At high data rates, external Mach-Zehnder modulators (MZM) are commonly preferred. By using multiple MZMs and phase modulators, different modulation formats can be achieved. In this thesis, MZMs are regarded as ideal components (broadband, infinite extinction ratio and zero insertion loss) albeit with nonlinear transfer function.

▷ Erbium-doped fibre amplifiers (EDFA) are the most commonly used amplifiers in deployed optical systems. At a system level, they can be regarded as black-boxes with gain that is insensitive to the modulation format, data rate or polarization state of the input signal. EDFAs produce optical noise that dominates over the thermal and shot noises produced by the optical receiver, and ultimately sets a limit to the performance of a system.

▷ Other important system components were described such as photodiodes, optical and electrical filters, and optical couplers.

▷ Attenuation is periodically compensated with EDFAs. Only considering the detrimental effect of optical noise, the optimum span length for typical standard single-mode fiber (SSMF) is around 21 km. From a cost point of view this is not economical and so spans of 80 km of fiber are more typical. There is a 6 dB sensitivity degradation when using such length compared to the optimum span length.

▷ Dispersion is an important detrimental effect that at high data rates, must be compensated for. Usually it is preferable to describe the dispersion of a fiber with the dispersion parameter D and the slope parameter S. The beta coefficients were expressed as a function of D and S assuming that D varies linearly with wavelength.

▷ Dispersion compensation is usually implemented using dispersion compensating fibers (DCF) in a two-stage amplifier configuration. The input power into the SSMF and the DCF are important design parameters that strongly affect the performance of a system. A simple analysis considering the DCF-induced nonlinear phase shift and the noise contribution of the two-stage amplifier concludes that 6.5 dB is the optimum difference between SSMF and DCF input powers.

▷ It was discussed that, in addition to the fiber's launch powers, the optimum performance of a system is also strongly influenced by the amount of pre-compensation and span residual dispersion. The most important criteria in the design of dispersion maps were reviewed, such as the straight-line rule. It is assumed that since propagation takes place in the pseudo-linear regime for the systems investigated in this thesis, the optimum performance is achieved with zero total residual dispersion.

▷ An algorithm is described that serves for estimating the maximum number of cascaded spans. It is based on the maximum nonlinear phase shift criterion and the straight-line rule.

▷ The theory of pseudo-random sequences is briefly described. The length of the sequences is important in order to correctly estimate the BER. Several criteria exist to determine the optimum sequence length. If multilevel modulation formats are investigated, binary sequences may fail to correctly estimate the BER. Following the recommendations of [SX07], pseudo-random quaternary and octonary sequences of 4096 symbols are used in this thesis. Raised cosine pulses with roll-off equal to 0.5 are used to model the electrical signals that convey the test sequences.

▷ A semi-analytical method for the estimation of the BER is described. It is based on the theory of Karhunen-Loéve series expansion. It is shown that the decision variables follow central and non-central $\mathcal{X}^2$ distributions whose exact probability density functions (PDF) are known and can be analytically calculated. The error probability is given by the integral of the PDF, which can be accurately approximated using the saddle-point approximation method.

▷ An algorithm specially designed for the global optimization of the performance of optical communication systems is introduced. It can be used, for example, to maximize the reach of a link or to minimize the required OSNR after a certain transmission

distance. It works by modeling the objective function as if it were generated by a random Gaussian process. Then, it finds the next set of parameters that maximizes the probability of finding a new optimum. Although the algorithm is computational intensive, it is successful in minimizing the required number of iterations needed to obtain the optimum with an arbitrary small error. The algorithm is as good as or better than other state-of-the art optimization procedures.

4

DQPSK Transmission Systems at 55.5 Gb/s

Differential quadrature phase-shift keying (DQPSK) is an attractive modulation scheme because of its high spectral efficiency and consequent resilience to narrow-band filtering, high tolerance to nonlinearities and relative simple transmitter and receiver implementation [WLR02, WSR03]. One alternative to implement 111 Gb/s per WDM channel is to use two polarization-multiplexed DQPSK tributaries at 55.5 Gb/s. A thorough analysis of the performance of DQPSK at such data-rate is investigated in the following chapter.

The chapter begins with a fundamental description of DQPSK in optical communication systems, i.e., transmitter and receiver structures, spectral characteristics and demodulation properties. It follows with the comparison of different "flavors" of DQPSK, such as return and non-return-to-zero signaling; dual-carrier implementation, where two optical signals are modulated at half the data rate and detected independently of each other; and stereo multiplexing, where two modulated optical carriers are linearly combined and received simultaneously. Finally, the propagation of WDM signals after 1040 km with optimum dispersion maps is thoroughly analyzed. The optimum link parameters are identified and the robustness of each transmission format with respect to variations in the dispersion map is assessed.

4.1   Transmitter and receiver design

This section begins with a general description of the transmitter structure for the generation of optical DQPSK modulation. The synthesis and spectral properties of non-return-to-zero (NRZ) and return-to-zero (RZ) pulses with different duty cycles are discussed.
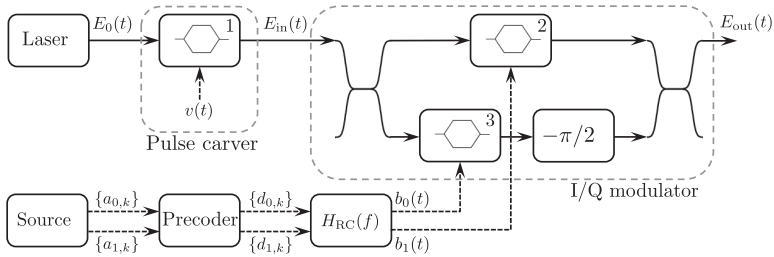
Figure 4.1: Block diagram of a DQPSK transmitter.
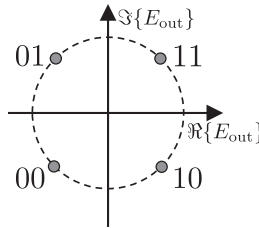
Figure 4.2: DQPSK Gray-coded constellation.

Afterwards, two alternatives to single-carrier transmission are presented: dual carrier and stereo multiplexing. The optimum filtering bandwidths and tolerance to optical noise of each format are compared in both, single-channel and WDM scenarios.

4.1.1   Differential encoding and modulation

Figure 4.1 depicts a block diagram of the transmitter for the generation of optical DQPSK modulation. The information bits are imprinted onto the phase of the optical carrier by means of a Mach-Zehnder-based optical IQ modulator. Due to the lack of an absolute phase reference in direct-detection receivers, the information must be encoded differentially, i.e., the data is conveyed in the phase difference of successive symbols and interferometric detection is employed at the receiver side.

The phases of the optical pulses output by the pulse carver are modulated by the electrical signals $b_0(t)$ and $b_1(t)$, whose amplitude vary between 0 for a logical zero, and $2V_\pi$ for a logical one and that, in turn, depend on the differentially encoded sequences represented by $\{d_{0,k}\}$ and $\{d_{1,k}\}$. The transfer function of the electrical pulse shaping filter $H_{\mathrm{RC}}(f)$ corresponds to the Fourier transform of (3.43).

Figure 4.2 depicts the constellation diagram of a DQPSK signal. Table 4.1 shows the resultant truth table for a precoder based on the previously depicted Gray-coded constellation points. By rearranging it in Karnaugh maps it is possible to obtain the binary

Table 4.1: Truth table of a DQPSK precoder

Present output		Previous output		Present input	
$d_{0,k}$ $d_{1,k}$ $\quad\phi_k$		$d_{0,k-1}$ $d_{1,k-1}$ $\quad\phi_{k-1}$		$\Delta\phi$	$a_{0,k}$ $a_{1,k}$
00	5	00	5	0	11
00	5	01	3	2	01
00	5	10	7	6	10
00	5	11	1	4	00
01	3	00	5	6	10
01	3	01	3	0	11
01	3	10	7	4	00
01	3	11	1	2	01
10	7	00	5	2	01
10	7	01	3	4	00
10	7	10	7	0	11
10	7	11	1	6	10
11	1	00	5	4	00
11	1	01	3	6	10
11	1	10	7	2	01
11	1	11	1	0	11

ϕ_k, ϕ_{k-1} and $\Delta\phi = \phi_k - \phi_{k-1}$ are expressed in multiples of $\pi/4$

logical relations between the input and output bit sequences of the precoder. They are given as

$$d_{0,k} = \bar{a}_{0,k}\bar{a}_{1,k}\bar{d}_{0,k-1} + \bar{a}_{0,k}a_{1,k}\bar{d}_{1,k-1} + a_{0,k}a_{1,k}d_{0,k-1} + a_{0,k}\bar{a}_{1,k}d_{1,k-1} \tag{4.1}$$

$$d_{1,k} = \bar{a}_{0,k}\bar{a}_{1,k}\bar{d}_{1,k-1} + \bar{a}_{0,k}a_{1,k}d_{0,k-1} + a_{0,k}a_{1,k}d_{1,k-1} + a_{0,k}\bar{a}_{1,k}\bar{d}_{0,k-1} \tag{4.2}$$

The optical signal at the output of the DQPSK transmitter is given by equation (3.6), for an input to the IQ modulator of the form $E_{\text{in}}(t) = \sqrt{P}p(t)e^{j\omega_c t}$. Without considering insertion loss, it can be written as

$$E_{\text{out}}(t) = \frac{\sqrt{P}}{2}p(t) \cdot \left(\cos\left(\pi \frac{b_0(t)}{2\,V_\pi} \right) + j \cdot \cos\left(\pi \frac{b_1(t)}{2\,V_\pi} \right) \right) \cdot e^{j\omega_c t}, \tag{4.3}$$

where P is the average power of the input optical field, $p(t)$ is the baseband representation of a train of pulses with unitary amplitude and ω_c is the angular frequency of the optical carrier.

Less complex alternative implementations of a DQPSK transmitter are realized using a Mach-Zehnder modulator in series with a phase modulator [WLR02] or by a single phase modulator [OF04] driven by a four level electrical signal. Their drawback is that since phase modulation does not occur instantly, the resulting modulated signal has a high residual chirp which reduces the tolerance against both chromatic dispersion and nonlinearities [SWR04, OF04]. Even more, any imperfections in the waveform of the

Table 4.2: Parameters of the drive signal for pulse carving

Pulse shape	Peak voltage V_p	Drive frequency f_p	Bias voltage v_bias	Phase ϕ_p
RZ-67%	V_π	$(2T_0)^{-1}$	V_π	$-\pi/2$
RZ-50%	$V_\pi/2$	$(T_0)^{-1}$	$V_\pi/2$	0
RZ-33%	V_π	$(2T_0)^{-1}$	0	0

electrical driving signals get directly mapped onto the phase of the optical carrier, thus potentially causing further performance degradation [GW05].

4.1.2   Pulse carving

The shape of the generated optical pulses significantly affects the overall performance of a communication system. The optimum pulse shape will depend on the transmission scenario, e.g., available bandwidth, transmission distance and type of link.

The most straightforward implementation of a DQPSK system uses *non-return-to-zero* (NRZ) pulses, where a pulse filling the entire symbol period is transmitted. Another common pulse shape is known as *return-to-zero* (RZ), where the optical power goes to zero in each symbol transition. RZ pulses are generated in the optical domain by means of a MZM used as a *pulse carver*. An advantage of pulse carving is that it increases the robustness of the system against imperfections in the transmitter. In high bit rate optical transmitters this can help to reduce the stringent requirements on, for example, the bandwidth of the modulator and driver amplifier voltage swing [vdB08]. Additionally, pulse carving reduces the unwanted chirp that arises between successive symbols [Sei10].

The train of pulses in (4.3) is determined by the pulse carver in Fig. 4.1 and is given by the expression

$$p(t) = \cos\left(\frac{\pi}{2V_\pi}v(t)\right), \tag{4.4}$$

where $v(t)$ is the sinusoidal driving voltage $v(t) = V_\mathrm{p}\cos(2\pi f_p t + \phi_p) + v_\mathrm{bias}$, with peak voltage V_p, frequency f_p, phase ϕ_p with respect to the clock driving MZM 2 and MZM 3 and bias voltage v_bias. Typical values for such parameters and the resultant duty cycles are listed in Table 4.2.

Observe that RZ-67% modulation also encodes a 180° phase shift between consecutive symbols. It is, therefore, often referred to as carrier-suppressed return-to-zero (CSRZ). Pulses with a duty cycle below 33% can be generated by cascading two pulse carvers with a time offset between the driving signals [GRB+03].

Figure 4.3 shows a comparison of the different pulse shapes in time and frequency domain. The pulses are generated at a symbol rate of $R_s = 27.75$ GS/s and have an average power of 0.5 mW. For representation purposes the OSNR of the signals is set to 40 dB. The eye diagrams of the transmitter optical signals are obtained without any optical filtering by
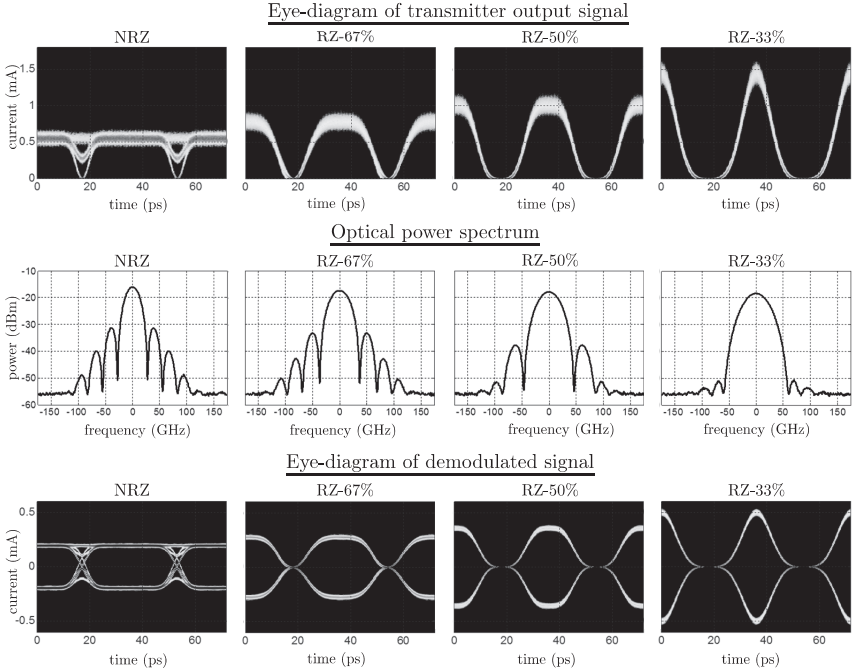
Figure 4.3: Eye-diagrams before and after demodulation (only in-phase component) and optical power spectra of DQPSK signals with different pulse shapes.

Table 4.3: Optical bandwidth (GHz) of DQPSK signals at 55.5 Gb/s

	NRZ	RZ-67%	RZ-50%	RZ-33%
3 dB	23.9	33.0	36.4	41.3
Main lobe	55.5	74.1	92.8	120.5

a photodiode with broad electrical bandwidth and ideal responsivity of 1 A/W, i.e, the electrical current coincides numerically with the optical power. The intensity dips that occur in NRZ pulses between symbol transitions due to the abrupt change in phase cause a mild residual chirp. This is, however, not problematic since the optical power is not significant at those instants [Sei10].

The smoothed[1] power spectra of the modulated signals are shown as well in Fig. 4.3.

---

[1]The plots were obtained by convolving the magnitude-squared Fourier transform of the signals with a 830 MHz-wide Gaussian window, which is equivalent to a 1.25 GHz-wide rectangular window.
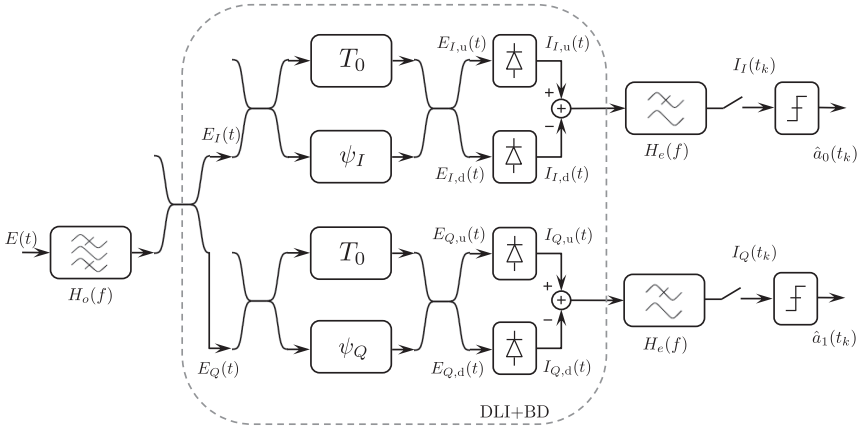
Figure 4.4: Block diagram of a DQPSK receiver using delay-line interferometers (DLI) and balanced detectors (BD).

Table 4.3 lists the double-sided 3 dB optical bandwidth of the pulses, as well as the spectral width of the main lobe. Narrower pulses have broader spectra thus making them, in principle, unattractive for scenarios where low spectral occupancy is required. Later in this section, the tolerance to narrow-band filtering of the pulses will be investigated.

4.1.3   Demodulation

The demodulation of DQPSK generally employs interferometric detection. The aim is to make the optical signal interfere with a delayed replica of itself by using delay-line interferometers. The delay is usually set to one symbol period T_0. As long as the phase of the optical carrier remains stable over two successive symbols, the transmitted signal can be successfully demodulated.

Figure 4.4 depicts the block diagram of a DQPSK receiver. The output electrical signals $I_I(t)$ and $I_Q(t)$ before sampling can be calculated by following the input signal $E(t) = A(t)e^{j\omega_c t}$ through the two branches of the receiver using equations (3.10) and (3.11). Without considering the optical and electrical filters, the electrical currents[2] at the output of the photodiodes of the upper branch can be written as

$$\begin{pmatrix} I_{I,\mathrm{u}}(t) \\ I_{I,\mathrm{d}}(t) \end{pmatrix} = \left| \frac{1}{2\sqrt{2}} \right|^2 \cdot \begin{pmatrix} |A(t-T_0) + A(t)e^{j\psi_I}|^2 \\ |A(t-T_0) - A(t)e^{j\psi_I}|^2 \end{pmatrix}$$
$$= \frac{1}{8} \cdot \begin{pmatrix} |A(t-T_0)|^2 + |A(t)|^2 + 2\Re\{A(t)A^*(t-T_0)e^{j\psi_I}\} \\ |A(t-T_0)|^2 + |A(t)|^2 - 2\Re\{A(t)A^*(t-T_0)e^{j\psi_I}\} \end{pmatrix}, \tag{4.5}$$

---

[2] "u" and "d" stand for up and down respectively.

which delivers

$$I_I(t) = I_{I,\mathrm{u}}(t) - I_{I,\mathrm{d}}(t)$$
$$= \tfrac{1}{2}\Re\{A(t)A^*(t - T_0)e^{j\psi_I}\}. \tag{4.6}$$

Since $A(t) = |A(t)|e^{j\varphi(t)}$, equation (4.6) can be rewritten as

$$I_I(t) = \frac{|A(t)||A(t - T_0)|}{2}\cos(\Delta\varphi(t) + \omega_c T_0 + \psi_I), \tag{4.7}$$

where $\Delta\varphi(t) = \varphi(t) - \varphi(t - T_0)$. A similar expression can be obtained for $I_Q(t)$. The phases ψ_I and ψ_Q can be controlled thermally (e.g., [AIM$^+$96]). They are set to $\psi_I = \pi/4 - \omega_c T_0$ and $\psi_I = -\pi/4 - \omega_c T_0$. Thus, the decision currents are given by

$$I_I(t) = \frac{|A(t)||A(t - T_0)|}{2\sqrt{2}}\left(\cos(\Delta\varphi(t)) - \sin(\Delta\varphi(t))\right), \tag{4.8}$$

$$I_Q(t) = \frac{|A(t)||A(t - T_0)|}{2\sqrt{2}}\left(\cos(\Delta\varphi(t)) + \sin(\Delta\varphi(t))\right). \tag{4.9}$$

The in-phase component takes positive values when the phase difference $\Delta\varphi$ is equal to $0°$ or $-90°$, and negative values when $\Delta\varphi$ is equal to $90°$ or $180°$. The quadrature component, on the other hand, take positive values when $\Delta\varphi$ is equal to $0°$ or $+90°$, and negative values when $\Delta\varphi$ is equal to $180°$ or $-90°$. In this way all four symbols are effectively retrieved by the depicted receiver. Figure 4.3 shows the eye-diagrams of the demodulated in-phase components of different pulse-shaped DQPSK signals.

The peak amplitude of the demodulated eye-diagrams is, according to (4.8), given by $\max_t\{I_I(t)\} = \max_t\{|A(t)|^2\}/(2\sqrt{2})$, assuming that $\max_t\{A(t)\} = \max_t\{A(t-T_0)\}$. Take for example the RZ-50% pulse train shown in Fig. 4.3. Its peak optical power is 1 mW and thus, the peak amplitude of the demodulated current is $0.001/(2\sqrt{2})$ A= 0.35 mA. In general, the optically and electrically filtered output currents will have a smaller amplitude than the unfiltered case.

Next, the decision currents will be derived taking into account the optical and electrical filters. In doing so, the receiver Hermitian kernel function $K(f_1, f_2)$, previously mentioned in chapter 3.3.2 and necessary for the semi-analytical calculation of the bit-error rate, will be obtained. Consider the electrical fields at the input of the photodiodes located at the in-phase branch of the receiver in Fig. 4.4:

$$E_{I,\mathrm{u}}(t) = A_{I,\mathrm{u}}(t)e^{j\omega_c t}, \tag{4.10}$$

$$E_{I,\mathrm{d}}(t) = A_{I,\mathrm{d}}(t)e^{j\omega_c t}. \tag{4.11}$$

Their complex amplitude $A_{I,\mathrm{u}}(t)$ and $A_{I,\mathrm{d}}(t)$ can be written in terms of the in-phase input electrical field's complex amplitude $A_I(t)$ as

$$A_{I,\mathrm{u}}(t) = j/2\left(A_I(t - T_0) + A_I(t)e^{j\psi_I}\right), \tag{4.12}$$

$$A_{I,\mathrm{d}}(t) = -1/2\left(A_I(t - T_0) - A_I(t)e^{j\psi_I}\right). \tag{4.13}$$

In turn, $A_I(t)$ can be expressed in the frequency domain as a function of the optical filter's input signal by

$$\tilde{A}_I(f) = j/\sqrt{2}H_o(f)\tilde{A}(f). \tag{4.14}$$

Applying the Fourier transform to (4.12) and (4.13) and using (4.14) we obtain

$$\tilde{A}_{I,\mathrm{u}}(f) = H_o(f)H_{I,\mathrm{u}}(f)\tilde{A}(f), \tag{4.15}$$

$$\tilde{A}_{I,\mathrm{d}}(f) = H_o(f)H_{I,\mathrm{d}}(f)\tilde{A}(f), \tag{4.16}$$

where the transfer functions representing the upper and lower branch of the delay interferometer correspond to

$$H_{I,\mathrm{u}}(f) = -\sqrt{2}/4\left(e^{-j2\pi fT_0 - j\omega_c T_0} + e^{j\psi_I}\right), \tag{4.17}$$

$$H_{I,\mathrm{d}}(f) = -j\sqrt{2}/4\left(e^{-j2\pi fT_0 - j\omega_c T_0} - e^{j\psi_I}\right). \tag{4.18}$$

Now, consider the output currents of the balanced photodiodes in the in-phase component of the receiver given by

$$\tilde{I}_{I,\mathrm{u}}(f) = \tilde{E}_{I,\mathrm{u}}(f) \star \tilde{E}_{I,\mathrm{u}}^*(-f) = \tilde{A}_{I,\mathrm{u}}(f) \star \tilde{A}_{I,\mathrm{u}}^*(-f), \tag{4.19}$$

$$\tilde{I}_{I,\mathrm{d}}(f) = \tilde{E}_{I,\mathrm{d}}(f) \star \tilde{E}_{I,\mathrm{d}}^*(-f) = \tilde{A}_{I,\mathrm{d}}(f) \star \tilde{A}_{I,\mathrm{d}}^*(-f), \tag{4.20}$$

where $\star$ represents convolution. The decision variable of the in-phase component can be written in the time domain as

$$I_I(t_k) = I_{I,1}(t_k) - I_{I,2}(t_k), \tag{4.21}$$

where the sampled filtered currents $I_{I,1}(t_k)$ and $I_{I,2}(t_k)$ are given by

$$I_{I,1}(t_k) = \int_{-\infty}^{\infty} \tilde{I}_{I,\mathrm{u}}(f)H_e(f)e^{j2\pi ft_k}\mathrm{d}f, \tag{4.22}$$

$$I_{I,2}(t_k) = \int_{-\infty}^{\infty} \tilde{I}_{I,\mathrm{d}}(f)H_e(f)e^{j2\pi ft_k}\mathrm{d}f, \tag{4.23}$$

and $H_e(f)$ is the transfer function of the electrical filter. Substituting (4.19) in (4.22) and (4.20) in (4.23), and expanding the convolution we get

$$I_{I,1}(t_k) = \iint_{-\infty}^{\infty} \tilde{A}_{I,\mathrm{u}}^*(-f')\tilde{A}_{I,\mathrm{u}}(f - f')H_e(f)e^{j2\pi ft_k}\mathrm{d}f'\mathrm{d}f,, \tag{4.24}$$

$$I_{I,2}(t_k) = \iint_{-\infty}^{\infty} \tilde{A}_{I,\mathrm{d}}^*(-f')\tilde{A}_{I,\mathrm{d}}(f - f')H_e(f)e^{j2\pi ft_k}\mathrm{d}f'\mathrm{d}f. \tag{4.25}$$

Next, two substitutions will be made in the previous equations. Firstly, by defining $f_2 = -f'$, we get $\mathrm{d}f_2 = -\mathrm{d}f'$. Since f_2 varies from $+\infty$ to $-\infty$, the negative sign does not need to be taken into account and only the variable change is performed. Secondly,

we define $f_1 = f + f_2$, where f_2 is constant, so that the expressions (4.24) and (4.25) can be written as

$$I_{I,1}(t_k) = \iint_{-\infty}^{\infty} \tilde{A}_{I,\mathrm{u}}^*(f_2) H_e(f_1 - f_2) \tilde{A}_{I,\mathrm{u}}(f_1) e^{j2\pi(f_1 - f_2)t_k} \mathrm{d}f_1 \mathrm{d}f_2, \tag{4.26}$$

$$I_{I,2}(t_k) = \iint_{-\infty}^{\infty} \tilde{A}_{I,\mathrm{d}}^*(f_2) H_e(f_1 - f_2) \tilde{A}_{I,\mathrm{d}}(f_1) e^{j2\pi(f_1 - f_2)t_k} \mathrm{d}f_1 \mathrm{d}f_2. \tag{4.27}$$

Substituting (4.15) and (4.16) into (4.26) and (4.27), and the resulting expressions into (4.21) delivers

$$I_I(t_k) = \iint_{-\infty}^{\infty} \tilde{A}^*(f_2) K_I(f_1, f_2) \tilde{A}(f_1) e^{j2\pi t_k(f_1 - f_2)} \mathrm{d}f_1 \mathrm{d}f_2, \tag{4.28}$$

where the Hermitian kernel function $K_I(f_1, f_2)$ is given by

$$\begin{aligned} K_I(f_1, f_2) = H_e(f_1 - f_2) \cdot (&H_o^*(f_2) H_{I,\mathrm{u}}^*(f_2) H_o(f_1) H_{I,\mathrm{u}}(f_1) \\ &- H_o^*(f_2) H_{I,\mathrm{d}}^*(f_2) H_o(f_1) H_{I,\mathrm{d}}(f_1)). \end{aligned} \tag{4.29}$$

Equivalently, the decision variable of the quadrature component can be written as

$$I_Q(t_k) = \iint_{-\infty}^{\infty} \tilde{A}^*(f_2) K_Q(f_1, f_2) \tilde{A}(f_1) e^{j2\pi t_k(f_1 - f_2)} \mathrm{d}f_1 \mathrm{d}f_2, \tag{4.30}$$

with

$$\begin{aligned} K_Q(f_1, f_2) = H_e(f_1 - f_2) \cdot (&H_o^*(f_2) H_{Q,\mathrm{u}}^*(f_2) H_o(f_1) H_{Q,\mathrm{u}}(f_1) \\ &- H_o^*(f_2) H_{Q,\mathrm{d}}^*(f_2) H_o(f_1) H_{Q,\mathrm{d}}(f_1)), \end{aligned} \tag{4.31}$$

where the delay interferometer transfer functions are given by

$$H_{Q,\mathrm{u}}(f) = j\sqrt{2}/4 \left(e^{-j2\pi f T_0 - j\omega_c T_0} + e^{j\psi_Q} \right) \tag{4.32}$$

$$H_{Q,\mathrm{d}}(f) = -\sqrt{2}/4 \left(e^{-j2\pi f T_0 - j\omega_c T_0} - e^{j\psi_Q} \right). \tag{4.33}$$

In conjunction with the semi-analytical method described in chapter 3.3.2, equations (4.29) and (4.31) are used to calculate the bit-error rate of the in-phase and quadrature components, BER_I and BER_Q, respectively. The aggregate bit-error rate is calculated as $\mathrm{BER} = (\mathrm{BER}_I + \mathrm{BER}_Q)/2$.

4.1.4 Receiver sensitivity and optical filter bandwidth optimization

The best performance of any optical modulation format impaired only by AWGN is obtained by using an optical receiver filter matched to the pulse shape and no post detection electrical filter [Hen89, PSPW02]. For such scenario, an analytical approximation
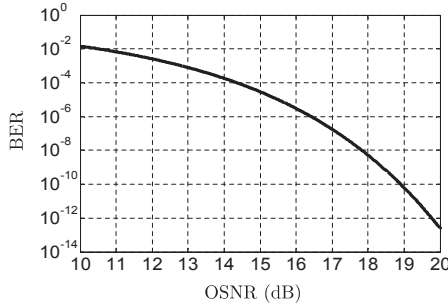
Figure 4.5: Ideal BER curve for back-to-back DQPSK at $R_s = 27.75$ GS/s.

of the BER for DQPSK modulation with interferometric detection has been obtained in [Pro00, SH04, Ho05] and is given by

$$\mathcal{P}_b \approx Q(a, b) - \left(\frac{I_0(ab)}{2} + \frac{I_1(ab)}{8} \left(\frac{b}{a} - \frac{a}{b} \right) \right) \cdot \exp\left(-\frac{a^2 + b^2}{2} \right), \qquad (4.34)$$

where

$$a = \sqrt{\rho_s(1 - \sqrt{1/2})}, \qquad (4.35)$$

$$b = \sqrt{\rho_s(1 + \sqrt{1/2})}, \qquad (4.36)$$

ρ_s is related to the OSNR by $\rho_s = 2B_{o,\text{ref}}/R_s \cdot \text{OSNR}$ with R_s equal to the symbol rate, I_m is the mth order modified Bessel function of the first kind and $Q(\cdot, \cdot)$ is the first order Marcum's Q-function[3]. Figure 4.5 depicts the BER vs. OSNR according to equation (4.34).

It is accustomed to describe the performance of a a particular communication system by the amount of OSNR (OSNR_{req}) required to achieve a certain BER. In the course of this thesis, OSNR_{req} is always calculated for a target BER of 10^{-4} using a reference bandwidth $B_{o,\text{ref}} = 12.5$ GHz. From Fig. 4.5, the back-to-back required OSNR for DQPSK at $R_s = 27.75$ GS/s using an optical matched filter, interferometric detection and no electrical post-detection filters corresponds to $\text{OSNR}_{\text{req}} = 14.35$ dB.

It is sometimes preferred to assess the performance of the transmission in terms of the minimum received power P_s required to achieve a target BER. This is usually referred to as *receiver sensitivity*. Assuming that the noise is produced by a single EDFA placed before the receiver's optical filter and according to (3.9) and (3.21), the receiver sensitivity can be written in terms of the OSNR_{req} by $P_s = h f_c F_n B_{o,\text{ref}} \cdot \text{OSNR}_{\text{req}}$. The minimum receiver sensitivity P_s^* is obtained using an ideal EDFA with $F_n = 2$, which for the curve depicted in Fig. 4.5 results in $P_s^* = -40.6$ dBm. It is also customary to express the

---

[3]See appendix A for a definition of the abovementioned mathematical functions.
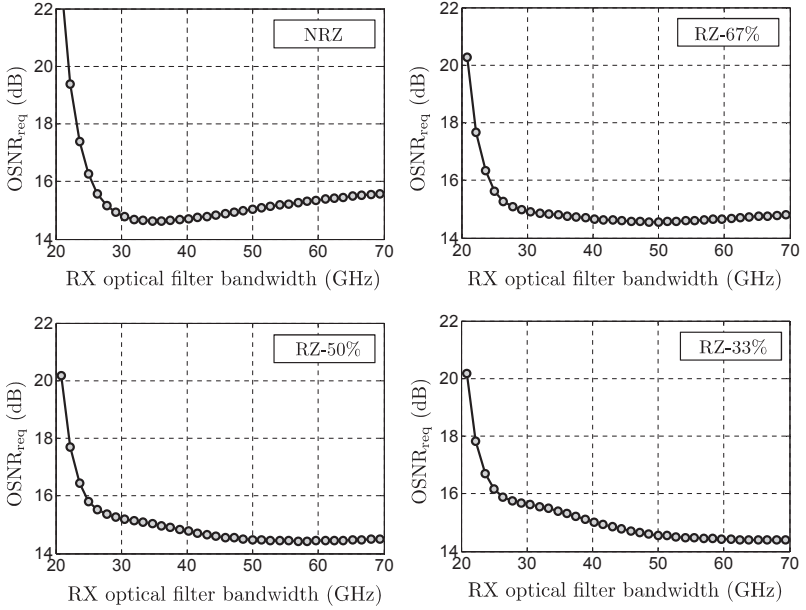
Figure 4.6: Tolerance to optical filtering of single-carrier single-channel DQPSK at 55.5 Gb/s.

ultimate performance of a modulation format in terms of the minimum number of photons per symbol required on average at the receiver input for achieving a target BER. This is usually referred to as the *quantum limit of photodetection* n_{ph}. It is related to the minimum receiver sensitivity by $n_{\mathrm{ph}} = P_s^*/(h f_c R_s)$. For optical DQPSK at $R_s = 27.75$ GS/s detected under the abovementioned conditions the quantum limit is $n_{\mathrm{ph}} = 25$ photons per symbol.

In practice, however, the received optical filter is usually not matched to the signal and the photodiodes' finite bandwidth induces post-detection electrical filtering. In this thesis, a generic optical filter is modeled with the Gaussian transfer function of 2nd order given by equation (3.12). The low-pass characteristic of the electrical components in the receiver can be modeled as a 5th order Bessel electrical filter with transfer function given by (3.13) and bandwidth $B_e = 0.75 R_s$.

The bandwidth of the optical filter can be varied in order to find the one that delivers the lowest required OSNR in a back-to-back configuration, i.e., in absence of a fiber link. The addition of optical noise is achieved by means of an attenuator in cascade with an EDFA, both placed between transmitter and receiver. The transmitted and received powers are fixed such that by increasing the attenuation, the optical gain increases accordingly and
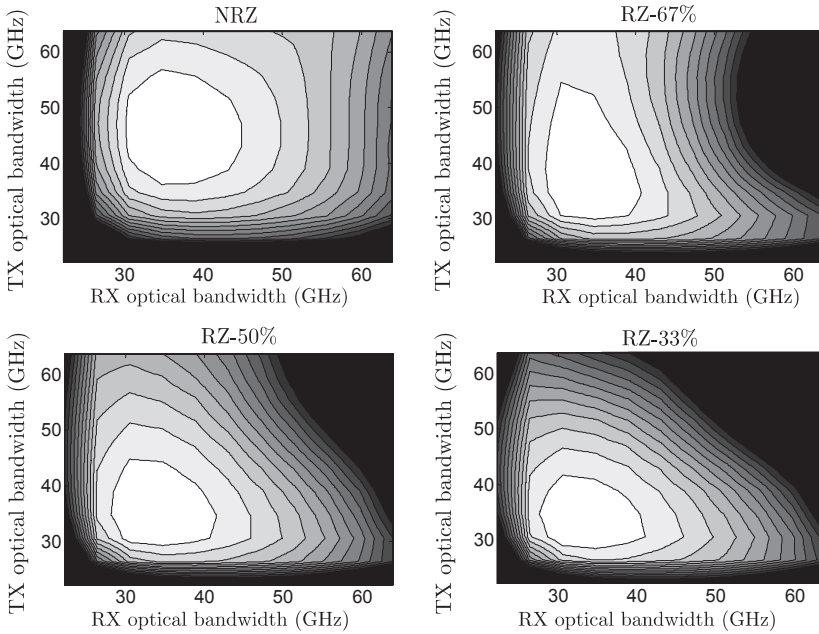
Figure 4.7: Tolerance to optical filtering in single-carrier WDM DQPSK at 55.5 Gb/s.

thus ASE noise is generated. This is equivalent as to vary the OSNR until a certain BER is achieved. The optimum filter bandwidth is found when the performance degradation induced by the residual unfiltered optical noise and by the signal distortion introduced by the narrow-band filtering are balanced.

Figure 4.6 shows the results of the optimization for the single-channel case and for each pulse shape, and Table 4.4 lists the optimum bandwidths, required OSNRs and the 2 dB penalties. It is remarkable that performance closely approaches the quantum limit, although the assumed Gaussian transmission characteristic is not even nearly matched to the optical pulse shapes. It is possible to observe that pulses with higher peak power have lower back-to-back $OSNR_{req}$, RZ-33% being the closest to the theoretical limit.

The optimum receiver performance relies on a balance between noise and inter-symbol interference (ISI) for NRZ transmission, while for RZ reception detection noise has to be traded against filter-induced signal energy rejection [WPSL01]. This is clearly seen in the shape of the resultant curves for RZ signals. At bandwidths lower than the optimum, the power of the signal decreases more rapidly than the power of the electrical ASE-ASE-beat noise, so that the influence of signal-independent electrical noise limits the performance

Table 4.4: Optimum optical filter bandwidths and required OSNRs in single-channel and WDM DQPSK at 55.5 Gb/s

	Single-channel			WDM		
	$H_{o,\mathrm{RX}}$ (GHz)	$\mathrm{OSNR_{req}}$ (dB)	2 dB penalty (GHz)	$H_{o,\mathrm{TX}}$ (GHz)	$H_{o,\mathrm{RX}}$ (GHz)	$\mathrm{OSNR_{req}}$ (dB)
NRZ	34.69	14.62	24.53	47.18	34.68	14.63
RZ-67%	48.56	14.55	23.36	34.68	34.68	14.42
RZ-50%	56.89	14.43	23.60	34.68	30.52	14.43
RZ-33%	69.38	14.40	23.83	34.68	30.52	14.46

well before ISI sets in. Observe that the optimum bandwidth is inversely proportional to the duty cycle.

On the other hand, NRZ pulses have a confined spectrum, and thus narrow bandwidths effectively suppress the noise without affecting the signal, and the optimum performance is solely limited by ISI. Consequently, NRZ is the pulse shape most robust to strong filtering but, at the same time, is the less tolerant to ISI – observe in Table 4.4 that the 2 dB penalty occurs much earlier in NRZ than in RZ pulses. Filtering above the optimum bandwidth delivers a stronger sensitivity degradation to NRZ pulses since, as opposed to RZ, little signal power is allocated in the outer part of the spectrum.

The situation is different in the WDM case. The optimum receiver filter bandwidth depends not only on the shape and width of the signal's own optical spectrum, but also on the spectrum width of the optical signals located in the adjacent channels, and on the channel separation itself. If not properly filtered, any leakage from the neighboring channels, commonly referred to as *WDM cross-talk*, will beat with the signal of interest producing distortion and a noticeable degradation in performance, far stronger than the degradation due to residual unfiltered noise. For this reason, the optimum receiver bandwidths in WDM scenarios tend to be narrower than in single-channel, especially for signals with wider spectrum such as RZ.

The control of cross-talk is done by proper optical filtering at the transmitter side. Figure 4.7 shows contour plots for the simultaneous optimization of transmitter and receiver filter bandwidths for the WDM case. Observe that all plots have the same scaling. The color gradient represents penalty with respect to the optimum required OSNR for each pulse shape. Contour lines are depicted in steps of 0.25 dB and penalties of more than 3 dB are shown black. Table 4.4 lists the optimum bandwidths and required OSNRs.

The optimum regions are located in the lower left corner of each plot where optical noise *and* cross-talk between channels are effectively suppressed. Notice that, although the optimum filter bandwidths are much narrower than the ones shown in Table 4.4 for the single-channel case, the required OSNRs remain similar and no major penalty is observed (RZ-67% performs even better with TX filtering). The reason for this is that the optical power lost by the filter at the transmitter side is restituted *before* transmission
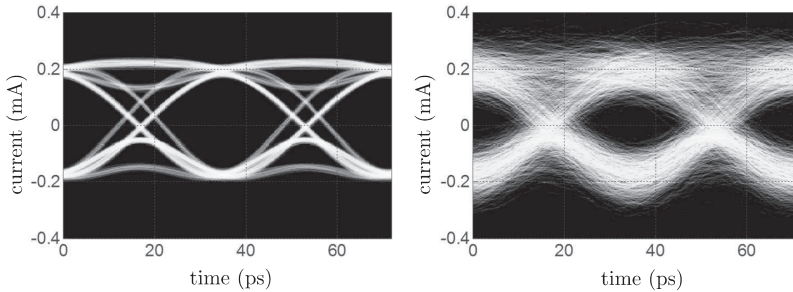
Figure 4.8: Eye-diagram of a DQPSK NRZ signal after optimum optical filtering without (left) and with optical noise (right).

and subsequent addition of noise. Thus, all the optical power of the signal is concentrated in a much more confined spectrum and, by having a narrower bandwidth, the receiver optical filter is able to reject the noise to a greater extent. Figure 4.8, left, depicts the resulting eye-diagram of a demodulated NRZ signal (in-phase) from the center channel of a WDM comb. The signal has a power of -3 dBm and is filtered with the values shown in Table 4.4. The right plot of Fig. 4.8 shows the same signal with the OSNR required to achieve a BER of 10^{-4}.

4.1.5 Dual-carrier DQPSK systems

One solution to transmit high data rates while using low-bandwidth components is to divide the bit stream into multiple sub-channels. The data in the sub-channels is conveyed by optical sub-carriers that are independently generated of each other and optically multiplexed before transmission. At the receiver side, the sub-carriers are separated *after* WDM demultiplexing via optical filters and demodulated independently of each other with dedicated receivers.

Naturally, using M parallel sub-carriers translates directly into components with one M^{th} of the required bandwidth. Additionally, an increase in tolerance to impairments that scale with the symbol rate, e.g., dispersion, is expected. On the other hand the number of required components in the transmitter and receiver sides increases, therefore, increasing the overall cost of the entire system[4]. Furthermore, a higher number of lasers and filters must be properly aligned in frequency to avoid cross-talk between sub-channels thus, also increasing the complexity of the transponders compared to a single-carrier solution. In this thesis, DQPSK systems using two optical carriers within one WDM channel will be

---

[4]In standards such as *synchronous optical network* (SONET) or *synchronous digital hierarchy* SDH, where the data rates per channel were periodically increased by four in each new generation, typically, only a 2.5-fold increase in transponder costs was observed [WE06]. Thus, doubling the number of transmitters and receivers with only half the bandwidth requirements would translate in an increase in the total cost by 60%.
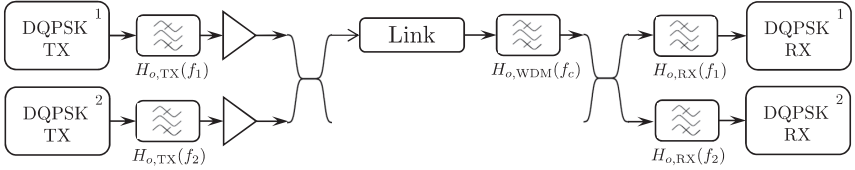
Figure 4.9: Block diagram of a dual-carrier DQPSK system.

considered as an alternative to the single-carrier case.

Figure 4.9 depicts a block diagram of the dual carrier DQPSK system. Two transmitters (shown in detail in Fig. 4.1) are used to independently modulate two optical carriers. They are centered at frequencies $f_1 = f_c - \Delta f_s/2$ and $f_2 = f_c + \Delta f_s/2$, where f_c is the center frequency of the WDM channel and Δf_s is the frequency separation between the carriers. The symbol rate of each sub-carrier is 13.875 GS/s which results in an aggregate data rate of 55.5 Gb/s. The modulated sub-carriers are firstly filtered in order to prevent any cross-talk between them, and subsequently amplified to half of the total power of the resulting signal. At the receiver side, after WDM demultiplexing, the sub-carriers are separated by optical bandpass filters centered at the respective frequencies and subsequently demodulated, each by a dedicated DQPSK receiver (see Fig. 4.4).

Theoretically, the performance of dual-carrier DQPSK is identical to the single-carrier case given that the frequency separation between sub-carriers is large ($\Delta f_s > 2R_s$). In general, the bandwidths of the transmitter filters, the WDM demultiplexer and the filters used to separate the sub-carriers must be simultaneously varied in order to optimize performance. Their optimum value is strongly dependent on the width of the spectrum and the sub-carrier frequency separation. However, a global optimization procedure (as described in ch. 3.3.3) reveals that the WDM demultiplexer ($H_{o,\text{WDM}}$) is redundant since the sub-carrier separation filters ($H_{o,\text{RX}}$) perform the same task, i.e., filtering out unwanted signals and optical noise. However, $H_{o,\text{WDM}}$ is always present in a WDM system and, therefore, imposes a limitation on the frequency separation between sub-carriers.

The bandwidths of the transmitter filters ($H_{o,\text{TX}}$), on the other hand, are much more critical design parameters. The filters are responsible of shaping the sub-carriers' spectra in order to minimize cross-talk between them and to avoid any non-symmetrical filtering caused by $H_{o,\text{WDM}}$. Similarly, the bandwidths of the sub-carrier separation filters $H_{o,\text{RX}}$ are chosen to balance performance degradation firstly due to noise and secondly, due to signal distortion caused by the adjacent sub-carrier.

Figure 4.10 shows the optimum regions for $H_{o,\text{TX}}$ and $H_{o,\text{RX}}$ when a 47 GHz optical filter is used as WDM demultiplexer. Only single-channel case is simulated. Three frequency separation are shown for comparison: $2R_s = 27.75$ GHz, $1.5R_s = 20.81$ GHz and $1R_s = 13.875$ GHz. Color gradient represents penalty with respect to the minimum required OSNR (among all pulse shapes) when $\Delta f_s = 2R_s$. Contour lines are depicted in steps of
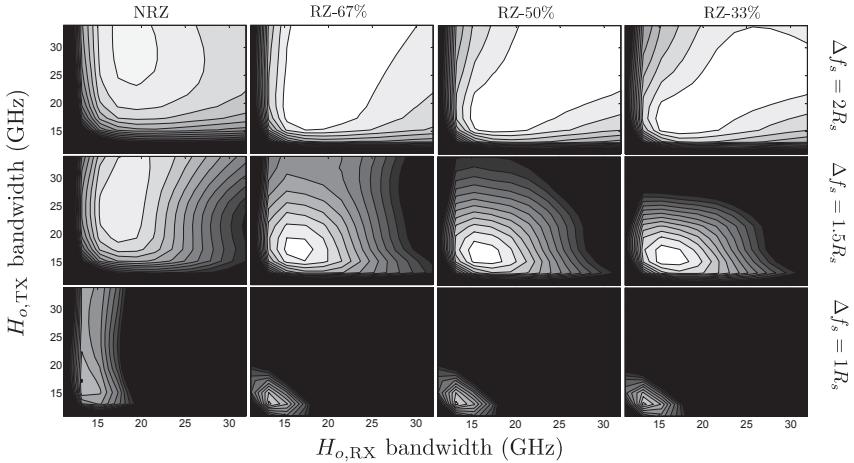
Figure 4.10: Tolerance to optical filtering of single-channel dual-carrier DQPSK at 55.5 Gb/s.

0.25 dB and penalties higher than 3 dB are shown black. The resulting optimum values are listed in Table 4.5.

In the first row of plots in Fig. 4.10, when the separation between sub-carriers is wide, it is possible to observe that cross-talk can be effectively suppressed either at the transmitter or receiver side. As expected for NRZ, penalty due to noise increases more rapidly than for RZ when enlarging the bandwidth of $H_{o,\text{RX}}$ (see Fig. 4.6, NRZ).

When the frequency separation between the sub-carriers is reduced to $\Delta f_s = 1.5R_s$, the contour plots resemble the WDM scenario shown for single-carrier in Fig. 4.7. Notice that the optimum regions are in the left corner of the plot, i.e., cross-talk is minimized by tight optical filtering at the transmitter side, and the receiver filter prevents the adjacent signals to interfere with the signal of interest. In this scenario, no performance degradation is observed.

On the other hand, when $\Delta f_s = 1R_s$, the sub-carriers must withstand strong narrow-band filtering in order for cross-talk to be minimized. We observe a degradation in performance of $\sim 0.5 - 0.8$ dB. This loss in performance makes such a narrow separation between sub-carriers unattractive in a 50 GHz channel. However, if the width of the WDM channel is reduced, sub-carriers with $\Delta f_s = 1R_s$ suffer the lowest penalty.

The tolerances of WDM dual-carrier DQPSK to WDM filtering using NRZ and RZ-33% are shown in Figure 4.11. The advantages of halving the symbol rate by using dual-carrier DQPSK will become evident when analyzing the tolerance to dispersion and the robustness of the dispersion maps in the following sections.
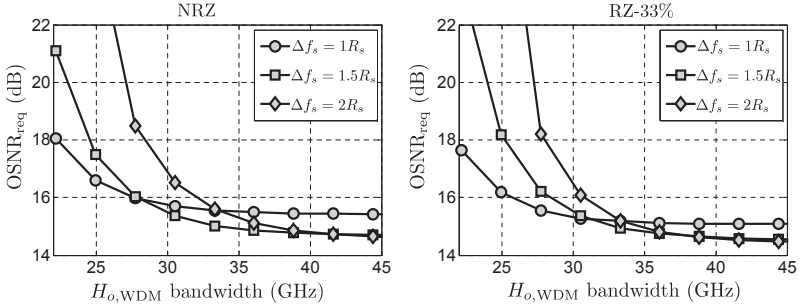
Figure 4.11: Tolerance to WDM demultiplexer bandwidth in single-channel dual-carrier DQPSK at 55.5 Gb/s.

Table 4.5: Optimum optical filter bandwidths and required OSNRs for dual-carrier DQPSK at 55.5 Gb/s

	Single-channel $\Delta f_s = 1R_s$			WDM $\Delta f_s = 1R_s$		
	$H_{o,\text{TX}}$ (GHz)	$H_{o,\text{RX}}$ (GHz)	OSNR_{req} (dB)	$H_{o,\text{TX}}$ (GHz)	$H_{o,\text{RX}}$ (GHz)	OSNR_{req} (dB)
NRZ	17.3	13.1	15.41	17.3	13.1	15.43
RZ-67%	13.1	13.1	15.12	13.1	13.1	15.13
RZ-50%	13.1	13.1	15.10	13.1	13.1	15.11
RZ-33%	13.1	13.1	15.07	13.1	13.1	15.08

	Single-channel $\Delta f_s = 2R_s$			WDM $\Delta f_s = 2R_s$		
	$H_{o,\text{TX}}$ (GHz)	$H_{o,\text{RX}}$ (GHz)	OSNR_{req} (dB)	$H_{o,\text{TX}}$ (GHz)	$H_{o,\text{RX}}$ (GHz)	OSNR_{req} (dB)
NRZ	29.8	19.4	14.66	25.6	17.3	14.85
RZ-67%	19.4	17.3	14.40	17.3	17.3	14.49
RZ-50%	17.3	17.3	14.40	17.3	17.3	14.63
RZ-33%	17.3	17.3	14.43	15.2	17.3	14.59

4.1.6 Stereo-multiplexed DQPSK systems

In [GCS$^+$09], a technique has been proposed to simultaneously demodulate two optical carriers using only one optical receiver. Using this technique it is possible to build a system using components with low bandwidth, as in dual-carrier DQPSK systems, and spare one DQPSK demodulator at the receiver side, therefore reducing costs. Instead of transmitting two sub-carriers $A_a(t)$ and $A_b(t)$ using two independent optical frequencies, [GCS$^+$09] proposes to transmit a linear combination of the two sub-carriers $(A_a(t)+A_b(t))$ and $(A_a(t)-A_b(t))$ on each frequency. In such way, the intermodulation products caused
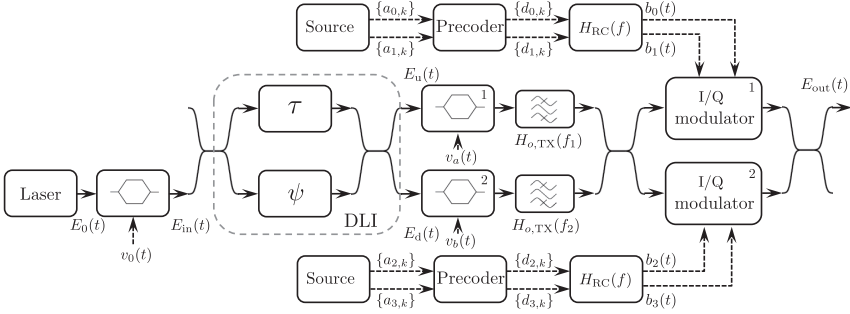
Figure 4.12: Block diagram of a stereo-multiplexed DQPSK transmitter.

by the beating of the two carriers at output of the photodiode are effectively suppressed. This is known as *stereo multiplexing* due to its resemblance to standard stereo broadcast systems [DeV61].

The technique is compatible with phase modulation if the separation between sub-carriers coincides with a multiple of the period of the delay-line interferometer's (DLI) periodic transfer function used for phase-to-intensity conversion. The intensity of the original sub-carriers is subsequently recovered using an additional electronic demodulator.

Figure 4.12 shows an implementation of a stereo-multiplexed DQPSK transmitter. Firstly, two phase-locked optical sub-carriers are generated by means of a MZM and a DLI. The MZM can be operated as a linear optical mixer by carefully avoiding its saturation region. Consider a sinusoidal electrical signal $v_0(t) = V_p \cos(2\pi \frac{\Delta f_s}{2} t) - V_\pi$ that modulates an optical carrier $E_0 = \sqrt{P} \cdot \exp(j\omega_c t)$. If $v_0(t)$ is set to drive the MZM in the linear region and assuming no optical loss, the input to the DLI can be written as $E_{\text{in}} = A(t) \cdot \exp(j\omega_c t)$, where

$$\tilde{A}(f) = \frac{\sqrt{P}}{2} \left(\delta \left(f - \frac{\Delta f_s}{2} \right) + \delta \left(f + \frac{\Delta f_s}{2} \right) \right). \tag{4.37}$$

The DLI acts as a filter that separates the sub-carriers from each other. This is done by setting the delay constant to $\tau = 1/(2\Delta f_s)$ and the phase to $\psi = -2\pi\tau\Delta f_s/2 - \omega_c\tau$, which results in the DLI transfer functions given by:

$$H_{\text{u}}(f) = \frac{\tilde{A}_{\text{u}}(f)}{\tilde{A}(f)} = je^{j\psi} \cdot \frac{\exp(-j2\pi\tau(f - \frac{\Delta f_s}{2})) + 1}{2}, \tag{4.38}$$

$$H_{\text{d}}(f) = \frac{\tilde{A}_{\text{d}}(f)}{\tilde{A}(f)} = -e^{j\psi} \cdot \frac{\exp(-j2\pi\tau(f - \frac{\Delta f_s}{2})) - 1}{2}. \tag{4.39}$$

Figure 4.13 depicts the transfer function of a DLI set to filter sub-carriers with $\Delta f_s = 27.75$ GHz. As a result, the optical sub-carriers can be written as $E_{\text{u}}(t) = A_{\text{u}}(t) \cdot e^{j\omega_c t}$
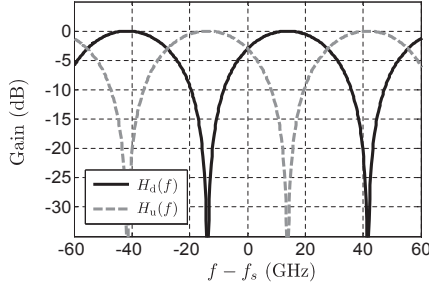
Figure 4.13: Transfer function of a DLI with $\tau = 1/55.5$ ns.

and $E_{\mathrm{d}}(t) = A_{\mathrm{d}}(t) \cdot e^{j\omega_c t}$ where by using (4.37)-(4.39) we obtain

$$E_{\mathrm{u}}(t) = \frac{\sqrt{P}}{2} \cdot je^{j\psi} \cdot e^{j2\pi\left(f_c - \frac{\Delta f_s}{2}\right)t}, \tag{4.40}$$

$$E_{\mathrm{d}}(t) = \frac{\sqrt{P}}{2} \cdot e^{j\psi} \cdot e^{j2\pi\left(f_c + \frac{\Delta f_s}{2}\right)t}. \tag{4.41}$$

Next, each sub-carrier is carved with $v_a(t)$ and $v_b(t)$ and optically filtered to narrow its spectrum. The resulting signals are recombined, modulated and recombined again to form the stereo signal given by

$$E_{\mathrm{out}}(t) = \frac{1}{\sqrt{2}} \left(\frac{A_a(t) - A_b(t)}{2} \cdot e^{j2\pi\frac{\Delta f_s}{2}t} + \frac{A_a(t) + A_b(t)}{2} \cdot e^{-j2\pi\frac{\Delta f_s}{2}t} \right) \cdot je^{j\psi} \cdot e^{j\omega_c t}, \tag{4.42}$$

where $A_a(t) = \sqrt{P}p_a(t)e^{j\varphi_a(t)}$ and $A_b(t) = \sqrt{P}p_b(t)e^{j\varphi_b(t)}$ are DQPSK modulated signals with pulses $p_a(t)$ and $p_b(t)$, respectively. Consider that irrespective of the amount of filtering, each sub-carrier is transmitted with a power equal to half of the total power of the signal.

By multiplexing the sub-carriers as in (4.42), only one optical DQPSK receiver is needed at the receiver side. In order to retrieve the transmitted bits encoded in the phase of $A_a(t)$ and $A_b(t)$, the output electrical currents of the I and Q branches of the DQPSK receiver must be further processed in the electrical domain, as shown in Fig. 4.14. According to (4.6), the electrical currents[5] are given by

$$I_I(t) = \tfrac{1}{2}\Re\{E(t)E^*(t - T_0)e^{j\psi_I}\}, \tag{4.43}$$

$$I_Q(t) = \tfrac{1}{2}\Re\{E(t)E^*(t - T_0)e^{j\psi_Q}\}. \tag{4.44}$$

Without considering the receiver optical filter $H_o(f)$ and after some algebraic detail[6],

---

[5]Observe that the photodiodes of the DQPSK receiver should have a bandwidth larger than Δf_s.
[6]See appendix C.
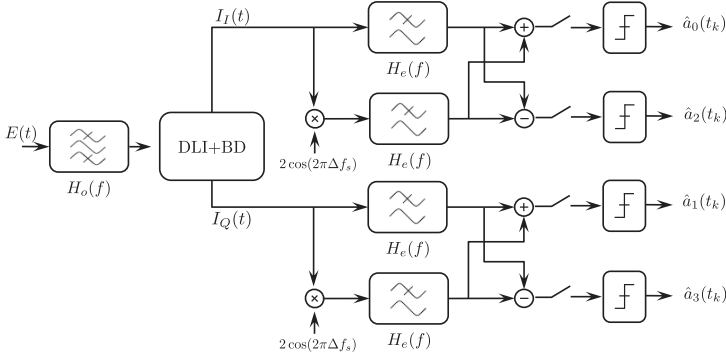
Figure 4.14: Block diagram of a stereo-multiplexed DQPSK receiver. DLI+BD stands for delay-line interferometers with balanced detectors, as shown in Fig.4.4

inserting (4.42) into (4.43) and (4.44) yields

$$
\begin{aligned}
I_I(t) = \tfrac{1}{8}\big(&|A_a|^2\cos(\Delta\varphi_a+\pi/4)+|A_b|^2\cos(\Delta\varphi_b+\pi/4)\\
&+\big(|A_a|^2\cos(\Delta\varphi_a+\pi/4)-|A_b|^2\cos(\Delta\varphi_b+\pi/4)\big)\cdot\cos(2\pi\Delta f_s t)\\
&-(|A_aA_b|\sin(\Delta\varphi_{ab}+\pi/4)-|A_aA_b|\sin(\Delta\varphi_{ba}+\pi/4))\cdot\sin(2\pi\Delta f_s t)\big),\quad(4.45)
\end{aligned}
$$

$$
\begin{aligned}
I_Q(t) = \tfrac{1}{8}\big(&|A_a|^2\cos(\Delta\varphi_a-\pi/4)+|A_b|^2\cos(\Delta\varphi_b-\pi/4)\\
&+\big(|A_a|^2\cos(\Delta\varphi_a-\pi/4)-|A_b|^2\cos(\Delta\varphi_b-\pi/4)\big)\cdot\cos(2\pi\Delta f_s t)\\
&-(|A_aA_b|\sin(\Delta\varphi_{ab}-\pi/4)-|A_aA_b|\sin(\Delta\varphi_{ba}-\pi/4))\cdot\sin(2\pi\Delta f_s t)\big).\quad(4.46)
\end{aligned}
$$

In equations (4.45) and (4.46) the time dependence of the variables was dropped for compact notation and the following substitutions were carried out:

$$
\begin{aligned}
\Delta\varphi_a &=\varphi_a(t)-\varphi_a(t-T_0), &(4.47)\\
\Delta\varphi_b &=\varphi_b(t)-\varphi_b(t-T_0), &(4.48)\\
\Delta\varphi_{ab} &=\varphi_a(t)-\varphi_b(t-T_0), &(4.49)\\
\Delta\varphi_{ba} &=\varphi_b(t)-\varphi_a(t-T_0). &(4.50)
\end{aligned}
$$

Observe that the variables of interest[7], $|A_a|^2\cos(\Delta\varphi_a\pm\pi/4)$ and $|A_b|^2\cos(\Delta\varphi_b\pm\pi/4)$, are summed in the baseband component of the electrical currents; and are subtracted in the in-phase component of the electrical currents oscillating at $f=\Delta f_s$. The intermodulation products, on the other hand, fall into the quadrature component of the electrical currents oscillating at $f=\Delta f_s$.

---

[7]See equation (4.7).

As depicted in Fig. 4.14, the information of channels a and b can be retrieved in the electrical domain. Firstly, the base-band component of the electrical currents is recovered by means of a low-pass filter ($H_e(f)$) with bandwidth $B_e \approx \Delta f_s/2$. Secondly, the in-phase component of the electrical currents oscillating at $f = \Delta f_s$ is down-mixed to $f = 0$ by means of a phase-locked electrical local oscillator and another low-pass filter ($H_e(f)$) with bandwidth $B_e \approx \Delta f_s/2$. Subsequently, both signals at the output of the low-pass filters are added to and subtracted from each other. Notice that the I and Q branches can be processed in the electrical domain independently of one another.

Stereo multiplexing is a form of linearly pre-coded frequency division multiplexing where the pre-coding matrix $\mathbf{P} = (\mathbf{p}_1 \ \mathbf{p}_2)$, with $\mathbf{p}_1 = (1 \ 1)^{\mathrm{T}}$ and $\mathbf{p}_2 = (-1 \ 1)^{\mathrm{T}}$ is equivalent to two-point inverse discrete Fourier transform matrix. Therefore, the information can also be recovered in the time domain, by sampling the currents $I_I(t)$ and $I_Q(t)$ at time intervals $t_k = \frac{k}{2\Delta f_s}$, with $k \in \mathbb{N}$. However this is challenging since the sampling instant would have to be carefully controlled in the absence of a well defined pulse.

In order to calculate the BER of a stereo-multiplexed signal with the technique described in chapter 3.3.2, the hermitian kernel function $K(f_1, f_2)$ should be derived. This has been done in [Coe10], and consist in substituting the transfer function of the electrical filters $H_e(f_1 - f_2)$ in (4.26) and (4.27) by the transfer function of the corresponding down-mixing and summation/subtraction circuits $H_e^a(f_1, f_2, \Delta f_s, t)$ and $H_e^b(f_1, f_2, \Delta f_s, t)$ given by

$$
\begin{aligned}
H_e^a(f_1, f_2, \Delta f_s, t) =& H_e(f_1 - f_2) + H_e(f_1 - f_2 - \Delta f_s) \cdot e^{-j2\pi\Delta f_s t} \\
& + H_e(f_1 - f_2 + \Delta f_s) \cdot e^{j2\pi\Delta f_s t}, \tag{4.51}
\end{aligned}
$$

$$
\begin{aligned}
H_e^b(f_1, f_2, \Delta f_s, t) =& H_e(f_1 - f_2) + H_e(f_1 - f_2 - \Delta f_s) \cdot e^{-j2\pi\Delta f_s t} \\
& - H_e(f_1 - f_2 + \Delta f_s) \cdot e^{j2\pi\Delta f_s t}, \tag{4.52}
\end{aligned}
$$

so that (4.29) and (4.31) can be rewritten for stereo-multiplexed DQPSK systems as

$$
\begin{aligned}
K_I^a(f_1, f_2) =& H_e^a(f_1, f_2, \Delta f_s, t) \cdot (H_o^*(f_2) H_{I,\mathrm{u}}^*(f_2) H_o(f_1) H_{I,\mathrm{u}}(f_1) \\
& - H_o^*(f_2) H_{I,\mathrm{d}}^*(f_2) H_o(f_1) H_{I,\mathrm{d}}(f_1)), \tag{4.53}
\end{aligned}
$$

$$
\begin{aligned}
K_Q^a(f_1, f_2) =& H_e^a(f_1, f_2, \Delta f_s, t) \cdot (H_o^*(f_2) H_{Q,\mathrm{u}}^*(f_2) H_o(f_1) H_{Q,\mathrm{u}}(f_1) \\
& - H_o^*(f_2) H_{Q,\mathrm{d}}^*(f_2) H_o(f_1) H_{Q,\mathrm{d}}(f_1)), \tag{4.54}
\end{aligned}
$$

$$
\begin{aligned}
K_I^b(f_1, f_2) =& H_e^b(f_1, f_2, \Delta f_s, t) \cdot (H_o^*(f_2) H_{I,\mathrm{u}}^*(f_2) H_o(f_1) H_{I,\mathrm{u}}(f_1) \\
& - H_o^*(f_2) H_{I,\mathrm{d}}^*(f_2) H_o(f_1) H_{I,\mathrm{d}}(f_1)), \tag{4.55}
\end{aligned}
$$

$$
\begin{aligned}
K_Q^b(f_1, f_2) =& H_e^b(f_1, f_2, \Delta f_s, t) \cdot (H_o^*(f_2) H_{Q,\mathrm{u}}^*(f_2) H_o(f_1) H_{Q,\mathrm{u}}(f_1) \\
& - H_o^*(f_2) H_{Q,\mathrm{d}}^*(f_2) H_o(f_1) H_{Q,\mathrm{d}}(f_1)). \tag{4.56}
\end{aligned}
$$

In conjunction with the semi-analytical method described in chapter 3.3.2, equations (4.53)-(4.56) are used to calculate the bit-error rate of the in-phase and quadrature components for each sub-channel, BER_I^a, BER_I^b and BER_Q^a, BER_Q^b, respectively. The aggregate bit-error rate is calculated as $\mathrm{BER} = (\mathrm{BER}_I^a + \mathrm{BER}_I^b + \mathrm{BER}_Q^a + \mathrm{BER}_Q^b)/4$.

The possibility of extending this multiplexing technique to more than two sub-carriers is thoroughly investigated in appendix D. It is shown that simultaneous demodulation using
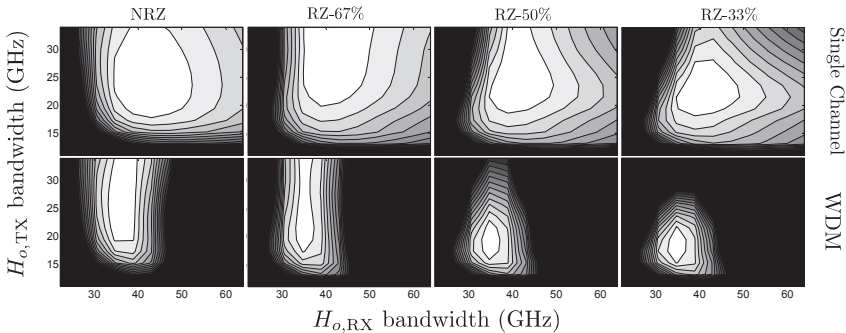
Figure 4.15: Tolerance to optical filtering of stereo-multiplexed DQPSK at 55.5 Gb/s.

direct detection of up to five sub-carriers is in principle possible, provided that the pre-coding matrix has complex values, i.e., the amplitude and the phase of the sub-carriers must be manipulated before multiplexing them. An example is given for a system using three intensity-modulated sub-carriers.

As in dual-carrier DQPSK systems, careful design of the optical filters at the transmitter and receiver sides must be carried out, in order to ensure the optimum performance of the system. The transmitter filters shape the spectrum so that cross-talk between sub-channels is minimized. Observe that this must be done *before* the modulation stage, since one modulator imprints the information of a sub-channel simultaneously in both sub-carriers. At the receiver side, the WDM demultiplexer filters out adjacent WDM channels and unwanted optical noise. The sub-carrier separation is performed by electrical filters, as shown in Fig. 4.14.

As it was previously mentioned, the separation between sub-carriers is limited to a multiple of the symbol-rate so that one DLI can perform phase-to-intensity conversion simultaneously in both frequencies. Simulations show that for a tight separation of $\Delta f_s = R_s$ the transmitter optical filters are unable to prevent cross-talk between sub-carriers without strongly distorting the signals. Any residual cross-talk between the sub-carriers at such narrow frequency separation, directly affects the channel that is summed and subtracted in both frequencies, in this case channel b, seriously compromising its performance. For this reason, only the case $\Delta f_s = 2R_s$ will be considered in the following analysis.

The simultaneous optimization of the bandwidths of $H_{o,\text{TX}}$, H_o and H_e shows that the most critical parameter is the bandwidth of the electrical filters. A value of ~ 10.4 GHz, equivalent to approximately 75% of the symbol rate, was found to be close to the optimum for all pulse shapes, provided that the bandwidth of the optical filters are also optimum. A narrower bandwidth induces strong signal distortion, whereas a wider one fails to prevent cross-talk between both baseband and passband components of the electrical signal.

Figure 4.15 shows contour plots with the performance of the system for various transmit-

Table 4.6: Optimum optical filter bandwidths and required OSNRs for stereo-multiplexed DQPSK at 55.5 Gb/s

	Single-channel			WDM		
	$H_{o,\text{TX}}$ (GHz)	$H_{o,\text{RX}}$ (GHz)	OSNR_{req} (dB)	$H_{o,\text{TX}}$ (GHz)	$H_{o,\text{RX}}$ (GHz)	OSNR_{req} (dB)
NRZ	23.5	43.0	15.48	23.5	34.7	15.96
RZ-67%	34.0	38.8	14.91	21.5	34.7	15.49
RZ-50%	23.5	38.8	14.98	19.4	34.7	15.44
RZ-33%	23.5	38.8	15.02	19.4	34.7	15.45

ter and receiver filter bandwidths. The contour lines depict penalties in steps of 0.25 dB with respect to the optimum required OSNR for each pulse shape, and penalties of more than 3 dB are shown black. Table 4.6 summarizes the optimum values for the bandwidths and the required OSNRs. Observe that the required OSNRs are higher for stereo than for the dual-carrier case. This penalty comes from the fact that the receiver optical filter for stereo systems is unable to properly reject the optical noise *in between* the sub-carriers. As expected, this penalty is higher for NRZ pulses. Referred to dual DQPSK, NRZ signals require 1 dB higher OSNR, whereas RZ signals require only 0.5 dB more.

In order to properly reject any cross-talk from adjacent WDM signals, the receiver optical filter needs to have a narrower bandwidth compared to the single-channel case. This causes asymmetrical filtering between the sub-carriers, i.e., one sub-carrier suffers from more attenuation in the higher part of its spectrum and the other one in the lower part and, therefore, the bandwidth of transmitter optical filters should be accordingly reduced. The effect of the narrower filtering in the WDM case, plus any residual cross-talk between WDM signals translates into an additional penalty of $\sim$ 0.5 dB for all pulse shapes. In summary, the gain of stereo multiplexing, in terms of reduction of the number of components at the receiver side, comes at an expense in receiver sensitivity of about ~0.5–1 dB.

4.2 Dispersion and nonlinear tolerances

In this section, fundamental characteristics of the three abovementioned formats are investigated. Firstly, back-to-back dispersion tolerances are discussed. Then, single-span transmission is simulated in order to quantify nonlinear tolerances. The optimum filter bandwidths shown in Tables 4.4, 4.5 and 4.6 are used in the rest of the simulations.

4.2.1 Dispersion tolerance

An important parameter in the performance evaluation of any optical transmission format is the tolerance to accumulated dispersion. As it was previously mentioned in chapter 3.2.2, systems operating at high data rates must compensate for the dispersion that
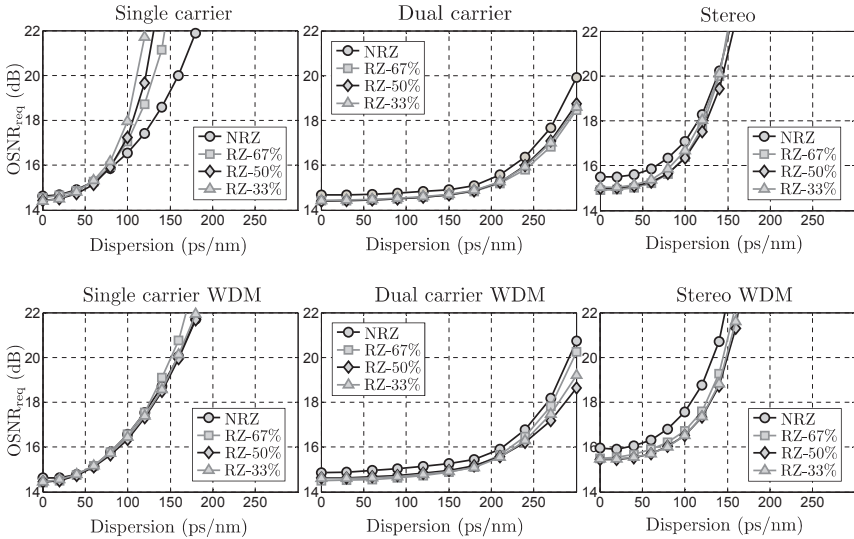
Figure 4.16: Tolerance to dispersion of DQPSK at 55.5 Gb/s.

Table 4.7: Dispersion tolerances (ps/nm) of DQPSK at 55.5 Gb/s – 2 dB penalties

	Single-channel			WDM		
	Single-carrier	Dual-carrier	Stereo	Single-carrier	Dual-carrier	Stereo
NRZ	101	247	107	101	242	107
RZ-67%	91	257	109	96	243	119
RZ-50%	88	251	111	101	253	121
RZ-33%	82	254	105	100	248	121

the signal accumulates along the link. Furthermore, if transmission takes place in the pseudo-linear regime, any residual dispersion at the end of the link is undesirable. For this purpose, dispersion compensating fibers are used in a multitude of configurations within the transmission system. However, because of changes in the chromatic dispersion parameter of the fibers due to, e.g., temperature [Vor07], transmission formats should have an inherent tolerance to uncompensated dispersion.

Using the optimum filter bandwidths derived in the last section, the required OSNRs for a target BER=10^{-4} were simulated for single-carrier, dual-carrier and stereo-multiplexed DQPSK systems using different pulse shapes. The simulations were carried out for single-channel and WDM configurations by sending the signals over a dispersive single-mode fiber. Other disturbing effects such as nonlinearities are neglected. Figure 4.16 depicts the simulation results and Table 4.7 lists the 2 dB penalties of each format.
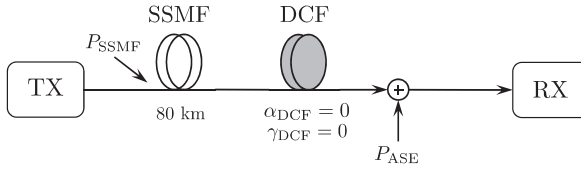
Figure 4.17: Block diagram of a single-span transmission link.

Three conclusions can be drawn from the simulation results. Firstly, the dispersion tolerance varies inversely with the bandwidth of the signals. This can be observed in the single-channel and single-carrier case. NRZ pulses have the narrowest bandwidth and therefore the highest tolerance, whereas RZ-33% pulses have the widest spectrum and thus, the lowest tolerance. However, if the signals are properly filtered and have a comparable bandwidth, as with the WDM single-carrier case, the tolerance to dispersion is similar for all pulses. Notice that, due to the narrow filtering to which RZ signals are exposed in a WDM scenario, the dispersion tolerances are comparable to those of NRZ signals.

Secondly, it is clear that halving the symbol rate in dual carrier systems translates into an enormous gain in dispersion tolerance. The tolerances are increased between 2.5 and 3 times compared to the single-carrier case. The signals have comparable bandwidths, which in turn, results in similar dispersion tolerances.

Thirdly, stereo multiplexing has a similar dispersion tolerance as the single-carrier case, although their symbol rate is reduced to half of it. The reason is that the sub-carrier that conveys the sum of the channels suffers a slightly different distortion due to dispersion than the sub-carrier that contains the difference of the channels. This is equivalent as if the pre-coding condition was affected by dispersion and, due to the squaring operation of the receiver, intermodulation products appear and interfere with the signals causing performance degradation. Additionally, observe that the tighter filtering of WDM stereo signals compared to the single-channel causes the tolerance to dispersion to increase.

4.2.2 Nonlinear tolerance

A straightforward approach to investigate the nonlinear properties of the abovementioned modulation formats is to use the single-span set-up shown in Figure 4.17. The optical signals are transmitted over 80 km of standard single-mode fiber. 100% of the accumulated dispersion is compensated for by an ideal DCF, i.e., linear without attenuation. The average input power to the SSMF is varied and the required OSNR for a BER of 10^{-4} is calculated. Figure 4.18 depicts the simulation results. The 2 dB penalties, referred to the back-to-back required OSNR are shown in Table 4.8. The optimum bandwidths obtained in chapter 4.1 are used in the simulations. Propagation in the standard single-mode fiber was simulated using the parameters shown in Table 1.1.

The single-channel single-carrier plot shows that, as expected, NRZ signals have the
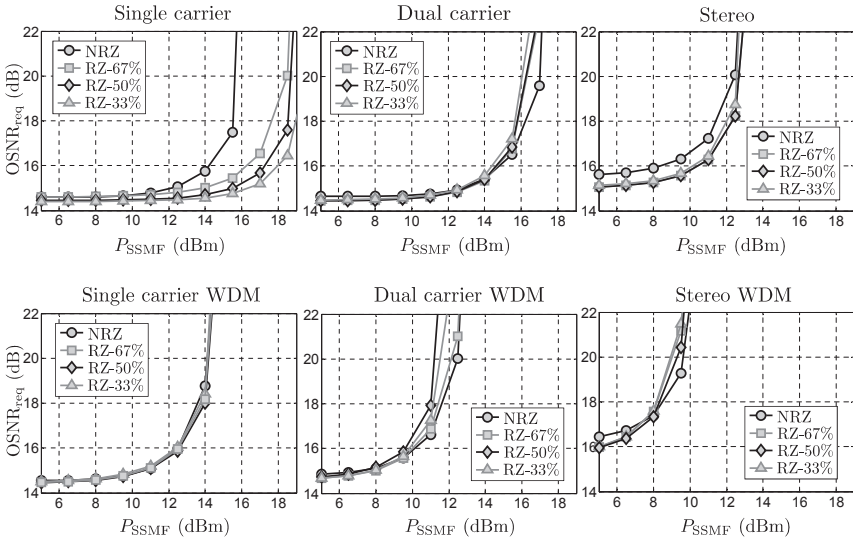
Figure 4.18: Tolerance to nonlinear effects in single-span transmission of DQPSK at 55.5 Gb/s. Optimum filter bandwidths were applied.

worst tolerance to intra-channel nonlinear effects. Additionally, one can observe that RZ signals improve their tolerance as their duty cycle decreases, showing the effectiveness of pulse carving against intra-channel nonlinear effects. On the other hand, in the WDM scenario[8], all pulses have a similar tolerance. With WDM nonlinear penalties of 1.8 and 1.9 dB, respectively, NRZ and RZ-67% signals seem to be less affected by inter-channel nonlinear effects than RZ-50% and RZ-33% signals, which show penalties of 4.9 and 5.6 dB.

The single-channel dual carrier case shows signals having a similar tolerance. The tolerance of RZ pulses is poorer than in the single-carrier case due to the the strong nonlinear interaction between sub-carriers. On the other hand, NRZ pulses do not seem to be strongly affected by the adjacent sub-carrier. In the WDM case dual-carrier signals suffer a strong nonlinear penalty, albeit similar for all pulse formats. Notice that, in this case all the signals have a similar bandwidth. The strong proximity of the sub-carriers in the WDM case increases the effect of the nonlinear effects and produce an extra ∼ 2 dB penalty compared to the single channel case.

Stereo-multiplexed signals, in turn, seem to be the least tolerant to nonlinearities. This results from the fact that each sub-carrier becomes a different nonlinear chirp that distorts

---

[8]Recall that, as in the rest of this thesis, in the WDM scenario 7 co-polarized and uncorrelated WDM channels with 50 GHz of frequency separation are simulated, and that performance measurements are related to the center channel.

Table 4.8: Single-span nonlinear tolerance (dB) of DQPSK at 55.5 Gb/s – 2 dB penalties

	Single-channel			WDM		
	Single-carrier	Dual-carrier	Stereo	Single-carrier	Dual-carrier	Stereo
NRZ	14.5	15.3	10.5	12.7	10.8	8.0
RZ-67%	16.8	15.1	11.5	12.9	10.5	7.8
RZ-50%	17.6	15.0	11.6	12.7	9.8	8.0
RZ-33%	18.4	14.8	11.4	12.8	10.2	7.8

the pre-coding condition which, in turn, produces intermodulation products that add to the penalty caused by the nonlinear effects themselves.

Observe that these conclusions may only prove useful for systems where dispersion is fully compensated at the end of each span. The absence of dispersion in the high power regions of the SSMF results in maximized iter-channel nonlinearities. In the praxis, however, dispersion is used to minimize the FWM efficiency and to increase the walk-off between WDM channels so that an averaging of the XPM occurs.

4.3 Optimum nonlinear transmission and dispersion map robustness

In this section, the optimum transmission of 55.5 Gb/s in 1040 km of SSMF is investigated. All transmission formats use the optimum bandwidths obtained in the previous sections and shown in Tables 4.4, 4.5 and 4.6. For both, non-dispersion-managed (NDM) and dispersion managed (DM) links the optimum transmission parameters are identified and the robustness of the optimum is analyzed. Using the NLPS criterion discussed in chapter 3.2.4, the maximum transmission reach of each modulation format is estimated.

4.3.1 Transmission in non-dispersion-managed links

In NDM links dispersion accumulates along propagation and is compensated either at the transmitter, receiver or a combination of both. Due to their high attenuation and nonlinearity, DCFs are not used in this type of links and normally, dispersion compensation is performed in the electrical domain. In the transmitter, this is usually done using electronic pre-distortion [KWM+05] where the inverse transfer function of the fiber is multiplied with the signal in the frequency domain, followed by a Fourier transform, in order to obtain a time-representation of the signal to be transmitted. At the receiver side, full optical field reconstruction [ME05] or coherent detection [vdBDF+07] can be used to enable electronic dispersion compensation. As previously mentioned, in this thesis the pre- and post- compensation of dispersion are performed in the optical domain using ideal DCFs, i.e., linear and non-attenuating fibers, so that the results of the analysis are independent of the method used for the compensation of dispersion.
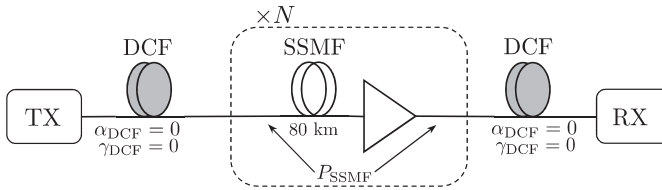
Figure 4.19: Block diagram of a non-dispersion-managed link.

The signals are sent through the link shown in Fig. 4.19 and the launch power and amount of pre-compensation are varied in order to find the maximum OSNR margin (ΔOSNR), defined as the difference between the accumulated OSNR (3.21) and the required OSNR for a target BER of 10^{-4}. In order to simplify the analysis, it is assumed that optimum transmission occurs when the residual dispersion at the end of the link is zero. The results are shown in the contour plots of Fig. 4.20 and the optimum points are listed in Table 4.9. The contour lines are in steps of 0.25 dB and express the penalty referred to the highest ΔOSNR for each format. Penalties of more than 3 dB are shown in black. Notice that the plots of stereo signals are centered differently than the plots of single and dual carrier signals.

The lack of in-line compensation results in highly dispersed optical waveforms propagating along the link. A high number of pulses within the signal overlap causing high power peaks and therefore, strong signal degradation through SPM. Previous studies [Sav06] have shown that for intensity modulated OOK systems the optimum strategy is to divide the compensation of dispersion equally between transmitter and receiver. We obtain the same conclusion in single-carrier DQSK systems. Observe that this is also in agreement with the straight-line rule (SLR), previously discussed in chapter 3.2.3. The SLR tends to make the dispersion map symmetrical around the middle which, for non-dispersion-managed links, results in an optimum pre-compensation of 50% of the total accumulated dispersion. This result comes from substituting $\mathcal{D}_{\text{res}} = D_{\text{SSMF}} L_{\text{SSMF}}$ into equation (3.33) and noticing that the last term of the right side dominates thus, $\mathcal{D}_{\text{pre}} \approx -N D_{\text{SSMF}} L_{\text{SSMF}}/2$.

On the other hand, for dual-carrier the optimum lies closer to a pre-compensation of 80%. The difference can be justified by noticing that, additionally to SPM, XPM between sub-carriers further degrades the signal. Additional dispersion is required in order to further decorrelate the sub-carriers so that the nonlinear chirp caused by XPM is averaged out throughout the link. The opposite occurs for stereo signals. It seems that excessive decorrelation causes nonlinearities to affect the pre-coding condition more than the degradation to the sub-carriers due to SPM and XPM itself. As a result the optimum pre-compensation lies around 35%.

For the WDM scenario we notice that optimum pre-compensation lies close to the 60% in all cases. As in the dual-carrier case, the extra decorrelation seems to be beneficial in order to minimize the effect of inter-channel XPM. For the WDM case, in general,

Single-carrier.

Dual-carrier.

Stereo.
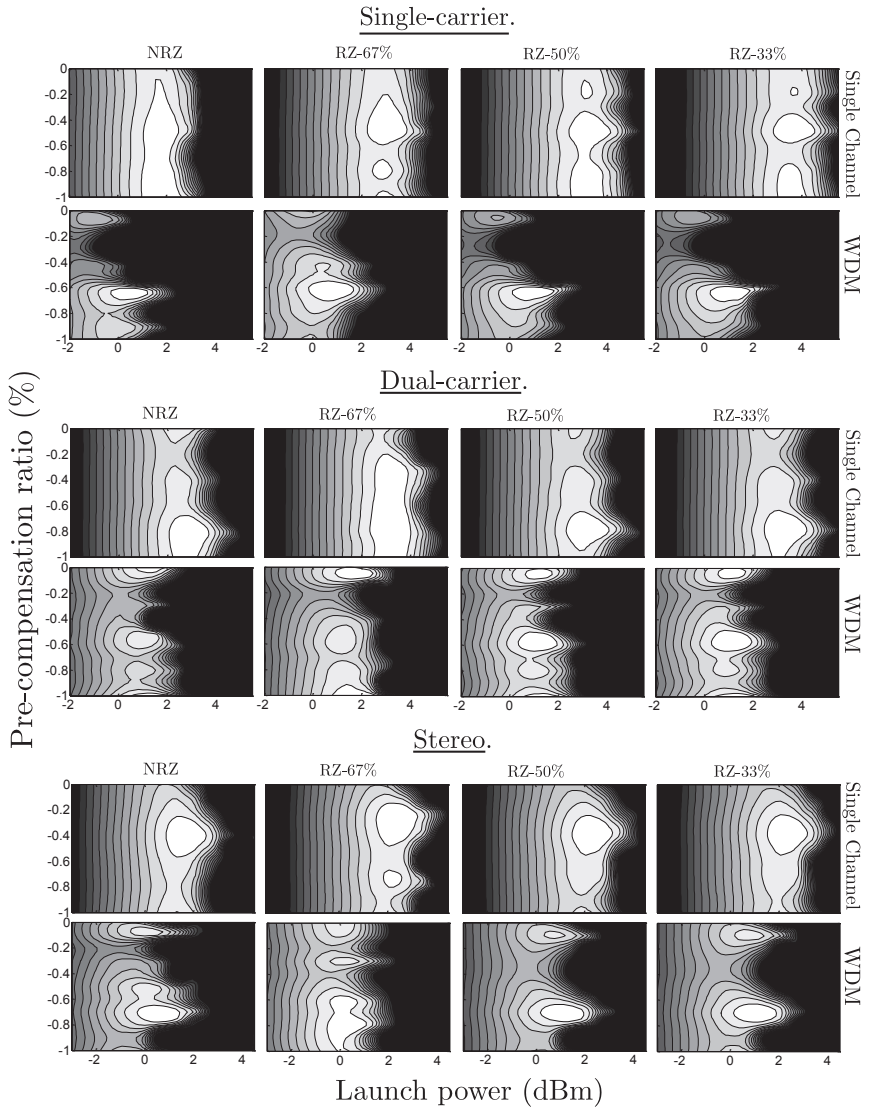
Figure 4.20: Performance of DQPSK in a non-dispersion-managed link.

Table 4.9: Optimum transmission parameters in non-dispersion-managed links. PR* represents the optimum pre-compensation ratio (%) and P^*_{SSMF} is the optimum power launched into the SSMF.

Single-carrier	Single-channel				WDM			
	PR*	P^*_{SSMF} (dBm)	OSNR_{req}* (dB)	ΔOSNR* (dB)	PR*	P^*_{SSMF} (dBm)	OSNR_{req}* (dB)	ΔOSNR* (dB)
NRZ	-0.5	1.9	16.29	8.06	-0.7	0.6	16.52	6.53
RZ-67%	-0.5	3.1	16.25	9.23	-0.6	0.8	16.33	6.90
RZ-50%	-0.5	3.4	16.27	9.59	-0.6	1.4	16.67	7.12
RZ-33%	-0.5	3.8	16.19	10.0	-0.6	1.4	16.57	7.22

Dual-carrier	Single-channel				WDM			
	PR*	P^*_{SSMF} (dBm)	OSNR_{req}* (dB)	ΔOSNR* (dB)	PR*	P^*_{SSMF} (dBm)	OSNR_{req}* (dB)	ΔOSNR* (dB)
NRZ	-0.8	3.1	16.36	9.12	-1.0	1.6	16.68	7.30
RZ-67%	-0.8	3.3	15.99	9.68	-1.0	1.8	16.33	7.83
RZ-50%	-0.8	3.3	16.12	9.54	-0.6	1.4	16.34	7.45
RZ-33%	-0.8	3.4	16.21	9.65	-0.6	1.4	16.41	7.38

Stereo	Single-channel				WDM			
	PR*	P^*_{SSMF} (dBm)	OSNR_{req}* (dB)	ΔOSNR* (dB)	PR*	P^*_{SSMF} (dBm)	OSNR_{req}* (dB)	ΔOSNR* (dB)
NRZ	-0.4	1.9	17.22	7.07	-0.7	0.5	17.86	5.12
RZ-67%	-0.3	2.4	16.65	8.20	-0.8	0.3	17.20	5.59
RZ-50%	-0.4	2.4	16.75	8.10	-0.7	1.1	17.39	6.15
RZ-33%	-0.4	2.4	16.80	8.05	-0.7	1.1	17.43	6.11

the contour of the black region seems to vary rather rapidly with the amount of pre-compensation. There is even a relatively high penalty when pre-compensating at $\sim 20\%$. It seems that for the particular sequences used for the simulations and for some values of dispersion, high power peaks form at some point in the propagation, inducing strong nonlinear chirp and a consequent decrease in performance.

In terms of the relative performances between all investigated formats, one observes that single- and dual-carrier perform very similar, whereas stereo is the least tolerant format against nonlinearities. In all cases NRZ is the pulse most affected by nonlinearities. The pulses that perform the best for each format are depicted in Fig. 4.21. Although single-carrier performs slightly better than dual-carrier in single-channel transmission, the opposite occurs in the WDM scenario. Stereo is only ~ 1 dB worse than single-carrier and ~ 2 dB worse than dual carrier in the WDM case.

The equivalent of the NLPS criterion in non-dispersion-compensated links is the P_{max} rule [FSE+99]. It states that the nonlinear signal distortion *only* depends on the total amount of nonlinear phase-shift $\phi^{\text{total}}_{\text{NL}} = N\gamma_{\text{SSMF}}L^{\text{SSMF}}_{\text{eff}}P_{\text{SSMF}}$. Unlike in dispersion-
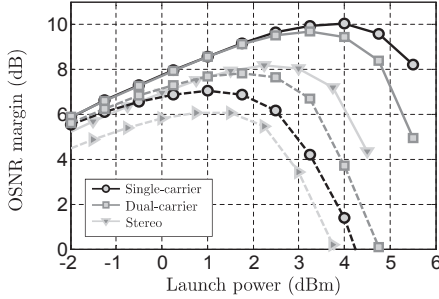
Figure 4.21: Nonlinear tolerance in non-dispersion-managed links with optimum pulse shapes. Solid line: single-channel (single-carrier: RZ-33%, dual-carrier: RZ-67%, stereo: RZ-67%), dashed-line: WDM (single-carrier: RZ-33%, dual-carrier: RZ-67%, stereo: RZ-50%).

managed links, $\phi_{\text{NL}}^{\text{total}}$ does not depend on the amount of pre-compensation. Thus, if the rule holds, it is possible to estimate the maximum transmission distance by finding the number of concatenated spans at which ΔOSNR equals zero. In calculating the accumulated OSNR for ΔN subsequent spans, the launch power P_{SSMF} is lowered such that $\phi_{\text{NL}}^{\text{total}}$ remains constant. If P_{SSMF}^* is the optimum power for $N = 13$, the optimum power for $N + \Delta N$ spans is given by

$$P_{\text{SSMF}}' = \frac{N}{N + \Delta N} P_{\text{SSMF}}^* \tag{4.57}$$

and from (3.38), the accumulated OSNR is calculated as

$$\text{OSNR}_{\text{acc}} = \frac{P_{\text{SSMF}}}{2\Phi_{\text{ASE}}^{\text{total}} B_{o,\text{ref}}} = \frac{P_{\text{SSMF}}'}{h f_c F_n (N + \Delta N) e^{\alpha_{\text{SSMF}} L_{\text{SSMF}}} B_{o,\text{ref}}}. \tag{4.58}$$

Using the above equations the maximum number of spans for each modulation format and pulse shape is calculated and listed in Table 4.10. All the obtained values were subsequently confirmed by simulating the maximum number of sections N_{max} with the same optimum pre-compensation and verifying that ΔOSNR > 0. In some cases we observed even a still positive OSNR margin of up to 0.8 dB. The values shown in Table 4.10 only represent an estimation of the maximum transmission distance since pre-compensation was not re-optimized for N_{max} and thus, still some performance improvement may exist.

4.3.2   Transmission in dispersion-managed links

The behavior of the investigated modulation formats in dispersion-managed links is more difficult to analyze due to the high number of parameters that influence the nonlinear propagation of the signals. The model of the link is shown in Fig. 4.22. The signals are first pre-compensated with a fraction (PR) of the accumulated dispersion per span, which in this case amounts to $L_{\text{SSMF}} D_{\text{SSMF}} = 1360$ ps/nm. Subsequently, transmission takes place in 13 spans (1040 km) composed of SSMF and DCF with dual-stage EDFAs. The

Table 4.10: Maximum number of cascaded spans in non-dispersion-managed links

| | Single-channel | | | | WDM | | | |
	NRZ	RZ-67%	RZ-50%	RZ-33%	NRZ	RZ-67%	RZ-50%	RZ-33%
Single-carrier	32	37	39	41	27	28	29	29
Dual-carrier	37	39	39	39	30	32	30	30
Stereo	29	33	32	32	23	24	26	26

length of the DCFs is set to compensate only a fraction (CR) of the accumulated dispersion per span. At the end of the link, any residual dispersion is brought back to zero with the post-compensating fiber. The pre-and post- compensating fibers are assumed linear and non-attenuating. Performance is measured in terms of the maximum OSNR margin ΔOSNR and is dependent on the set of parameters $\mathcal{S}_{DM} = \{P_{SSMF}, P_{DCF}, \mathcal{D}_{pre}, \mathcal{D}_{res}\}$. For convenience, the results are expressed in terms of $\mathcal{S}_{DM} = \{P_{SSMF}, P_{DCF}, PR, CR\}$ where PR and CR relate to the amount of pre-compensated dispersion $\mathcal{D}_{pre}$ and the residual dispersion per span $\mathcal{D}_{res}$ by $PR = \mathcal{D}_{pre}/(L_{SSMF}D_{SSMF})$ and $CR = (1-\mathcal{D}_{res}/(L_{SSMF}D_{SSMF}))$, respectively.

For a fair comparison between the investigated modulation formats, the optimum performance of the system is obtained with the global optimization algorithm (GOA) previously introduced in chapter 3.3.3. The boundaries of the search space are given by $P_{SSMF} = [-3, 7]$, $P_{DCF} = [-8, 3]$, $PR = [-1, 0]$ and $CR = [0.7, 1.1]$. The algorithm is set to find the maximum OSNR margin ΔOSNR* and the optimum set of parameters $\mathcal{S}_{DM}^* = \{P_{SSMF}^*, P_{DCF}^*, PR^*, CR^*\}$ in 200 iterations, which correspond to only 2% simulations of an equivalent grid search (assuming a "rough" grid of 10 points per parameter). For convenience, granularities of 0.1 dBm for the input powers, 0.05 for PR and 0.01 for CR were set.

The results of the GOA are shown in Table 4.11. The optimum power differences (ΔP^*) between SSMF and DCF are very close to the previously estimated optimum of 6.5 dB (see ch. 3.2.2). The power difference is higher for single-carrier $(\overline{\Delta P}^* = 7.2$ dB) than for dual-carrier and stereo $(\overline{\Delta P}^* = 6.2$ dB and $\overline{\Delta P}^* = 6.8$ dB, respectively). The average optimum power difference is 0.4–0.9 dB lower for WDM transmission than for the single-channel case. Observe that for all formats, NRZ always perform the worst.

In order to further understand the behavior of the investigated formats a qualitative robustness analysis is performed by exploring the regions around the optimum parameters. For visualization purposes we take two 2-dimensional slices out of the 4-dimensional region around the optimum. This is done by fixing the pair (PR^*, CR^*) and varying the input powers (P_{SSMF}, P_{DCF}) in order to obtain a *power plot*; or fixing (P_{SSMF}^*, P_{DCF}^*) and vary the pre-compensation and span compensation ratios (PR, CR), in which case we obtain a *dispersion plot*.

Figures 4.23 and 4.24 show the power plots for each modulation format and pulse shape, for the single-channel and WDM cases. The contour levels show penalties referred to the
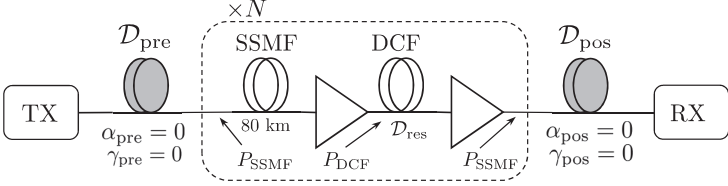
Figure 4.22: Block diagram of a dispersion-managed link.

Table 4.11: Optimum transmission parameters in dispersion-managed links

Single-Carrier	Single-channel					WDM				
	P^*_{SSMF} (dBm)	P^*_{DCF} (dBm)	PR*	CR*	ΔOSNR* (dB)	P^*_{SSMF} (dBm)	P^*_{DCF} (dBm)	PR*	CR*	ΔOSNR* (dB)
NRZ	3.2	-4.2	-0.45	0.94	8.32	2.7	-5.4	-0.45	0.94	7.75
RZ-67%	4.7	-3.9	-0.05	1.02	9.78	2.9	-3.6	-0.55	0.93	8.48
RZ-50%	5.1	-2.7	-0.45	0.94	10.32	2.5	-3.3	-0.75	0.91	8.43
RZ-33%	4.8	-0.4	-0.80	0.90	10.68	2.4	-2.7	-0.75	0.91	8.38

Dual Carrier	Single-channel					WDM				
	P^*_{SSMF} (dBm)	P^*_{DCF} (dBm)	PR*	CR*	ΔOSNR* (dB)	P^*_{SSMF} (dBm)	P^*_{DCF} (dBm)	PR*	CR*	ΔOSNR* (dB)
NRZ	6.2	-0.1	-0.45	0.94	11.39	3.8	-1.8	-0.85	0.86	9.23
RZ-67%	6.6	0.7	-0.60	0.92	12.20	3.8	-2.0	-0.90	0.86	9.51
RZ-50%	6.6	-0.1	-0.65	0.91	12.08	4.0	-2.0	-1.00	0.85	9.56
RZ-33%	6.2	0.2	-0.65	0.91	11.88	3.9	-0.8	-0.85	0.86	9.57

Stereo	Single-channel					WDM				
	P^*_{SSMF} (dBm)	P^*_{DCF} (dBm)	PR*	CR*	ΔOSNR* (dB)	P^*_{SSMF} (dBm)	P^*_{DCF} (dBm)	PR*	CR*	ΔOSNR* (dB)
NRZ	0.7	-6.3	-0.80	0.75	5.09	-0.2	-6.2	-0.95	0.79	3.95
RZ-67%	1.5	-5.3	-0.75	0.75	6.51	0.3	-6.3	-1.00	0.77	4.76
RZ-50%	1.3	-5.4	-0.75	0.75	6.20	0.4	-6.2	-0.75	0.75	4.86
RZ-33%	1.3	-5.7	-0.60	0.75	6.16	0.4	-5.8	-0.95	0.75	4.88
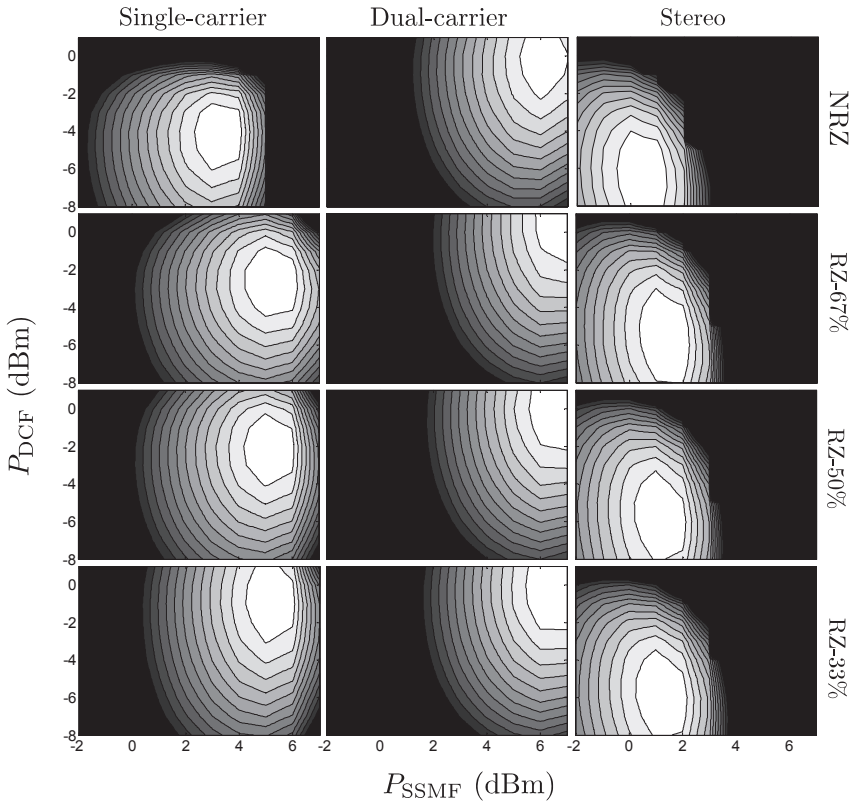
Figure 4.23: Robustness against variations in input powers, for optimum PR and CR, in single-channel transmission.

maximum ΔOSNR of each case. Lines are in steps of 0.25 dB and penalties of more than 3 dB are depicted black. The plots can be qualitatively described in the following way: formats with a good performance show a "hill" closer to the upper right corner of the frame. The horizontal and vertical widths of the hill indicates robustness to variations in the optimum SSMF and DCF input powers, respectively.

From Fig. 4.23 it is clear that dual-carrier perform the best and is the most tolerant[9]

---

[9]Observe that "tolerance" is referred to the position of the hills, i.e., it reflects the amount of detrimental effects that the signals are able to withstand, whereas "robustness" refers to the size of the hills, i.e., it reflects how much deviation in the optimum parameters of the link the transmission format is able to withstand. "Performance" is directly related to ΔOSNR.
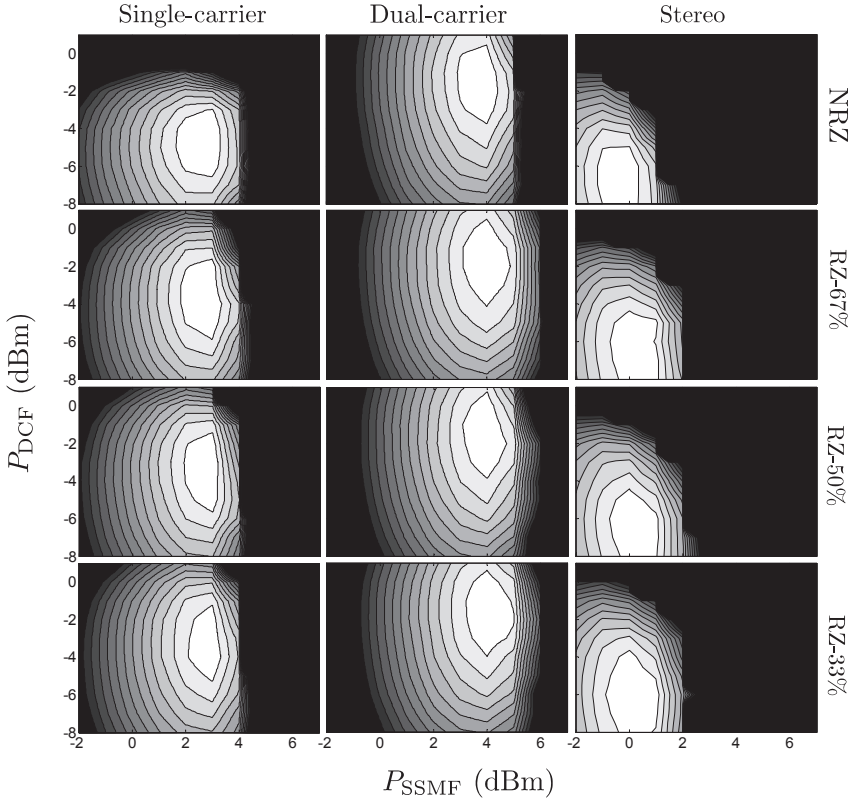
Figure 4.24: Robustness against variations in input powers, for optimum PR and CR, in WDM transmission.

format against nonlinear effects, followed by single-carrier and stereo. All formats are slightly more robust against variations in DCF input power than in SSMF input power. And once again, NRZ seems to be the poorest format in terms of performance and robustness, specially in single-carrier signals.

Notice that, in spite of being in the pseudo-linear regime of propagation, where intrachannel effects are the limiting effects on the performance of the systems, the reduction in size of the hills indicate a loss in robustness due to the inter-channel nonlinearities. Dual-carrier is specially affected by inter-channel nonlinear effects, as it is possible to observe by comparing Fig. 4.23 with Fig. 4.24. The hills locate at ~ 2.5 dB lower SSMF power than the single-channel case. The difference is ~ 2 dB and ~ 1 dB for single-carrier and stereo,
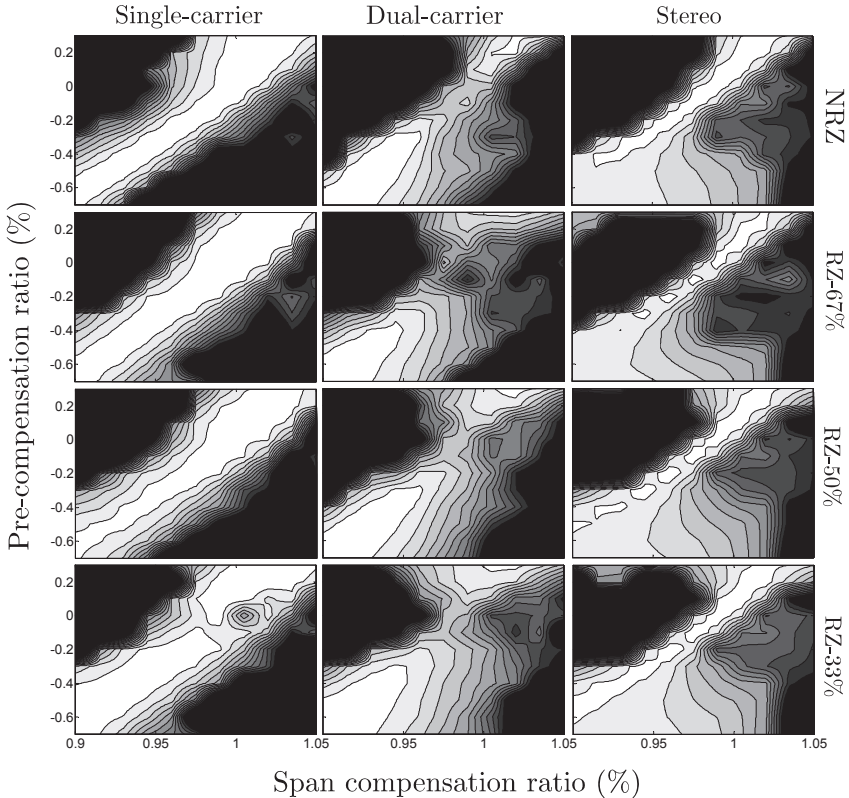
Figure 4.25: Robustness against variations in pre-compensation and span residual dispersion, for optimum P_{SSMF} and P_{DCF}, in single-channel transmission.

respectively. Single-carrier NRZ signals, although having the poorest performance seems to be less affected, in terms of robustness of the input powers, by WDM transmission than the rest.

Figures 4.25 and 4.26 show the dispersion plots for each modulation format and pulse shape, for the single-channel and WDM cases. The contour levels show penalties referred to the maximum ΔOSNR of each case. For visualization purposes, this time the contour lines are in steps of 1 dB and penalties of more than 10 dB are depicted black.

Although the input powers set the ultimate limit in performance, they must be set under careful consideration of the dispersion map. The plots depict clearly an optimum region in
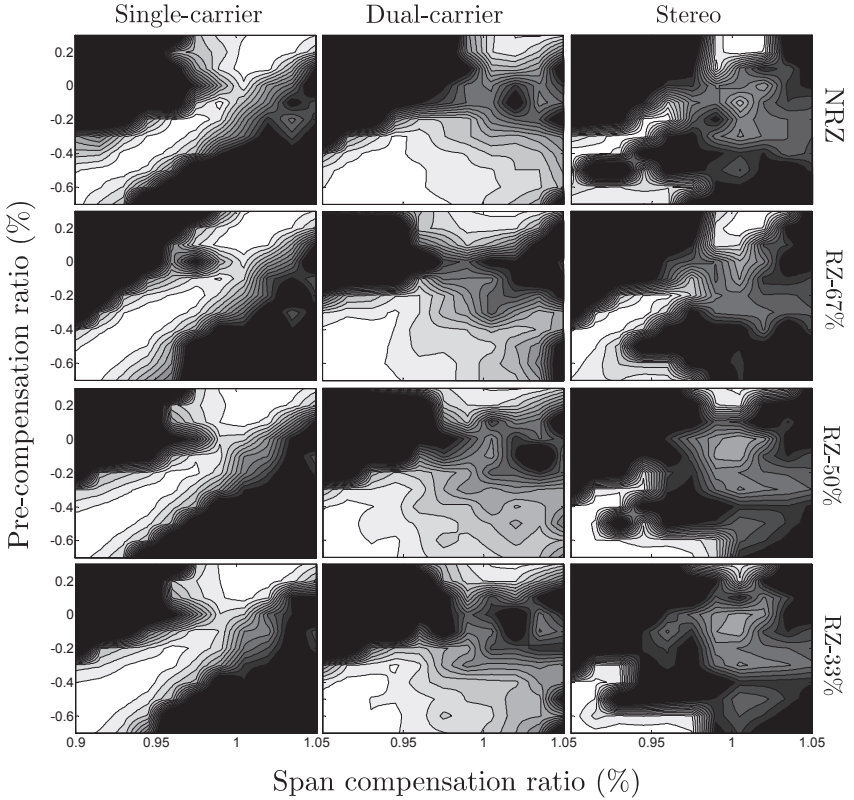
Figure 4.26: Robustness against variations in pre-compensation and span residual dispersion, for optimum P_{SSMF} and P_{DCF}, in WDM transmission.

diagonal form in shape of a "bridge" between the left lower corner and right upper corner of the plots, just as predicted by the straight-line rule. In general the optimum regions found by the GOA lie in the lower left corner of the plots, on the diagonal where pre-compensation is negative and spans are slightly under-compensated just for the dispersion map to be symmetrical with respect to the center point. Further to the lower left corner of the plots the bridge starts to widen but at some point they begin to decrease in "height". Robustness is given by how broad the bridges are, specially close to the lower left corner.

From Fig. 4.25 one can observe that NRZ single-carrier signals are less robust to variations in the dispersion map than RZ signals. Although not particularly noticeable in the plot, the optimum region starts widening more rapidly for RZ than for NRZ pulses. Dual-
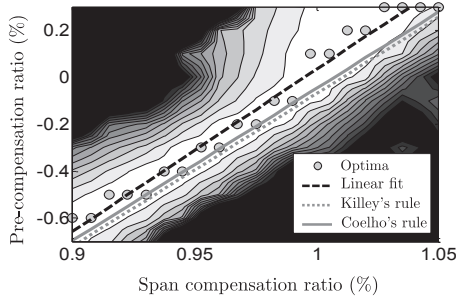
Figure 4.27: The straight-line rule.

carrier signals show a noticeable loss in performance of 3 to 5 dB close to (PR,CR)=(0,1). This is where the average accumulated dispersion along the link is minimum and thus, nonlinearities affect the signals the most. At this point the nonlinear interaction between sub-carriers is maximized and a subsequent penalty appears. It is remarkable that moving away from this point towards the left corner of the plots (i.e., increasing dispersion) immediately minimizes the penalty due to the nonlinear crosstalk between sub-carriers. Furthermore, the optimum region stars widening at a higher rate than in the case of single-carrier signals providing higher tolerance to variations in the optimum dispersion map parameters and better nonlinear tolerance and system performance altogether. The wide regions also appear in stereo signals but, interestingly, the detrimental effect due to inter-carrier nonlinear crosstalk is not present. It seems as if the nonlinear chirp induced by the sub-carriers in each other is effectively canceled in the demodulation process.

A similar behavior can be observed in the WDM case (Fig. 4.26). Close to the center of the plots the nonlinear crosstalk between WDM channels is maximized and a *strong* penalty occurs. In general, we notice that systems using two sub-carriers are more robust to variations in the dispersion maps provided that they operate far from the (PR,CR)=(0,1) point.

As previously mentioned, the straight-line rule (SLR) is successful in predicting the diagonal shape of the optimum regions. Although it was developed with only the intra-channel effects in mind, we observe from Figs 4.25 and 4.26, that it fits also the multi-carrier signals and the WDM scenario. Notice the at least the slope of the straight-line fits almost perfectly with all the investigated systems indicating that symmetric dispersion maps are optimum.

Figure 4.27 shows the dispersion plot of NRZ single-carrier single-channel with the minimum points for each CR and its linear fit. Observe that Killey's rule, written in equation (3.33), and the further refinement of the SLR in equation (3.34), hereafter referred to as Coelho's rule after [Coe10], are very close to the linear fit. Therefore, we attempt to estimate the maximum transmission distance using the SLR in conjunction with the NLPS criterion previously described in chapter 3.2.4.

Table 4.12: Maximum number of cascaded spans and $OSNR^*_{req}$ (dB) in dispersion-managed links

$OSNR^*_{req}$	Single-channel				WDM			
	NRZ	RZ-67%	RZ-50%	RZ-33%	NRZ	RZ-67%	RZ-50%	RZ-33%
Single-carrier	16.08	15.64	15.97	15.79	15.97	15.83	15.63	15.69
Dual-carrier	16.24	15.94	15.91	15.84	16.21	15.91	16.03	16.10
Stereo	17.14	16.55	16.68	16.65	18.20	17.07	17.16	17.17

N_{max}	Single-channel				WDM			
	NRZ	RZ-67%	RZ-50%	RZ-33%	NRZ	RZ-67%	RZ-50%	RZ-33%
Single-carrier	33	39	41	42	31	34	34	33
Dual-carrier	47	52	51	50	37	38	38	38
Stereo	22	26	27	25	20	21	21	22

The estimations were subsequently simulated in order to confirm them. In just a few cases we noticed that the estimations and consequent system configurations given by the NLPS criterion where not accurate. They occurred when the optimum points found by the GOA did not lie close enough to the line predicted by the SLR. However, by applying the GOA to those systems with the purpose to maximize the number of spans it can concatenate, we could confirm that the estimations given by the NLPS criterion where accurate (±1 span) and only the systems configurations where different. This indicates that the premise of the NLPS criterion holds and that, independently of the number of sections, a system is limited by the maximum nonlinear phase shift it can tolerate. This is also valid for multi-carrier and WDM systems.

The maximum number of spans obtained for each format are shown in Table 4.12. The results confirm that dual-carrier perform the best among all investigated systems with a maximum transmission distance of 52 spans (4160 km) for single-channel transmission and 38 spans (3040 km) for the WDM case.

By comparing Tables 4.12 and 4.10 it is possible to observe that careful control of the nonlinearities via in-line dispersion compensation increases the maximum transmission distance in dual-carrier systems up to 33% and 26% in the single-channel and WDM cases, respectively. For single-carrier signals the increase is small (up to 5%) for single-channel, whereas for WDM transmission in-line compensation can improve the reach of the system up to 21%. On the other hand, stereo signals perform worse in DM links, with degradation in the maximum reach of up to 20%.

Finally, the total residual dispersion after 1040 km is varied in order to find its optimum value and tolerance. Figure 4.28 depicts the resulting curves showing the required OSNR versus total residual dispersion. The system configurations are determined by the optimum set of parameters found with the GOA shown in Table 4.11. Table 4.13 lists the optimum points and 2 dB tolerances.
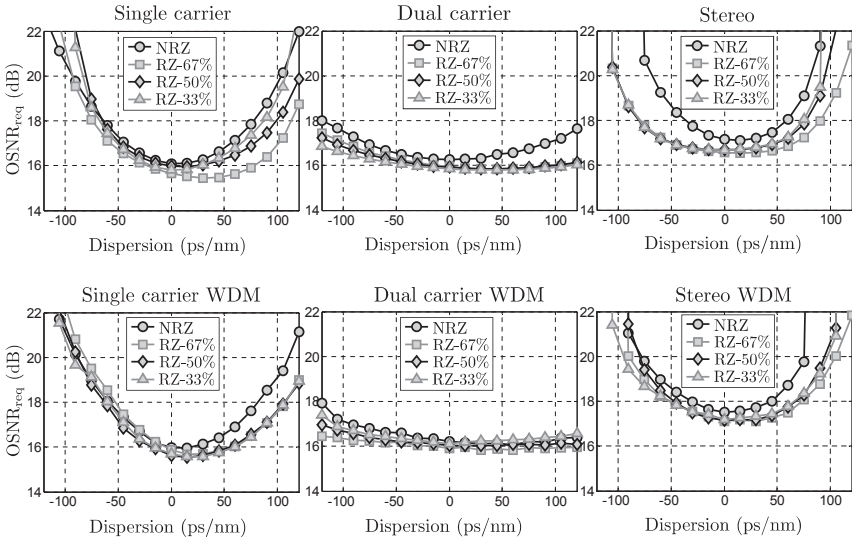
Figure 4.28: Tolerance to residual dispersion of DQPSK at 55 Gb/s.

Observe that, unlike the linear case, the tolerance curves are not symmetrical around zero. Some positive residual dispersion seems to be beneficial to combat the nonlinear chirp that the signal acquires while propagating. Notice that, in general, signals are more tolerant to positive than negative residual dispersion.

As expected for signals propagating in the pseudo-linear regime, the optimum residual dispersion is very close to zero. It is possible to observe that for dual-carrier signals the optimum residual dispersion is slightly higher than that of single-carrier signals. On the other hand, stereo signals require very little residual dispersion, just enough to cancel some nonlinear residual chirp, but not too much so that the pre-coding condition is affected. Similar to the linear case, dual-carrier systems are far more robust than single-carrier signals to uncompensated dispersion. Stereo on the other hand remains as tolerant as single-carrier. WDM transmission does not seem to greatly impact the tolerance of the signals to residual dispersion.

4.4   Summary

DQPSK modulation is a very attractive transmission format mainly due to its high spectral efficiency and consequent robustness against narrow-band filtering, high tolerance to nonlinearities and relative simple transceiver design. One alternative to implement 111 Gb/s per WDM channel is to use two polarization-multiplexed DQPSK tributaries at 55.5 Gb/s and thus, a thorough analysis of the performance of this modulation format

Table 4.13: Tolerance to residual dispersion (ps/nm) of DQPSK at 55.5 Gb/s – 2 dB penalties

Single-channel	Single-carrier			Dual-carrier			Stereo		
	$\mathcal{D}_{\mathrm{acc}}^-$	$\mathcal{D}_{\mathrm{acc}}^*$	$\mathcal{D}_{\mathrm{acc}}^+$	$\mathcal{D}_{\mathrm{acc}}^-$	$\mathcal{D}_{\mathrm{acc}}^*$	$\mathcal{D}_{\mathrm{acc}}^+$	$\mathcal{D}_{\mathrm{acc}}^-$	$\mathcal{D}_{\mathrm{acc}}^*$	$\mathcal{D}_{\mathrm{acc}}^+$
NRZ	72	7	72	129	0	145	72	15	60
RZ-67%	95	30	77	175	45	180	103	15	81
RZ-50%	78	15	83	191	45	176	95	15	70
RZ-33%	65	0	83	212	45	186	89	0	81

WDM	Single-carrier			Dual-carrier			Stereo		
	$\mathcal{D}_{\mathrm{acc}}^-$	$\mathcal{D}_{\mathrm{acc}}^*$	$\mathcal{D}_{\mathrm{acc}}^+$	$\mathcal{D}_{\mathrm{acc}}^-$	$\mathcal{D}_{\mathrm{acc}}^*$	$\mathcal{D}_{\mathrm{acc}}^+$	$\mathcal{D}_{\mathrm{acc}}^-$	$\mathcal{D}_{\mathrm{acc}}^*$	$\mathcal{D}_{\mathrm{acc}}^+$
NRZ	64	7	73	192	60	153	70	0	70
RZ-67%	69	22	80	239	45	175	77	0	94
RZ-50%	68	15	83	198	30	193	70	0	85
RZ-33%	74	22	77	150	0	192	85	0	89

at such data-rate has been investigated. The contribution of this chapter can be resumed in the following main points:

▷ In DQPSK modulation, the information is conveyed by the phase difference of successive symbols. Two bits per symbol are simultaneously transmitted in four phase states of the optical signal. The most common transmitter implementation uses a differential encoder for the quaternary data that modulates the in-phase and quadrature components of the optical signal in a parallel manner. At the receiver side, phase-to-intensity conversion is carried out with two delay interferometers with balanced photodiodes. The mathematical equations that describe the whole transmission system were derived, including the Hermitian kernels used for the BER estimation.

▷ By using an extra MZM at the transmitter side, it is possible to modify the shape of the pulses that convey the phase information. Six pulses are investigated in this chapter: NRZ and RZ with duty cycles of 67%, 50% and 33%. NRZ signals have the narrowest spectrum of all. For RZ signals, the lower the duty cycle, the broader is the spectrum.

▷ The best performance of a system is achieved by using a matched optical filter at the receiver and no post-detection electrical filter. In this case, DQPSK ideally requires 14.35 dB OSNR in order to achieve a BER of 10^{-4}. This is equivalent to a receiver sensitivity of -40.6 dBm or a quantum limit of 25 photons per symbol.

▷ The optimum filter bandwidths and receiver performances have been obtained for each pulse format. The optimum receiver performance relies on a balance between noise and inter-symbol interference for NRZ transmission, whereas for RZ signals

detection noise has to be traded against filter-induced signal energy rejection. In WDM systems, a transmitter filter is used to minimize cross-talk between neighboring channels.

▷ NRZ signals require the narrowest filter bandwidth to achieve optimum sensitivity, but have the worst robustness against deviations of the optimum bandwidth. The optimum receiver filter bandwidth of RZ signals gets wider and the required OSNR gets lower as the duty cycle of the signals reduces.

▷ DQPSK transmission using two optical carriers at half the symbol rate has been investigated as well. By using dual-carrier DQPSK, it is assumed that not only the bandwidth requirements of the transceivers is relaxed but also that the robustness against some detrimental effects that depend on the symbol rate would be improved. The performance of dual-carrier transmission is theoretically equal to single-carrier transmission provided that the cross-talk between sub-carriers is minimized. The optimum filter bandwidths and performances for different pulse shapes and sub-carrier separations have been obtained.

▷ Stereo multiplexing has been proposed as a way of detecting two carriers simultaneously using only one DQPSK modulator. Demultiplexing of the sub-carriers is subsequently carried out electronically. The transmitter and receiver design has been described in detail and the optimum filter bandwidths and performances for different pulse shapes have been obtained. The gain of stereo multiplexing, in terms of reduction of the number components at the receiver side, comes at an expense in receiver sensitivity of about ∼0.5–1 dB.

▷ A novel mathematical framework has been proposed and used to model the effect of square-law detection in linearly pre-coded FDM signals. It is shown that the Stereo multiplexing can be extended up to five sub-carriers only if complex pre-coding is used. An explicit example using 3 sub-carriers is given. The framework is also useful in analyzing other direct-detected multi-carrier modulation formats, e.g., OFDM.

▷ The dispersion tolerance of the different pulse and transmission formats has been investigated. Dispersion tolerance is higher for signals with narrower bandwidths. The narrow-band filtering used in WDM systems to minimize cross-talk has the side effect of increasing dispersion tolerance. As expected, dual-carrier DQPSK provides approximately a 2.5-fold increase in tolerance to dispersion. On the other hand, since dispersion alters the pre-coding condition of stereo signals, only a slight increase in dispersion tolerance was observed for RZ pulses (∼ 20%).

▷ The nonlinear tolerance of the different pulses and transmission formats was investigated as well. For this purpose, propagation in a single-span link was analyzed. We observed that RZ carving is effective in reducing intra-channel nonlinear effects. The lower the duty cycle, the better is the tolerance. On the other hand, no difference between the pulses was observed regarding tolerance to inter-channel effects. Dual carrier and stereo perform worse than single-carrier.

▷ Propagation in non-dispersion-managed links was investigated. The optimum pre-compensation ratios and launch powers were obtained for each format. The maximum number of cascaded spans was calculated using the P_{max} rule. The longest reach was achieved in the single-channel case by single-carrier RZ-33% signals with 41 spans. In the WDM case, dual-carrier RZ-67% achieved the maximum of 32 spans. Stereo reached 6 spans fewer than the best formats in both single-carrier and WDM transmission.

▷ Propagation in dispersion-managed links was investigated as well. The optimum transmission parameters and performances were obtained using the global optimization algorithm. Afterwards, a thorough analysis of the robustness of the investigated formats to deviations of the optimum parameters was carried out. It was shown that the straight-line rule is valid also for multi-carrier and WDM transmission. Using the NLPS criterion and the straight-line rule, the maximum reach of each format was estimated. In single-channel as in WDM dual-carrier RZ-67% achieved the maximum number of cascaded spans, which equals 52 and 38, respectively. This is $\sim 20\%$ and $\sim 10\%$ more than the best single-carrier pulse and almost 50% more than the best stereo signals for single-channel and WDM transmission, respectively. Subsequently, the tolerance to residual dispersion was investigated. The optimum residual dispersion is not far from zero ps/nm and only a very small performance improvement was observed.

5

DQPSK Transmission at 55.5 Gb/s Using Nyquist pulses

In this chapter, we consider reducing the bandwidth of the optical signals by encoding the transmitted symbols into spectrally efficient Nyquist pulses. The motivation to investigate such pulses was triggered by the answer to the following question: Is it possible to linearly pre-code orthogonal frequency division multiplexed (OFDM) signals so that they are compatible with direct detection? We consider OFDM signals because of their minimal spectral occupancy. Firstly, we show that the squaring operation of the photodiode at the receiver side generates intermodulation products between the sub-carriers that interfere with the signal of interest, unless the sub-carriers are linearly pre-coded with the discrete Fourier transform matrix. Subsequently, it is shown that this is equivalent to serial transmission of modulated symbols encoded in Nyquist pulses, specifically *sinc* pulses, generated in the frequency domain. By means of spectral shaping we attempt to increase the tolerance of the signals to transmission impairments. For this purpose, we introduce *raised cosine* and *Hamming pulses*. Finally we use the same propagation scenarios as in chapter 4 in order to assess the performance of Nyquist pulses and compare them to the more classic (non) return-to-zero pulses.

5.1 Direct detection of OFDM signals

OFDM signals are attractive, among other reasons, because of their very low spectral occupancy. Such signals are composed of a sum of overlapping sub-carriers, each with a very narrow spectrum. Since the sub-carriers are orthogonal to each other, no interference is caused by the overlapping (see Fig. 5.1).
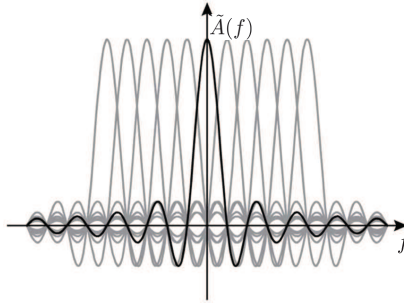
Figure 5.1: Overlapping orthogonal sub-carriers.

The time domain baseband representation of an OFDM signal composed of N_s sub-carriers can be written as[1]

$$A(t) = \sum_{m=-\infty}^{\infty} \sum_{n=-N_s/2}^{N_s/2-1} x_{mn} s_n(t - mT_s), \qquad (5.1)$$

where x_{mn} is the information symbol of the nth subcarrier s_n at the mth OFDM symbol of duration T_s. The sub-carriers are of the form

$$s_n(t) = e^{j2\pi f_n t}\Pi(t), \qquad (5.2)$$

where $f_n = n/T_s$. The rectangular window $\Pi(t)$ is inherent to transmitters that digitally process the information symbols in block form, i.e., that in each OFDM symbol take into account only a finite subset of information symbols from the whole information sequence. It is analytically defined as

$$\Pi(t) = \begin{cases} 1 & , \, 0 < t \leq T_s \\ 0 & , \, \text{else.} \end{cases} \qquad (5.3)$$

Observe that the rectangular window gives each subcarrier its $\text{sinc}\,(T_s f)$ shape in the frequency domain[2]. It follows directly from the orthogonality property between any two sub-carriers within an OFDM symbol, that the amplitude of the mth subcarrier is zero when $f = f_n, \forall n$ except when $n = m$ (as seen in Fig. 5.1). This can be mathematically expressed as

$$\frac{1}{T_s} \int_0^{T_s} s_n s_m^* = \delta_{nm}, \qquad (5.4)$$

---

[1]The amplitude normalization factor is absent for simplicity of notation. In general, the amplitude of the resultant digital signals must be properly normalized in order to match the dynamic range of the digital-to-analog converters.

[2]The normalized *sinus cardinalis* function is defined as $\text{sinc}\,(x) = \sin(\pi x)/(\pi x)$.

where $*$ denotes complex conjugation and δ_{nm} is the Kronecker delta function with $\delta_{nm} = 1$ when $n = m$ and $\delta_{nm} = 0$ otherwise.

The OFDM signal described in (5.1) has a compact spectrum with bandwidth $B \approx N_s/T_s$ when N_s is high, which makes it very attractive for systems where signals with low spectral occupancy are required. However, multi-carrier signals are inherently incompatible with direct-detection. This is because the squaring operation of the photodiodes causes intermodulation products between the sub-carriers to appear and interfere with the signal of interest. Some techniques have been proposed to overcome this problem but the trade off is either reduced spectral efficiency, by sending an optical carrier located far distant in spectrum from the signal [LDA06], or reduced sensitivity, because of the high power needed for the optical carrier [SSBP08]. In [GCS⁺10] it was shown that, by linearly pre-coding the sub-carriers with the DFT matrix, intermodulation products would be effectively suppressed at the sampling instant.

Assume that the information bits are encoded in the phase difference between the successive information symbols x_n and x_{n-1} and, for simplicity, consider only one OFDM symbol in (5.1). The information symbols in each OFDM symbol are linearly pre-coded with the square matrix $\mathbf{P}$ and $E(t) = A(t) \cdot e^{j\omega_c t}$ with

$$A(t) = \sum_{n=-N_s/2}^{N_s/2-1} \mathbf{p}_n \mathbf{x} e^{j2\pi f_n t} \tag{5.5}$$

is the input field to the DQPSK receiver shown in Fig. 4.4. In (5.5), $\mathbf{p}_n$ is the nth row of $\mathbf{P}$ and $\mathbf{x} = (x_{-N/2} \dots x_0 \dots x_{N/2-1})^{\text{T}}$. Using $\psi_I = \pi/4 - \omega_c T_0$, the output signal of the in-phase branch can be written according to (4.6) as

$$I_I(t) = \frac{1}{2} \Re \left\{ \sum_{n=-N_s/2}^{N_s/2-1} \mathbf{p}_n \mathbf{x} e^{j2\pi f_n t} \cdot \sum_{m=-N_s/2}^{N_s/2-1} (\mathbf{p}_m \mathbf{x})^* e^{-j2\pi f_m(t-T_0)} e^{j\frac{\pi}{4}} \right\}. \tag{5.6}$$

The delay of the interferometer is set to $T_0 = T_s/N_s$ and the electrical signal is sampled at a rate $t_k = kT_s/N_s$, with $-\frac{N_s}{2} \leq k \leq \frac{N_s}{2} - 1$. For mathematical convenience, the resulting decision variable can be expressed in matrix form as

$$I_I(t_k) = \frac{1}{2} \Re \left\{ \sum_{n=-N_s/2}^{N_s/2-1} \mathbf{p}_n \mathbf{x} e^{j2\pi \frac{nk}{N_s}} \cdot \sum_{m=-N_s/2}^{N_s/2-1} (\mathbf{p}_m \mathbf{x})^* e^{-j2\pi \frac{n(k-1)}{N_s}} e^{j\frac{\pi}{4}} \right\}$$

$$= \frac{1}{2} \Re \left\{ \left(\mathbf{r}_k \mathbf{\Omega}^{-1} \mathbf{P} \mathbf{x} \right) \left(\mathbf{r}_{k-1} \mathbf{\Omega}^{-1} \mathbf{P} \mathbf{x} \right)^{\text{T}} e^{j\frac{\pi}{4}} \right\}, \tag{5.7}$$

where $\mathbf{\Omega}$ corresponds to the $N_s \times N_s$ DFT matrix with elements $\omega_{mn} = e^{-j2\pi \frac{mn}{N_s}}$ and $\mathbf{r}_k$ is the kth row of the $N_s \times N_s$ identity matrix. Observe that in (5.7) the element containing the original transmitted data in the kth sampling instant is given by the product of the information symbols with subscripts $n = k$ and $m = k-1$. All other terms cause unwanted interference. However, if $\mathbf{P} = \mathbf{\Omega}$, intermodulation products are effectively suppressed at
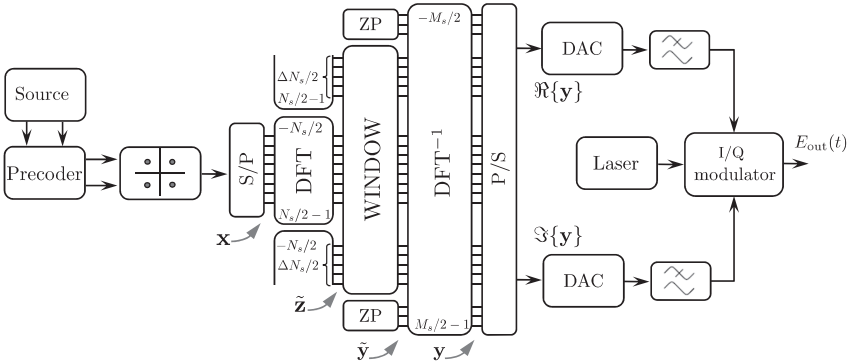
Figure 5.2: Block diagram of a transmitter for the generation of Nyquist pulses in the frequency domain.

the sampling instant and the in-phase and, analogously, the quadrature decision variables reduce to

$$I_I(t_k) = \tfrac{1}{2}\Re\{x_k x_{k-1}^* e^{j\frac{\pi}{4}}\},$$ (5.8)

$$I_Q(t_k) = \tfrac{1}{2}\Re\{x_k x_{k-1}^* e^{-j\frac{\pi}{4}}\}.$$ (5.9)

5.2   Generation of Nyquist pulses in the frequency domain

The DFT pre-coding operation described in the previous section is equivalent to performing digital signal processing over the information vector $\mathbf{x}$ in the frequency domain. The resulting signal in (5.5) is a particular member of a broader family of signals that convey the transmitted information symbols *serially* by means of spectrally efficient Nyquist pulses.

Consider the transmitter shown in Fig. 5.2. A stream of modulated information symbols is parallelized to form the vector $\mathbf{x}$ of N_s elements, which is then transformed to the frequency domain by means of the DFT of size N_s.

The output vector $\tilde{\mathbf{x}}$ with elements

$$\tilde{x}_k = \sum_{n=-N_s/2}^{N_s/2-1} x_n e^{-j2\pi\frac{nk}{N_s}},$$ (5.10)

where $-\frac{N_s}{2} \leq k \leq \frac{N_s}{2} - 1$, is cyclically extended to form the vector $\tilde{\mathbf{z}}$ of elements

$$\tilde{z}_k = \begin{cases} \tilde{x}_{k+N_s} & , & -\frac{N_s}{2} - \frac{\Delta N_s}{2} \leq k \leq -\frac{N_s}{2} - 1 \\ \tilde{x}_k & , & -\frac{N_s}{2} \leq k \leq \frac{N_s}{2} - 1 \\ \tilde{x}_{k-N_s} & , & \frac{N_s}{2} \leq k \leq \frac{N_s}{2} + \frac{\Delta N_s}{2} - 1. \end{cases}$$ (5.11)

where $-\frac{N_s}{2} - \frac{\Delta N_s}{2} \leq k \leq \frac{N_s}{2} + \frac{\Delta N_s}{2} - 1$.

The additional ΔN_s samples ($\Delta N_s < N_s$) are related to the excess bandwidth of the resulting signal $\Delta B = \Delta N_s / N_s$. Subsequently, $\tilde{\mathbf{z}}$ is element-wise multiplied by a windowing vector $\tilde{\mathbf{w}}$ of size $N_s + \Delta N_s$ and elements $\tilde{w}_k$, zero-padded and transformed back to the time domain with the M_s-points ($M_s > N_s + \Delta N_s$) inverse DFT matrix. The resulting vector $\mathbf{y}$ has elements given by

$$y_k = \sum_{m=-M_s/2}^{M_s/2-1} \tilde{y}_m e^{j2\pi \frac{mk}{M_s}}, \tag{5.12}$$

where $-\frac{M_s}{2} \leq k \leq \frac{M_s}{2} - 1$ and

$$\tilde{y}_m = \begin{cases} \tilde{w}_m \tilde{z}_m & , \; -\frac{N_s}{2} - \frac{\Delta N_s}{2} \leq m \leq \frac{N_s}{2} + \frac{\Delta N_s}{2} - 1 \\ 0 & , \; \text{else.} \end{cases} \tag{5.13}$$

The serialized real and imaginary parts of $\mathbf{y}$ are digital-to-analog (DAC) converted at a rate of $f_s = M_s/T_s$ and the resultant electrical signal is low-pass filtered and used to modulate an optical carrier. The MZM-based IQ modulator should be properly driven to avoid the saturation region. The resulting symbol rate is $R_s = f_s N_s / M_s$.

In the next section, it will be shown that the input samples to the DACs correspond to the digital version of a waveform that convey the information symbols x_k serially using pulses $g(k)$, i.e.,

$$y_k = \sum_{n=-N_s/2}^{N_s/2-1} x_n \cdot g(k - n\frac{M_s}{N_s}) \tag{5.14}$$

with $-\frac{M_s}{2} \leq k \leq \frac{M_s}{2} - 1$. The pulses fulfill the Nyquist criterion of zero inter-symbol interference [Pro00], i.e.,

$$g(n\frac{M_s}{N_s}) = \begin{cases} N_s & , \; n = 0 \\ 0 & , \; n \neq 0, \end{cases} \tag{5.15}$$

where $-\frac{N_s}{2} \leq n \leq \frac{N_s}{2} - 1$.

Observe that the energy of a Nyquist pulse is not totally contained in the pulse slot but spread among all N_s symbols within a block. The duty cycle d_c can be calculated numerically by solving the equation $|g(k_{\text{HWHM}})|^2 = |g(0)|^2 / 2$ for $k > 0$, where k_{HWHM} is the *half-width at half-maximum* sample. Since the pulse slot duration is M_s / N_s samples, the duty cycle is given by

$$d_c = \frac{2k_{\text{HWHM}}}{M_s / N_s} \times 100\%. \tag{5.16}$$

5.3   Spectral shaping

The selection of a windowing function will determine the spectral characteristics and subsequent performance of the transmitted signals. In the following section, three types

of Nyquist pulses will be analyzed. The most spectrally efficient of all is the sinc pulse. Raised cosine and Hamming pulses are introduced as alternatives to sinc pulses since they trade off very well spectral occupancy by increased horizontal eye opening and reduced power fluctuations.

5.3.1   Sinc pulses

The most spectrally efficient pulse is obtained when $\Delta N_s = 0$, or equivalently, when a rectangular window of width N_s is applied (see Fig. 5.3). The window's elements are defined as $\tilde{w}_k = \mathrm{rect}(k)$ where

$$\mathrm{rect}(k) = \left\{ \begin{array}{ll} 1 & , \ -\frac{N_s}{2} \leq k \leq \frac{N_s}{2} - 1 \\ 0 & , \ \mathrm{else}, \end{array} \right. \tag{5.17}$$

Combining equations. (5.10)-(5.13) with (5.17) yields the electrical signal with samples

$$\begin{aligned} y_k &= \sum_{m=-N_s/2}^{N_s/2-1} \sum_{n=-N_s/2}^{N_s/2-1} x_n e^{-j2\pi \frac{nm}{N_s}} e^{j2\pi \frac{mk}{M_s}} \\ &= \sum_{n=-N_s/2}^{N_s/2-1} x_n e^{-j\pi N_s} \sum_{m=0}^{N_s-1} e^{j2\pi m(k/M_s - n/N_s)} \\ &= \sum_{n=-N_s/2}^{N_s/2-1} x_n e^{j\pi(N_s-1)(k/M_s - n/N_s)} \frac{\sin\left(\pi N_s(k/M_s - n/N_s)\right)}{\sin\left(\pi(k/M_s - n/N_s)\right)}. \end{aligned} \tag{5.18}$$

In obtaining (5.18), the mathematical identity

$$\sum_{l=0}^{L-1} e^{j2\pi lx} = e^{j\pi(L-1)x} \frac{\sin(\pi L x)}{\sin(\pi x)} \tag{5.19}$$

was used and, since N_s is usually an even number, $e^{-j\pi N_s} = 1$.

Equation (5.18) is equivalent as (5.14) with the base pulse $g(k)$ given by

$$g(k) = e^{-j\pi(N_s-1)k/M_s} \frac{\sin\left(\pi N_s k/M_s\right)}{\sin\left(\pi k/M_s\right)}. \tag{5.20}$$

The sine-over-sine function in (5.20) is usually referred to as *Dirichlet kernel* [OS89] or *aliased sinc* [SI07] since it is obtained by applying the fourier transform to a *sampled* rectangular window. The linear phase term multiplying the aliased sinc comes from the causal nature of the implementation shown in Fig. 5.2. In the rest of this thesis $g(k)$ in (5.20) will be simply referred to as *sinc* pulse. Observe that the sinc pulse fulfills (5.15)

In Figure 5.4, one isolated pulse is depicted with its amplitude in both, linear and logarithmic scales. Additionally, the power spectrum[3] of a DQPSK modulated signal using

---

[3]The plots were obtained by convolving the magnitude-squared Fourier transform of the optical signals with a 830 MHz-wide Gaussian window, which is equivalent to a 1.25 GHz-wide rectangular window.
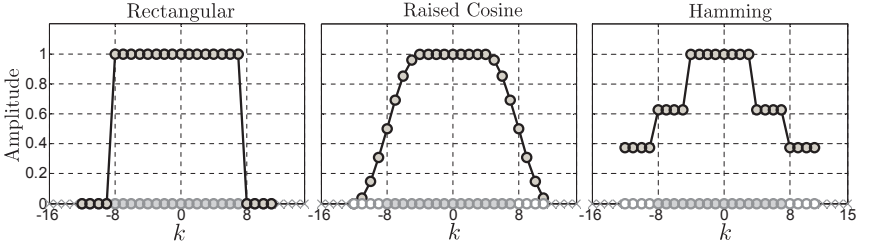
Figure 5.3: Example of different windows with $N_s = 16$ (gray circles), $\Delta N_s = 8$ (white circles) and ZP=8 (crosses). For Hamming window[4] $\alpha_{\mathrm{H}} = 0.38$.

sinc pulses is plotted. The pulses are generated at a symbol rate of $R_s = 27.75$ GS/s and have an average power of 0.5 mW. For representation purposes the OSNR of the signals is set to 40 dB in the spectrum plots. It is possible to observe that sinc pulses have the narrowest attainable spectrum. The width of the spectrum is approximately equal to the symbol rate when N_s is large. According to (5.16), the duty cycle of a sinc pulse is 88.6%.

The eye diagram of the received and demodulated in-phase component of a noiseless sinc pulse is shown as well. It is obtained without any optical filtering by a photodiode with broad electrical bandwidth and ideal responsivity of 1 A/W. Due to the relatively high amplitude of the side-lobes, the horizontal opening of the eye diagram is rather small. This is important if sampling at the receiver side is not carried out at the optimum instant. Furthermore, high amplitude side-lobes will cause high power fluctuations in the signal that are not desirable due to constraints in the dynamic range of the amplifiers and DACs, linearity of the modulators and also, because of performance degradation through the fiber's nonlinear effects, e.g. see [GFCH08]. It is therefore worthwhile to look into other pulse shapes, which can trade off some bandwidth occupancy against side-lobes with lower amplitude.

5.3.2 Raised cosine pulses

Pulses with a raised cosine spectrum have been widely used in practical communication systems [Pro00]. They give the designer a trade off between spectral occupancy and rate of decay in the amplitude of the side-lobes of the pulse. Consider the case when $\Delta N_s \neq 0$ and a raised cosine window is used. Its elements are given by

$$\tilde{w}_k = \begin{cases} 1 & , \quad \frac{(1-\beta_r)}{2}N_s > |k| \\ \frac{1}{2} + \frac{1}{2}\cos\left(\frac{\pi}{\beta_r N_s}(|k| - \frac{(1-\beta_r)}{2}N_s)\right) & , \quad \frac{(1-\beta_r)}{2}N_s \leq |k| \leq \frac{(1+\beta_r)}{2}N_s \\ 0 & , \quad \text{else,} \end{cases} \quad (5.21)$$

---

[4]Strictly speaking, this window corresponds to the Fourier transform of the generalized Hamming window, as defined in [Har78].
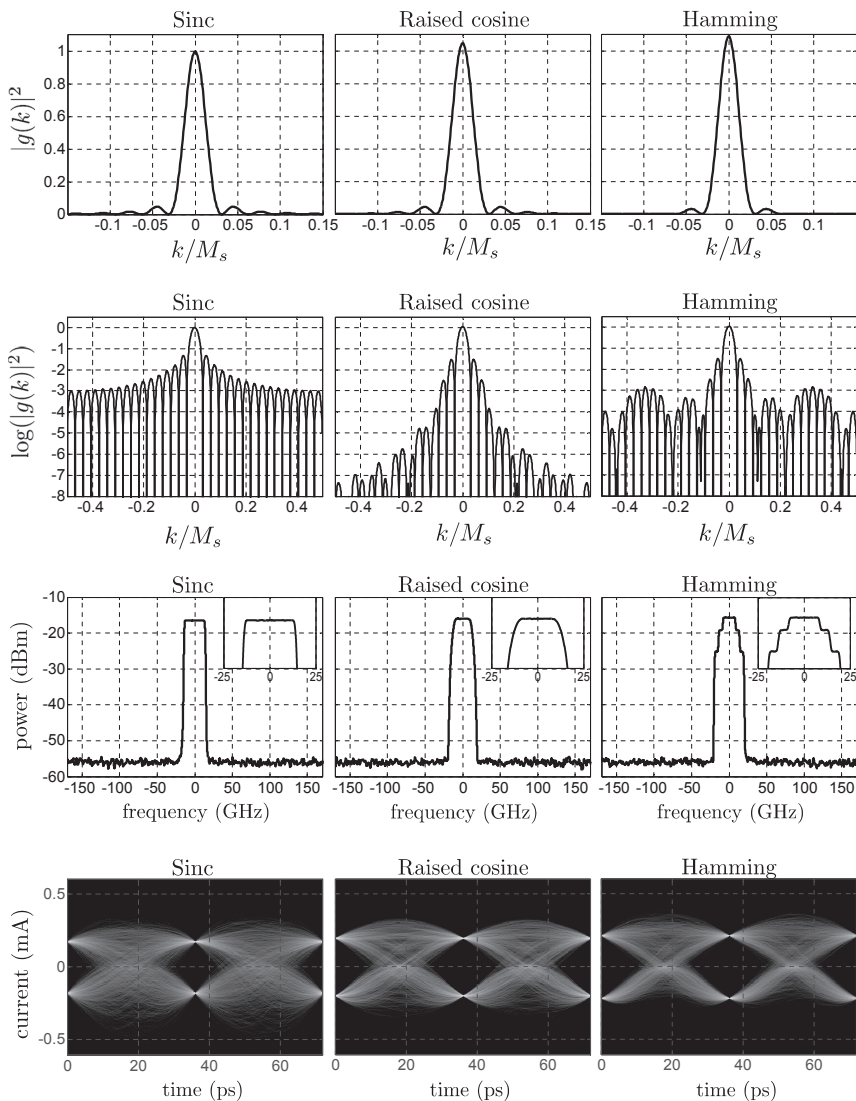
Figure 5.4: Comparison between different Nyquist pulses. Raised cosine and Hamming pulses have $\beta_r = 0.4$. For Hamming pulses $\alpha_H = 0.4$. Observe that all pulses and signals have the same average power. Eye diagrams depict 4096 data symbols.
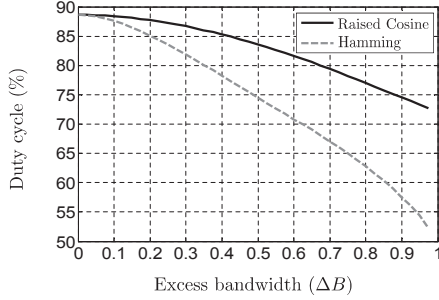
Figure 5.5: Duty cycle vs. excess bandwidth. α_H is chosen so that the side-lobe power of the Hamming pulses is minimized for each excess bandwidth.

where $-\frac{M_s}{2} \leq k \leq \frac{M_s}{2} - 1$. β_r is the window's roll-off that, similar to the excess bandwidth, is defined as $\beta_r = \Delta N_s / N_s$. Fig. 5.3 depicts an example of a raised cosine window. Analogously to the derivation of the sinc pulse and after extensive algebra, combining eqs. (5.10)-(5.13) with (5.21) delivers

$$g(k) = e^{-j\pi(N_s-1)k/M_s} \frac{\sin\left(\pi N_s k / M_s\right)}{\sin\left(\pi k / M_s\right)} \frac{\cos\left(\pi \beta_r N_s k / M_s\right)}{1 - \left(2\beta_r N_s k / M_s\right)^2}. \tag{5.22}$$

Figure 5.4, depicts the resulting pulse with $\beta_r = 0.4$ and the optical spectrum and eye diagram of a DQPSK signal at 55.5 Gb/s. It can be observed that the pulse's side-lobes decay much faster than the side-lobes of a sinc pulse. This translates into an eye diagram with wider horizontal opening. Since the main-lobe of the pulses with a raised cosine spectrum contains more power than that of the sinc pulses, the vertical amplitude of their eye-diagram is wider as well. The duty cycle depends on the roll-off of the window. Using equation (5.16) duty cycle vs. window roll-off is calculated and depicted in Figure 5.5. For example, for β_r of 20%, 40% and 60%, the approximate duty cycles are 87.7%, 85.3% and 81.6%, respectively.

For simplicity, in the rest of this thesis, pulses with a raised cosine spectrum will be referred to as *raised cosine* (RC) pulses[5].

5.3.3 Hamming pulses

Further reduction of the pulse's side-lobes can be obtained using the window given by

$$\tilde{w}_k = \alpha_H \cdot \text{rect}(k) + (1 - \alpha_H)\left(\text{rect}(k - \beta_r N_s / 2) + \text{rect}(k + \beta_r N_s / 2)\right), \tag{5.23}$$

where $-\frac{M_s}{2} \leq k \leq \frac{M_s}{2} - 1$ and $\text{rect}(k)$ is defined in (5.17). This window correspond to the Fourier transform of a *generalized Hamming window* [Har78] (see Fig. 5.3). It provides

---

[5]Pulses with a raised cosine spectrum should not be confused with the raised cosine time waveform of the electrical signals defined in chapter 3.3.1.

an additional parameter $\alpha_H \in [0,1]$ which can be varied in order to optimize the decay of the pulse's side-lobes for a given excess bandwidth. Again, analogously to the derivation of the sinc pulse, combining eqs. (5.10)-(5.13) with (5.23) yields

$$g(k) = e^{-j\pi(N_s-1)k/M_s} \frac{\sin(\pi N_s k/M_s)}{\sin(\pi k/M_s)} \left(\alpha_H + (1-\alpha_H) \cdot 2\cos(\pi\beta_r N_s k/M_s)\right). \qquad (5.24)$$

Equation (5.24) is hereafter referred to as *Hamming pulse*. Figure 5.4 depicts a Hamming pulse with 40% excess bandwidth and $\alpha_H = 0.4$, and the optical spectrum and eye diagram of a DQPSK signal at 55.5 Gb/s. Clearly, for the same excess bandwidth as the RC-pulses, Hamming pulses deliver a wider horizontal and vertical eye opening. On the other hand, for the same excess bandwidth, the width of the spectrum seems slightly wider than for RC-pulses. This translates into smaller duty cycles. Figure 5.5 depicts the duty cycle of hamming pulses vs. window roll-off. For each roll-off, α_H is chosen so that the side-lobe power of the resultant pulse is minimized (see ch. 5.4). For example, for the pairs (β_r, α_H) equal (20%, 0.325), (40%, 0.5) and (60%, 0.6), the duty cycles are 85.1%, 78.2% and 70.8%, respectively.

5.4   Horizontal eye-opening and IAPR

As previously discussed, the amplitude of the side-lobes of the pulses directly affects the horizonal opening of the demodulated eye diagrams, which is important in order to have robustness against deviations of the optimum sampling instant at the receiver. Furthermore, the side-lobes directly contribute to the dynamic power range of the resultant signals. Signals with large dynamic range are susceptible to nonlinear distortions when they pass through analog components such as power amplifiers and modulators. Even more, high peaks in the signal power during propagation contribute to signal distortion due to the fiber's nonlinearities.

It is therefore of interest to quantify and minimize the power contained in the side-lobes of the investigated pulses. For a pulse $g(k)$, with $-\frac{M_s}{2} \leq k \leq \frac{M_s}{2} - 1$, the power of the side-lobes is given by

$$P_{sl} = \frac{2}{M_s} \cdot \sum_{k=\lceil M_s/N_s \rceil}^{M_s} |g(k)|^2. \qquad (5.25)$$

Observe that the side-lobe power in (5.25) depends on the oversampling factor M_s/N_s, but converges rapidly to a limit value. We observed that it is sufficient to choose $M_s/N_s > 4$ to achieve 99.9% of the limit value of P_{sl}. The power of the side-lobes increases with the size of the DFT, however, less than 0.5% of variation in P_{sl} was found to exist when $N_s > 32$.

Under the abovementioned conditions, Fig. 5.6 (left) shows a contour plot depicting the power of the side-lobes of Hamming pulses relative to the total pulse power, for different values of β_r and α_H. Sinc pulses are equivalent to Hamming pulses with $\alpha_H = 0$ which deliver a rather high relative side-lobe power of 9.7%. A minimum of 1.8% is obtained
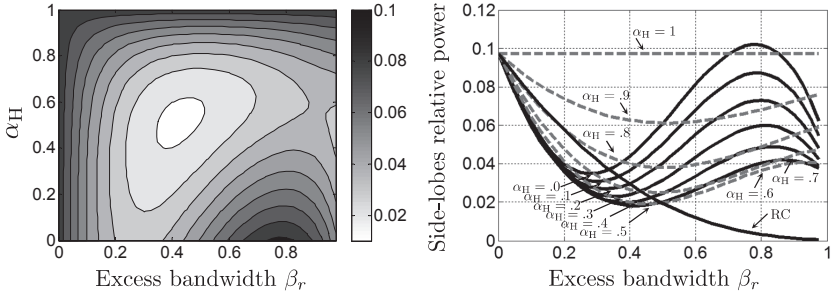
Figure 5.6: Power of the side-lobes relative to the total power of a pulse – for Hamming pulses (left) and comparison to raised cosine pulses (right).
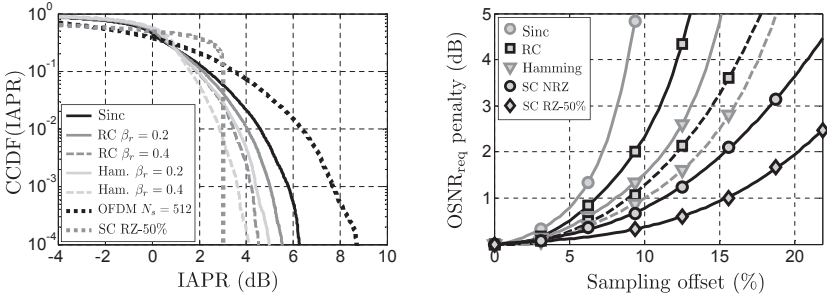
Figure 5.7: Complementary cumulative density function of the IAPR of different signals at 55.5 Gb/s (left) and tolerance to sampling offset (right).

when $\beta_r = 0.42$ and $\alpha_H = 0.52$. Figure 5.7 (right) simply takes horizontal slices from the left figure. It is possible to observe that for each β_r, there exist a value of α_H that minimizes P_{sl}. Additionally it depicts the relative side-lobe power of a raised cosine pulse. Observe that for roll-offs of less than 50%, there is always a Hamming pulse which delivers lower side-lobe power than a raised cosine pulse.

Minimizing the side-lobe power of the pulses directly translates into minimizing the power fluctuation of the resultant signals. One metric used to characterize the power fluctuation of a signal is the *instantaneous-to-average power ratio* (IAPR), defined for an optical signal $E(t)$ of duration T as

$$\text{IAPR}(t) = \frac{|E(t)|^2}{\mathcal{E}\{|E(t)|^2\}}, \tag{5.26}$$

with $t \in [0, T]$. Similarly, for a complex digital baseband signal $\mathbf{y}$ of length N_{seq} and

Table 5.1: Tolerance to sampling offset (in % of pulse slot duration) – 2 dB penalties

Sinc	RC-20%	Hamming 20%	RC-40%	Hamming 40%	NRZ	RZ-50%
7.2	9.4	11.3	12.2	13.8	15.4	20.2

samples y_k, it is given by

$$\text{IAPR}_k = \frac{|y_k|^2}{\frac{1}{N_{\text{seq}}} \sum_{l=0}^{N_{\text{seq}}-1} |y_l|^2}, \tag{5.27}$$

with $0 < k < N_{\text{seq}} - 1$. As opposed to the more commonly used peak-to-average power ratio[6] (PAPR) [SD09] which normally characterizes multi-carrier signals and is measured in a block-wise manner, IAPR is suitable to characterize single-carrier signals that are generated in a per-symbol basis. It has been shown in [LMZW08] that if signals are required to be able to tolerate certain amounts of nonlinear distortion (as in nonlinear optical systems) the statistics of the IAPR become more meaningful than those of the PAPR when addressing methods for the reduction of the signal's power fluctuations. Observe that since the IAPR is representative of all samples in a signal and not only the worst sample of a block, the probability that it exceeds a particular value is lower than the probability of the PAPR to exceed the same value.

Figure 5.7 (left) depicts the complementary cumulative distribution function (CCDF) of the IAPR, which shows the probability of the IAPR to exceed a certain value. The curves were obtained numerically. The CCDF for single-carrier DQPSK with RZ-50% is shown as a reference. Observe that, as expected, there is a null probability that its IAPR is higher than 3 dB. Additionally, the CCDF of an OFDM signal with 512 DQPSK-modulated sub-carriers is depicted as well. For such signal, there is a probability of 10^{-3} that the IAPR exceeds ~ 7.8 dB. Simply by pre-coding the OFDM signal with the DFT matrix, i.e., using sinc pulses, results in a improvement of 2 dB at the same probability[7]. Signals using RC-pulses with 20% excess bandwidth further reduce their IAPR in 1 dB whereas Hamming pulses with the same excess bandwidth reduce it by 1.5 dB. Additional 20% of excess bandwidth translates into another 1 dB reduction in IAPR at 10^{-3}.

We may expect that pulses with non-zero excess bandwidth have a better nonlinear tolerance than sinc pulses and that, in turn, Hamming pulses are more robust to non-linearities than RC-pulses for a given excess bandwidth. The nonlinear tolerance of all pulses is investigated in chapter 5.6.2.

As previously mentioned, the minimization of the side-lobe power of the pulses directly

---

[6]The PAPR of the mth block of an optical signal $E(t)$ composed of M blocks of duration T_s each, is defined as $\text{PAPR}_m = \max\{|E(t)|^2\}/\mathcal{E}\{|E(t)|^2\}$, with $t \in [(m-1) \cdot T_s, m \cdot T_s]$ and $1 < m < M$.

[7]DFT pre-coding has attracted much attention as a way to reduce the nonlinear penalty of OFDM signals in optical fiber systems [SD09]. The terms *DFT-spread* OFDM or *single-carrier frequency division multiple access* (SC-FDMA) are as well used to describe the same concept. SC-FDMA has been chosen as the standard uplink transmission format in the long term evolution (LTE) of the GSM/UMTS cellular network [3GP] mainly due to the low power fluctuation of the transmitted signals, which in turn translates into a direct improvement in energy efficiency of the power amplifiers in the user equipments.
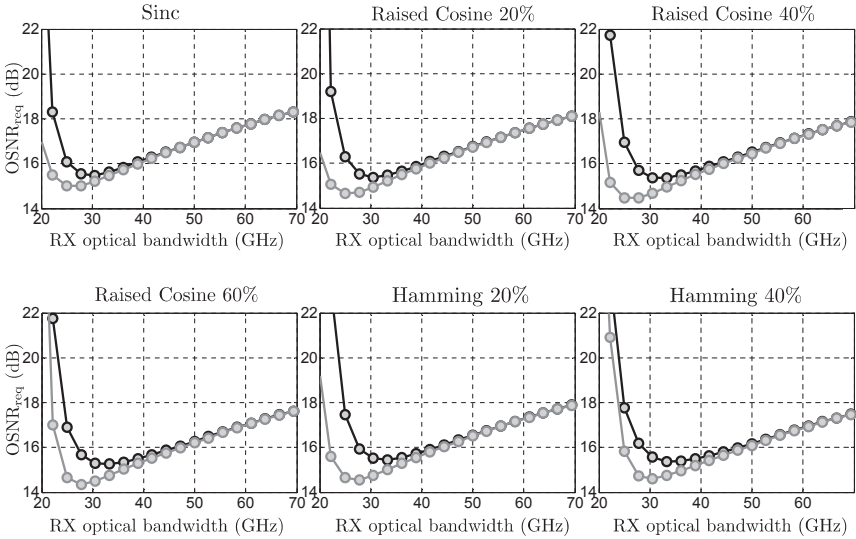
Figure 5.8: Tolerance to optical filtering of single-channel DQPSK Nyquist signals at 55.5 Gb/s. Gray curves depict pre-emphasized signals.

translates into a more opened eye-diagram, specially in the temporal direction. This is important if sampling at the receiver is not performed at the optimum instant. Figure 5.7 (right) depicts curves showing the degradation in required OSNR due to constant offset of the sampling instant from the middle of the pulse, relative to the pulse width. Observe that these simulations take into account the reduction in horizontal eye-opening due to optical filtering, which is realized using filter bandwidths according to the optimization procedure detailed in the next section. Table 5.1 summarizes the 2 dB penalties.

It is possible to observe that sinc pulses are extremely sensitive to errors in the sampling instant, with a 2 dB penalty of around 7% of the pulse duration. That is approximately half as robust as a NRZ pulse and one third of a RZ-50% pulse. Increasing the excess bandwidth of the Nyquist pulses directly translates into an improvement in the tolerance to sampling offset. Naturally, since Hamming pulses allocate less power in the side-lobes than RC-pulses for a given excess bandwidth, they deliver higher tolerance to sampling offset as well.

5.5 Optimum filtering

In this section, the optimum bandwidth of the receiver optical filter is identified for the abovementioned Nyquist pulses. For this purpose, the receiver sensitivity of single-carrier DQPSK signals at 55.5 Gb/s is considered. Sinc pulses are compared to RC and Hamming

Table 5.2: Optimum optical filter bandwidths and required OSNRs of single-channel DQPSK Nyquist signals at 55.5 Gb/s

	wo/pre-emph.		w/pre-emph.	
	$H_{o,\mathrm{RX}}$ (GHz)	$\mathrm{OSNR_{req}}$ (dB)	$H_{o,\mathrm{RX}}$ (GHz)	$\mathrm{OSNR_{req}}$ (dB)
Sinc	30.52	15.48	26.36	15.01
RC-20%	30.52	15.38	24.97	14.64
RC-40%	31.91	15.37	26.36	14.47
RC-60%	33.3	15.25	27.75	14.35
Ham-20%	33.3	15.44	27.75	14.55
Ham-40%	34.68	15.38	30.52	14.61

pulses with excess bandwidths of 20% and 40%, which can be regarded as a modest and a moderate increase in transmitter complexity and spectral occupancy. A rather significant excess bandwidth of 60% is also considered, but only using RC-pulses since, according to Fig. 5.6 (right), they are clearly superior to Hamming pulses in terms of reduced side-lobe power. Therefore a total of 6 pulses are investigated. A direct comparison can be made with the four (N)RZ pulses used for single-carrier transmission considered in the last chapter.

As in chapter 4.1.4, the transmitter shown in Fig. 5.2 is connected to the receiver depicted in Fig. 4.4 and the required OSNR for a BER of 10^{-4} is calculated for different bandwidths of the receiver optical filter. The filter is modeled with a second order Gaussian transfer function as in (3.12). The low-pass characteristic of the electrical components in the receiver are modeled as a 5th order Bessel electrical filter with transfer function given by (3.13) and bandwidth $B_e = 0.75R_s$.

One advantage of generating the transmitted signal digitally in the frequency domain, is that it is relatively straightforward to *pre-emphasize* the signal in order to minimize the distortion caused by the narrow-band optical filtering. Provided that the transfer function $H_o(f)$ of the filter is known beforehand, pre-emphasis is carried out by multiplying $\tilde{w}_m \tilde{z}_m$ in equation (5.13) with the inverse of the optical filter transfer function $H_o(f_m)^{-1}$, at frequencies $f_m = mR_s/N_s$.

Figure 5.8 depicts the simulation results for the single-channel case and Table 5.2 lists the optimum bandwidths and required OSNRs. Firstly, it is possible to see that the shape of the curves is similar to that of NRZ pulses in Fig. 4.6. The tightly confined spectrum of Nyquist signal allows it to tolerate strong narrow-band filtering but, on the other hand, causes the sensitivity degradation to increases rapidly when filtering *above* the optimum bandwidth. Nyquist signals have less allocated power in the outer part of the spectrum than NRZ signals and, therefore, the slope of sensitivity degradation is much steeper (~ 0.0705 dB/GHz vs. ~ 0.0346 dB/GHz).

Secondly, without pre-emphasis the optimum bandwidths are proportional to the excess bandwidth of the pulses. Observe that Hamming pulses are less tolerant to filtering
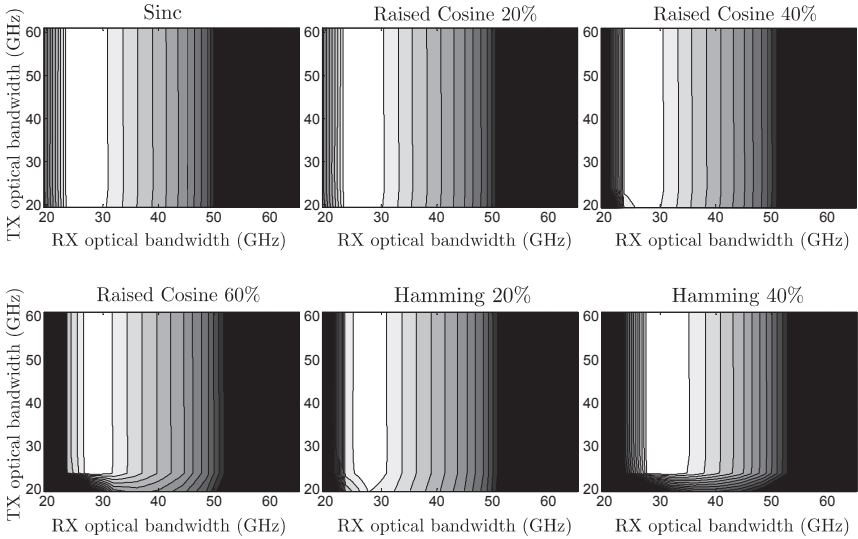
Figure 5.9: Tolerance to transmitter and receiver optical filtering of pre-emphasized WDM DQPSK Nyquist signals at 55.5 Gb/s.

than RC-pulses for a given excess bandwidth: RC-60% pulses have the same optimum bandwidth as Hamming with $\Delta B = 20\%$. Remarkably, pre-emphasis clearly helps in suppressing ISI, further improving the tolerance to narrow-band filtering by 4–5.5 GHz; and reducing the required OSNR by 0.4–0.9 dB. Pre-emphasis is seen to be specially effective for RC-pulses, even driving the performance of RC-60% very close to the theoretical limit.

In the case of WDM systems, a transmitter optical filter is usually present to prevent WDM cross-talk. However, since the compact spectrum of Nyquist signals already prevents any interference between WDM channels to occur, a transmitter optical filter only induces ISI when narrow filtering bandwidths are used. The ISI caused by the transmitter filter can be effectively removed by means of pre-emphasis and, consequently, its bandwidth has no influence in the performance of the system. Nevertheless, for the sake of completeness, transmitter and receiver bandwidths are varied and the optimum bandwidths and required OSNRs are obtained. Figure 5.9 shows the optimization result. As usual, the color gradient represents penalty with respect to the optimum required OSNR for each pulse shape, the contour lines are depicted in steps of 0.25 dB and penalties of more than 3 dB are shown black.

Notice that with Fig. 5.9, it is easy to qualitatively evaluate the robustness of the signals to deviations of the optimum receiver bandwidth. For example, it is clear that Hamming-20% is less robust than RC-20%.
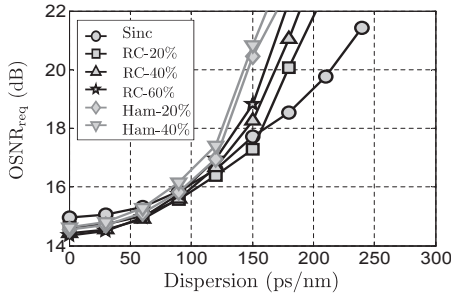
Figure 5.10: Dispersion tolerance of DQPSK Nyquist signals at 55.5 Gb/s.

Table 5.3: Dispersion tolerance (ps/nm) of single-channel DQPSK Nyquist signals at 55.5 Gb/s – 2 dB penalties

Sinc	RC-20%	RC-40%	RC-60%	Ham-20%	Ham-40%
129	128	113	105	109	100

5.6 Dispersion and nonlinear tolerance

In this section the six abovementioned pulse formats are investigated regarding dispersion and nonlinear tolerances. Pre-emphasis and the optimum filter bandwidths shown in Table 5.2 are used in the following simulations.

5.6.1 Dispersion tolerance

As in chapter 4.2.1, the required OSNRs for a target BER=10^{-4} were simulated for the different pulse shapes. The simulations were carried out for single-channel and WDM configurations by sending the signals over a dispersive single-mode fiber. Other disturbing effects such as nonlinearities are neglected.

Since WDM cross-talk is absent already without using any extra filtering at the transmitter side, the tolerance to dispersion in single channel signals is equivalent to that of WDM signals. Figure 5.10 depicts the simulation results and Table 5.3 lists the 2 dB penalties of each format. Clearly, the tolerance to dispersion is dependent on the bandwidth of the signals. Sinc pulses are more tolerant than RC-pulses which, in turn, are more tolerant than Hamming pulses. Recall that the dispersion tolerance of properly filtered (N)RZ signal is ~ 100 ps/nm/km (see Table 4.7). In comparison, Nyquist pulses bring up to $\sim 30\%$ more tolerance to dispersion with sinc and RC-20% shaping, whereas RC-pulses with larger excess bandwidths and Hamming pulses are only slightly more tolerant than (N)RZ formats.
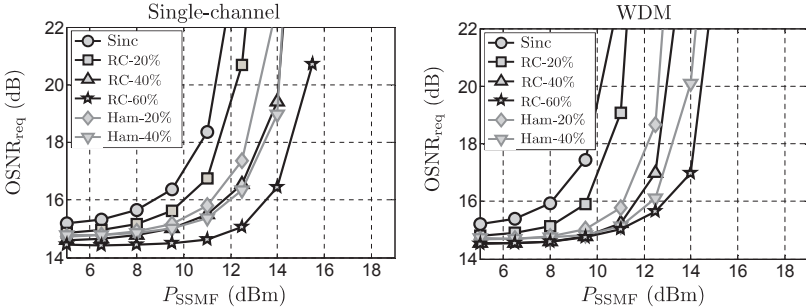
Figure 5.11: Tolerance to nonlinear effects in single-span transmission of DQPSK Nyquist signals at 55.5 Gb/s.

Table 5.4: Single-span nonlinear tolerance (dB) of DQPSK Nyquist at 55.5 Gb/s – 2 dB penalties

	Single-channel	WDM
Sinc	9.9	8.7
RC-20%	10.8	9.7
RC-40%	12.3	12.0
RC-60%	13.8	13.4
Ham-20%	11.7	11.4
Ham-40%	12.6	12.5

5.6.2   Nonlinear tolerance

As in chapter 4.2.2, the tolerance of the different Nyquist pulses against nonlinear effects is investigated using the single-span set-up shown in Figure 4.17. The optical signals are transmitted over 80 km of standard single-mode fiber. 100% of the accumulated dispersion is compensated for by a linear, non-attenuating DCF. The average input power to the SSMF is varied and the required OSNR for a BER of 10^{-4} is calculated. Figure 5.11 depicts the simulation results. The 2 dB penalties, referred to the back-to-back required OSNR are shown in Table 5.4. Propagation in the standard single-mode fiber was simulated using the parameters shown in Table 1.1.

As discussed in chapter 5.4, the IAPR of the signals directly correlates with their non-linear tolerance. In this regard, sinc pulses suffer the most from nonlinear effects, whereas shaping is effective in minimizing this penalty. As expected, Hamming pulses perform better than RC-pulses for a given excess bandwidth. Note that the additional penalty due to inter-channel nonlinear effects is only 1.2 dB for sinc pulses and is effectively minimized for signals with larger excess bandwidths, e.g., Hamming pulses with $\Delta B = 40\%$ suffer only an additional 0.1 dB nonlinear penalty due to WDM nonlinear cross-talk.

Compared to (N)RZ formats, Nyquist signals have a poor nonlinear tolerance if the IAPR is not sufficiently reduced. For example, sinc pulses are 4 dB worse than the worse (N)RZ pulse (NRZ) in the WDM scenario. Nevertheless, this difference can be kept to a minimum of 0.2–0.4 dB for pulses using ΔB =40%. RC-60% pulses even show a 0.5 dB advantage in nonlinear tolerance over the best (N)RZ pulse (RZ-67%).

5.7   Optimum nonlinear transmission and dispersion map robustness

In this section, the optimum transmission of Nyquist pulses at 55.5 Gb/s in 1040 km of SSMF is investigated. Pre-emphasis and the optimum filter bandwidths shown in Table 5.2 are used in the following simulations. For both, non-dispersion-managed (NDM) and dispersion managed (DM) links the optimum transmission parameters are identified and the robustness of the optimum is analyzed. Using the NLPS criterion discussed in chapter 3.2.4, the maximum transmission reach of each modulation format is estimated. The optimum parameters and performances can be directly compared to those obtained for single-carrier formats using (N)RZ pulses in chapter 4.3.

5.7.1   Transmission in non-dispersion-managed links

Similarly to chapter 4.3, the signals using Nyquist pulses are sent through the link shown in Fig. 4.19 (1040 km) and the launch power and amount of pre-compensation are varied in order to find the maximum OSNR margin (ΔOSNR), defined as the difference between the accumulated OSNR (3.21) and the required OSNR for a target BER of 10^{-4}. In order to simplify the analysis, it is assumed that optimum transmission occurs when the residual dispersion at the end of the link is zero.

Using the digital transmitter shown in Fig. 5.2 it is straightforward to implement the pre-compensation of dispersion by multiplying $\tilde{w}_m \tilde{z}_m$ in equation (5.13) with the inverse of the chromatic dispersion transfer function $H_{CD}(f_m)^{-1}$, at frequencies $f_m = mR_s/N_s$. The transfer function is given by (2.91). Without attenuation and neglecting dispersion slope it yields

$$H_{CD}(f_m) = \exp\left(-j\frac{\beta_2}{2}(2\pi f_m)^2 \cdot \text{PR} \cdot N \cdot L\right), \tag{5.28}$$

where N is the number of spans, L is the span length and PR is the dispersion pre-compensation ratio.

However, since the transmitter generates the signals in a block-wise manner, the amount of pre-compensation will still produce inter-block interference (IBI). The duration of the interference of one block onto the next one is equal to the walk-off experienced by the outer frequency components of the spectrum due to group velocity dispersion. For a certain amount of pre-distortion $\mathcal{D}_{\text{pre}} = \text{PR} \cdot N \cdot L \cdot D_{\text{SSMF}}$, the walk-off ΔT_{CD} can be written as

$$\Delta T_{CD} = \mathcal{D}_{\text{pre}} \frac{c}{f_c^2} R_s (1 + \Delta B), \tag{5.29}$$

where c is the speed of light in vacuum and f_c is the carrier optical frequency. Observe that the term multiplying $\mathcal{D}_{\mathrm{pre}}$ in (5.29) is simply the bandwidth of the signal in wavelength units.

The effect of IBI is especially detrimental if it occurs often, i.e., if short blocks are generated or equivalently, if the DFT size in the transmitter is small. Thus, if pre-compensation is to be directly applied in the frequency domain, a guard interval should be inserted between blocks. Even better, the multiplication with the inverse transfer function of the fiber should be implemented using overlap methods such as overlap-add or overlap-save over successive blocks [OS89]. According to (5.29), for a 13 span link with $D_{\mathrm{SSMF}} = 17$ ps/nm, a 100% pre-compensation ratio would lead to IBI of duration equal to ~ 3929 ps, which amounts to 108 symbols at the investigated symbol rate. Such an overlapping would have to occur in the transmitter in order to suppress IBI[8].

So that the results of the analysis are independent of the method used for the compensation of dispersion, pre- and post- compensation of dispersion are performed in the optical domain using linear and non-attenuating DCFs, i.e., no IBI occurs when dispersion is totally compensated for.

The simulation results are depicted in the contour plots of Fig. 5.12 and 5.13, and the optimum points are listed in Table 5.5. The contour lines are in steps of 0.25 dB and express the penalty referred to the highest ΔOSNR for each format. Penalties of more than 3 dB are shown in black.

For the single-channel case, the optimum pre-compensation is seen to lie, for all pulses, close to 50% of the total accumulated dispersion. Similarly, for all pulses, the optimum launch power is 1.6–1.8 dBm. Compared to single-carrier (N)RZ formats (see Table 4.9), Nyquist pulses require slightly higher OSNR that is reached at lower launch powers, which indicates lower nonlinear tolerances. The optimum power difference is only -0.3 dB for sinc, compared to NRZ, but -1.5 to -2.2 dB for Nyquist pulses compared to RZ pulses.

The WDM case shows that pre-compensation ratios of more than 93% are optimum. Very likely, the high amount of pre-compensation is useful as a way of further decorrelating the high power fluctuations of the Nyquist signals. The power penalty due to WDM nonlinear cross-talk is between 1.2 and 1.5 dB for all pulses except Ham-40%, in which case only a 0.4 dB penalty is observed. Notice that these penalties are smaller compared to the ones found in (N)RZ signals.

Using equations (4.57) and (4.58), the maximum number of concatenated spans for each pulse shape is calculated and listed in Table 5.6. All the obtained values were subsequently corroborated by simulating the maximum number of sections N_{max} with the same optimum pre-compensation and verifying that ΔOSNR > 0. It is seen that the maximum number of spans is 30–32 for all pulses in the single-channel case. In the WDM case the maximum reach reduces to 25–30 spans. Clearly, since transmission is limited by nonlinear effects, signals with low IAPR perform better.

---

[8]Observe that the low amounts of dispersion render IBI irrelevant in the dispersion tolerance tests discussed in chapter 5.6.1.
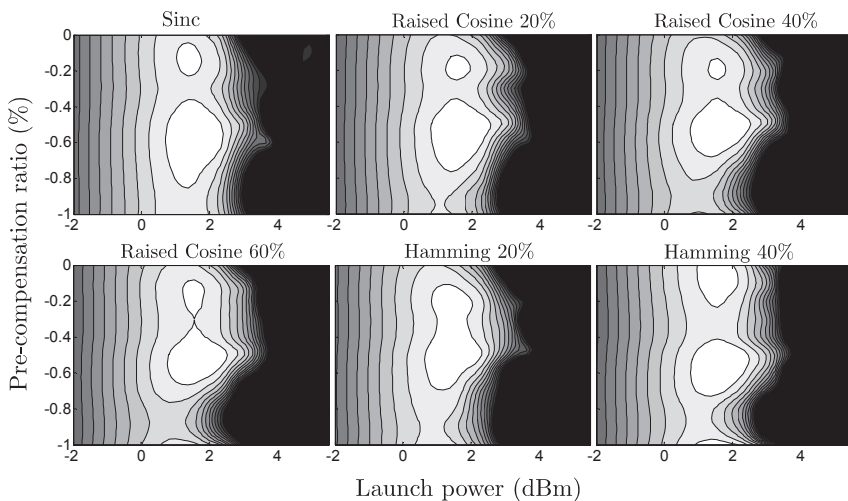
Figure 5.12: Performance of single-carrier single-channel DQPSK Nyquist signals at 55.5 Gb/s in a non-dispersion-managed link.
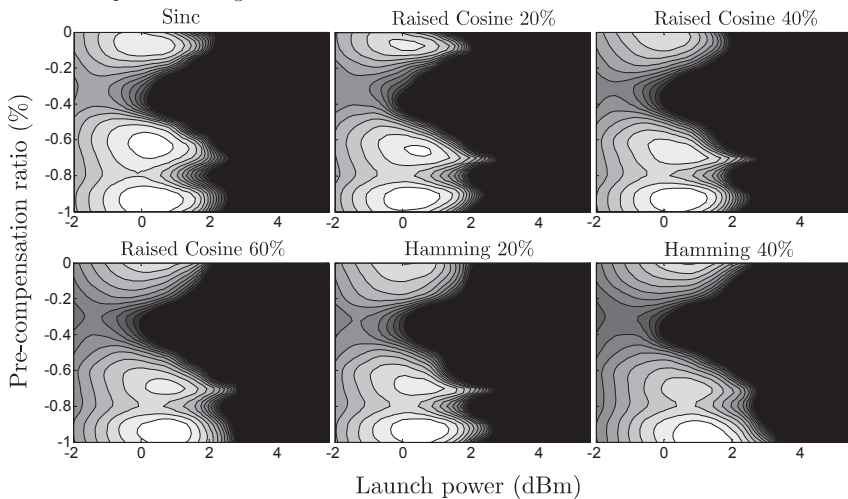
Figure 5.13: Performance of single-carrier WDM DQPSK Nyquist signals at 55.5 Gb/s in a non-dispersion-managed link.

Table 5.5: Optimum transmission parameters in non-dispersion-managed links

	Single-channel				WDM			
	PR*	P^*_{SSMF} (dBm)	$\text{OSNR}_{\text{req}}{}^*$ (dB)	ΔOSNR^* (dB)	PR*	P^*_{SSMF} (dBm)	$\text{OSNR}_{\text{req}}{}^*$ (dB)	ΔOSNR^* (dB)
Sinc	-0.57	1.6	16.68	7.30	-0.93	0.3	16.65	6.02
RC-20%	-0.53	1.8	16.45	7.71	-0.93	0.3	16.20	6.46
RC-40%	-0.53	1.8	16.29	7.88	-0.93	0.6	16.19	6.85
RC-60%	-0.53	1.8	16.20	7.97	-0.95	0.8	16.03	7.19
Ham-20%	-0.50	1.6	16.40	7.57	-0.93	0.6	16.32	6.72
Ham-40%	-0.55	1.8	16.39	7.77	-1.00	1.4	16.53	7.26

Table 5.6: Maximum number of cascaded spans in non-dispersion-managed links

	Single-channel	WDM
Sinc	30	25
RC-20%	31	27
RC-40%	32	28
RC-60%	32	29
Ham-20%	31	28
Ham-40%	32	30

Notice that the maximum reach of (N)RZ signals in the WDM scenario is 27–29 spans. So, regarding sensitivity, in NDM links with WDM transmission we do not observe any important gain nor penalty by using Nyquist pulses. Naturally, the full advantage of Nyquist pulses can be appreciated in a scenario were the signals are exposed to very strong narrow-band filtering, as shown in the next chapter.

5.7.2   Transmission in dispersion-managed links

Next, the behavior of the abovementioned pulse formats is investigated in dispersion-managed (DM) links. The model of the link is shown in Fig. 4.22. The signals are first pre-compensated with a fraction (PR) of the accumulated dispersion per span. Subsequently, transmission takes place in 13 spans (1040 km) composed of SSMF and DCF with dual-stage EDFAs. The length of the DCFs is set to compensate only a fraction (CR) of the accumulated dispersion per span. At the end of the link, any residual dispersion is brought back to zero with the post-compensating fiber. The pre-and post- compensating fibers are assumed linear and non-attenuating. Performance is measured in terms of the maximum OSNR margin ΔOSNR which is dependent on the set of parameters $\mathcal{S}_{\text{DM}} = \{P_{\text{SSMF}}, P_{\text{DCF}}, \text{PR}, \text{CR}\}$.

The optimum performance of the system is obtained with the global optimization algorithm previously introduced in chapter 3.3.3. The boundaries of the search space are given by $P_{\text{SSMF}} = [-3,\ 7]$, $P_{\text{DCF}} = [-8,\ 3]$, PR = $[-1,\ 0]$ and CR = $[0.7,\ 1.1]$. The algorithm

Table 5.7: Optimum parameters in dispersion-managed links

Single-Carrier	Single-channel					WDM				
	P^*_{SSMF} (dBm)	P^*_{DCF} (dBm)	PR*	CR*	ΔOSNR* (dB)	P^*_{SSMF} (dBm)	P^*_{DCF} (dBm)	PR*	CR*	ΔOSNR* (dB)
Sinc	1.5	-4.8	-1.00	0.86	6.21	0.9	-6.2	-1.00	0.80	5.76
RC-20%	2.0	-4.3	-0.85	0.90	7.20	1.8	-4.8	-0.60	0.93	6.84
RC-40%	2.8	-3.6	-0.60	0.93	8.20	2.1	-4.9	-0.85	0.89	7.75
RC-60%	3.1	-3.4	-0.50	0.94	8.60	2.6	-3.7	-0.60	0.93	8.23
Ham-20%	2.6	-4.3	-0.65	0.92	7.79	2.0	-3.5	-0.70	0.92	7.49
Ham-40%	2.6	-3.5	-0.65	0.92	7.93	2.2	-4.4	-0.50	0.94	7.65

is set to find the maximum OSNR margin ΔOSNR* and the optimum set of parameters $\mathcal{S}^*_{\mathrm{DM}} = \{P^*_{\mathrm{SSMF}}, P^*_{\mathrm{DCF}}, \mathrm{PR}^*, \mathrm{CR}^*\}$ in 200 iterations. The results of the optimization procedure are shown in Table 5.7.

Similarly to single-carrier (N)RZ signals (see Table 4.11), the optimum power differences (ΔP^*) between SSMF and DCF are very close (± 0.4 dB) to the previously estimated optimum of 6.5 dB (see ch. 3.2.2). On the other hand, more variation in the optimum power difference was found to exist in the WDM case: ΔP^* varies between 5.5 dB and 7.1 dB.

Next, extensive simulations were carried out in order to further investigate the robustness of Nyquist pulses to deviations of the optimum parameters of the DM link. Simulation results are depicted as power and dispersion plots in the following Figures. The contour levels relate to penalties with respect to the maximum ΔOSNR of each case. For the power plots, contour lines are in steps of 0.25 dB and penalties of more than 3 dB are shown black. For the dispersion plots, contour lines are in steps of 1 dB and penalties of more than 10 dB are shown black.

Figures 5.14 and 5.15 correspond to the power plots for the single-channel and WDM cases, respectively. It is possible to observe that the hills "move" towards the upper-right corner when the excess bandwidth increases, pointing out the increased tolerance towards nonlinearities. The relatively similar size of the hills indicate that all formats are more or less equally robust against variations in the optimum input powers.

With the exception of sinc and RC-20% pulses, the position as well as the size of the hills vary only slightly when going from single-channel to WDM transmission. The high power fluctuation of sinc and RC-20% signals clearly has a detrimental effect on the robustness of their optimum.

More differences between the pulses can be seen in Figures 5.16 and 5.17, which depict the dispersion plots for the single-channel and WDM cases, respectively. It is interesting to observe that the optimum regions in the lower-left corner of the plots get wider as the bandwidth of the signals decreases. On the other side, close to (PR,CR)=(0,1) nonlinear effects become stronger and signals with higher power fluctuations, such as signals using
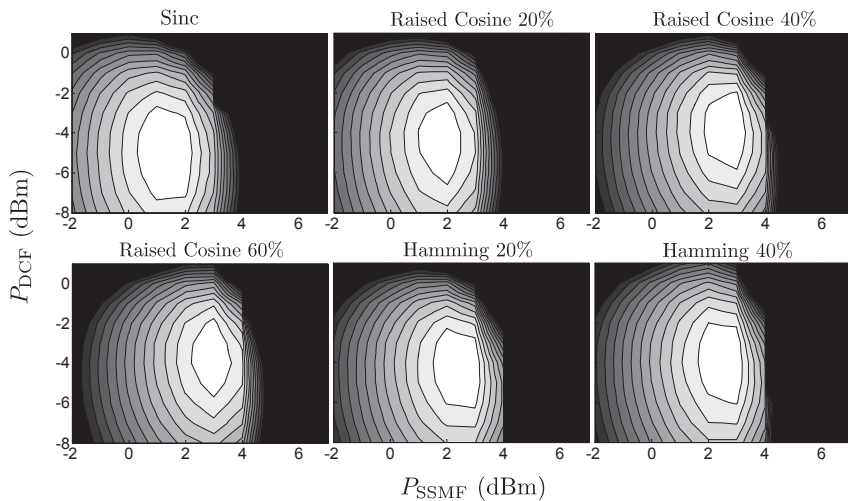
Figure 5.14: Robustness against variations in input powers in single-channel transmission.
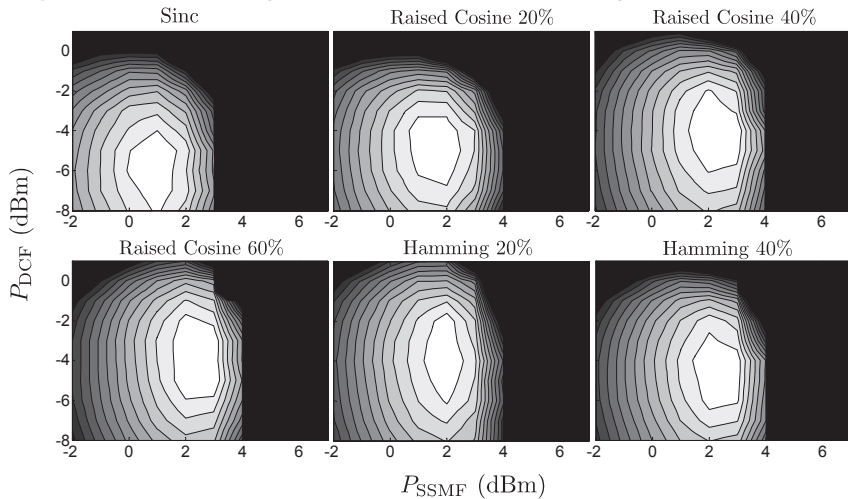
Figure 5.15: Robustness against variations in input powers in WDM transmission.
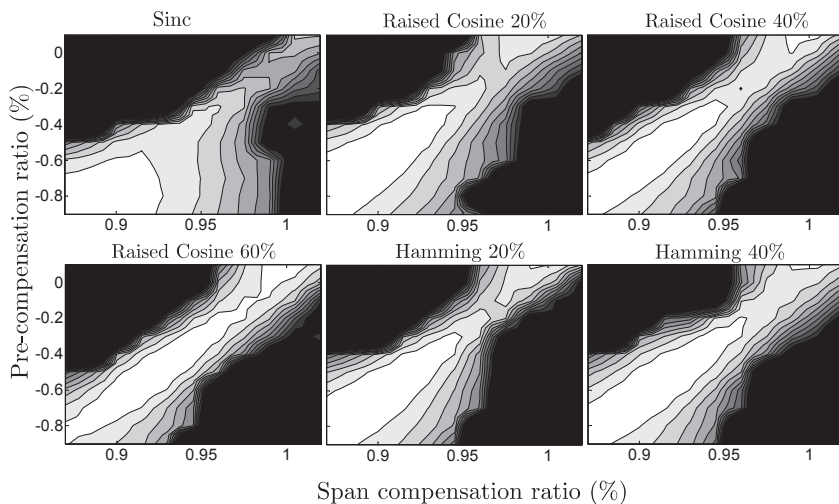
Figure 5.16: Robustness against variations in pre-compensation and span residual dispersion in single-channel transmission.
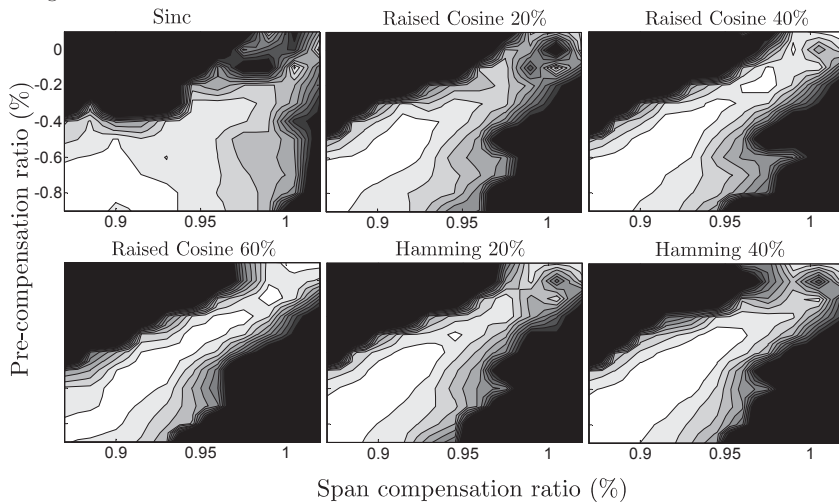
Figure 5.17: Robustness against variations in pre-compensation and span residual dispersion in WDM transmission.

Table 5.8: Maximum number of cascaded spans and OSNR$^*_{\text{req}}$ (dB) in dispersion-managed links

	Single-channel		WDM	
	OSNR$_{\text{req}}$*	$N_{\max}$	OSNR$_{\text{req}}$*	$N_{\max}$
Sinc	16.82	26	16.60	24
RC-20%	16.28	29	16.36	28
RC-40%	16.03	33	15.71	31
RC-60%	15.90	34	15.82	33
Ham-20%	16.15	31	16.12	30
Ham-40%	16.17	32	15.93	31
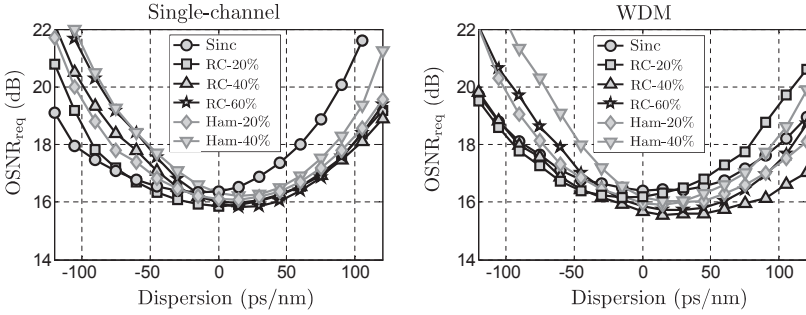
Figure 5.18: Tolerance to residual dispersion of DQPSK Nyquist signals at 55 Gb/s.

Table 5.9: Tolerance to residual dispersion (ps/nm) of DQPSK Nyquist signals at 55.5 Gb/s – 2 dB penalties

	Single-channel			WDM		
	$\mathcal{D}^-_{\text{acc}}$	$\mathcal{D}^*_{\text{acc}}$	$\mathcal{D}^+_{\text{acc}}$	$\mathcal{D}^-_{\text{acc}}$	$\mathcal{D}^*_{\text{acc}}$	$\mathcal{D}^+_{\text{acc}}$
Sinc	95	-15	80	112	0	94
RC-20%	90	0	95	82	-15	96
RC-40%	80	15	87	89	15	110
RC-60%	72	22	72	73	22	83
Ham-20%	94	15	81	86	15	100
Ham-40%	81	15	73	67	22	73

sinc pulses, degrade very rapidly. The same behavior can be observed for both single-channel and WDM transmission.

Next, an estimation of the maximum number of concatenated spans is carried out using the NLPS criterion previously described in chapter 3.2.4. The estimations were subsequently simulated in order to confirm that the OSNR margin was still positive. Table 5.8 lists the results.

For single-channel transmission, a maximum number of 34 spans is obtained by using RC-60% pulses, which is 8 spans fewer than the maximum reach achieved with RZ-33% signals (see Table 4.12). WDM transmission, on the other hand, does not suppose a big difference (1–2 spans) in terms of the maximum number of spans reached using Nyquist pulses. For example, RC-60% pulses achieve a maximum of 33 spans, which is only one less than the best RZ format (34 for RZ-50%). Compared to transmission in NDM links, Nyquist pulses in DM links perform slightly better, e.g., WDM RC-60% signals achieves 4 more spans in DM compared to NDM links.

Finally, the total residual dispersion at the end of the link is varied in order to find its optimum value and tolerance. Figure 5.18 depicts the resulting curves showing the required OSNR versus total residual dispersion. The system configurations are determined by the optimum set of parameters shown in Table 5.7. The results are listed in Table 5.9.

As expected for signals propagating in the pseudo-linear regime, the optimum residual dispersion is very close to zero. Some small positive residual dispersion seem to be beneficial to combat any residual nonlinear chirp that the signal acquires throughout the propagation. And it is seen that the higher the bandwidth of the signals (or the lower their IAPR), the higher is the optimal residual dispersion. Little difference is found between single-channel and WDM transmission. Compared to (N)RZ formats (see Table 4.13), Nyquist pulses seem to be slightly more tolerant to residual dispersion: 3–16 ps/nm in average for single-channel and WDM respectively. This is due to the compact spectrum of the signals using Nyquist formats.

In the scenario investigated in this chapter (single-carrier DQPSK at 55.5 Gb/s), the performance of Nyquist pulses in not radically different than the performance of (N)RZ pulses. The advantage of using Nyquist pulses will be evident in the next chapter, when very high spectral efficiency is required and the signals are impaired by strong narrowband filtering and WDM cross-talk.

5.8   Summary

In this chapter, we investigated the possibility of transmitting and directly detecting highly spectrally efficient optical signals, such as those obtained using orthogonal frequency multiplexing. It has been shown however, that the squaring operation of the photodiode produces inter-modulation products to appear and interfere with the signal of interest. In order to overcome this problem, linear pre-coding of the information symbols was proposed. It was shown that only pre-coding with the DFT matrix was able to sup-

press the inter-modulation products, and that this was equivalent to serial transmission of the information symbols by means of Nyquist pulses. The contribution of this chapter can be resumed in the following main points:

▷ A thorough mathematical analysis of the generation of Nyquist pulses in the frequency domain has been carried out. It was shown that cyclically extending the output of the DFT pre-coding block and applying a windowing function before the inverse DFT, the temporal and spectral characteristics of the resultant pulses can be easily shaped.

▷ It was shown that, although sinc pulses are the most spectrally efficient ones, they are not robust enough to errors in the optimum sampling time at the receiver side. Furthermore, sinc pulses present very high power fluctuations which are not desirable due to constraints in the dynamic range of the amplifiers and DACs, linearity of the modulators and also, because of performance degradation through the fiber's nonlinear effects.

▷ Both issues are caused by the high side-lobe power of the pulses. As an alternative, raised-cosine and Hamming pulses were proposed. It was shown that, for a given excess bandwidth of less than 50%, Hamming pulses are more effective in reducing the side-lobe power than raised cosine pulses. However, the narrow-band filtering tolerances show that raised cosine pulses have a narrower bandwidth.

▷ As expected, the optimum receiver filter bandwidths for signals using Nyquist pulses is narrower than for signals using (N)RZ pulses. This in turn, translates into up to 30% more tolerance to dispersion than properly filtered (N)RZ signals in the WDM scenario.

▷ The nonlinear tolerance of signals using Nyquist pulses is directly correlated to their IAPR. Nyquist signals with high IAPR (e.g., sinc and RC-20%) show a poorer tolerance compared to (N)RZ signals. If the IAPR is sufficiently reduced, as in RC-60% signals, the tolerance to nonlinearities can be up to 0.5 dB better than (N)RZ signals.

▷ Propagation in non-dispersion-managed links was investigated. The optimum pre-compensation ratios and launch powers were obtained for all the investigated Nyquist pulses. The maximum number of cascaded spans was calculated using the P_{max} rule. The longest reach was achieved in single-channel and WDM transmission by Hamming pulses with 40% excess bandwidth where transmission in up to 32 and 30 spans was possible, respectively. This is 9 spans fewer than the best of (N)RZ signals in the single-channel case, but one span more than in the WDM case.

▷ Propagation in dispersion-managed links was investigated as well. The optimum transmission parameters and performances were obtained using the global optimization algorithm. As with (N)RZ signals in the previous chapter, a thorough analysis of the robustness of the investigated formats to deviations of the optimum parameters was done. Using the NLPS criterion and the straight-line rule, the maximum

reach of each format was estimated. In the single-channel and WDM transmission scenarios, RC-60% signals achieved the maximum number of cascaded spans: 34 and 33, respectively. For WDM transmission, this is only one less concatenated span compared to the best single-carrier RZ format (RZ-50%). Subsequently, the tolerance to residual dispersion was investigated. The optimum residual dispersion is not far from zero ps/nm and only a very small performance improvement was observed.

At this point, a summary of the investigated formats can be made. Figure 5.19 depicts an overview of the estimated maximum number of concatenated spans for the investigated formats in the different transmission scenarios. Clearly, dual-carrier signals perform the best among all investigated formats. For single- and dual carrier formats, performance in DM links is superior than in NDM links, provided of course that transmission takes place in the optimum operation point. Observe that the opposite is true for stereo-multiplexed signals.
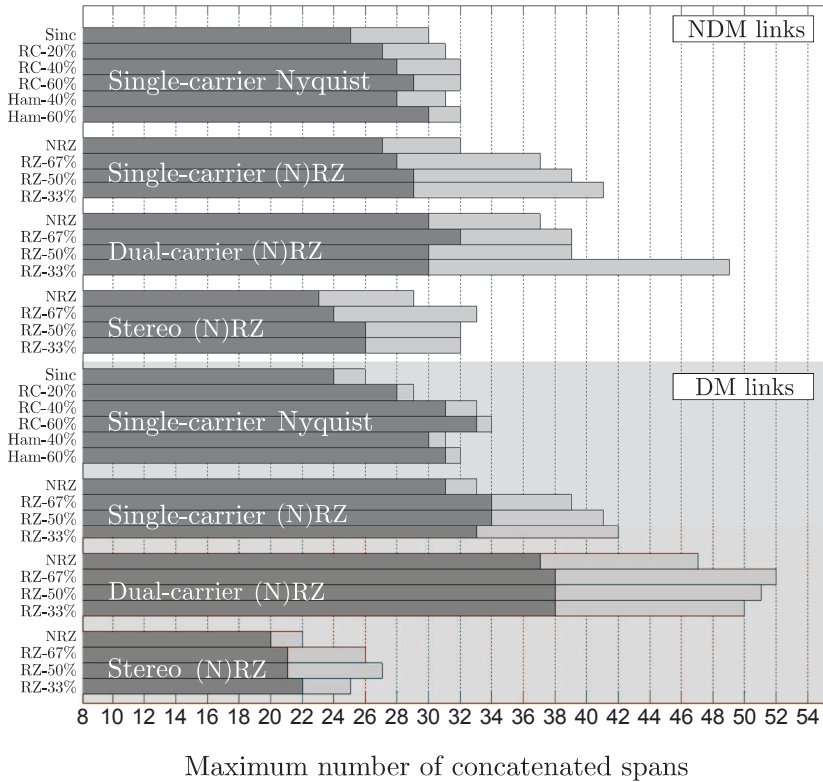
Figure 5.19: Maximum number of cascaded sections per transmission format. Single-channel and WDM transmission are depicted in light and dark gray bars, respectively.

6

ASK-DQPSK Transmission at 111 Gb/s

In this chapter we investigate the transmission of 111 Gb/s signals in a WDM grid with 50 GHz of channel separation. Firstly, it is explained why ASK-DQPSK is an attractive modulation format for this scenario. Then, a thorough description of the transmitter and receiver architectures is given. As in the previous chapters, the performance of the transmission format is assessed emphasizing the difference between (N)RZ and Nyquist pulses. It will be shown that only Nyquist signals are able to cope effectively with the high cross-talk that the signals are exposed to. (N)RZ signals on the other hand are unsuited for WDM transmission at such narrow channel separation and high symbol rate.

6.1   Modulation formats for 111 Gb/s

Compared to the scenarios studied in chapters 4 and 5, now we are interested in transmitting double as much data within the same bandwidth. It is easy to see why DQPSK signals are not suited for the task. Since the WDM channel separation is only 50 GHz, DQPSK signals with symbol rate of 55.5 GS/s would suffer strong sensitivity degradation either due to WDM cross-talk, or due to narrow-band filtering by optical filters with bandwidths well below the symbol rate. Alternatively, modulation formats that convey 3 bits per symbol such as D8PSK and ASK-DQPSK may be considered. Then, the resultant symbol rate would be only 37 GS/s.

Differential 8-PSK (D8PSK) is an extension of DQPSK, where optical signals with constant amplitude and eight phase levels are used to convey three bits per symbol (see Fig. 6.1). The multilevel nature of the signal allows for different transmitter and receiver
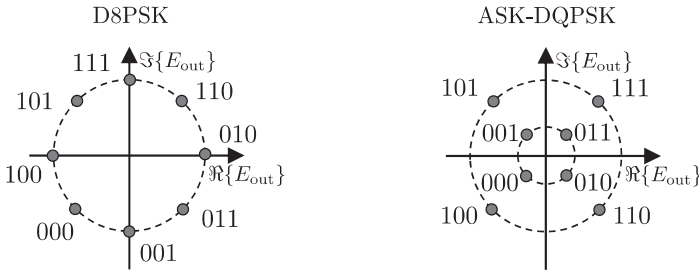
Figure 6.1: Gray-coded constellations.

implementations. One transmitter implementation uses three optical phase modulators serially concatenated [Sei10]. This type of transmitter adds chirp to the optical signal at the symbol transitions which, in the presence of dispersion and nonlinearities, translates into additional performance degradation. Another one, uses a DQPSK transmitter with a phase modulator at the output which shifts the signal by $\pi/4$ depending on the binary electrical input [OS05a, KL04].

Delay demodulation of a D8PSK signal generates electrical signals with four levels and therefore, two possible receiver implementations exist: multilevel electrical decision using two optical delay interferometers, or bilevel electrical decision using four optical delay interferometers. It has been shown [OS05a] that bilevel decision has 3 dB sensitivity gain over multilevel decision.

Amplitude-shift keying DQPSK (ASK-DQPSK) is a very simple variation of DQPSK in which a third binary information stream is encoded in the intensity of the optical DQPSK signal. Because of the shape of the resultant constellation diagram (see Fig. 6.1), ASK-DQPSK is sometimes referred to as *star 8-quadrature-amplitude modulation* (star 8-QAM) [LK97a]. The transmitter consists of a DQPSK transmitter with a MZM at the output which modulates the intensity of the signal. At the receiver side a photodiode detects the intensity of the signal and a DQPSK demodulator recovers the information conveyed by the phase of the signal.

The analytical expressions for the bit-error probabilities obtained in [NSY06] can be used to estimate the ideal performance of the abovementioned modulation formats at 111 Gb/s. Figure 6.2 depicts the results. Observe that for ASK-DQPSK firstly the optimum ratio between the amplitude rings of the constellation must be found (see ch. 6.2.3).

The curves indicate that for ASK-DQPSK an OSNR of 19.27 dB is required for a BER of 10^{-4}. D8PSK requires an OSNR of 21.05 dB. The relatively large implementation effort of D8PSK in addition to its poor sensitivity makes it very unattractive in comparison to ASK-DQPSK, specially in a transmission scenario where signals suffer important sensitivity degradation due to strong narrow-band filtering and WDM cross-talk. For this reason, only ASK-DQPSK will be further considered in the rest of the chapter.
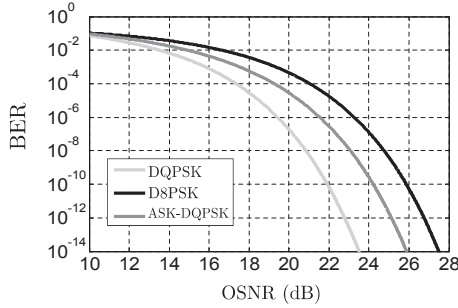
Figure 6.2: BER of modulation formats at 111 Gb/s. For ASK-DQPSK, the amplitude ratio is optimally set to $A_R = 0.465$.

Observe that the gain in spectral efficiency by using ASK-DQPSK, comes at the expense of ~ 1.9 dB in sensitivity, when comparing to DQPSK. As previously mentioned, this is necessary if WDM signals separated by only 50 GHz are to be transmitted at 111 Gb/s and no other form of multiplexing is utilized, e.g., polarization multiplexing. In the rest of the chapter the generation, transmission and reception of 111 Gb/s ASK-DQPSK signals is thoroughly investigated. The pulses introduced in the previous chapters will be compared once again, this time in a scenario where spectral occupancy is a key aspect determining the performance of the system.

6.2 ASK-DQPSK generation and demodulation

6.2.1 Transmitter design

Figure 6.3 depicts a block diagram of the transmitter for the generation of optical ASK-DQPSK modulation using (N)RZ pulses. Two of the binary information streams are imprinted onto the phase of the optical carrier by means of a Mach-Zehnder-based optical IQ modulator. As in DQPSK, the data is conveyed in the phase difference of successive symbols so that interferometric detection can be performed at the receiver. The differential encoder processes the information streams according to (4.1) and (4.2). The phases of the optical pulses output by the pulse carver (see ch. 4.1.2) are modulated by the electrical signals $b_0(t)$ and $b_1(t)$, whose amplitudes vary between 0 and $2V_\pi$ and that, in turn, depend on the differentially encoded sequences represented by $\{d_{0,k}\}$ and $\{d_{1,k}\}$. Observe that the waveforms of the electrical signals are determined by $H_{\mathrm{RC}}(f)$ in Fig. 6.3. The resulting pulse-shapes are given by (3.43).

The intensity of the resultant optical signal is modulated by the electrical signal $b_2(t)$, whose amplitude varies between 0 and $\frac{2V_\pi}{\pi} \arccos(A_R)$, where $A_R \in [0, 1]$ is the amplitude ratio. It is defined in this thesis as the ratio between the amplitudes of the inner and the
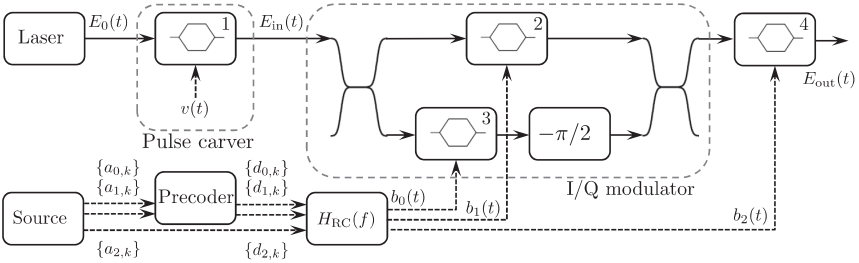
Figure 6.3: Block diagram of an ASK-DQPSK transmitter.

outer constellation rings[1].

The optical signal at the output of the ASK-DQPSK transmitter can be calculated using equations 3.5 and 3.6. If the input optical field into the IQ modulator is of the form $E_{\text{in}}(t) = \sqrt{P}p(t)e^{j\omega_c t}$, the output optical field can be written as

$$E_{\text{out}}(t) = \frac{\sqrt{P}}{2}p(t) \cdot \left(\cos\left(\pi \frac{b_0(t)}{2\,\mathrm{V}_\pi} \right) + j \cdot \cos\left(\pi \frac{b_1(t)}{2\,\mathrm{V}_\pi} \right) \right) \cdot \cos\left(\pi \frac{b_2(t)}{2\,\mathrm{V}_\pi} \right) \cdot e^{j\omega_c t}, \quad (6.1)$$

where P is the average power of the input optical field, $p(t)$ is the baseband representation of a train of pulses with unitary amplitude given by equation (4.4) and ω_c is the angular frequency of the optical carrier.

ASK-DQPSK modulation can also be implemented using Nyquist pulses for improved spectral occupancy, as described in chapter 5. Two differentially-encoded binary streams of digital data and a third one are firstly combined to form the ASK-DQPSK symbol and then digitally processed as shown in Figure 5.2 to obtain the electrical signals that complexly modulate the optical field. The sampling rate is given by $f_s = R_s M_s / N_s$, where R_s is the symbol rate, N_s is the DFT size and $M_s > N_s$ is the inverse DFT size.

6.2.2   Receiver design

The receiver is implemented as shown in Figure 6.4. Firstly, an optical coupler divides the signal power equally into the ASK and DQPSK branches. The demodulation of the DQPSK signal is carried out as described in chapter 4.1.3. The demodulation of the ASK branch consist simply in detecting the intensity of the optical signal using a photodiode. Thus, neglecting the effect of the optical and electrical filters, for an input optical field of

---

[1]Observe that in the literature, e.g., [OS05b, Coe10], the amplitude ratio is usually defined as the ratio between the amplitudes of the outer and the inner constellation rings which, for optimization purposes, may be numerically inconvenient since it would take values between 1 and ∞.
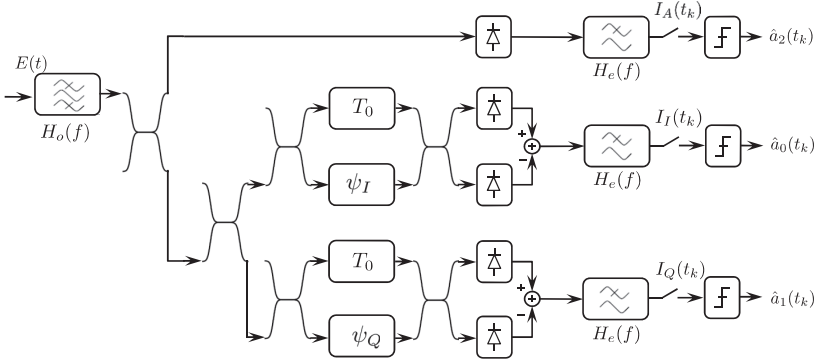
Figure 6.4: Block diagram of an ASK-DQPSK receiver.

the form $E(t) = A(t)e^{j\omega_c t}$, the decision currents can be written as

$$I_A(t) = \frac{|A(t)|^2}{2}, \tag{6.2}$$

$$I_I(t) = \frac{|A(t)||A(t-T_0)|}{4}\left(\cos(\Delta\varphi(t)) - \sin(\Delta\varphi(t))\right), \tag{6.3}$$

$$I_Q(t) = \frac{|A(t)||A(t-T_0)|}{4}\left(\cos(\Delta\varphi(t)) + \sin(\Delta\varphi(t))\right), \tag{6.4}$$

where $\Delta\varphi(t) = \varphi(t) - \varphi(t - T_0)$ is the phase difference between successive symbols.

The Hermitian kernels of the decision variables I_I and I_Q are equivalent to the ones derived in chapter 4 for DQPSK, but considering an additional optical coupler. The kernel of I_A can be easily derived in a similar way. They can be written as:

$$K_I(f_1, f_2) = \tfrac{1}{2}H_e(f_1 - f_2)\cdot(H_o^*(f_2)H_{I,\mathrm{u}}^*(f_2)H_o(f_1)H_{I,\mathrm{u}}(f_1)$$
$$- H_o^*(f_2)H_{I,\mathrm{d}}^*(f_2)H_o(f_1)H_{I,\mathrm{d}}(f_1)), \tag{6.5}$$

$$K_Q(f_1, f_2) = \tfrac{1}{2}H_e(f_1 - f_2)\cdot(H_o^*(f_2)H_{Q,\mathrm{u}}^*(f_2)H_o(f_1)H_{Q,\mathrm{u}}(f_1)$$
$$- H_o^*(f_2)H_{Q,\mathrm{d}}^*(f_2)H_o(f_1)H_{Q,\mathrm{d}}(f_1)), \tag{6.6}$$

$$K_A(f_1, f_2) = \tfrac{1}{2}H_o^*(f_2)H_e(f_1 - f_2)H_o(f_1), \tag{6.7}$$

where $H_{I,\mathrm{u}}$, $H_{I,\mathrm{d}}$, $H_{Q,\mathrm{u}}$ and $H_{Q,\mathrm{d}}$ are given by equations (4.17), (4.18), (4.32) and (4.33), respectively.

The abovementioned equations can be used in conjunction with the semi-analytical method described in chapter 3.3.2 in order to calculate the bit-error rate of the intensity, in-phase and quadrature components, BER_A, BER_I and BER_Q, respectively. The overall bit-error rate is calculated as $\mathrm{BER} = (\mathrm{BER}_A + \mathrm{BER}_I + \mathrm{BER}_Q)/3$.

Observe that when calculating the BER of the ASK branch, the decision threshold must be optimized due to the dependence of the signal-ASE beating term on the received signal

power. An expression for the optimum threshold is derived in [Mar90, NSY06] that can serve as a starting point in the optimization procedure. For an input signal to the ASK-DQPSK receiver with optical power representing a logical one P_1, the optimum threshold is given by

$$\gamma_{th} = \left(\frac{(1 + A_R)}{2} \sqrt{P_1/2} \right)^2 \tag{6.8}$$

6.2.3   Amplitude ratio optimization

Notice that the term $|A(t)||A(t - T_0)|$ in equations 6.3 and 6.4 may assume three possible values: K, $K \cdot A_R$ and $K \cdot A_R^2$, where K is a constant. Therefore the DQPSK branch outputs a 6-level eye diagram. Since they represent only two logical levels (determined by $\Delta\varphi(t)$), bilevel electrical decision is sufficient. Figures 6.5 and 6.6 depict the resultant demodulated eye diagrams of the in-phase and intensity branches for a back-to-back simulation. NRZ, RZ-33%, sinc and RC-60% signals of 0.5 mW are shown for comparison. For visualization purposes, the OSNR of the (N)RZ signals is set to 40 dB. For all signals, broadband optical and electrical filters are used.

Observe that, as the amplitude ratio grows larger, so does the eye opening of the DQPSK branch. However, at the same time, the eye opening of the ASK branch gets smaller. An optimization procedure is therefore required in order to select the amplitude ratio that properly balance the eye openings of both ASK and DQPSK branches in order to achieve optimal performance. A straightforward way to do so is to use the analytical expression for the BER obtained in [NSY06], which reads

$$\mathcal{P}_b \approx \frac{1}{6} \Bigg(1 - Q\left(2\sqrt{\theta}, (1 + A_R)\sqrt{\theta}\right) + Q\left(2A_R\sqrt{\theta}, (1 + A_R)\sqrt{\theta}\right) + $$

$$Q\left(\sqrt{2\theta(2 - \sqrt{2})}, \sqrt{\theta(2 + \sqrt{2})}\right) + Q\left(A_R\sqrt{\theta(2 - \sqrt{2})}, A_R\sqrt{\theta(2 + \sqrt{2})}\right) + $$

$$Q\left(\sqrt{\theta(A_R^2 - A_R\sqrt{2} + 1)}, \sqrt{\theta(A_R^2 + A_R\sqrt{2} + 1)}\right) - a - b - c \Bigg), \tag{6.9}$$

where

$$\theta = \rho_s/(1 + A_R^2), \tag{6.10}$$

$$a = \tfrac{1}{2}e^{-2\theta} \cdot I_0(\theta\sqrt{2}), \tag{6.11}$$

$$b = \tfrac{1}{2}e^{-2A_R^2\theta} \cdot I_0(A_R^2\theta\sqrt{2}), \tag{6.12}$$

$$c = e^{-\theta(1 + A_R^2)} \cdot I_0(\theta\sqrt{1 + A_R^4}). \tag{6.13}$$

In (6.10), ρ_s is related to the OSNR by $\rho_s = 2B_{o,\text{ref}}/R_s \cdot \text{OSNR}$. I_m is the mth order modified Bessel function of the first kind and $Q(\cdot, \cdot)$ is Marcum's Q-function of the first order[2]. In obtaining (6.9), the threshold is set as in (6.8).

---

[2]See appendix A for a definition of Marcum's Q-function.
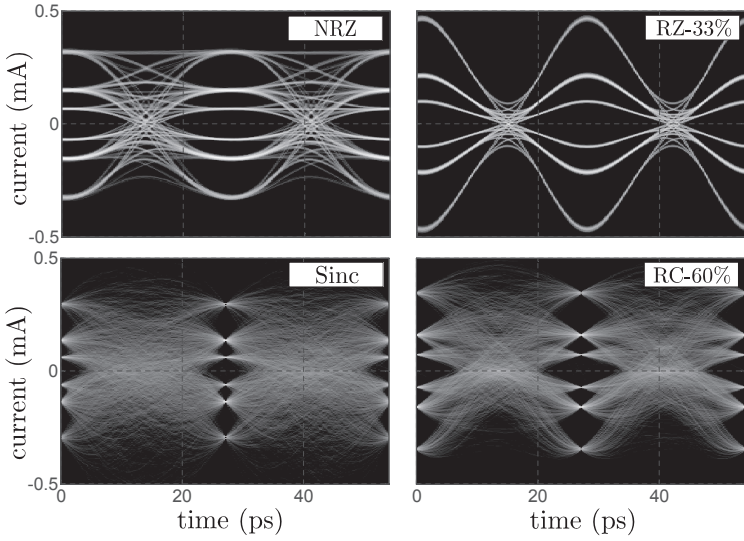
Figure 6.5: Eye diagrams of the demodulated signals at the DQPSK (in-phase) branch.
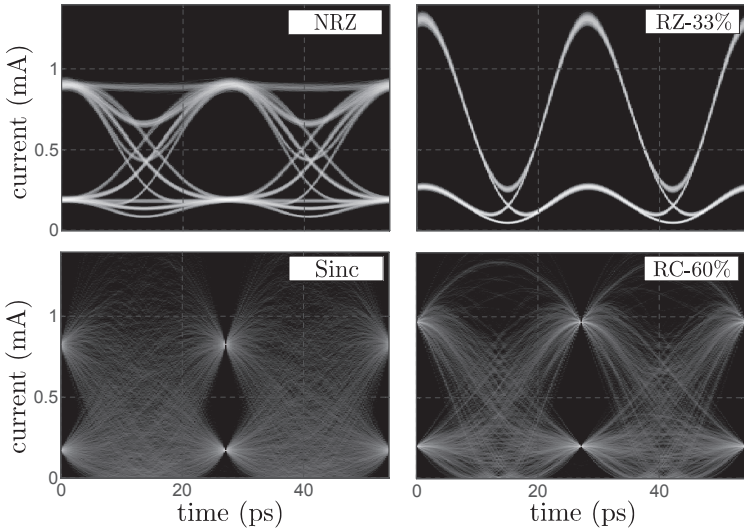
Figure 6.6: Eye diagrams of the demodulated signals at the ASK branch.
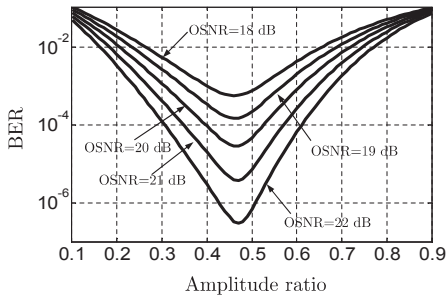
Figure 6.7: Amplitude ratio optimization using a matched filter.

Figure 6.7 depicts the BER vs. A_R for several OSNRs using equation 6.9 which is valid when a matched filter is used for reception. The optimum amplitude ratio of ~ 0.465 is consistent with [OS05b], in which optimum amplitude ratios for different pulse shapes were studied. Since little variation of the optimum A_R was found to exist between NRZ and RZ signals, in the rest of this chapter its value is fixed to $A_R = 0.465$ for all pulse formats. At the end of this chapter a short analysis is carried out in which A_R is used as a fine tuning parameter for further optimizing the quality of the transmission after nonlinear propagation.

6.3   Optimum filtering, back-to-back required OSNR and cross-talk

In this section, the optimum bandwidths of the optical filters and the receiver sensitivities of the signals are identified. For the single-channel scenario, the transmitters shown in Figures 6.3 and 5.2 are connected to the receiver depicted in Fig. 6.4 and the required OSNR for a BER of 10^{-4} is calculated for different bandwidths of the receiver optical filter. Pre-emphasis is used for Nyquist pulses. The optical filter is modeled with a second order Gaussian transfer function as in (3.12). The low-pass characteristic of the electrical components in the receiver are modeled as a 5th order Bessel electrical filter with transfer function given by (3.13) and bandwidth $B_e = 0.75R_s$. Figure 6.8 depicts the simulation results and Table 6.1 lists the optimum bandwidths and required OSNRs.

The shapes of the curves are similar to the DQPSK case shown in Fig. 4.6 for (N)RZ signals and Fig. 5.8 for Nyquist pulses. Again, the optimum performance of NRZ signals is determined by a trade-off between collected ASE noise and ISI, whereas for RZ signals it is between collected ASE noise and signal power loss. The optimum bandwidths are far above the WDM channel separation, which indicates that in such scenario (N)RZ signals would have to suffer strong filtering penalties in order to avoid WDM cross-talk. Interestingly, we observe a second local optimum for RZ signals close to the symbol rate, that gets more pronounced with smaller duty cycles. It is located at 40.7 GHz, 38.8 GHz
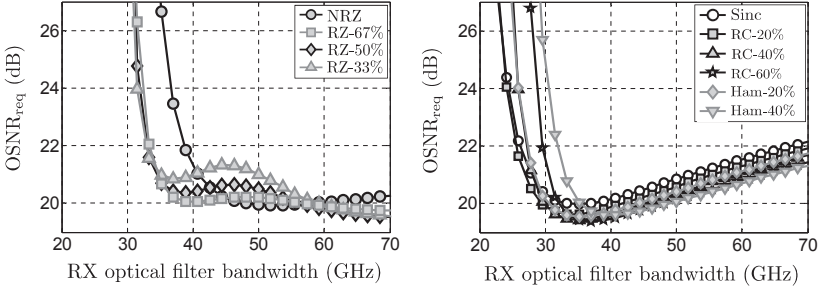
Figure 6.8: Tolerance to receiver optical filtering of single-channel ASK-DQPSK signals at 111 Gb/s.

Table 6.1: Optimum optical filter bandwidths, required OSNRs and WDM cross-talk of ASK-DQPSK signals at 111 Gb/s

	Single-channel		WDM			
	$H_{o,\mathrm{RX}}$ (GHz)	$\mathrm{OSNR_{req}}$ (dB)	$H_{o,\mathrm{TX}}$ (GHz)	$H_{o,\mathrm{RX}}$ (GHz)	$\mathrm{OSNR_{req}}$ (dB)	cross-talk[†] (dB)
Sinc	35.15	19.94	35.15	35.15	19.95	-38.90
RC-20%	33.30	19.60	35.15	35.15	19.60	-38.40
RC-40%	35.15	19.37	35.15	35.15	19.51	-24.20
RC-60%	37.00	19.34	35.15	40.78	20.03	-12.90
Ham-20%	35.15	19.53	35.15	35.15	19.73	-38.90
Ham-40%	40.00	19.56	35.15	46.25	25.41	-5.70
NRZ	51.80	19.94	62.90	40.70	25.84	-9.24
RZ-67%	72.15	19.73	40.70	40.70	23.71	-10.60
RZ-50%	81.40	19.46	40.70	40.70	22.45	-9.55
RZ-33%	91.40	19.41	40.70	40.70	22.35	-8.91

[†]The induced WDM cross-talk is defined as the power ratio between an optical channel and its neighbor, at the neighbor's center frequency.

and 37 GHz, for RZ pulses with duty cycles 67%, 50% and 33%, respectively. The required OSNR penalties of filtering at those bandwidths, compared to the optimum are respectively 0.34 dB, 0.91 dB and 1.44 dB.

Similarly to NRZ, signals using Nyquist pulses are optimally filtered just before ISI sets in. Observe that the required OSNR decreases proportional to the bandwidth of the shaped pulses. Sinc pulses are the exception, which may be due to the fact that the amplitude ratio of the signals is not optimized for each filter bandwidth. Due to the compactly allocated power in the spectrum of Nyquist signals, the penalty of filtering above the optimum grows more rapidly than in the NRZ case.
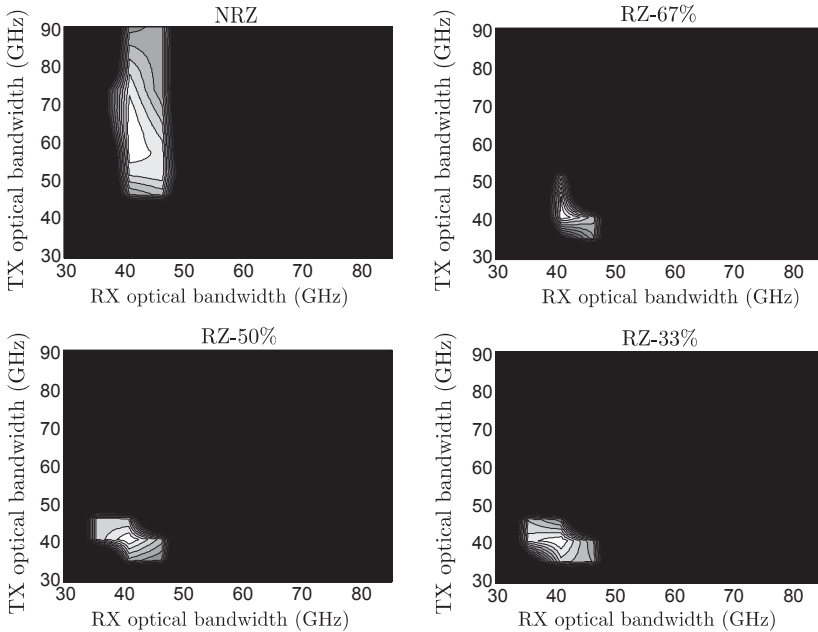
Figure 6.9: Tolerance to transmitter and receiver optical filtering of WDM ASK-DQPSK signals at 111 Gb/s using (N)RZ pulses

Next, the optimum filtering in the WDM case is investigated. In order to do so, the bandwidths of the transmitter and the receiver optical filters are jointly optimized. Recall that the transmitter filter is in charge of shaping the signal so that WDM cross-talk is avoided which, in turn, allows the receiver filter to take care of the rejection of ASE noise only. Observe that the OSNR is not affected by the power loss caused by the transmitter filter.

Simulation results are depicted in Figures 6.9 and 6.10. The color gradient represents penalty with respect to the optimum required OSNR for each pulse shape. Because of the very low robustness of the optima in (N)RZ signals, contour lines are depicted in steps of 1 dB and penalties of more than 10 dB are shown black. For Nyquist pulses contour lines are in steps of 0.25 dB and penalties of more than 3 dB are shown black. Table 6.1 lists the optimum bandwidths and required OSNRs.

From Figure 6.9, it easy to see that the high spectral occupancy makes (N)RZ signals very unattractive for the transmission of 111 Gb/s in a dense WDM scenario. Observe that the penalty due to ISI grows as rapidly as the penalty due to WDM cross-talk, and
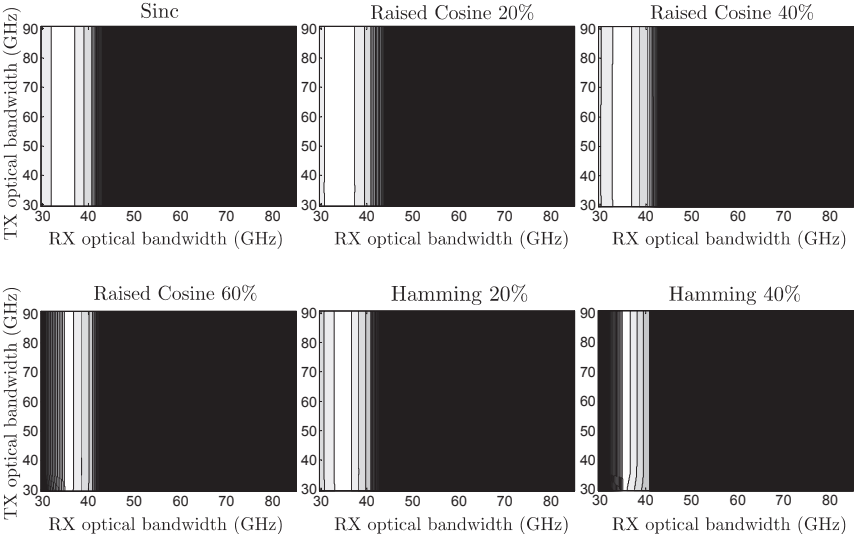
Figure 6.10: Tolerance to transmitter and receiver optical filtering of WDM ASK-DQPSK signals at 111 Gb/s using Nyquist pulses
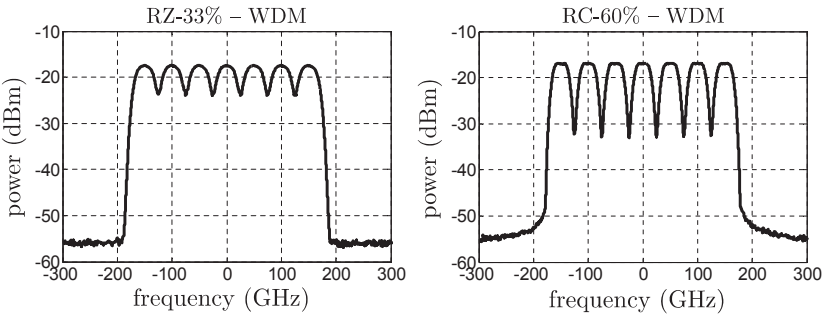
Figure 6.11: Spectra of 7×111 Gb/s ASK-DQPSK WDM signals in a 50 GHz grid.

therefore, the optimum regions are rather small. In addition, there is a big penalty in sensitivity which indicates that large amounts of ISI must be tolerated in order to avoid strong interference from neighboring channels. The compact spectrum of NRZ signals provides higher robustness against variations in the optimum filtering bandwidths but, since NRZ is specially affected by ISI, the sensitivity degradation of the optimum is much stronger than that of RZ signals.

On the other hand, since Nyquist pulses have small bandwidths, WDM cross-talk can be kept to a minimum without having to resort on strong optical filtering thus, keeping ISI to a minimum as well. As previously mentioned in chapter 5.5, the signals can be also pre-emphasize to take into account the effect of the transmitter optical filter. As it will be shown, this can be helpful in order to increase the sensitivity of the signals, but detrimental if it causes interference to the neighboring channels.

Since pre-emphasis is used, the performance depicted in Figure 6.10 is independent of the bandwidth of the transmitter optical filter. Nevertheless, observe that it is easy to qualitatively evaluate the robustness of the signals to deviations of the optimum receiver bandwidth. For example, it is clear that Ham-20% is less robust than RC-20% and that the robustness of raised cosine signals decreases with additional excess bandwidth.

Observe that the penalty between the single-channel and the WDM cases is minimum for all pulses except for Ham-40% pulses which clearly suffer from strong interference from the neighboring channel. The induced WDM cross-talk can be quantified by looking at the power ratio between a channel and its neighbor, at the neighbor's center frequency. Results are shown in Table 6.1. Still, Ham-40% signals will be further considered in order to investigate the impact of strong interference on other figures of merit such as dispersion and nonlinear tolerances.

Figure 6.11 further illustrates the advantage of Nyquist pulses over RZ pulses regarding spectral occupancy. It shows the spectra of 7 multiplexed ASK-DQPSK signals at 111 Gb/s. Optimally filtered RZ-33% and RC-60% are depicted. The optical power is 0.5 mW per channel and the OSNR is set to 40 dB. The smoothed plots where obtained by convolving the magnitude-squared Fourier transform of the optical signals with a Gaussian window of 830 MHz of bandwidth.

6.4   Dispersion and nonlinear tolerance

In this section, all the abovementioned pulse formats are investigated regarding dispersion and nonlinear tolerances. Pre-emphasis and the optimum filter bandwidths derived in the last section were used in the simulations.

6.4.1   Dispersion tolerance

The signals are sent over a dispersive single-mode fiber and the required OSNR for a target BER=10^{-4} is calculated for different amounts of dispersion. Other disturbing effects such as nonlinearities are neglected. Figure 6.12 depicts the simulation results and Table 6.2
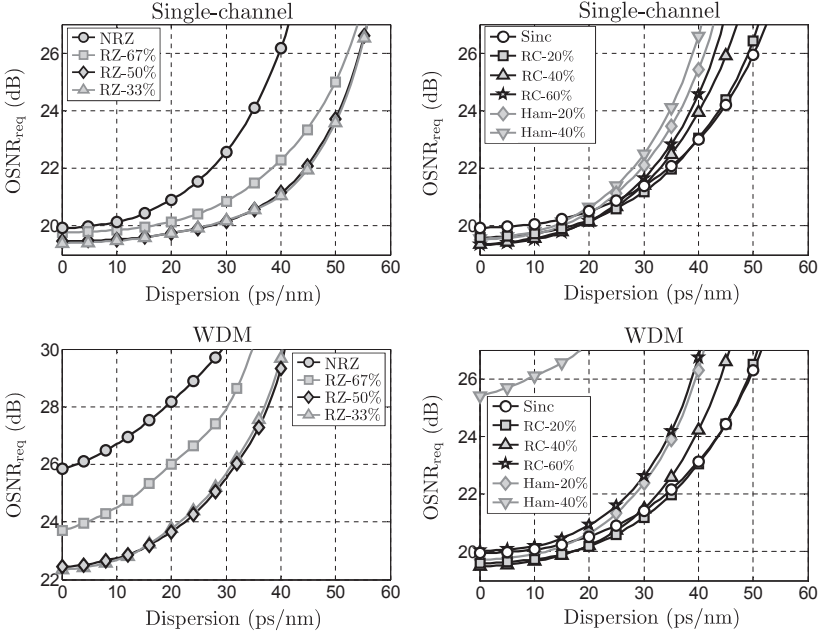
Figure 6.12: Tolerance to dispersion of ASK-DQPSK at 111 Gb/s.

lists the 2 dB penalties of each format. Observe that the amplitude ratio is fixed for all pulses and all values of dispersion.

Although the symbol rate of ASK-DQPSK is only 4/3 times that of DQPSK, we observe almost a four-fold degradation in tolerance to dispersion compared to the single-carrier DQPSK signals investigated in the previous chapters. Surprisingly, the (N)RZ formats with narrow bandwidths are the most affected by dispersion[3]. Furthermore, they appear slightly more tolerant than Nyquist signals in the single-channel case. For Nyquist pulses the opposite occurs: as in DQPSK modulation, the lower the bandwidth of the signals, the more tolerant they become against residual dispersion.

Since no dramatic filtering occurs in the WDM case, Nyquist signals do not suffer any penalty regarding dispersion tolerance. The tight filtering of (N)RZ pulses on the other hand, translates not only into degraded sensitivity but also into a decrease in dispersion tolerance.

The results suggest that residual dispersion can be a limiting factor at 111 Gb/s and

---

[3]This is in agreement with [OS05b], in which it is also shown that the amplitude ratio A_r can be used as an optimization parameter in order to minimize the degradation caused by dispersion.

Table 6.2: Dispersion tolerances (ps/nm) of ASK-DQPSK at 111 Gb/s – 2 dB penalties

	Single-channel	WDM
Sinc	33	33
RC-20%	32	32
RC-40%	29	30
RC-60%	28	26
Ham-20%	26	26
Ham-40%	24	20
NRZ	26	17
RZ-67%	36	18
RZ-50%	41	23
RZ-33%	41	23

should be addressed when designing the system. For example in [BBK08, GHC⁺10], electronic post-processing is proposed as a method to increase the tolerance to residual dispersion in direct detected communication systems.

6.4.2   Nonlinear tolerance

The tolerance of the different pulse formats against nonlinear effects is investigated using the single-span set-up shown in Figure 4.17. The optical signals are transmitted over 80 km of standard single-mode fiber. 100% of the accumulated dispersion is compensated for by a linear, non-attenuating DCF. The average input power to the SSMF is varied and the required OSNR for a BER of 10^{-4} is calculated. Figure 6.13 depicts the simulation results. The 2 dB penalties, referred to the back-to-back required OSNR are shown in Table 6.3. Propagation in the standard single-mode fiber was simulated using the parameters shown in Table 1.1. The results regarding nonlinear tolerance of ASK-DQPSK modulation are compared to those obtained for DQPSK modulation in Figures 4.18 and 5.11.

The relation between the curves of single-channel (N)RZ formats is similar in ASK-DQPSK as to that of DQPSK. However, we observe a penalty difference between the two modulation formats that vary between 4.3 to 4.9 dB, depending on the duty cycle of the pulses. The penalty difference can be attributed to the multilevel nature of the amplitude of ASK-DQPSK signals.

As in the DQPSK case, large penalty differences where found to exist in (N)RZ signals due to inter-channel nonlinear effects. Compared to the single-channel case, differences of 2.8 and 2.9 dB are observed for NRZ and RZ-67% formats, respectively, whereas RZ-50% and RZ-33% suffer degradations in nonlinear penalty of 5.2 and 5.4 dB. Notice that little variation was found between the nonlinear tolerance of WDM-(N)RZ DQPSK signals (0.2 dB), whereas a variation of up to 2 dB between WDM-(N)RZ ASK-DQPSK is observed.

Single-channel Nyquist signals have similar nonlinear penalties between them, with a
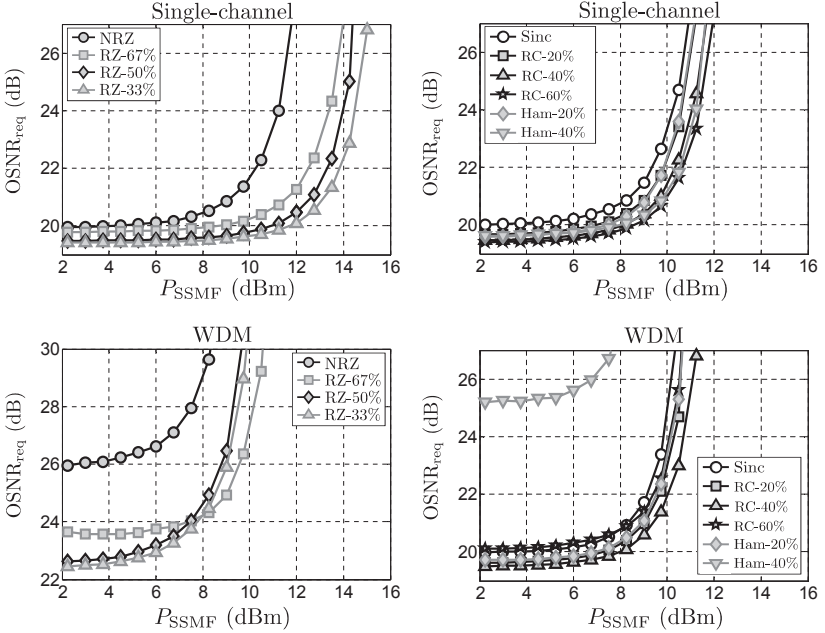
Figure 6.13: Tolerance to nonlinear effects in single-span transmission of ASK-DQPSK at 111 Gb/s.

maximum variation of 1 dB, which is dependent on the IAPR of the signals. Because of their high power fluctuation, in average, ASK-DQPSK Nyquist signals are 2.45 dB less tolerant to intra-channel nonlinearities than signals using (N)RZ formats.

Compared to the DQPSK case, we observe penalty differences that, surprisingly, increase when the IAPR of the signals decreases. The penalty differences range from 0.6–2.3 dB which is less than the differences found in (N)RZ formats (4.3–4.9 dB), clearly suggesting that the nonlinear penalty of Nyquist pulses is much more influenced by the high power fluctuation of the signals, than by the multilevel nature of the amplitude of the ASK-DQPSK modulation format.

Nyquist signals do not seem to be strongly affected by inter-channel nonlinearities, showing differences in nonlinear penalties compared to the single-channel case of 0.1–0.8 dB. A notable exception occurs with Ham-40% pulses, that suffer a degradation in nonlinear tolerance of 2.6 dB. As expected, the high linear cross-talk that Ham-40% signals produce to each other is strongly affecting their nonlinear tolerance.

In summary, for the WDM case, only RZ-67% signals perform as good Nyquist signals,

Table 6.3: Single-span nonlinear tolerance (dB) of ASK-DQPSK at 111 Gb/s – 2 dB penalties

	Single-channel	WDM
Sinc	9.3	9.1
RC-20%	9.6	9.4
RC-40%	9.9	9.8
RC-60%	10.2	9.4
Ham-20%	9.6	9.3
Ham-40%	10.3	7.7
NRZ	10.2	7.4
RZ-67%	12.3	9.4
RZ-50%	13.0	7.8
RZ-33%	13.5	8.1

with still a 0.4 dB difference compared to the best Nyquist pulse (RC-40%).

6.5 Optimum nonlinear transmission and dispersion map robustness

In this section, the optimum transmission of ASK-DQPSK modulation at 111 Gb/s is investigated. Due to the large required OSNR of ASK-DQPSK, only 7 spans are considered for transmission in the SSMF (560 Km). The optimum filter bandwidths shown in Table 6.1 are used for the simulations. Pre-emphasis is used in Nyquist signals as well. For both non-dispersion-managed (NDM) and dispersion managed (DM) links the optimum transmission parameters are identified and the robustness of the optimum is analyzed. Using the NLPS criterion discussed in chapter 3.2.4, the maximum transmission reach of each modulation format is estimated.

6.5.1 Transmission in non-dispersion-managed links

The signals are sent through the link shown in Fig. 4.19 (560 km) and the launch power and amount of pre-compensation are varied in order to find the maximum OSNR margin (ΔOSNR), defined as the difference between the accumulated OSNR (3.21) and the required OSNR for a target BER of 10^{-4}. In order to simplify the analysis, it is assumed that optimum transmission occurs when the residual dispersion at the end of the link is zero. Notice that pre- and post- compensation of dispersion are performed in the optical domain using linear, non-attenuating DCFs.

Results for the single-channel case are depicted in the contour plots of Figures 6.14 and 6.15. The contour lines are in steps of 0.25 dB and express the penalty referred to the highest ΔOSNR for each format. Penalties of more than 3 dB are shown in black. The optimum points are listed in Table 6.4.

For the single-channel scenario, we notice that there are two optimum regions with less

Table 6.4: Optimum transmission parameters in non-dispersion-managed links

	Single-channel				WDM			
	PR^*	P^*_{SSMF} (dBm)	$\mathrm{OSNR_{req}}^*$ (dB)	$\Delta \mathrm{OSNR}^*$ (dB)	PR^*	P^*_{SSMF} (dBm)	$\mathrm{OSNR_{req}}^*$ (dB)	$\Delta \mathrm{OSNR}^*$ (dB)
Sinc	-1.00	1.2	21.51	4.78	-1.00	0.06	21.57	3.59
RC-20%	-1.00	1.4	21.15	5.33	-1.00	0.44	21.29	4.25
RC-40%	-1.00	1.4	20.95	5.53	-1.00	0.25	21.02	4.34
RC-60%	-1.00	1.6	20.96	5.70	-1.00	0.06	21.75	3.41
Ham-20%	-1.00	1.4	21.04	5.44	-1.00	0.44	21.43	4.11
Ham-40%	-0.93	1.8	21.10	5.76	–	–	–	–
NRZ	-0.90	1.8	21.5	5.35	–	–	–	–
RZ-67%	-0.22	2.9	21.44	6.54	–	–	–	–
RZ-50%	-0.90	3.1	21.04	7.13	–	–	–	–
RZ-33%	-0.90	3.4	20.96	7.58	–	–	–	–
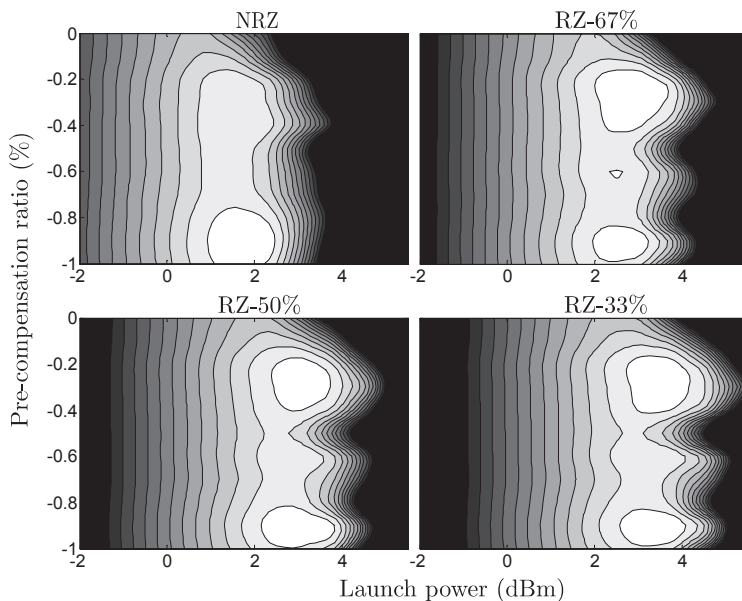
Figure 6.14: Performance of single-channel ASK-DQPSK at 111 Gb/s using (N)RZ pulses, in a non-dispersion-managed link.
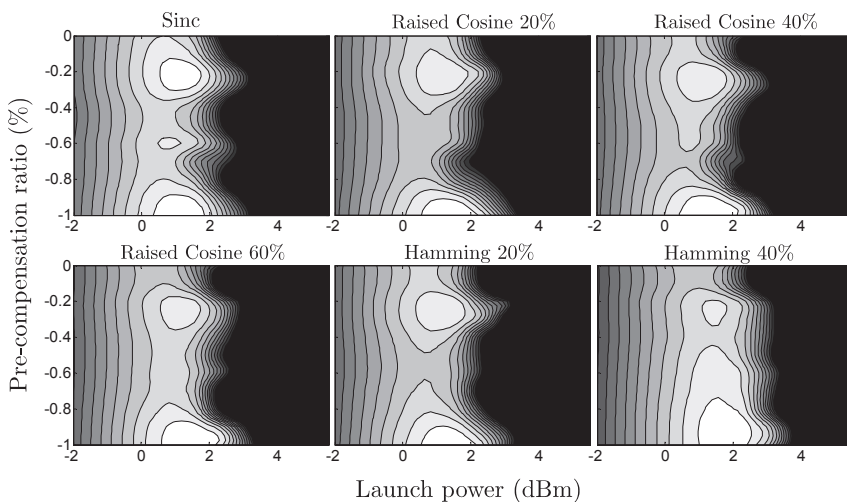
Figure 6.15: Performance of single-channel ASK-DQPSK at 111 Gb/s using Nyquist pulses, in a non-dispersion-managed link.
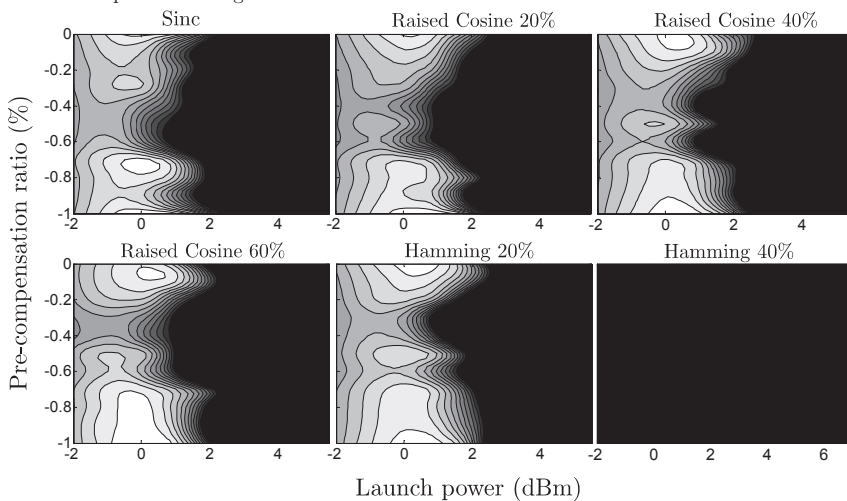
Figure 6.16: Performance of WDM ASK-DQPSK at 111 Gb/s using Nyquist pulses, in a non-dispersion-managed link.

Table 6.5: Maximum number of cascaded spans in non-dispersion-managed links

	Single-channel	WDM
Sinc	12	10
RC-20%	12	11
RC-40%	13	11
RC-60%	13	10
Ham-20%	13	11
Ham-40%	13	–
NRZ	13	–
RZ-67%	14	–
RZ-50%	15	–
RZ-33%	16	–

than 0.25 dB difference on required OSNR between them. For (N)RZ they lie around pre-compensations of 30% and 90%, whereas for Nyquist pulses they lie around 20% and 100%. The influence of pre-compensation on the performance of the transmission starts at ~ 2 dB lower launch powers in Nyquist and NRZ signals, compared to RZ signals.

Unfortunately, the propagation in WDM scenario was only successful for signals that were not strongly impacted by WDM cross-talk. These include all Nyquist pulses except Ham-40%. (N)RZ and Ham-40% were so heavily distorted that it was impossible to achieve a BER of 10^{-4}. Nyquist pulses, on the other hand, did achieve the target BER. Results are shown in Fig. 6.16. Differences of up to 1.6 dB were found to exist between the optimum launch power in single-carrier and WDM.

Using equations (4.57) and (4.58), the maximum number of spans for each pulse shape is calculated and listed in Table 6.5. All the obtained values were subsequently corroborated by simulating the maximum number of sections $N_{\max}$ with the same optimum pre-compensation and verifying that ΔOSNR > 0. It is seen that the maximum number of spans in the single-channel case is 12 to 13 for Nyquist pulses and 13 to 16 for (N)RZ formats. In the WDM case the maximum reach reduces to 10–11 spans for the Nyquist pulses that did withstand propagation.

6.5.2   Transmission in dispersion-managed links

Next, optimum transmission in dispersion-managed links is investigated. The model of the link is shown in Fig. 4.22. The signals are first pre-compensated with a fraction (PR) of the accumulated dispersion per span. Subsequently, transmission takes place in 7 spans (560 km) composed of SSMF and DCF with dual-stage EDFAs. The length of the DCFs is set to compensate only a fraction (CR) of the accumulated dispersion per span. At the end of the link, any residual dispersion is brought back to zero with the post-compensating fiber. The pre- and post- compensating fibers are assumed linear and non-attenuating. Performance is measured in terms of the maximum OSNR margin ΔOSNR which is dependent on the set of parameters $\mathcal{S}_{DM} = \{P_{SSMF}, P_{DCF}, PR, CR\}$.

Table 6.6: Optimum transmission parameters in dispersion-managed links

Single-Carrier	Single-channel					WDM				
	P^*_{SSMF} (dBm)	P^*_{DCF} (dBm)	PR*	CR*	ΔOSNR* (dB)	P^*_{SSMF} (dBm)	P^*_{DCF} (dBm)	PR*	CR*	ΔOSNR* (dB)
Sinc	2.1	-4.1	-0.70	0.92	4.62	1.0	-4.6	-0.60	0.93	3.96
RC-20%	1.7	-4.7	-0.70	0.92	4.62	0.9	-5.0	-0.70	0.93	4.26
RC-40%	2.3	-4.3	-0.80	0.92	5.45	1.4	-4.3	-0.90	0.90	4.56
RC-60%	2.5	-4.2	-0.70	0.93	5.73	1.0	-4.3	-0.80	0.93	3.96
Ham-20%	2.4	-4.2	-0.80	0.92	5.46	1.5	-5.3	-0.90	0.90	4.49
Ham-40%	2.6	-3.8	-0.70	0.93	5.61	–	–	–	–	–
NRZ	1.9	-4.9	-0.80	0.92	4.78	–	–	–	–	–
RZ-67%	3.8	-2.4	-1.00	0.85	6.73	–	–	–	–	–
RZ-50%	4.2	-2.0	-0.85	0.90	7.33	–	–	–	–	–
RZ-33%	4.9	-1.9	-0.85	0.94	7.90	–	–	–	–	–

The optimum performance of the system is obtained with the global optimization algorithm previously introduced in chapter 3.3.3. The boundaries of the search space are given by $P_{\text{SSMF}} = [-3, \, 7]$, $P_{\text{DCF}} = [-8, \, 3]$, PR $= [-1, \, 0]$ and CR $= [0.7, \, 1.1]$. The algorithm is set to find the maximum OSNR margin ΔOSNR* and the optimum set of parameters $\mathcal{S}^*_{\text{DM}} = \{P^*_{\text{SSMF}}, P^*_{\text{DCF}}, \text{PR}^*, \text{CR}^*\}$ in 200 iterations. The results of the optimization procedure are shown in Table 6.6.

Similarly to single-carrier DQPSK signals (see Tables 4.11 and 5.7), the optimum power differences (ΔP^*) between SSMF and DCF are very close ($\pm$0.3 dB) to the previously estimated optimum of 6.5 dB (see ch. 3.2.2). On the other hand, more variation in the optimum power difference was found to exist in the WDM case: ΔP^* varies between 5.3 and 6.8 dB.

The robustness of the system to deviations of the optimum parameters is quantified with power and dispersion plots[4]. The contour lines of the power plots are in steps of 0.25 dB and penalties of more than 3 dB are depicted black. For the dispersion plots, contour lines are in steps of 1 dB and penalties of more than 10 dB are depicted black.

The power plots of the single-channel case correspond to Figures 6.17 and 6.18. Observe that the size of the hills of the RZ signals is quite similar, suggesting similar robustness against deviations of the optimum input powers. But the position of the hills changes towards the upper-right corner of the plots as the duty cycle of the pulses is reduced, suggesting an overall better performance, i.e., higher ΔOSNRs. NRZ pulses on the other side perform the worst regarding both robustness and performance.

A similar analysis can be made for the single-carrier Nyquist signals. It is seen that the lower the duty cycle, the better is the performance and the robustness of the transmission. Still, there is almost 1.5 dB average ΔOSNR difference between (N)RZ and Nyquist

---

[4]See chapter 4.3.2 for a detailed explanation of power and dispersion plots.
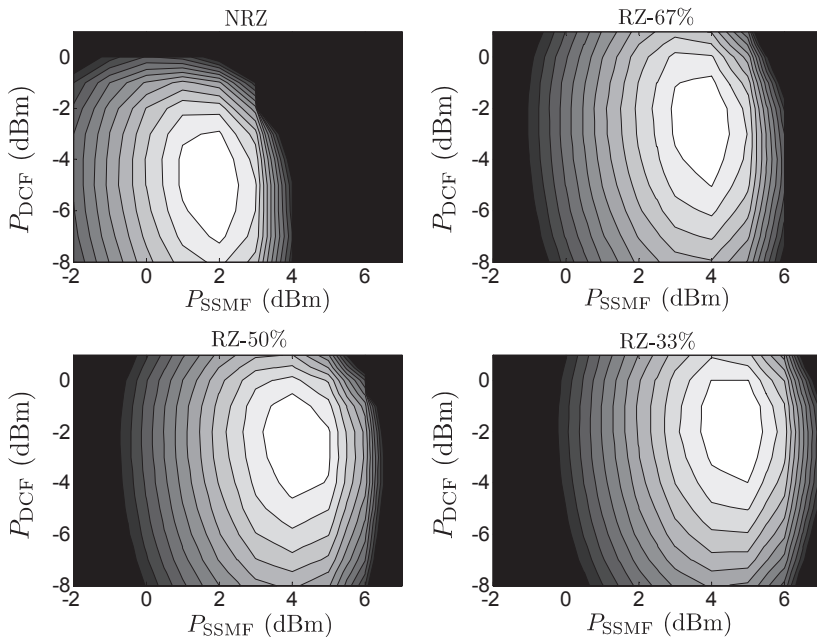
Figure 6.17: Robustness against variations in input powers in single-channel transmission using (N)RZ pulses.
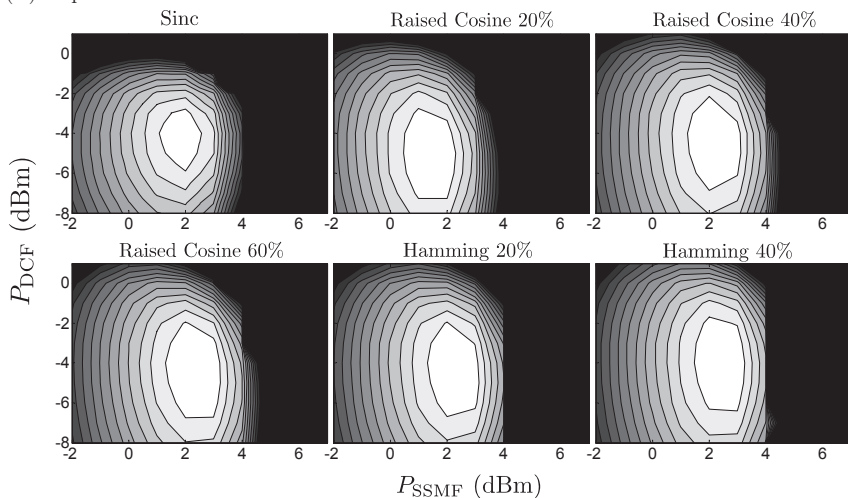
Figure 6.18: Robustness against variations in input powers in single-channel transmission using Nyquist pulses.
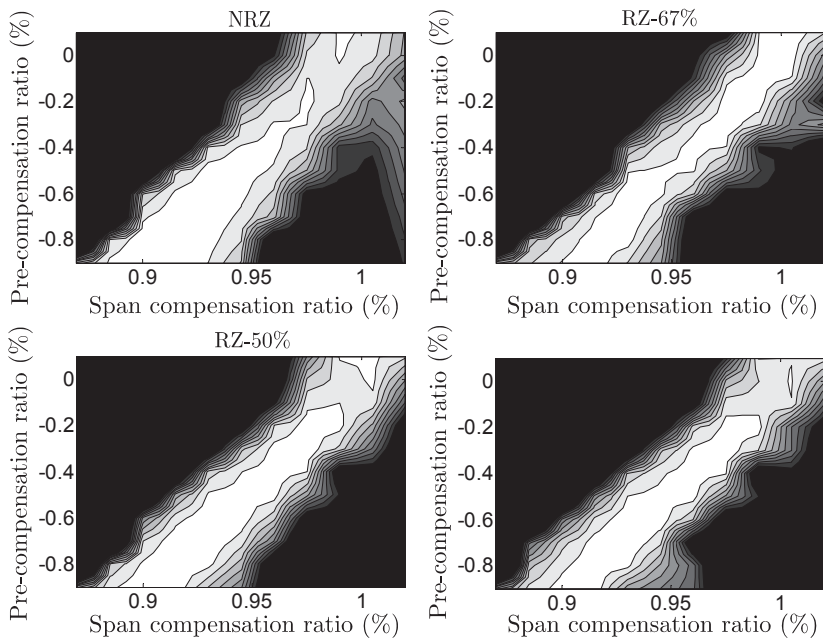
Figure 6.19: Robustness against variations in pre-compensation and span residual dispersion in single-channel transmission using (N)RZ pulses.
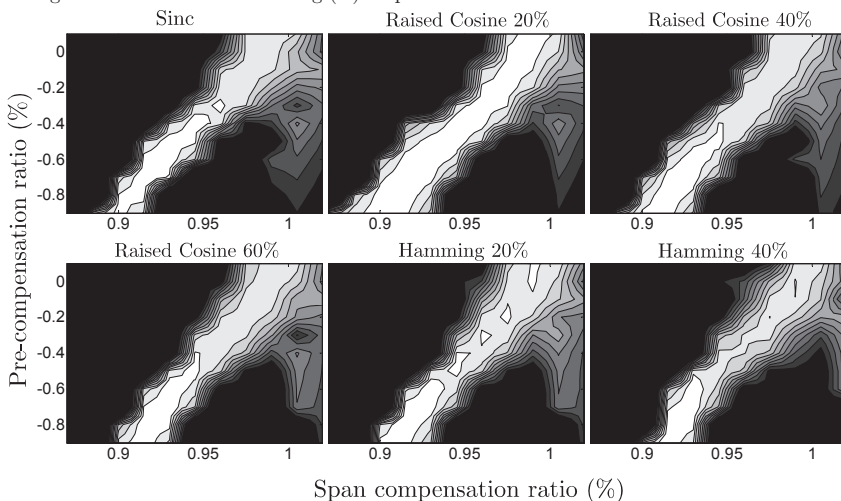
Figure 6.20: Robustness against variations in pre-compensation and span residual dispersion in single-channel transmission using Nyquist pulses.
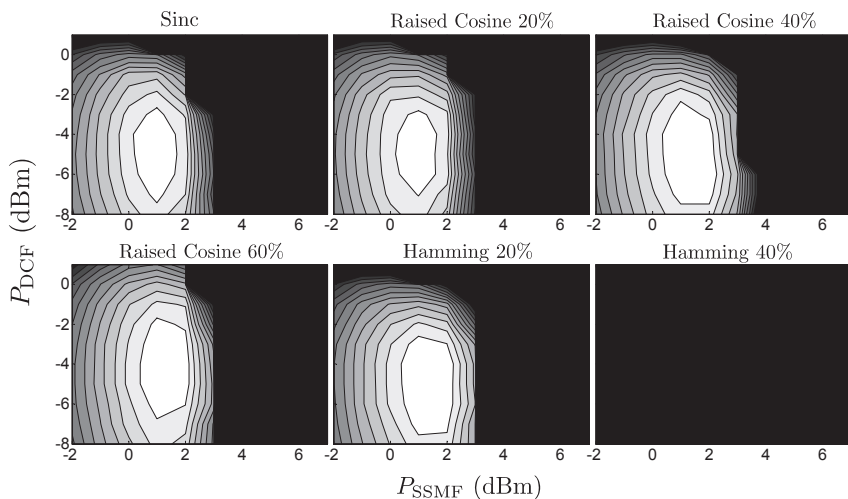
Figure 6.21: Robustness against variations in input powers in WDM transmission using Nyquist pulses.
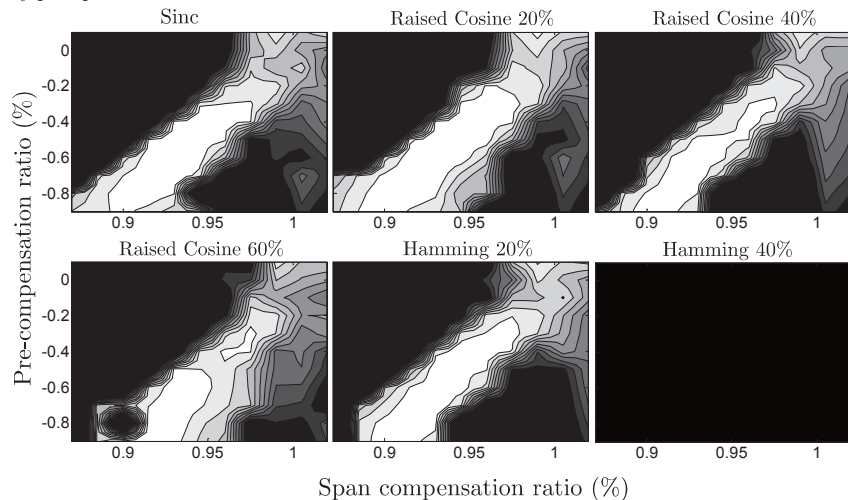
Figure 6.22: Robustness against variations in pre-compensation and span residual dispersion in WDM transmission using Nyquist pulses.

Table 6.7: Maximum number of cascaded spans and $\text{OSNR}^*_{\text{req}}$ (dB) in dispersion-managed links

	Single-channel		WDM	
	$\text{OSNR}_{\text{req}}{}^*$	N_{max}	$\text{OSNR}_{\text{req}}{}^*$	N_{max}
Sinc	21.62	11	21.78	10
RC-20%	21.67	11	21.33	11
RC-40%	21.07	12	21.19	11
RC-60%	20.86	13	21.30	10
Ham-20%	21.09	12	20.98	11
Ham-40%	21.16	13	–	–
NRZ	21.30	12	–	–
RZ-67%	21.43	14	–	–
RZ-50%	21.19	16	–	–
RZ-33%	21.22	17	–	–

signals.

The dispersion plots of the single-channel case are shown in Figures 6.19 and 6.20. We observe the same slope of the optimum regions in all plots, and the same slope compared to the DQPSK cases described in the previous chapters, confirming that the straight-line rule is not dependent on modulation formats. However, we see that, with the exception of NRZ, the optimum regions do not get noticeably broader in the lower-left corner of the plots. This is, most probably, due to the poor nonlinear tolerance of the modulation format. In addition, it is seen that Nyquist signals are less robust to deviations of the optimum dispersion values than (N)RZ signals.

As in NDM links, signals heavily impacted by WDM cross-talk were not able to withstand propagation over 7 spans in a WDM scenario. Only Nyquist pulses (except Ham-40%) achieved the target BER. Table 6.6 lists the optimum parameters and robustness of the optimum is depicted in Figures 6.21 and 6.22.

We observe a decrease in the optimum input power difference and a consequent reduction in OSNR margin. The size of the hills in the power plots indicate that robustness is maintained in the WDM case. The reduction in input powers also has the consequence of increasing the robustness to deviations of the optimum dispersion values, compared to the single-channel case.

Next, an estimation of the maximum number of concatenated spans is carried out using the NLPS criterion previously described in chapter 3.2.4. The estimations were subsequently simulated in order to confirm that the OSNR margin was still positive. Table 6.7 lists the results.

For single-channel transmission, a maximum number of 13 spans is obtained by using RC-60% pulses, which is 4 spans fewer than the maximum reach achieved with RZ-33% signals. Clearly, the lower the duty cycle, the better is the performance. In the WDM case the maximum reach of Nyquist pulses is reduced to a maximum of 11 spans. Interestingly,
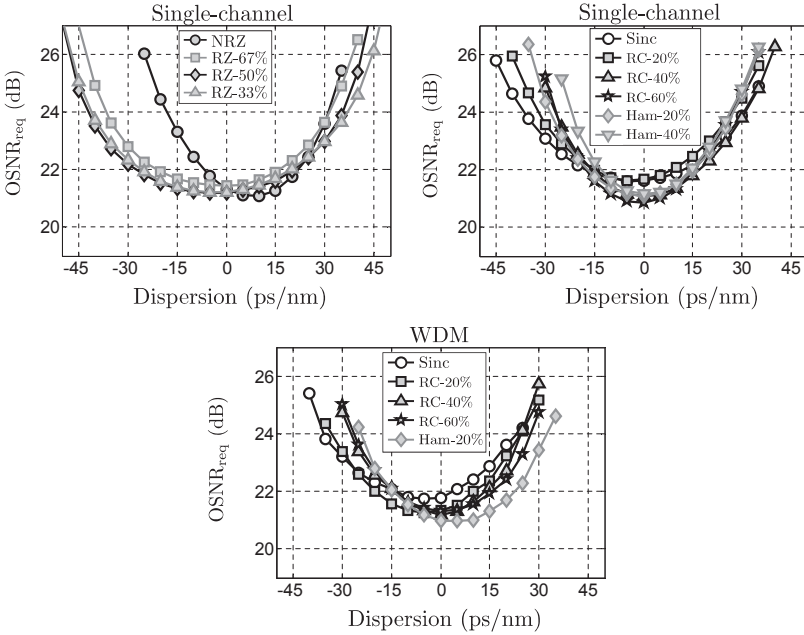
Figure 6.23: Tolerance to residual dispersion of ASK-DQPSK at 111 Gb/s

RC-60% pulses do not perform the best, very likely due to the strong linear WDM cross-talk it suffers from neighboring channels (see Table 6.1). Remarkably, the maximum number of spans is equal in NDM and DM links (see Table 6.5).

Subsequently, the total residual dispersion at the end of the link is varied in order to find its optimum value and tolerance. Figure 6.23 depicts the resulting curves showing the required OSNR versus total residual dispersion. The system configurations are determined by the optimum set of parameters shown in Table 6.6. The results are listed in Table 6.8.

As expected for signals propagating in the pseudo-linear regime, the optimum residual dispersion is very close to zero. Only (N)RZ signals show a slightly better performance when a small amount of residual dispersion is left uncompensated. All pulse formats show similar tolerances. The situation is almost identical for Nyquist signals propagation in the WDM scenario. The tolerance to residual dispersion is slightly reduced.

Finally, the amplitude ratio of the signals is varied in order to asses its influence on the performance after propagation. The optimum parameter listed in Table 6.6 were used for the simulations. Figure 6.24 depicts the results. It is seen that, with the exception of NRZ signals, the optimum amplitude ratio remains the same before and after propagation. For

Table 6.8: Tolerance to residual dispersion (ps/nm) of ASK-DQPSK at 111 Gb/s – 2 dB penalties

	Single-channel			WDM		
	$\mathcal{D}_{\mathrm{acc}}^{-}$	$\mathcal{D}_{\mathrm{acc}}^{*}$	$\mathcal{D}_{\mathrm{acc}}^{+}$	$\mathcal{D}_{\mathrm{acc}}^{-}$	$\mathcal{D}_{\mathrm{acc}}^{*}$	$\mathcal{D}_{\mathrm{acc}}^{+}$
Sinc	29	-5	33	30	-5	26
RC-20%	25	-5	29	24	-5	25
RC-40%	22	0	26	24	0	21
RC-60%	22	0	21	23	0	25
Ham-20%	24	0	23	25	5	23
Ham-40%	19	0	22	–	–	–
NRZ	23	10	28	–	–	–
RZ-67%	34	0	28	–	–	–
RZ-50%	38	0	31	–	–	–
RZ-33%	37	0	32	–	–	–

NRZ, a new optimum amplitude ratio of 0.435 was found to achieve a 0.25 dB improvement in required OSNR.

6.6   Summary

This chapter described the transmission of signals at 111 Gb/s with channel separation of only 50 GHz. For this purpose DQPSK, ASK-DQPSK and D8PSK formats were initially considered. It was shown that although DQPSK has the lowest OSNR requirement of all ($\sim$ 17.37 dB for a BER of 10^{-4}) it would incur in a pronounced sensitivity degradation due to narrow-band filtering. Since the other formats transmit at a lower symbol rate, performance degradation due to filtering and/or cross-talk is within an acceptable range. Regarding implementation effort, D8PSK requires a double amount of optical components as DQPSK at the receiver side, whereas ASK-DQPSK only needs an extra photodiode. In addition, D8PSK requires a higher OSNR than ASK-DQPSK to deliver the target BER (21.05 dB vs. 19.27 dB). For these reasons, ASK-DQPSK was the modulation format of choice for this chapter. In summary, the following are the main results:

  ▷ The generation and demodulation of ASK-DQPSK signals was thoroughly described. The transmitter consist of a DQPSK modulator with a MZM used as intensity modulator at the output. Equivalently, a digital transmitter can be used to generate Nyquist pulses with ASK-DQPSK modulation. At the receiver side, a DQPSK demodulator is used to recover the information conveyed in the phase of the optical signal, and a photodiode is used to recover the intensity. The equations describing the generation and demodulation were obtained, including an estimate of the optimum electrical decision threshold for the ASK branch. The Hermitian kernels for the calculation of the BER were given as well.
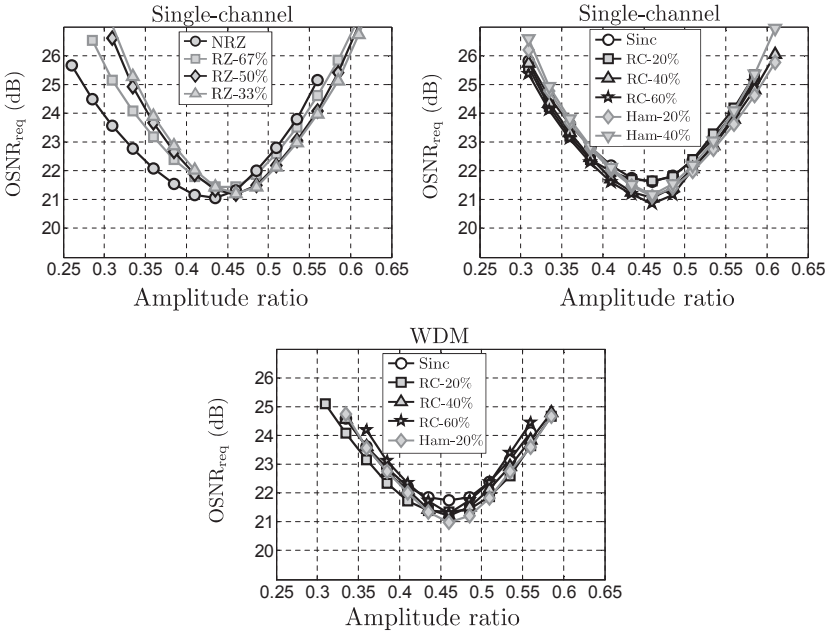
Figure 6.24: Optimization of the amplitude ratio for transmission in DM links with optimum parameters

▷ An important parameter in ASK-DQPSK signals is the amplitude ratio between the constellation rings. An large amplitude ratio results in a largely opened eye diagram in the DQPSK branch but translates in a small opening in the eye diagram of the ASK branch, and vice versa. Therefore, an optimization procedure was carried out to find the amplitude ratio that minimizes the BER. Using an analytical expression for the BER, it was found that the optimum A_R is 0.465. Later, it was shown that this value is not strongly dependent of the pulse shape, and that its optimum value remained unchanged (except for NRZ pulses) after propagation in DM links.

▷ The optimum transmitter and receiver filter bandwidths were identified along with the back-to-back required OSNR for each pulse shape. Nyquist signals perform slightly better than (N)RZ signals, albeit at much narrower bandwidths. The broad spectrum of the (N)RZ signals compared to the small WDM channel separation causes a sensitivity degradation that increases rapidly with deviations of the optimum transmitter and receiver filter bandwidths. The linear WDM cross-talk was subsequently calculated. It was shown later on that linear cross-talk is very detrimental in the nonlinear propagation of WDM signals.

▷ Although the symbol rate of ASK-DQPSK is only 4/3 times that of DQPSK, we observed almost a four-fold degradation in tolerance to dispersion compared to the single-carrier DQPSK case. As opposed to DQPSK signals, (N)RZ formats with narrow bandwidths are the most affected by dispersion. The contrary occurs with Nyquist signals. The obtained results suggest that residual dispersion can be a limiting factor at 111 Gb/s and should be addressed when designing the system.

▷ The multilevel nature in the amplitude of ASK-DQPSK was found to have a significant impact on the nonlinear tolerance. At the same time, the high power fluctuation of the Nyquist signals negatively influences their tolerance to intra-channel nonlinearities compared to (N)RZ signals. On the other hand, Nyquist signals do not seem specially affected by the nonlinear cross-talk between WDM channels, as opposed to (N)RZ signals. As expected, signals affected by strong nonlinear cross-talk see their nonlinear tolerance reduced.

▷ The propagation of ASK-DQPSK signals in NDM links was investigated. The optimum pre-compensation ratios and launch powers were obtained for all the investigated Nyquist pulses and the maximum number of cascaded spans was calculated using the P_{max} rule. For the single-channel case, Nyquist signals were not able to achieve more than 13 concatenated spans, whereas (N)RZ signals achieved up to 16. On the other hand, (N)RZ did not withstand WDM propagation at all, whereas Nyquist signals achieved up to 11 concatenated spans.

▷ Propagation in dispersion-managed links was investigated as well. The optimum transmission parameters and performances were obtained using the global optimization algorithm. The robustness of the investigated formats to deviations of the optimum parameters was investigated. Using the NLPS criterion and the straight-line rule, the maximum reach of each format was estimated as well. For the single-channel case and as in NDM links, Nyquist signals were not able to achieve more than 13 concatenated spans, whereas (N)RZ signals achieved up to 17. Again, as in NDM links, (N)RZ did not withstand WDM propagation at all, whereas Nyquist signals achieve up to 11 concatenated spans.

▷ Subsequently, the tolerance to residual dispersion was investigated. The optimum residual dispersion is not far from zero ps/nm and only a very small performance improvement was observed. Additionally, it was shown that the optimum AR remained similar to the one obtained in the back-to-back ideal case, for all pulse shapes except NRZ. For NRZ, a new optimum amplitude ratio of 0.435 was found to achieve a 0.25 dB improvement in required OSNR after propagation in DM links.

Figure 5.19 depicts an overview of the estimated maximum number of concatenated spans for the investigated formats in the different transmission scenarios. As it was previously mentioned, it is possible to observe that (N)RZ signals perform better than Nyquist signals in the single-carrier case. Their broad spectrum however, prevents them to be used at all for the WDM scenario. Observe that there is little difference between the NDM and the DM cases.
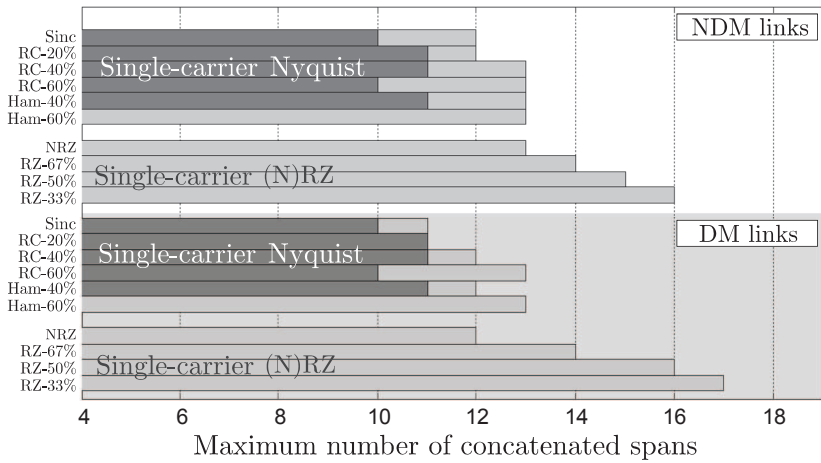
Figure 6.25: Maximum number of cascaded sections per transmission format. Single-channel and WDM transmission are depicted in light and dark gray bars, respectively.

7

Conclusions

The goal of this thesis was to investigate the performance limits of multilevel phase-modulated and direct detected WDM systems at 100 Gb/s with 50 GHz channel spacing. Particularly, we were interested in comparing different transmission formats at their optimum operation points. We focused on the difference in tolerance to propagation impairments and overall performance of single- and dual-carrier formats, using different pulse shapes, in single-channel and WDM scenarios. The main contributions of this work can be summarized as follows:

▷ The fundamental theory of propagation of light in single-mode optical fiber was thoroughly reviewed. The nonlinear Schroedinger equation (NLSE) was obtained and used throughout this thesis to simulate the investigated scenarios. Subsequently, a system of coupled NLSEs was derived which is helpful in the analysis of the nonlinear interaction of propagating WDM signals. Practical aspects regarding the numerical solution of the NLSE were given, particularly regarding the selection of a suitable step size for the simulations.

▷ Theoretical and practical considerations were given regarding the modeling and simulation of the different components of the transmission systems investigated in this thesis. Additionally, the proper evaluation of the performance of an optical communication link was reviewed: Firstly, the theory of pseudo-random sequences is briefly discussed and secondly, a semi-analytical method for the evaluation of the BER is described.

▷ A special focus of this thesis was put into the optimum design of dispersion maps and the selection of fiber launch powers in dispersion managed links. Firstly, a review of the existing engineering rules was given such as the straight-line rule (SLR). It

was found that the SLR is valid regardless of the modulation format or number of sub-carriers of the optical signals, and irrespective of wether single-channel or WDM transmission takes place. Subsequently, a method based on the SLR and the nonlinear phase shift criterion was presented which successfully estimates the maximum transmission distances achieved by the investigated formats.

▷ Although the SLR is successful in predicting the optimum dispersion map of dispersion managed links, the overall optimum performance is given by the proper selection of suitable fiber launch powers. A mathematical algorithm was specially designed for the global optimization of the performance of an optical communication system. It was used to maximize the OSNR margin after a certain transmission distance. Although the algorithm is computational intensive, it is successful in minimizing the required number of iterations needed to obtain the optimum with an arbitrary small error. By using the algorithm, it was possible to compare the investigated transmission formats at their optimum operation points. Furthermore, it was possible to evaluate the robustness of the investigated formats to deviations of their optimum parameters.

▷ Using the abovementioned models and simulation tools, we were able to compare the overall performance and robustness of different transmission formats to detrimental fiber effects. Particularly we focused on DQPSK signals at 55.5 Gb/s using (non) return-to-zero pulses with different duty cycles. The propagation of single-channel and WDM transmission were considered. Signals using single-carrier and dual-carrier configurations were compared in a handful of different scenarios: Firstly, back-to-back generation and demodulation was analyzed with the purpose of optimizing transmitter and receiver optical filter bandwidths and find the minimum required OSNRs of the investigated formats. Secondly, dispersion tolerances were assessed. Thirdly, a single-span configuration was used to evaluate the tolerances to nonlinear effects. And finally, the transmission in 1040 km of SSMF in dispersion and non-dispersion managed links was investigated. The optimum transmission parameters were identified and, as previously mentioned, the robustness of the investigated formats to deviations of their optimum parameters was evaluated.

▷ Stereo multiplexing has been proposed as a way of detecting two carriers simultaneously using only one DQPSK modulator. The transmitter and receiver design was described in detail. The gain of stereo multiplexing, in terms of reduction of the number components at the receiver side compared to dual-carrier transmission, comes at an expense in receiver sensitivity of about $\sim 0.5 - 1$ dB. Additionally, a novel mathematical framework is presented that models the effect of square-law detection in linearly pre-coded FDM signals. It is used to show that stereo multiplexing can be extended up to five sub-carriers only if complex pre-coding is used. The framework is also useful in analyzing other direct-detected multi-carrier modulation formats, e.g., OFDM.

▷ We introduce Nyquist pulses as a way of minimizing the spectral occupancy of the signals. Firstly, the generation of the pulses in the frequency domain was described.

Secondly, spectral shaping was introduced and successfully used to increase the robustness of the Nyquist signals to transmission impairments. Thirdly, the performance of the signals was quantified within the same scenarios used for characterizing (non) return-to-zero signals.

▷ Finally, this thesis investigates the transmission of 111 Gb/s signals encoding 3 bits per transmitted symbol. This scenario is characterized by the strong WDM cross-talk and narrow-band filtering to which the signals are exposed, because of their broad spectrum and small channel separation. ASK-DQPSK is used as the modulation format for such scenario. As in the previous chapters, the performance of the transmission format is assessed emphasizing the difference between (N)RZ and Nyquist pulses. It was shown that only Nyquist signals are able to cope effectively with the high cross-talk that the signals are exposed to and that, (N)RZ signals are unsuited for WDM transmission at such narrow channel separation and high symbol rate.

There is still a number of interesting topics that remain open for future research. Among others:

▷ A natural extension of this work is to include polarization effects and quantify the penalty that the systems incur with respect to different PMD values. The power exchange between polarizations affects the intensity of the nonlinear effects and therefore small deviations of the optimum parameters may occur. This is specially interesting for WDM scenarios: the initial state of polarization of the WDM signals may not only affect the values of the optimum parameters but also, it could even be considered as an extra parameter in the optimization procedure.

▷ One other possible research topic could be the joint optimization of transmission systems where different modulation formats and data rates coexist. For example, the optimization algorithm could be used to determine the optimum launch powers and dispersion maps of 10 Gb/s signals in the presence of 100 Gb/s signals.

▷ Finally it would be interesting to extend this work in order to include digitally coherent detected systems. Not only the optimization algorithm could be used to determine the optimum transmission performance of such systems, but also, Nyquist signals could be used in scenarios where WDM cross-talk is an issue. Additionally, spectral shaping should be considered as a way to reduce the power fluctuations of multi-carrier signals such as OFDM[1].

---

[1]Initial work has already been undertaken in this subject in [AKJ+12, AJK+13].

A

Definition of Some Mathematical Functions

The following mathematical functions are used in this thesis:

▷ The Bessel function [AS64]:

$$J_m(z) = \left(\frac{z}{2}\right)^m \sum_{k=0}^{\infty} \frac{(-z^2/4)^k}{k!\Gamma(m+k+1)},$$ (A.1)

with $z \in \mathbb{Z}$ and $m \in \mathbb{R}$. Γ is the gamma function defined as

$$\Gamma(x) = \int_0^{\infty} e^{-t} t^{x-1} \mathrm{d}t,$$ (A.2)

with $x \in \mathbb{R}$.

▷ The Neumann function [AS64]:

$$N_m(z) = \frac{J_m(z)\cos(m\pi) - J_{-m}(z)}{\sin(m\pi)}$$ (A.3)

with $z \in \mathbb{Z}$ and $m \in \mathbb{R}$. $J_m(z)$ is the Bessel function in (A.1).

▷ The modified Bessel function of the first kind [AS64]:

$$I_m(z) = \left(\frac{z}{2}\right)^m \sum_{k=0}^{\infty} \frac{(z^2/4)^k}{k!\Gamma(m+k+1)},$$ (A.4)

with $z \in \mathbb{Z}$ and $m \in \mathbb{R}$.

▷ The modified Bessel function of the second kind [AS64]:

$$K_m(z) = \left(\frac{\pi}{2}\right) \frac{I_{-m}(z) - I_m(z)}{\sin(m\pi)} \tag{A.5}$$

with $z \in \mathbb{Z}$ and $m \in \mathbb{R}$. $I_m(z)$ is the modified Bessel function of the first kind in (A.4).

▷ Marcum's Q-function of the first order [Shn89]:

$$Q(a,b) = \int_b^\infty x \exp\left(-\frac{(x^2 + a^2)}{2}\right) I_0(ax)\mathrm{d}x, \tag{A.6}$$

where $a, b \in \mathbb{Z} \geq 0$. $I_0(z)$ is the modified Bessel function of the first kind with $m = 0$ in (A.4).

B

Generator Polynomials of Pseudo-random Sequences

Table B.1 lists the generator polynomial coefficients that can be used to generate pseudo-random sequences up to order 25, as explained in chapter 3.3.1. A detailed discussion on the generation and properties of pseudo-random sequences can be found in [MS76, Gol67].

Table B.1: Primitive polynomial coefficients $(c_0 \cdots c_{n_s})$

Degree (n_s)	Coefficients GF2	Coefficients GF4
2	111	112
3	1011	1123
4	10011	11333
5	100101	113202
6	1000011	1000113
7	10000011	11230312
8	101100011	112211103
9	1000010001	1010213013
10	10000001001	10113013233
11	100000000101	101021210223
12	1000010011001	1000001001113
13	10000000011011	10103020013013
14	101100000000011	101030200120133
15	1000000000000011	1000011110303132
16	10010000000101001	10010031120102023
17	100000000000001001	100010102100013023
18	1000000000010000001	1000110120212210032
19	10000000000001100011	11221101032030010223
20	100000000000000001001	113310122221001211003
21	1000000000000000000101	1123020033303101100232
22	10000000000000000000011	10113113301303022210103
23	100000000000000000100001	110103121020322330130223
24	1000000000000000000011011	100010002011211010202222012
25	10000000000000000000001001	1133013130133133212012021302

Degree (n_s)	Coefficients GF8	Coefficients GF16
2	165	17B
3	1434	1D5A
4	14514	16727
5	104412	11DB1E
6	1411453	1CEAB43
7	16716035	111194FE
8	102671777	11A183FE7
9	1411077155	1166248FE7
10	10006046723	1A1254957BB
11	161725255752	1C84D9899209
12	1256437353477	1D87EB7AEEAF5
13	10006246316747	10C15A4C45745E
14	161747620012627	11BAF48705F0F05
15	1656655116503744	17733278DF0C73DA
16	12112337764707775	1A6A58F71BB67F2F5
17	121320413751241053	17DDC8CAFDCFC6D47A
18	1270252454760330226	1171954BEF2C737247E
19	16153344340650534534	110CF2859573C7337387
20	121517405426344507037	1CE77CA3A0734CF0F7529
21	1000206210562176313043	1DE4C0368A9D2CCC3E63E5
22	14365275745177026067204	1D4B3B7632A1BB6332E59D3
23	127203402072501456254202	1CF1CF889712A67ACE2B9FCA
24	1004205135673603116470662	111133EE01F85D138909D9E4B
25	16342306345523706035535143	1170F3EEBD5C4A2B54D1E07FA3

Demodulation of stereo-multiplexed DQPSK signals

The following appendix details the algebraic procedure used to obtain equations (4.45) and (4.46). For this purpose, we recall equations (4.43) and (4.44), which represent the electrical currents at the output of the photodiodes of the in-phase and quadrature branches of the DQPSK receiver. In general, they can be written as:

$$I_i(t) = \tfrac{1}{2}\Re\{E(t)E^*(t - T_0)e^{j\psi_i}\}. \tag{C.1}$$

Observe that $\psi_i = \phi_i - \omega_c T_0$, where $\phi_i = \pi/4$ when i represents the in-phase branch of the receiver and $\phi_i = -\pi/4$ when i represents the quadrature branch of the receiver.

For a more compact notation, the following variables are introduced:

$$A_a = A_a(t), \tag{C.2}$$
$$A_b = A_b(t), \tag{C.3}$$
$$A'_a = A_a^*(t - T_0), \tag{C.4}$$
$$A'_b = A_b^*(t - T_0) \tag{C.5}$$

which, in addition to equation (4.42), yield the following expressions for $E(t)$ and $E^*(t - T_0)$

respectively:

$$E(t) = \frac{1}{\sqrt{2}} \left(\frac{A_a - A_b}{2} \cdot e^{j2\pi\frac{\Delta f_s}{2}t} + \frac{A_a + A_b}{2} \cdot e^{-j2\pi\frac{\Delta f_s}{2}t} \right) \cdot je^{j\psi} \cdot e^{j\omega_c t}, \tag{C.6}$$

$$E^*(t - T_0) = \frac{1}{\sqrt{2}} \left(\frac{A_a' - A_b'}{2} \cdot e^{-j2\pi\frac{\Delta f_s}{2}(t-T_0)} + \frac{A_a' + A_b'}{2} \cdot e^{j2\pi\frac{\Delta f_s}{2}(t-T_0)} \right) \cdot je^{-j\psi} \cdot e^{-j\omega_c(t-T_0)}. \tag{C.7}$$

Notice that $\Delta f_s = 2R_s = 2/T_0$ and therefore $e^{\pm j2\pi\frac{\Delta f_s}{2}(t-T_0)} = e^{\pm j2\pi\frac{\Delta f_s}{2}t}$.

Observe that the product $E(t)E^*(t - T_0)$ in (C.1) gives rise to three main contributing terms to the electrical current $I_i(t)$, one located at $f = 0$ and the other two oscillating at $f = \pm\Delta f_s$. We introduce therefore the baseband complex signals $A^0(t)$, $A^+(t)$ and $A^-(t)$, which are related to the output electrical current by

$$I_i(t) = \frac{1}{16}\Re\{A^0(t)e^{j\phi_i} + A^+(t)e^{j(2\pi\Delta f_s t+\phi_i)} + A^-(t)e^{-j(2\pi\Delta f_s t-\phi_i)}\}, \tag{C.8}$$

and are given by

$$A^0(t) = (A_a - A_b)(A_a' - A_b') + (A_a + A_b)(A_a' + A_b')$$
$$= 2(A_a A_a' + A_b A_b'), \tag{C.9}$$
$$A^+(t) = (A_a - A_b)(A_a' + A_b')$$
$$= A_a A_a' + A_a A_b' - A_a' A_b - A_b A_b', \tag{C.10}$$
$$A^-(t) = (A_a + A_b)(A_a' - A_b')$$
$$= A_a A_a' - A_a A_b' + A_a' A_b - A_b A_b'. \tag{C.11}$$

The real part of the terms in equations(C.9)-(C.11) which multiply the complex exponential waves at frequencies $f = 0$ and $f = \pm\Delta f_s$ in (C.8) can be stated explicitly as follows:

Firstly, for $f = 0$,

$$\Re\{A_a A_a' e^{j\phi_i}\} = |A_a|^2 \cos(\Delta\varphi_a + \phi_i), \tag{C.12}$$
$$\Re\{A_b A_b' e^{j\phi_i}\} = |A_b|^2 \cos(\Delta\varphi_b + \phi_i). \tag{C.13}$$

Secondly, for $f = +\Delta f_s$,

$$
\begin{aligned}
\Re\{A_a A_a' e^{j(2\pi\Delta f_s t + \phi_i)}\} =& |A_a|^2 \cos(2\pi\Delta f_s t + \Delta\varphi_a + \phi_i) \\
=& |A_a|^2 \cos(\Delta\varphi_a + \phi_i)\cos(2\pi\Delta f_s t) - \\
& |A_a|^2 \sin(\Delta\varphi_a + \phi_i)\sin(2\pi\Delta f_s t),
\end{aligned} \tag{C.14}
$$

$$
\begin{aligned}
\Re\{A_b A_b' e^{j(2\pi\Delta f_s t + \phi_i)}\} =& |A_a|^2 \cos(2\pi\Delta f_s t + \Delta\varphi_b + \phi_i) \\
=& |A_a|^2 \cos(\Delta\varphi_b + \phi_i)\cos(2\pi\Delta f_s t) - \\
& |A_a|^2 \sin(\Delta\varphi_b + \phi_i)\sin(2\pi\Delta f_s t),
\end{aligned} \tag{C.15}
$$

$$
\begin{aligned}
\Re\{A_a A_b' e^{j(2\pi\Delta f_s t + \phi_i)}\} =& |A_a A_b| \cos(2\pi\Delta f_s t + \Delta\varphi_{ab} + \phi_i) \\
=& |A_a A_b| \cos(\Delta\varphi_{ab} + \phi_i)\cos(2\pi\Delta f_s t) - \\
& |A_a A_b| \sin(\Delta\varphi_{ab} + \phi_i)\sin(2\pi\Delta f_s t),
\end{aligned} \tag{C.16}
$$

$$
\begin{aligned}
\Re\{A_a' A_b e^{j(2\pi\Delta f_s t + \phi_i)}\} =& |A_a A_b| \cos(2\pi\Delta f_s t + \Delta\varphi_{ba} + \phi_i) \\
=& |A_a A_b| \cos(\Delta\varphi_{ba} + \phi_i)\cos(2\pi\Delta f_s t) - \\
& |A_a A_b| \sin(\Delta\varphi_{ba} + \phi_i)\sin(2\pi\Delta f_s t).
\end{aligned} \tag{C.17}
$$

And finally, for $f = -\Delta f_s$,

$$
\begin{aligned}
\Re\{A_a A_a' e^{-j(2\pi\Delta f_s t - \phi_i)}\} =& |A_a|^2 \cos(-2\pi\Delta f_s t + \Delta\varphi_a + \phi_i) \\
=& |A_a|^2 \cos(\Delta\varphi_a + \phi_i)\cos(2\pi\Delta f_s t) + \\
& |A_a|^2 \sin(\Delta\varphi_a + \phi_i)\sin(2\pi\Delta f_s t),
\end{aligned} \tag{C.18}
$$

$$
\begin{aligned}
\Re\{A_b A_b' e^{-j(2\pi\Delta f_s t - \phi_i)}\} =& |A_a|^2 \cos(-2\pi\Delta f_s t + \Delta\varphi_b + \phi_i) \\
=& |A_a|^2 \cos(\Delta\varphi_b + \phi_i)\cos(2\pi\Delta f_s t) + \\
& |A_a|^2 \sin(\Delta\varphi_b + \phi_i)\sin(2\pi\Delta f_s t),
\end{aligned} \tag{C.19}
$$

$$
\begin{aligned}
\Re\{A_a A_b' e^{-j(2\pi\Delta f_s t - \phi_i)}\} =& |A_a A_b| \cos(-2\pi\Delta f_s t + \Delta\varphi_{ab} + \phi_i) \\
=& |A_a A_b| \cos(\Delta\varphi_{ab} + \phi_i)\cos(2\pi\Delta f_s t) + \\
& |A_a A_b| \sin(\Delta\varphi_{ab} + \phi_i)\sin(2\pi\Delta f_s t),
\end{aligned} \tag{C.20}
$$

$$
\begin{aligned}
\Re\{A_a' A_b e^{-j(2\pi\Delta f_s t - \phi_i)}\} =& |A_a A_b| \cos(-2\pi\Delta f_s t + \Delta\varphi_{ba} + \phi_i) \\
=& |A_a A_b| \cos(\Delta\varphi_{ba} + \phi_i)\cos(2\pi\Delta f_s t) + \\
& |A_a A_b| \sin(\Delta\varphi_{ba} + \phi_i)\sin(2\pi\Delta f_s t).
\end{aligned} \tag{C.21}
$$

In equations (C.12)-(C.21), the trigonometric identity $\cos(\alpha + \beta) = \cos\alpha\cos\beta - \sin\alpha\sin\beta$ was used. Observe that it is assumed that $|A_a|^2 = |A_a'|^2$ and $|A_b|^2 = |A_b'|^2$. Additionally,

the following substitutions were carried out:

$$\Delta\varphi_a = \varphi_a(t) - \varphi_a(t - T_0), \tag{C.22}$$
$$\Delta\varphi_b = \varphi_b(t) - \varphi_b(t - T_0), \tag{C.23}$$
$$\Delta\varphi_{ab} = \varphi_a(t) - \varphi_b(t - T_0), \tag{C.24}$$
$$\Delta\varphi_{ba} = \varphi_b(t) - \varphi_a(t - T_0). \tag{C.25}$$

In conclusion, it is possible to observe that the output electrical current $I_i(t)$ has a base band component $I_i^{\text{BB}}(t)$ and an intermediate frequency component $I_i^{\text{IF}}(t)$ that, using (C.12)-(C.21), can be written as

$$
\begin{aligned}
I_i^{\text{BB}}(t) =& \tfrac{1}{16}\Re\{A^0(t)e^{j\phi_i}\} \\
=& \tfrac{1}{8}\big(|A_a|^2 \cos(\Delta\varphi_a + \phi_i) + |A_b|^2 \cos(\Delta\varphi_b + \phi_i)\big),
\end{aligned}
\tag{C.26}
$$

$$
\begin{aligned}
I_i^{\text{IF}}(t) =& \tfrac{1}{16}\Re\{A^+(t)e^{j(2\pi\Delta f_s t+\phi_i)} + A^-(t)e^{-j(2\pi\Delta f_s t-\phi_i)}\} \\
=& \tfrac{1}{8}\big(\big(|A_a|^2 \cos(\Delta\varphi_a + \phi_i) - |A_b|^2 \cos(\Delta\varphi_b + \phi_i)\big) \cdot \cos(2\pi\Delta f_s t) \\
& - \big(|A_a A_b| \sin(\Delta\varphi_{ab} + \phi_i) - |A_a A_b| \sin(\Delta\varphi_{ba} + \phi_i)\big) \cdot \sin(2\pi\Delta f_s t)\big).
\end{aligned}
\tag{C.27}
$$

Thus, $I_i(t) = I_i^{\text{BB}}(t) + I_i^{\text{IF}}(t)$ which, in turn, corresponds to (4.45) when $\phi_i = \pi/4$ and to (4.46) when $\phi_i = -\pi/4$.

D

Square-law Detection of Pre-coded FDM Signals

Stereo multiplexing has been proposed as a way to simultaneously detect and demodulate two optical carriers. It is based on the linear pre-coding the information symbols of the sub-carriers. So naturally, it is of interest to determine if such a technique can be used with a higher number of optical carriers. Particularly, the following appendix presents a novel mathematical framework which is useful to model the intermodulation products that result from the nonlinear operation of a square-law detector over linearly pre-coded frequency division multiplexed (FDM) signals.

D.1   Intensity modulation with real pre-coding

A frequency division multiplexed optical signal composed of M linearly pre-coded sub-carriers can be written as

$$\hat{x}(t) = \sum_{m=0}^{M-1} \mathbf{p}_m \mathbf{x} e^{j2\pi m \Delta f_s t}, \tag{D.1}$$

where $\mathbf{x} = (x_0(t), x_1(t), \cdots, x_{M-1}(t))^{\mathrm{T}}$ is a column vector composed of intensity-only modulated signals, i.e., $x_m(t) = |x_m(t)|$. The $1 \times M$ vector $\mathbf{p}_m$ is the mth row of the square matrix $\mathbf{P}$. The FDM signal in(D.1) can be written in matrix form as $\hat{\mathbf{x}} = \mathbf{P}\mathbf{x}$. The mth row of $\hat{\mathbf{x}}$ represents the modulation of the Mth subcarrier, separated in frequency from the first sub-carrier by $m\Delta f_s$. Firstly, assume $\mathbf{P}$ as a real-valued matrix with non-zero rows and columns.

After some algebraic details, the resulting electrical signal after square-law detection

$y(t) = |\hat{x}(t)|^2$, can be written as

$$y(t) = \mathbf{x}^\mathrm{T}\mathbf{H}_0\mathbf{x} + 2\sum_{m=1}^{M-1} \mathbf{x}^\mathrm{T}\mathbf{H}_m\mathbf{x}\cos(2\pi m\Delta f_s t), \tag{D.2}$$

with

$$\mathbf{H}_m = \mathbf{P}^\mathrm{T}\mathcal{H}_m\mathbf{P}, \tag{D.3}$$

where $\mathcal{H}_m$ is an $M \times M$ matrix () with elements

$$h_{m,ij} = \begin{cases} 1 & , i = j - m \\ 0 & , \text{else.} \end{cases} \tag{D.4}$$

Take for example the case where $M = 2$ and no pre-coding is applied, i.e., $\mathbf{P}$ is the identity matrix. The resultant matrices are given by

$$\mathcal{H}_0 = \begin{pmatrix} 1 & 0 \\ 0 & 1 \end{pmatrix}, \mathcal{H}_1 = \begin{pmatrix} 0 & 1 \\ 0 & 0 \end{pmatrix}, \tag{D.5}$$

which, according to (D.3) results in

$$\mathbf{H}_0 = \begin{pmatrix} 1 & 0 \\ 0 & 1 \end{pmatrix}, \mathbf{H}_1 = \begin{pmatrix} 0 & 1 \\ 0 & 0 \end{pmatrix}. \tag{D.6}$$

Using (D.6) and dropping the time dependence of the variables for compact notation, (D.2) yields

$$y(t) = x_0^2 + x_1^2 + 2x_0 x_1 \cos(2\pi\Delta f_s t). \tag{D.7}$$

Clearly, intermodulation terms appear in the pass-band component of $y(t)$. The principle of stereo multiplexing is to choose a suitable matrix $\mathbf{P}$ such that intermodulation between sub-carriers does not occur. This is true when $\mathbf{H}_m$ fulfills $\mathbf{H}_m + \mathbf{H}_m^\mathrm{T} = \mathbf{D}_m, \forall m$, where $\mathbf{D}_m$ is a diagonal matrix. Using (D.3), this condition can also be written as

$$\mathbf{P}^\mathrm{T}\left(\mathcal{H}_m + \mathcal{H}_m^\mathrm{T}\right)\mathbf{P} = \mathbf{D}_m. \tag{D.8}$$

Take, for example, a stereo-multiplexed signal. The pre-coding matrix in this case is

$$\mathbf{P} = \frac{1}{\sqrt{2}}\begin{pmatrix} 1 & 1 \\ 1 & -1 \end{pmatrix}. \tag{D.9}$$

Equation (D.3) yields the matrices

$$\mathbf{H}_0 = \begin{pmatrix} 1 & 0 \\ 0 & 1 \end{pmatrix}, \mathbf{H}_1 = \frac{1}{2}\begin{pmatrix} 1 & 1 \\ -1 & -1 \end{pmatrix}, \tag{D.10}$$

which fulfill (D.8). The resulting electrical signal is thus,

$$y(t) = (x_0^2 + x_1^2) + (x_0^2 - x_1^2)\cos(2\pi\Delta f_s t). \tag{D.11}$$

Observe that, since both matrices in (D.10) comply with (D.8), the resulting photo-detected signal in (D.11) is free of intermodulation products. There are M^2 elements in $\mathbf{P}$ and $M^2(M-1)/2$ conditions to fulfill in (D.8). Therefore, the maximum size of the pre-coding matrix capable of diagonalizing $\mathbf{H}_m + \mathbf{H}_m^{\mathrm{T}}, \forall m$ yields $M \leq 3$.

However, it is easy to show that for $M = 3$, such a pre-coding matrix does not exist. Equation (D.8) implies that $\mathbf{P}$ should, at least, simultaneously diagonalize the matrices $\mathcal{H}_{s,1} = \mathcal{H}_1 + \mathcal{H}_1^{\mathrm{T}}$ and $\mathcal{H}_{s,2} = \mathcal{H}_2 + \mathcal{H}_2^{\mathrm{T}}$. This is only possible if these two matrices share a common *eigenspace*, in which case $\mathbf{P}$ correspond to the matrix of common eigenvectors. This condition is fulfilled only if $\mathcal{H}_{s,1}$ commutes[1] with $\mathcal{H}_{s,2}$, which is not the case.

D.2 Intensity modulation with complex pre-coding

If $\mathbf{P}$ is allowed to have complex elements, i.e., $\mathbf{P} = \mathbf{U} + j\mathbf{V}$ with $\mathbf{U}, \mathbf{V} \in \mathbb{R}^{M \times M}$, then, the received electrical signal has power in both, in-phase and quadrature components. In this case, it can be written as

$$y(t) = \mathbf{x}^{\mathrm{T}}\mathbf{H}_{I,0}\mathbf{x} + 2\sum_{m=1}^{M-1} \mathbf{x}^{\mathrm{T}}\mathbf{H}_{I,m}\mathbf{x}\cos(2\pi m\Delta f_s t) + \mathbf{x}^{\mathrm{T}}\mathbf{H}_{Q,m}\mathbf{x}\sin(2\pi m\Delta f_s t), \quad \text{(D.12)}$$

where

$$\mathbf{H}_{I,m} = \mathbf{U}^{\mathrm{T}}\mathcal{H}_m\mathbf{U} + \mathbf{V}^{\mathrm{T}}\mathcal{H}_m\mathbf{V}, \quad \text{(D.13)}$$

$$\mathbf{H}_{Q,m} = \mathbf{V}^{\mathrm{T}}\mathcal{H}_m\mathbf{U} - \mathbf{U}^{\mathrm{T}}\mathcal{H}_m\mathbf{V}. \quad \text{(D.14)}$$

Now, two matrices $\mathbf{U}$ and $\mathbf{V}$ can be used in order to diagonalize M of the $2M-1$ resulting matrices $\mathbf{H}_{I,m} + \mathbf{H}_{I,m}^{\mathrm{T}}$ and $\mathbf{H}_{Q,m} + \mathbf{H}_{Q,m}^{\mathrm{T}}$. By doing so, the intermodulation products will fall in the remaining frequency/quadrature components.

For example, take the complex pre-coding matrix

$$\mathbf{P} = \frac{1}{\sqrt{8}}\begin{pmatrix} 1 & 1 & 1 \\ 0 & 0 & 2 \\ -1 & -1 & 1 \end{pmatrix} + \frac{j}{\sqrt{8}}\begin{pmatrix} -1 & -1 & -1 \\ -2 & 2 & 0 \\ -1 & -1 & 1 \end{pmatrix} \quad \text{(D.15)}$$

Equations (D.13) and (D.14) yield: $\mathbf{H}_{I,0}$ equals to the identity matrix and

$$\mathbf{H}_{I,1} = \frac{1}{2}\begin{pmatrix} 1 & 0 & 0 \\ 0 & -1 & 0 \\ 0 & 0 & 1 \end{pmatrix}, \mathbf{H}_{Q,1} = \frac{1}{2}\begin{pmatrix} 1 & 0 & 0 \\ 0 & -1 & 0 \\ 0 & 0 & -1 \end{pmatrix}, \quad \text{(D.16)}$$

$$\mathbf{H}_{I,2} = \frac{1}{2}\begin{pmatrix} 0 & 0 & 0 \\ 0 & 0 & 0 \\ 0 & 0 & 0 \end{pmatrix}, \mathbf{H}_{Q,2} = \frac{1}{4}\begin{pmatrix} 1 & 1 & -1 \\ 1 & 1 & -1 \\ 1 & 1 & -1 \end{pmatrix}. \quad \text{(D.17)}$$

---

[1]Two matrices $\mathbf{A}$ and $\mathbf{B}$ are said to commute if $\mathbf{AB} = \mathbf{BA}$.

Observe that, by pre-coding with (D.15), $\mathbf{H}_I$ and $\mathbf{H}_Q$, representing the baseband and first pass-band respectively, fulfill (D.8). On the other hand, $\mathbf{H}_{Q,2}$ does not, which results in one intermodulation product $x_0 x_1$ to appear in the quadrature component of the electrical signal located at $f = 2\Delta f_s$. Additionally, the pre-coding deprives the in-phase component at this frequency of electrical power.

The use of three sub-carriers in combination with complex pre-coding is cumbersome in practice since careful control of the amplitude and phase of three phased-locked FDM optical signals should be guaranteed. Notice that a complex pre-coding matrix offers $2M^2$ elements to fulfill $M^2(M-1)/2$ conditions thus, increasing the maximum size of a potentially effective pre-coding matrix to $M \leq 5$. Because of its complexity and since it falls out of the scope of this thesis, the simultaneous diagonalization of a subset of M matrices $\mathbf{H}_{I,m} + \mathbf{H}_{I,m}^\mathrm{T}$ and $\mathbf{H}_{Q,m} + \mathbf{H}_{Q,m}^\mathrm{T}$, when M equals four and five, is left as an open problem for the sake of mathematical interest.

D.3   Quadrature-amplitude modulation with complex pre-coding

If the phase and the amplitude of the FDM sub-carriers are modulated, a general expression for the received photo-detected current can be obtained by expressing the FDM optical signal in matrix notation as

$$\hat{\mathbf{x}} = \mathbf{P}\boldsymbol{\Phi}\mathbf{x}, \tag{D.18}$$

where $\mathbf{P} = \mathbf{U} + j\mathbf{V}$ with $\mathbf{U}, \mathbf{V} \in \mathbb{R}^{M \times M}$, $\mathbf{x}$ is a column vector with real elements representing the amplitude of the sub-carriers and $\boldsymbol{\Phi}$ is a diagonal $M \times M$ matrix with elements in the main diagonal representing the phase information of the sub-carriers, i.e., $\boldsymbol{\Phi} = \mathfrak{D}\{(e^{j\phi_0}, e^{j\phi_1}, \cdots, e^{j\phi_{M-1}})^\mathrm{T}\}$. In rectangular form the phase modulation matrix can be rewritten as $\boldsymbol{\Phi} = \mathbf{C} + j\mathbf{S}$ with $\mathbf{C}, \mathbf{S} \in \mathbb{R}^{M \times M}$, such that, according to (D.18), $\hat{\mathbf{x}}$ can be expressed as a symbol-wise complex pre-coded intensity modulated signal:

$$\hat{\mathbf{x}} = (\mathbf{U} + j\mathbf{V})(\mathbf{C} + j\mathbf{S})\mathbf{x} \tag{D.19}$$
$$= ((\mathbf{UC} - \mathbf{VS}) + j(\mathbf{US} + \mathbf{VC}))\,\mathbf{x}, \tag{D.20}$$

and, therefore, equations (D.12)-(D.14) can be used to obtain the photo-detected current

$$y(t) = \mathbf{x}^\mathrm{T}\hat{\mathbf{H}}_{I,0}\mathbf{x} + 2\sum_{m=1}^{M-1}\mathbf{x}^\mathrm{T}\hat{\mathbf{H}}_{I,m}\mathbf{x}\cos(2\pi m\Delta f_s t) + \mathbf{x}^\mathrm{T}\hat{\mathbf{H}}_{Q,m}\mathbf{x}\sin(2\pi m\Delta f_s t), \tag{D.21}$$

with

$$\hat{\mathbf{H}}_{I,m} = \mathbf{C}^\mathrm{T}\mathbf{H}_{I,m}\mathbf{C} + \mathbf{S}^\mathrm{T}\mathbf{H}_{I,m}\mathbf{S} + \mathbf{C}^\mathrm{T}\mathbf{H}_{Q,m}\mathbf{S} + \mathbf{S}^\mathrm{T}\mathbf{H}_{Q,m}\mathbf{C}, \tag{D.22}$$
$$\hat{\mathbf{H}}_{Q,m} = \mathbf{C}^\mathrm{T}\mathbf{H}_{Q,m}\mathbf{C} + \mathbf{S}^\mathrm{T}\mathbf{H}_{Q,m}\mathbf{S} - \mathbf{C}^\mathrm{T}\mathbf{H}_{I,m}\mathbf{S} + \mathbf{S}^\mathrm{T}\mathbf{H}_{I,m}\mathbf{C}, \tag{D.23}$$

where $\mathbf{H}_{I,m}$ and $\mathbf{H}_{Q,m}$ are defined by (D.13) and (D.14), respectively.

For quadrature-amplitude modulated (QAM) signals, the information is encoded on the vectors $\mathbf{x}_I = \mathbf{Cx}$ and $\mathbf{x}_Q = \mathbf{Sx}$, and unless phase-to-intensity conversion is performed before photo-detection (as in stereo DQPSK systems, see ch. 4.1.6), strong mixing between $\mathbf{x}_I$ and $\mathbf{x}_Q$ occurs and the original information cannot be retrieved. In such a case, it is accustomed to generate and transmit one unmodulated carrier within the whole FDM signal, and to deprive some sub-carriers of optical power, see [LDA06, AL06]. The unmodulated carrier acts as a local oscillator (LO) when photo-detection occurs allowing $\mathbf{x}_I$ and $\mathbf{x}_Q$ to be coherently detected. The unwanted intermodulation and intensity products between the rest of the sub-carriers fall in unused frequency slots of the received electrical signal. Such a system can be conveniently modeled and analyzed using (D.21).

In other systems, e.g. [Hew07], *all* sub-carriers of an FDM signal contain optical power and are modulated, except for one that acts as LO. Unwanted intermodulation terms appear as interference to the (self-) coherently demodulated $\mathbf{x}_I$ and $\mathbf{x}_Q$, but the power ratio between signal and interference is enlarged by increasing the power of the unmodulated sub-carrier. In turn, this deteriorates the tolerance to noise. The expression derived in (D.21) can be used to calculate analytically the power of the intermodulation products for a certain pre-coding matrix, and to choose $\mathbf{P}$ such that the signal-to-interference ratio is optimized. This falls out of the scope of this thesis and is, therefore, left as an open problem.

E

Notation, Symbols and Abbreviations

Mathematical notation

$\star$	convolution
$\cdot$	vector dot product
$\times$	vector cross product
∇	nabla operator
$(\,\cdot\,)^{\mathrm{T}}$	transpose of a vector
$\|\mathbf{x}\|$	Euclidean distance
$\mathbf{H}^{-1}$	inverse of a matrix
$\mathfrak{D}\{\mathbf{x}\}$	diagonal matrix with vector $\mathbf{x}$ in the main diagonal
$\Re\{x\}$	real part of argument
$\Im\{x\}$	imaginary part of argument
x^{*}	conjugate of argument
$\ln(x)$	natural logarithm
$\log(x)$	logarithm to base 10
$\mathrm{sgn}\,(x)$	sign of x
$\mathrm{sinc}\,(x)$	sinus cardinalis, $\mathrm{sinc}\,(x) = \sin(\pi x)/(\pi x)$
δ_{kl}	Kronecker delta function
$\delta(\,\cdot\,)$	Dirac delta function
$|x|$	absolute value of argument
$\lceil x \rceil$	ceiling of argument

$\mathfrak{F}\{x(t)\}$	Fourier transform
$\mathfrak{F}^{-1}\{x(t)\}$	inverse Fourier transform
J_m	Bessel function with order m
N_m	Neumann function with order m
I_m	modified Bessel function of the first kind with order m
K_m	modified Bessel function of the second kind with order m
$Q(\,\cdot\,,\,\cdot\,)$	first order Marcum's Q function
Γ	gamma function
$\Phi(\,\cdot\,)$	normal cumulative distribution function
$\mathcal{E}\{x\}$	expectation of a random variable x
$\mathrm{Var}\{x\}$	variance of a random variable x
$\mathcal{P}(x)$	probability of occurrence of event x
p_{Y_k}	probability density function of variable Y_k
$x \sim \mathcal{N}(\mu, \sigma^2)$	the random variable x is Gauss distributed with mean μ and variance σ^2

Physical constants

c	speed of light in free space	$2.99792458 \cdot 10^8 \,\mathrm{m\,s^{-1}}$
e	base of the natural logarithm	2.718281828
ε_0	free space permittivity	$8.8541878 \cdot 10^{-12} \,\mathrm{A\,s\,V^{-1}\,m^{-1}}$
h	Planck constant	$6.62606896 \cdot 10^{-34} \,\mathrm{W\,s^2}$
j	imaginary unit	$\sqrt{-1}$
μ_0	free space permeability	$4\pi \cdot 10^{-7} \,\mathrm{V\,s\,A^{-1}\,m^{-1}}$
π		3.14159265
Z_0	impedance of free space	$\sqrt{\mu_0/\varepsilon_0} \approx 376.73 \,\Omega$

List of Symbols

α	attenuation	m^{-1} or dB/km
α_c	MZM linear frequency chirp parameter	
α_{DCF}	DCF attenuation	m^{-1} or dB/km
α_{H}	Hamming pulse/window tuning parameter	
α_{SSMF}	SSMF attenuation	m^{-1} or dB/km
β	propagation constant	m^{-1}
β_m	m^{th} order coefficient in Taylor series expansion of $\beta(\omega)$ at $\omega = \omega_c$	$\mathrm{s}^m\,\mathrm{m}^{-1}$
$\beta_m^{(k)}$	m^{th} order coefficient in Taylor series expansion of $\beta(\omega)$ at $\omega = \omega_k$	$\mathrm{s}^m\,\mathrm{m}^{-1}$
β_r	roll-off factor	
β_x, β_y	propagation constant in x/y polarization	m^{-1}
$\Delta\beta$	phase matching coefficient	m^{-1}
γ	nonlinear fiber parameter	$\mathrm{W}^{-1}\,\mathrm{m}^{-1}$
γ_{DCF}	DCF nonlinear fiber parameter	$\mathrm{W}^{-1}\,\mathrm{m}^{-1}$
γ_k	nonlinear fiber parameter at wavelength λ_k	$\mathrm{W}^{-1}\,\mathrm{m}^{-1}$
γ_r	nonlinear fiber parameter at reference wavelength λ_r	$\mathrm{W}^{-1}\,\mathrm{m}^{-1}$
γ_{SSMF}	SSMF nonlinear fiber parameter	$\mathrm{W}^{-1}\,\mathrm{m}^{-1}$
γ_{th}	decision threshold	A
ε_{i}	positive real number at iteration i of the GOA	
$\varepsilon_{\mathrm{NL}}$	first order perturbation constant	
$\boldsymbol{\varepsilon}_r$	relative permittivity tensor	
$\tilde{\varepsilon}_r$	relative permittivity (frequency domain)	
$\hat{\varepsilon}_r$	perturbed relative permittivity (frequency domain)	
ζ	normalized length variable	
η	FWM efficiency	
η'	FWM efficiency altered by SSF method	
η_i	mean square variation of f as $\boldsymbol{x}$ changes, at iteration i	
$\hat{\eta}_i$	maximum likelihood estimator of η_i	
κ	coupler splitting factor	
$\kappa(\omega)$	separation constant	m^{-2}
λ	wavelength	m
λ_f, λ_l	first and last wavelength within a WDM comb	m
λ_k	wavelength of kth channel within a WDM comb	m
λ_r	reference wavelength	m
$\mu_{f,k}(\boldsymbol{x})$	mean of f in simplex k at $\boldsymbol{x}$	
$\Delta\nu$	laser linewidth	Hz
$\Pi(t)$	rectangular window (time domain)	

ρ	radial cylindrical coordinate	m
ρ_f	free charge density	$\mathrm{A\,s\,m^{-3}}$
σ_{PN}^2	phase noise variance	
σ_{n}^2	AWGN variance	W
$\sigma_{f,k}^2(\boldsymbol{x})$	variance of f in simplex k at $\boldsymbol{x}$	
τ	delay of delay line interferometer	s
τ	normalized time variable	
$\Delta\tau$	differential group delay	s
ϕ	angular cylindrical coordinate	
Φ_{ASE}	single-sided PSD per polarization of ASE noise	$\mathrm{W\,Hz^{-1}}$
$\Phi_{\mathrm{ASE}}^{\mathrm{total}}$	accumulated Φ_{ASE} after N spans	$\mathrm{W\,Hz^{-1}}$
ϕ_k	phase of kth symbol	
ϕ_{NL}	nonlinear phase shift	
$\phi_{\mathrm{NL}}^{\mathrm{max}}$	maximum nonlinear phase increment due to $\hat{N}(t)$ for NLPR method in SSF method	
$\phi_{\mathrm{NL,max}}^{\mathrm{total}}$	maximum total nonlinear phase shift	
ϕ_p	phase of pulse carver driving voltage with respect to clock	
$\Delta\varphi$	random phase variation due to phase noise	
$\Delta\varphi$	phase difference between consecutive symbols	
$\boldsymbol{\chi}^{(1)}$	linear material susceptibility tensor (time domain)	$\mathrm{s^{-1}}$
$\tilde{\boldsymbol{\chi}}^{(1)}$	linear material susceptibility tensor (frequency domain)	
$\chi_{kl}^{(1)}$	element of linear material susceptibility tensor (time domain)	$\mathrm{s^{-1}}$
$\tilde{\chi}_{kl}^{(1)}$	element of linear material susceptibility tensor (frequency domain)	
$\boldsymbol{\chi}^{(3)}$	cubic material susceptibility tensor (time domain)	$\mathrm{m^2\,V^{-2}\,s^{-3}}$
$\chi_{klmn}^{(3)}$	element of cubic material susceptibility tensor (time domain)	$\mathrm{m^2\,V^{-2}\,s^{-3}}$
$\boldsymbol{\chi}^{(n)}$	n^{th} order material susceptibility tensor	
ψ_I, ψ_Q	phase shift of delay line interferometer	
$\Psi_{I(t_k)}(\xi)$	moment generating function (ξ is the Laplace variable)	
ω	angular frequency variable	Hz
ω'	translated angular frequency variable	Hz
ω_c	angular frequency of optical carrier	Hz
ω_k	angular frequency of kth channel within a WDM comb	Hz
ω_{mn}	element of Ω (DFT matrix)	
$\Delta\omega_k$	angular frequency separation of kth channel with respect to center frequency of a WDM comb	Hz

$\mathbf{\Omega}$	DFT matrix	
a	fiber core radius	m
$a_{i,k}$	k^{th} bit of ith data sequence	
$\mathbf{a}_k$	vector of coefficients for mean of simplex k	
$a(z,t)$	dimensionless optical signal	
A_{eff}	effective mode area	m^2
A_R	amplitude ratio between constellation rings in ASK-DQPSK	
$\hat{A}, \hat{B}, \hat{C}, \hat{D}$	normalization functions	
$A(t)$	general base band signal (time domain)	
$\tilde{A}(f)$	Fourier transform of general base band signal (frequency domain)	
$A(z,t)$	normalized complex envelope of modulated optical field (time domain)	$\sqrt{\text{W}}$
$\tilde{A}(z,\omega)$	normalized complex envelope of modulated optical field (frequency domain)	$\sqrt{\text{W}}\,\text{s}$
$A_k(z,t)$	normalized complex envelope of the kth modulated optical field in a WDM comb with k^{th} propagation constant (time domain)	$\sqrt{\text{W}}$
$\tilde{A}_k(z,\omega)$	normalized complex envelope of kth modulated optical field in a WDM comb with k^{th} propagation constant (frequency domain)	$\sqrt{\text{W}}\,\text{s}$
$b_i(t)$	MZM driving i^{th} data signal	V
$\mathbf{B}$	Magnetic flux density	$\text{V}\,\text{s}\,\text{m}^{-2}$
B_e	one-sided 3-dB bandwidth of electrical filter	Hz
B_o	two-sided 3-dB bandwidth of optical filter	Hz
$B_{o,\text{eff}}$	effective optical filter bandwidth	Hz
$B_{o,\text{ref}}$	reference optical filter bandwidth	Hz
ΔB	excess bandwidth	
$\mathbf{C}_k$	symmetrical variance coefficients matrix of simplex k	
d	dimension of search space	
d_c	duty cycle	
$d_{i,k}$	differentially encoded k^{th} bit of ith sequence	
D	dispersion parameter	$\text{ps}\,\text{nm}^{-1}\,\text{km}^{-1}$
D_{SSMF}	SSMF dispersion parameter	$\text{ps}\,\text{nm}^{-1}\,\text{km}^{-1}$
D_{DCF}	DCF dispersion parameter	$\text{ps}\,\text{nm}^{-1}\,\text{km}^{-1}$
D_f, D_l	dispersion parameters of first and last wavelengths within a WDM comb	$\text{ps}\,\text{nm}^{-1}\,\text{km}^{-1}$
D_r	dispersion parameter at reference wavelength λ_r	$\text{ps}\,\text{nm}^{-1}\,\text{km}^{-1}$
$\mathcal{D}_{\text{pre}}$	amount of pre-compensation of dispersion	$\text{ps}\,\text{nm}^{-1}$

$\mathcal{D}_{\mathrm{res}}$	amount of residual dispersion per span	$\mathrm{ps\,nm^{-1}}$
$\mathcal{D}_{\mathrm{acc}}$	amount of accumulated dispersion at the end of the link	$\mathrm{ps\,nm^{-1}}$
$\mathcal{D}_{\mathrm{pos}}$	amount of post-compensation of dispersion	$\mathrm{ps\,nm^{-1}}$
$\hat{D}(t), \hat{D}_k(t)$	linear operator of the SSF method (for k^{th} channel in a WDM comb) (time domain)	$\mathrm{m^{-1}}$
$\hat{D}(\omega), \hat{D}_k(\omega)$	linear operator of the SSF method (for k^{th} channel in a WDM comb) (frequency domain)	$\mathrm{m^{-1}\,s}$
D_{PMD}	PMD value	$\mathrm{ps\,\sqrt{km}^{-1}}$
$\mathbf{D}$	Electric flux density	$\mathrm{A\,s\,m^{-2}}$
$\mathbf{D}_m$	diagonal matrix	
$\mathbf{e}$	polarization state vector	
e_k	bit error at sampling instant t_k	
$\mathbf{E}$	Electric field (time domain)	$\mathrm{V\,m^{-1}}$
$\tilde{\mathbf{E}}$	Electric field (frequency domain)	$\mathrm{V\,s\,m^{-1}}$
E_k	element of electric field (time domain)	$\mathrm{V\,m^{-1}}$
$\tilde{E}_k$	element of electric field (frequency domain)	$\mathrm{V\,s\,m^{-1}}$
$\underline{E}_x, \underline{E}_y$	complex slowly-varying envelope of x/y component of electric field (time domain)	$\mathrm{V\,m^{-1}}$
$\underline{\tilde{E}}_x, \underline{\tilde{E}}_y$	complex slowly-varying envelope of x/y component of electric field (frequency domain)	$\mathrm{V\,s\,m^{-1}}$
$E_0(\omega)$	amplitude of electric field (frequency domain)	$\mathrm{V\,s\,m^{-1}}$
$E_{\mathrm{in}}, E_{\mathrm{out}}$	input/ouput normalized electrical fields	$\sqrt{\mathrm{W}}$
$E_{\mathrm{I}}, E_{\mathrm{Q}}$	in-phase and quadrature incident normalized electrical fields	$\sqrt{\mathrm{W}}$
$E_x(t), E_y(t)$	normalized received electrical fields in x/y polarizations	$\sqrt{\mathrm{W}}$
f	frequency variable	Hz
f_c	frequency of optical carrier	Hz
f_n	frequency of nth subcarrier	Hz
f_p	pulse carver driving frequency	Hz
f_s	sampling rate	Hz
Δf	frequency separation	Hz
$\mathbf{f}$	vector of functional evaluations	
$\mathbf{f}_{\mathrm{r}}$	ranked vector of functional evaluations	
F	modal distribution	
F_n	noise figure	$\varnothing$ or dB
$F_{n,\mathrm{total}}$	total noise figure	$\varnothing$ or dB
$g(t), g(k)$	pulse	
G	gain	$\varnothing$ or dB
$G(x)$	generator polynomial in x over $\mathrm{GF}(2^r)$	
$\mathbf{H}$	magnetic field (time domain)	$\mathrm{A\,m^{-1}}$

$\tilde{\mathbf{H}}$	magnetic field (frequency domain)	$\mathrm{A\,s\,m^{-1}}$
H_k	element of magnetic field (time domain)	$\mathrm{A\,m^{-1}}$
$\tilde{H}_k$	element of magnetic field (frequency domain)	$\mathrm{A\,s\,m^{-1}}$
$H_e(f)$	electrical filter transfer function	
$H_o(f)$	optical filter transfer function	
$H_{o,\mathrm{TX}}(f), H_{o,\mathrm{RX}}(f)$	transmitter and receiver optical filter transfer functions or bandwidths	Hz
$H_{o,\mathrm{WDM}}(f)$	WDM demultiplexer transfer function or bandwidth	Hz
$H_I(f), H_Q(f)$	delay line interferometer transfer functions	
$H_{\mathrm{RC}}(f)$	electrical raised-cosine pulse shaping filter	
$H_{\mathrm{CD}}(f)$	chromatic dispersion transfer function	
I	intensity	$\mathrm{W\,m^{-2}}$
$I(t)$	photocurrent (time domain)	A
$I(t_k)$	sampled photocurrent (time domain)	A
$\mathbf{I}_n$	$n \times n$ identity matrix	
$\mathbf{J}$	electric current density	$\mathrm{A\,m^{-2}}$
k_0	free space angular wave number	$\mathrm{m^{-1}}$
k_1	fiber's core angular wave number	$\mathrm{m^{-1}}$
k_c	fiber's cladding angular wave number	$\mathrm{m^{-1}}$
$K(f_1, f_2)$	Hermitian kernel function	
K_{ml}	element of Hermitian matrix	
$\mathbf{K}$	Hermitian matrix	
L	fiber length	km
L_{eff}	effective length	m
L_{D}	dispersion length	m
L_{NL}	nonlinear length	m
L_{span}	fiber length per span	km
L_{SSMF}	SSMF fiber length per span	km
L_{DCF}	DCF fiber length per span	km
$L_{\mathrm{span}}^{\mathrm{opt}}$	optimum fiber length per span	km
L_{total}	length of fiber link	km
M_s	inverse DFT points	
$M_{\mathrm{A}}(i)$	moving average at iteration i	
$\mathbf{M}$	magnetic polarization	$\mathrm{V\,s\,m^{-2}}$
n	refractive index	
$\overline{n}$	normalized refractive index	
n_0	order of optical Gaussian filter	
n_1	fiber's core refractive index	
n_c	fiber's cladding refractive index	
n_2	nonlinear index coefficient	$\mathrm{m^2\,W^{-1}}$

n_s	number of shift registers	
n_{ph}	number of photons per symbol	
n_{sp}	EDFA's spontaneous emission factor	
$n_x(t), n_y(t)$	AWGN noise signals in x/y polarizations	$\sqrt{\mathrm{W}}$
N	number of concatenated spans in a multi-span transmission link	
N_b	number of boundary points for the GOA	
N_i	number of iterations set for the GOA	
N_{max}	maximum number of concatenated spans in a multi-span transmission link	
N_s	number of subcarriers / DFT points	
N_{seq}	length of sequence	
N_t	total number of functional evaluations at iteration i	
$\hat{N}(t), \hat{N}_k(t)$	nonlinear operator of the SSF method (for k^{th} channel in a WDM comb) (time domain)	m^{-1}
$\hat{N}(\omega), \hat{N}_k(\omega)$	nonlinear operator of the SSF method (for k^{th} channel in a WDM comb) (frequency domain)	$\mathrm{m}^{-1}\,\mathrm{s}$
ΔN	increment in number of spans	
$p(t)$	dimensionless train of pulses	
$p_k(z,t)$	k^{th} modulated pulse within a train of pulses	$\sqrt{\mathrm{W}}$
P	power	W or dBm
P_1	optical power of a logical one	W or dBm
P_{ASE}	average ASE noise power	W or dBm
P_{r}	power ratio	
P_s	receiver sensitivity	W or dBm
P_{sl}	power of the side-lobes of a Nyquist pulse	W or dBm
P_{sol}	soliton peak power	W or dBm
P_{SSMF}	SSMF input power	W or dBm
P_{DCF}	DCF input power	W or dBm
ΔP	power difference	dB
$\overline{\Delta P}^*$	mean optimum power difference	dB
$\mathbf{P}$	linear pre-coding matrix	
$\mathbf{p}_n$	n^{th} row of linear pre-coding matrix	
$\mathbf{P}$	material polarization (time domain)	$\mathrm{A\,s\,m}^{-2}$
$\tilde{\mathbf{P}}$	material polarization (frequency domain)	$\mathrm{A\,s^2\,m}^{-2}$
P_k	k^{th} element of material polarization (time domain)	$\mathrm{A\,s\,m}^{-2}$
$\tilde{P}_k$	k^{th} element of material polarization (frequency domain)	$\mathrm{A\,s^2\,m}^{-2}$
$\mathcal{P}_b$	bit error probability	
$\mathcal{P}_k$	probability to find a new optimum within simplex k	
r_{eff}	effective fiber core radius	m

$\mathbf{r}$	position vector	m
$\mathbf{r}_k$	k^{th} row of the $N_s \times N_s$ identity matrix	
R	responsivity of photodiode	A W^{-1}
R_s	symbol rate	S/s
$R_{\text{R}}(i)$	rank ratio at iteration i	
s_n	n^{th} subcarrier within one OFDM symbol	
S	dispersion slope parameter	$\text{ps nm}^{-2}\,\text{km}^{-1}$
S_r	dispersion slope parameter at reference wavelength λ_r	$\text{ps nm}^{-2}\,\text{km}^{-1}$
$S(z,t)$	complex slowly-varying envelope of modulated optical field (time domain)	V m^{-1}
$\tilde{S}(z,\omega)$	complex slowly-varying envelope of modulated optical field (frequency domain)	V s m^{-1}
$\mathcal{S}$	parameters search space	
$\mathcal{S}_k$	k^{th} simplex	
t	time variable	s
t'	local time	s
t_k	sampling instant	s
t_s	sampling time offset	s
T	signal duration	s
T_0	symbol/pulse duration	s
T_s	OFDM symbol duration	s
ΔT_{CD}	chromatic dispersion induced walk-off	s
$u(t), u_1(t), u_2(t)$	MZM driving voltage signals	V
$u(z,t), u(\zeta,\tau)$	dimensionless optical signal	
$U_k(z,t)$	normalized complex envelope of the kth modulated optical field within a WDM comb (time domain)	$\sqrt{\text{W}}$
$\tilde{U}_k(z,\omega)$	normalized complex envelope of kth modulated optical field within a WDM comb (frequency domain)	$\sqrt{\text{W}}\,\text{s}$
v_g	group velocity	m s^{-1}
$v(t)$	pulse carver driving signal	V
v_{bias}	pulse carver biasing voltage	V
V	normalized frequency	
V_π	MZM driving voltage to produce a phase shift of π	V
V_{p}	pulse carver peak driving voltage	V
x_{mn}	information symbol of the nth subcarrier at the mth OFDM symbol	
x_n	n^{th} information symbol	
x, y, z	cartesian coordinates	m
$\mathbf{x}$	information vector	
$\hat{\mathbf{x}}, \hat{\mathbf{y}}, \hat{\mathbf{z}}$	cartesian unit vectors	

$\boldsymbol{x}$	vector of parameters to optimize	
$\boldsymbol{x}_{\mathrm{v}}$	vertices of simplex	
$\boldsymbol{x}^{*}$	optimum vector of parameters	
$\mathrm{d}z$	step size of the SSF method (constant)	m
$\mathrm{d}z_n$	step size of the SSF method (variable)	m
Z_f	wave impedance	Ω

List of abbreviations

AM	amplitude modulation
ASE	amplified spontaneous emission
ASK	amplitude-shift keying
AWGN	additive white Gaussian noise
BD	balanced detector
BER	bit-error rate
c.c.	conjugate complex
CCDF	complementary cumulative distribution function
CD	chromatic dispersion
CR	span compensation ratio
CSRZ	carrier-suppressed return-to-zero
CW	continuous wave
D8PSK	differential 8-PSK
DAC	digital to analog converter
DCF	dispersion-compensating fiber
DFB	distributed feedback (laser)
DFT	discrete Fourier transform
DGD	differential group delay
DLI	delay line interferometer
DM	dispersion managed (links)
DPSK	differential phase-shift keying
DQPSK	differential quadrature phase-shift keying
DWDM	dense wavelength division multiplexing
ECL	external cavity laser
EDFA	erbium-doped fiber amplifier
FDM	frequency division multiplexing
FEC	forward error correction
FM	frequency modulation
FWHM	full width at half maximum
FWM	four-wave mixing
GF	Galois field
GOA	global optimization algorithm

GVD	group velocity dispersion
Ham	Hamming pulse
HSPA	high speed packet access
HWHM	half width at half maximum
I	in-phase
IAPR	instantaneous-to-average power ratio
IBI	inter-block interference
IEEE	Institute of Electric and Electronic Engineers
IFWM	intra-channel four-wave mixing
IM/DD	intensity modulation / direct detection
ISI	inter-symbol interference
ISPM	intra-channel self-phase modulation
ITU	International Telecommunication Union
ITU-T	telecommunication section of the ITU
IXPM	intra-channel cross-phase modulation
LFSR	linear feedback shift register
LO	local oscillator
LTE	long term evolution
MGF	moment generating function
MLE	maximum likelihood estimator
MZM	Mach-Zehnder modulator
NDM	non-dispersion managed (links)
NLPR	nonlinear phase rotation (method)
NLPS	nonlinear phase shift (criterion)
NLSE	nonlinear Schroedinger equation
NPN	nonlinear phase noise
NRZ	non-return-to-zero
OFDM	orthogonal frequency division multiplexing
OOK	on-off keying
OSNR	optical signal-to-noise ratio
ΔOSNR	optical signal-to-noise ratio margin
$OSNR_{acc}$	accumulated optical signal-to-noise ratio
$OSNR_{req}$	required optical signal-to-noise ratio
PAPR	peak-to-average power ratio
PBS	polarization beam splitter
PDF	probability density function
PDM	polarization division multiplexing
PMD	polarization mode dispersion
PR	pre-compensation ratio
PSD	power spectral density

PSK   phase-shift keying
Q   quadrature
QAM   quadrature amplitude modulation
QPSK   quadrature phase-shift keying
RC   raised cosine
RX   receiver
RZ   return-to-zero
SBS   stimulated Brillouin scattering
SC   single-carrier
SDH   synchronous digital hierarchy
SLR   straight-line rule
SONET   synchronous optical network
SOP   state of polarization
SPM   self-phase modulation
SRS   stimulated Raman scattering
SSF   split-step Fourier (method)
SSMF   standard single-mode fiber
TF   transfer function
TX   transmitter
UMTS   universal mobile telecommunications system
WDM   wavelength division multiplexing
XPM   cross-phase modulation

Bibliography

[3GP]   3GPP, The 3rd Generation Partnership Project. *www.3gpp.org.*

[ABF02]   J.C. Antona, S. Bigo, and J.P. Faure. Nonlinear cumulated phase as a criterion to assess performance of terrestrial wdm systems. In *Optical Fiber Communication Conference and Exhibit, 2002. OFC 2002*, pages 365 – 367, mar 2002.

[Agr01]   G.P. Agrawal. *Nonlinear fiber optics.* Academic Press, San Diego, 3rd edition, 2001.

[Agr02]   G.P. Agrawal. *Fiber-optic communication systems.* John Wiley & Sons, Inc., New York, 3rd edition, 2002.

[Agr04]   G.P. Agrawal. *Lightwave technology: Components and devices.* John Wiley & Sons, Inc., Hoboken, 2004.

[AIM$^+$96] M. Abe, Y. Inoue, K. Moriwaki, M. Okuno, and Y. Ohmori. Optical path length trimming technique using thin film heaters for silica-based waveguides on Si. *Electronics Letters*, 32(19):1818 –1820, sep 1996.

[AJK$^+$13] S. Adhikari, S.L. Jansen, M. Kuschnerov, O. Gaete, B. Inan, M. Bohn, and W. Rosenkranz. Analysis of spectral shaping on DFT-OFDM. *Photonics Technology Letters, IEEE*, 25(3):287–290, 2013.

[AKJ$^+$12] S. Adhikari, M. Kuschnerov, S.L. Jansen, A. Lobato, O. Gaete, B. Inan, and W. Rosenkranz. Spectral shaping on DFT-OFDM for higher transmission reach. In *Signal Processing in Photonic Communications*, page SpTu2A.3. Optical Society of America, 2012.

[AL06]   J. Armstrong and A.J. Lowery. Power efficient optical OFDM. *Electronics Letters*, 42(6):370 – 372, march 2006.

[Arf85]   G. Arfken. *Mathematical Methods for Physicists.* Academic Press, New York, 1985.

[AS64]   M. Abramowitz and I.A. Stegun. *Handbook of Mathematical Functions: With Formulars, Graphs, and Mathematical Tables.* Applied mathematics series. Dover Publications, Incorporated, 1964.

[BBB99]   G. Bellotti, A. Bertaina, and S. Bigo. Dependence of self-phase modulation impairments on residual dispersion in 10-Gb/s-based terrestrial transmissions using standard fiber. *Photonics Technology Letters, IEEE*, 11(7):824 –826, jul 1999.

[BBK08]   H. Bulow, F. Buchali, and A. Klekamp. Electronic dispersion compensation. *Lightwave Technology, Journal of*, 26(1):158 –167, jan.1, 2008.

[BCC+00]   G. Bosco, A. Carena, V. Curri, R. Gaudino, P. Poggiolini, and S. Benedetto. Suppression of spurious tones induced by the split-step method in fiber systems simulation. *Photonics Technology Letters, IEEE*, 12(5):489 –491, may 2000.

[BMM+04]   B. Bakhshi, M. Manna, G. Mohs, D.I. Kovsh, R.L. Lynch, M. Vaa, E.A. Golovchenko, W.W. Patterson, W.T. Anderson, P. Corbett, Shijun Jiang, M.M. Sanders, Haifeng Li, G.T. Harvey, A. Lucero, and S.M. Abbott. First dispersion-flattened transpacific undersea system: from design to terabit/s field trial. *Lightwave Technology, Journal of*, 22(1):233 – 241, jan. 2004.

[Boy08]   R. W. Boyd. *Nonlinear optics*. Academic Press, San Diego, USA, 3rd edition, 2008.

[BP04]   G. Bosco and P. Poggiolini. On the Q factor inaccuracy in the performance analysis of optical direct-detection DPSK systems. *Photonics Technology Letters, IEEE*, 16(2):665 –667, feb. 2004.

[BSO08]   A. Bononi, P. Serena, and A. Orlandini. A unified design framework for single-channel dispersion-managed terrestrial systems. *Lightwave Technology, Journal of*, 26(22):3617 –3631, nov.15, 2008.

[Car99]   A.V.T. Cartaxo. Cross-phase modulation in intensity modulation-direct detection WDM systems with multiple optical amplifiers and dispersion compensators. *Lightwave Technology, Journal of*, 17(2):178 –190, feb 1999.

[CGH09]   L.D. Coelho, O. Gaete, and N. Hanik. An algorithm for global optimization of optical communication systems. *AEU - International Journal of Electronics and Communications*, 63(7):541 – 550, 2009.

[CGS+09]   L.D. Coelho, O. Gaete, E.-D. Schmidt, B. Spinnler, and N. Hanik. Global optimization of RZ-DPSK and RZ-DQPSK systems at various data rates. In *Optical Fiber Communication - incudes post deadline papers, 2009. OFC 2009. Conference on*, pages 1 –3, march 2009.

[CGS+10]   L.D. Coelho, O. Gaete, E.-D. Schmidt, B. Spinnler, and N. Hanik. Impact of PMD and nonlinear phase noise on the global optimization of DPSK and DQPSK systems. In *Optical Fiber Communication , 2010 Conference on (OFC/NFOEC)*, pages 1 –3, march 2010.

[CMG⁺09]   L. D. Coelho, L. Molle, D. Gross, N. Hanik, R. Freund, C. Caspar, E.-D. Schmidt, and B. Spinnler. Modeling nonlinear phase noise in differentially phase-modulated optical communication systems. *Optics Express*, 17(5):3226–3241, March 2009.

[Coe10]   L.D. Coelho. *Modeling, simulation and optimization of optical communication systems using advanced modulation formats*. PhD thesis, Technische Universität München, Munich, Germany, November 2010.

[DBDB02]   E. Desurvire, D. Bayart, B. Desthieux, and S. Bigo. *Erbium-doped fiber amplifiers: Device and system developments*. John Wiley & Sons, Inc., New York, 2002.

[DDKB04]   A. Del Duce, R.I. Killey, and P. Bayvel. Comparison of nonlinear pulse interactions in 160-Gb/s quasi-linear and dispersion managed soliton systems. *Lightwave Technology, Journal of*, 22(5):1263 – 1271, may 2004.

[DeV61]   Adrian J. DeVries. Design of stereophonic receiver for a stereo system in the FM band using an AM subcarrier. *Broadcast and Television Receivers, IRE Transactions on*, BTR-7(2):67 –72, july 1961.

[EFS⁺00]   J.P. Elbers, A. Farbert, C. Scheerer, C. Glingener, and G. Fischer. Reduced model to describe SPM-limited fiber transmission in dispersion-managed lightwave systems. *Selected Topics in Quantum Electronics, IEEE Journal of*, 6(2):276 –281, mar/apr 2000.

[Eld92]   IV Elder, J.F. Global Rd optimization when probes are expensive: the GROPE algorithm. In *Systems, Man and Cybernetics, 1992., IEEE International Conference on*, pages 577 –582 vol.1, oct 1992.

[EMR99]   R. J. Essiambre, B. Mikkelsen, and G. Raybon. Intra-channel cross-phase modulation and four-wave mixing in high-speed TDM systems. *Electronics Letters*, 35(18):1576–1578, September 1999.

[FABH02]   Y. Frignac, J.C. Antona, S. Bigo, and J.P. Hamaide. Numerical optimization of pre- and in-line dispersion compensation in dispersion-managed systems at 40 Gbit/s. In *Optical Fiber Communication Conference and Exhibit, 2002. OFC 2002*, pages 612 – 613, mar 2002.

[FB00]   Y. Frignac and S. Bigo. Numerical optimization of residual dispersion in dispersion-managed systems at 40 Gbit/s. In *Optical Fiber Communication Conference, 2000*, volume 1, pages 48 –50 vol.1, 2000.

[FNM⁺04]   M. Funabashi, H. Nasu, T. Mukaihara, T. Kimoto, T. Shinagawa, T. Kise, K. Takaki, T. Takagi, M. Oike, T. Nomura, and A. Kasukawa. Recent advances in DFB lasers for ultradense WDM applications. *Selected Topics in Quantum Electronics, IEEE Journal of*, 10(2):312 – 320, march-april 2004.

[For97]   F. Forghieri. Modeling of wavelength multiplexed lightwave systems. In *Optical Fiber Communication. OFC 97., Conference on*, page 27, feb 1997.

[For00]   E. Forestieri. Evaluating the error probability in lightwave systems with chromatic dispersion, arbitrary pulse shape and pre- and postdetection filtering. *Lightwave Technology, Journal of*, 18(11):1493 –1503, nov 2000.

[Fra99]   C. Francia. Constant step-size analysis in numerical simulation for correct four-wave-mixing power evaluation in optical fiber transmission systems. *Photonics Technology Letters, IEEE*, 11(1):69 –71, jan 1999.

[FSE+99]   A. Farbert, C. Scheerer, J.P. Elbers, C. Glingener, and G. Fischer. Optimised dispersion management scheme for long-haul optical communication systems. *Electronics Letters*, 35(21):1865 –1866, oct 1999.

[GAB10]   E. Grellier, J. Antona, and S. Bigo. Are multilevel pseudorandom sequences really needed to emulate highly dispersive optical transmission systems? In *Optical Communication (ECOC), 2010 36th European Conference and Exhibition on*, pages 1 –3, sept. 2010.

[GCS+08]   O. Gaete, L.D. Coelho, B. Spinnler, E.D. Schmidt, and N. Hanik. Global optimization of optical communication systems. In *Optical Communication, 2008. ECOC 2008. 34th European Conference on*, pages 1 –2, sept. 2008.

[GCS+09]   O. Gaete, L.D. Coelho, B. Spinnler, M.S. Alfiad, S.L. Jansen, and N. Hanik. Stereo multiplexing for direct detected optical communication systems. In *Optical Fiber Communication - incudes post deadline papers, 2009. OFC 2009. Conference on*, pages 1 –3, march 2009.

[GCS+10]   O. Gaete, L.D. Coelho, B. Spinnler, S. Hellerbrand, E.-D. Schmidt, and N. Hanik. A digital subcarrier multiplexing technique for increased spectral efficiency in optical systems using direct detection. In *Optical Fiber Communication (OFC), collocated National Fiber Optic Engineers Conference, 2010 Conference on (OFC/NFOEC)*, pages 1 –3, march 2010.

[GCS12]   O. Gaete, L.D. Coelho, and B. Spinnler. Performance of stereo multiplexing in single channel and DWDM systems using direct detection with optimum dispersion maps. *Journal of Networks*, 7(5), 2012.

[GCSH10a]   O. Gaete, L. Coelho, B. Spinnler, and N. Hanik. Performance of stereo multiplexing in systems using direct detection with optimum dispersion maps. In *Transparent Optical Networks (ICTON), 2010 12th International Conference on*, pages 1 –4, 27 2010-july 1 2010.

[GCSH10b] O. Gaete, L.D. Coelho, B. Spinnler, and N Hanik. Block- vs. symbol-wise differential encoding in spectrally efficient digital subcarrier multiplexing for direct detection. In *Conference on Signal Processing in Photonic Communications (SPPcom2010)*, 2010.

[GCSH11] O. Gaete, L. Coelho, B. Spinnler, and N. Hanik. Pulse shaping using the discrete fourier transform for direct detection optical systems. In *Transparent Optical Networks (ICTON), 2011 13th International Conference on*, pages 1 –4, june 2011.

[GFCH08] B. Goebel, B. Fesl, L.D. Coelho, and N. Hanik. On the effect of FWM in coherent optical OFDM systems. In *Proceedings of the Optical Fiber Communication Conference (OFC)*, page JWA58, San Diego, CA, USA, February 2008.

[GHC+10] O. Gaete, S. Hellerbrand, L.D. Coelho, B. Spinnler, and N. Hanik. Linear equalization in spectrally efficient digital subcarrier multiplexing for direct detection. In *OptoeElectronics and Communications Conference (OECC), 2010 15th*, pages 466 –467, july 2010.

[GJC+11] O. Gaete, H. Jalloul, L.D. Coelho, B. Spinnler, and N. Hanik. Transmission of 111 Gb/s on a 50 GHz grid using single polarization, direct detection and digital subcarrier multiplexing. In *Optical Fiber Communication Conference and Exposition (OFC/NFOEC), 2011 and the National Fiber Optic Engineers Conference*, pages 1 –3, march 2011.

[GM90] J. P. Gordon and L. F. Mollenauer. Phase noise in photonic communications systems using linear amplifiers. *Opt. Lett.*, 15:1351–1353, 1990.

[GNWK+05] L. Gruner-Nielsen, M. Wandel, P. Kristensen, C. Jorgensen, L.V. Jorgensen, B. Edvold, B. Palsdottir, and D. Jakobsen. Dispersion-compensating fibers. *Lightwave Technology, Journal of*, 23(11):3566 – 3579, nov. 2005.

[Goe10] B. Goebel. *Information-theoretic aspects of fiber-optic communication channel*. PhD thesis, Technische Universität München, Munich, Germany, October 2010.

[Gol67] S. W. Golomb. *Shift Register Sequences*. Holden-Day, Inc., San Francisco, USA, 1967.

[GRB+03] A.H. Gnauck, G. Raybon, P.G. Bernasconi, J. Leuthold, C.R. Doerr, and L.W. Stulz. 1-Tb/s (6 x 170.6 Gb/s) transmission over 2000-km NZDF using OTDM and RZ-DPSK format. *Photonics Technology Letters, IEEE*, 15(11):1618 –1620, nov. 2003.

[GSD+06] V.S. Grigoryan, M. Shin, P. Devgan, J. Lasri, and P. Kumar. Soa-based regenerative amplification of phase-noise-degraded dpsk signals: dynamic

analysis and demonstration. *Lightwave Technology, Journal of*, 24(1):135 – 142, jan. 2006.

[Gue90]   C. Guenther. Parallel generation of recurring sequences. In Jean-Jacques Quisquater and Joos Vandewalle, editors, *Advances in Cryptology - EU-ROCRYPT 89*, volume 434 of *Lecture Notes in Computer Science*, pages 503–522. Springer Berlin / Heidelberg, 1990.

[GW05]   A.H. Gnauck and P.J. Winzer. Optical phase-shift-keyed transmission. *Lightwave Technology, Journal of*, 23(1):115 – 130, jan. 2005.

[GWL63]   J. P. Gordon, L. R. Walker, and W. H. Louisell. Quantum statistics of masers and attenuators. *Physical Review*, 130(2):806–812, April 1963.

[Han95]   N. Hanik. *Auswirkung nichtlinearer Fasereffekte auf die digitale Sig-nalübertragung in Monomode-Glasfasern*. PhD thesis, Technische Uni-versität München, Munich, Germany, May 1995.

[Har78]   F.J. Harris. On the use of windows for harmonic analysis with the discrete fourier transform. *Proceedings of the IEEE*, 66(1):51 – 83, jan. 1978.

[HEG+04]   N. Hanik, A. Ehrhardt, A. Gladisch, C. Peucheret, P. Jeppesen, L. Molle, R. Freund, and C. Caspar. Extension of all-optical network-transparent domains based on normalized transmission sections. *Lightwave Technol-ogy, Journal of*, 22(6):1439 – 1453, june 2004.

[Hel77]   R. W. Hellwarth. Third-order optical susceptibilities of liquids and solids. *Progress in Quantum Electronics*, 5(1):1–68, 1977.

[Hel78]   C.W. Helstrom. Approximate evaluation of detection probabilities in radar and optical communications. *Aerospace and Electronic Systems, IEEE Transactions on*, AES-14(4):630 –640, july 1978.

[Hen89]   P. Henry. Error-rate performance of optical amplifiers. In *Optical Fiber Communication Conference, Vol. 5 of 1989 OSA Technical Digest Series (Optical Society of America, 1989), paper THK3.*, 1989.

[Hew07]   D.F. Hewitt. Orthogonal frequency division multiplexing using baseband optical single sideband for simpler adaptive dispersion compensation. In *Optical Fiber Communication and the National Fiber Optic Engineers Conference, 2007. OFC/NFOEC 2007. Conference on*, pages 1 –3, march 2007.

[HK04a]   K.-P. Ho and J.M. Kahn. Electronic compensation technique to mitigate nonlinear phase noise. *Lightwave Technology, Journal of*, 22(3):779 – 783, march 2004.

[HK04b]   K.-P. Ho and J.M. Kahn. Spectrum of externally modulated optical sig-nals. *Lightwave Technology, Journal of*, 22(2):658 – 663, feb. 2004.

[Ho05]   K.-P. Ho. *Phase-modulated optical communication systems*. Springer, New York, 2005.

[IEEa]   IEEE 802.11, The Woking Group for Wireless Local Area Networks Standards. *www.ieee802.org/11*.

[IEEb]   IEEE P802.3bm 40 Gb/s and 100 Gb/s Fiber Optic Task Force. *http://grouper.ieee.org/groups/802/3/bm/*.

[Inf12]   Infinera Corporation. *DWDM Coherent Technology*, 2012.

[INS82]   M. Izutsu, Y. Nakai, and T. Sueta. Operation mechanism of the single-mode optical-waveguide Y junction. *Opt. Lett.*, 7(3):136–138, Mar 1982.

[Int98]   International Telecommunication Union (ITU) - ITU-T Recommendation G.692, Geneva, Switzerland. *Optical interfaces for multichannel systems with optical amplifiers*, 1998.

[Int03]   International Telecommunication Union (ITU), vol. G. Sup. 39. *Optical system design and engineering considerations*, October 2003.

[Isl04]   M. N. Islam. *Raman amplifiers for telecommunications 1*. Springer Verlag, 2004.

[ITU02]   ITU-T. *G.694.1: Spectral grids for WDM applications: DWDM frequency grid*, June 2002.

[ITU09]   ITU-T G.709/Y.1331 Telecommunication Standardization Sector of ITU. *Internet Protocol Aspects - Transport Interfaces for the Optical Transport Network*, 2009.

[Jan06]   S. L. Jansen. *Optical phase conjugation in fiber-optic transmission systems*. PhD thesis, Technische Universiteit Eindhoven, Eindhoven, The Netherlands, June 2006.

[JB00]   M. C. Jeruchem and P. Balaban. *Simulation of Communication Systems: Modeling, Methodology and Techniques*. Kluwer Academic Publishers, New York, USA, 2nd edition, 2000.

[Jer84]   M. Jeruchim. Techniques for estimating the bit error rate in the simulation of digital communication systems. *Selected Areas in Communications, IEEE Journal on*, 2(1):153 – 170, jan 1984.

[JMST09]   S. L. Jansen, I. Morita, T. C. W. Schenk, and H. Tanaka. 121.9-Gb/s PDM-OFDM transmission with 2-b/s/Hz spectral efficiency over 1000 km of SSMF. *IEEE/OSA Journal of Lightwave Technology*, 27(3):177–188, February 2009.

[JvdBM+05]   S.L. Jansen, D. van den Borne, C.C. Monsalve, S. Spalter, P.M. Krumm-
              rich, G.D. Khoe, and H. de Waardt. Reduction of gordon-mollenauer
              phase noise by midlink spectral inversion. *Photonics Technology Letters,
              IEEE*, 17(4):923 –925, april 2005.

[KA85]   T. Koch and R. Alferness. Dispersion compensation by active predistorted
              signal synthesis. *Lightwave Technology, Journal of*, 3(4):800 – 805, aug
              1985.

[KA03]   Y. S. Kivshar and G. P. Agrawal. *Optical solitons : from fibers to photonic
              crystals*. Academic Press, San Diego, USA :, 2003.

[Kei91]   G. Keiser. *Optical fiber communications*. McGraw-Hill International Edi-
              tions, 2nd edition, 1991.

[KK97a]   I. P. Kaminov and T. L. Koch. *Optical fiber telecommunications III A*.
              Academic Press, San Diego, USA, 1997.

[KK97b]   I. P. Kaminov and T. L. Koch, editors. *Optical fiber telecommunications
              III B*. Academic Press, San Diego, 1997.

[KL02]   I. P. Kaminov and T. Li, editors. *Optical fiber telecommunications IV A:
              Components*. Academic Press, San Diego, 2002.

[KL04]   C. Kim and G. Li. Direct-detection optical differential 8-level phase-
              shift keying (OD8PSK) for spectrally efficient transmission. *Opt. Express*,
              12(15):3415–3421, Jul 2004.

[KSS97]   N. Kikuchi, K. Sekine, and S. Sasaki. Analysis of cross-phase modulation
              (XPM) effect on WDM transmission performance. *Electronics Letters*,
              33(8):653 –654, apr 1997.

[KTMB00]   R.I. Killey, H.J. Thiele, V. Mikhailov, and P. Bayvel. Reduction of intra-
              channel nonlinear distortion in 40-Gb/s-based WDM transmission over
              standard fiber. *Photonics Technology Letters, IEEE*, 12(12):1624 –1626,
              dec 2000.

[Kum05]   S. Kumar. Effect of dispersion on nonlinear phase noise in optical trans-
              mission systems. *Opt. Lett.*, 30:3278–3280, 2005.

[Kus62]   H.J. Kushner. A versatile stochastic model of a function of unknown and
              time varying form. *Journal of Mathematical Analysis and Applications*,
              5(1):150 – 167, 1962.

[Kus63]   H.J. Kushner. A new method of locating the maximum of an arbitrary
              multipeak curve in the presence of noise. *Proc. Joint automatic control
              conf.*, 1963.

[KWM⁺05]   R.I. Killey, P.M. Watts, V. Mikhailov, M. Glick, and P. Bayvel. Electronic dispersion compensation by signal predistortion using digital processing and a dual-drive Mach-Zehnder modulator. *IEEE Photonics Technology Letters*, 17(3):714–716, March 2005.

[LDA06]   A.J. Lowery, L. Du, and J. Armstrong. Orthogonal frequency division multiplexing for adaptive dispersion compensation in long haul wdm systems. In *Optical Fiber Communication Conference, 2006 and the 2006 National Fiber Optic Engineers Conference. OFC 2006*, pages 1 – 3, march 2006.

[LK97a]   Yu-Chuan Lin and C.-C.Jay Kuo. Classification of quadrature amplitude modulated (QAM) signals via sequential probability ratio test (SPRT). *Signal Processing*, 60(3):263 – 280, 1997.

[LK97b]   C. Lorattanasane and K. Kikuchi. Design theory of long-distance optical transmission systems using midway optical phase conjugation. *Lightwave Technology, Journal of*, 15(6):948 –955, jun 1997.

[LMZW08]   Qijia Liu, Xiaoli Ma, G.T. Zhou, and Jie Wu. Peak-to-average power ratio versus instantaneous-to-average power ratio for OFDM. In *Signals, Systems and Computers, 2008 42nd Asilomar Conference on*, pages 938 –942, oct. 2008.

[Mar90]   D. Marcuse. Derivation of analytical expressions for the bit-error probability in lightwave systems with optical amplifiers. *Lightwave Technology, Journal of*, 8(12):1816 –1823, dec 1990.

[MCS00]   A. Mecozzi, C.B. Clausen, and M. Shtaif. System impact of intra-channel nonlinear effects in highly dispersed optical pulse transmission. *Photonics Technology Letters, IEEE*, 12(12):1633 –1635, dec 2000.

[ME05]   M.E. McCarthy and A.D. Ellis. Low-cost receiver side electronic dispersion compensation of the full optical field. In *Optical Fibre Communications and Electronic Signal Processing, 2005. The IEE Seminar on*, dec. 2005.

[MM99]   P. V. Mamyshev and N. A. Mamysheva. Pulse-overlapped dispersion-managed data transmission and intrachannel four-wave mixing. *Opt. Lett.*, 24(21):1454–1456, Nov 1999.

[MM06]   C. R. Menyuk and B. S. Marks. Interaction of polarization mode dispersion and nonlinearity in optical fiber transmission systems. *IEEE/OSA Journal of Lightwave Technology*, 24(7):2806–2826, July 2006.

[MMW97]   D. Marcuse, C. R. Menyuk, and P. K. A. Wai. Application of the manakov-PMD equation to studies of signal propagation in optical fibers with randomly varying birefringence. *IEEE/OSA Journal of Lightwave Technology*, 15(9):1735–1746, September 1997.

[MS76]   F.J. MacWilliams and N.J.A. Sloane. Pseudo-random sequences and arrays. *Proceedings of the IEEE*, 64(12):1715 – 1729, dec. 1976.

[Neu88]   E.-G. Neumann. *Single mode fibers*. Springer Verlag, 1988.

[Nog07]   K. Noguchi, editor. *Ultrahigh-speed optical transmission technology*. Springer, 2007.

[NSY06]   M. Nazarathy, E. Simony, and Y. Yadin. Analytical evaluation of bit error rates for hard detection of optical differential phase amplitude shift keying (DPASK). *Lightwave Technology, Journal of*, 24(5):2248 – 2260, may 2006.

[OF04]   M. Ohm and T. Freckmann. Comparison of different DQPSK transmitters with NRZ and RZ impulse shaping. In *Advanced Modulation Formats, 2004 IEEE/LEOS Workshop on*, pages 7 – 8, july 2004.

[OS89]   A. V. Oppenheim and R. W. Schafer. *Discrete-Time Signal Processing*. Prentice-Hall: Englewood Cliffs, NJ, 1989.

[OS05a]   M. Ohm and J. Speidel. Optimal receiver bandwidths, bit error probabilities and chromatic dispersion tolerance of 40Gbit/s optical 8-DPSK with NRZ and RZ impulse shaping. In *Optical Fiber Communication Conference, 2005. Technical Digest. OFC/NFOEC*, volume 5, page 3 pp. Vol. 6, march 2005.

[OS05b]   M. Ohm and J. Speidel. Receiver sensitivity, chromatic dispersion tolerance and optimal receiver bandwidths for 40 Gbit/s 8-level optical ASK-DQPSK and optical 8-DPSK. In *6. ITG Fachtung Photonische Netze, Leipzig, Germany*, pages pp. 211–217, May 2005.

[Per89]   C.D. Perttunen. A nonparametric global optimization method using the rank transformation. In *Decision and Control, 1989., Proceedings of the 28th IEEE Conference on*, pages 888 –893 vol.1, dec 1989.

[Pro00]   J. G. Proakis. *Digital communications*. McGraw-Hill, New York, 4rd edition, 2000.

[PSPW02]   M. Pfennigbauer, M.M. Strasser, M. Pauer, and P.J. Winzer. Dependence of optically preamplified receiver sensitivity on optical and electrical filter bandwidths-measurement and simulation. *Photonics Technology Letters, IEEE*, 14(6):831 –833, june 2002.

[Que87]   F. Quellette. Dispersion cancellation using linearly chirped bragg grating filters in optical waveguides. *Optic Letters*, 12:10, 1987.

[Ran05]   S. Randel. *Analyse faseroptischer Übertragungssysteme mit Wellenlängenmultiplex bei 160 Gbit/s Kanaldatenrate*. PhD thesis, Technische Universität Berlin, Berlin, Germany, May 2005.

[RBF09]   P. Ramantanis, H. Badaoui, and Y. Frignac. Quaternary sequences comparison for the modeling of optical DQPSK dispersion managed transmission systems. In *Optical Fiber Communication - incudes post deadline papers, 2009. OFC 2009. Conference on*, pages 1 –3, march 2009.

[Sal78]   B. Saleh. *Photoelectron Statistics*. Springer Verlag, Berlin, 1978.

[Sav06]   S.J. Savory. Optimum electronic dispersion compensation strategies for nonlinear transmission. *Electronics Letters*, 42(7):407 – 408, march 2006.

[SBW87]   N. Shibata, R. Braun, and R. Waarts. Phase-mismatch dependence of efficiency of wave generation through four-wave mixing in a single-mode optical fiber. *Quantum Electronics, IEEE Journal of*, 23(7):1205 – 1210, jul 1987.

[Sch04]   T. Schneider. *Nonlinear optics in telecommunications*. Springer, Berlin, 2004.

[SD09]   W. Shieh and I. Djordjevic. *OFDM for Optical Communications*. Elsevier Science, 2009.

[Sei10]   M. Seimetz. *High-order modulation for optical fiber transmission*. Springer, 2010.

[SH04]   S. Savory and A. Hadjifotiou. Laser linewidth requirements for optical DQPSK systems. *Photonics Technology Letters, IEEE*, 16(3):930 –932, march 2004.

[Sha49]   C.E. Shannon. Communication in the presence of noise. *Proceedings of the IRE*, 37(1):10 – 21, jan. 1949.

[Shn89]   D.A. Shnidman. The calculation of the probability of detection and the generalized marcum q-function. *Information Theory, IEEE Transactions on*, 35(2):389–400, 1989.

[SHZM03]   O. V. Sinkin, R. Holzlöhner, J. Zweck, and C. R. Menyuk. Optimization of the split-step Fourier method in modeling optical-fiber communications systems. *IEEE/OSA Journal of Lightwave Technology*, 21(1):61–68, January 2003.

[SI07]   J.O. Smith III. *Mathematics of the Discrete Fourier Transform: With Audio Applications*. BookSurge Publishing, 2007.

[SMKT00]   A. Sano, Y. Miyamoto, S. Kuwahara, and H. Toba. A 40-Gb/s/ch WDM transmission with SPM/XPM suppression through prechirping and dispersion management. *Lightwave Technology, Journal of*, 18(11):1519 – 1527, nov 2000.

[SOB07]   P. Serena, A. Orlandini, and A. Bononi. The memory of opti-
             mized dispersion-managed periodic optical links. *Optical Communication
             (ECOC), 2007 33rd European Conference and Ehxibition of*, pages 1 –2,
             sept. 2007.

[SSBP08]   M. Schuster, B. Spinnler, C.-A. Bunge, and K. Petermann. Compatible
             single-sideband modulation for optical transmission of ofdm-signals using
             direct detection. *Photonic Networks, 2008 ITG Symposium on*, pages 1
             –5, april 2008.

[STM+98]   I. Shake, H. Takara, K. Mori, S. Kawanishi, and Y. Yamabayashi. In-
             fluence of inter-bit four-wave mixing in optical TDM transmission. *Elec-
             tronics Letters*, 34(16):1600 –1601, aug 1998.

[Stu88]   B.E. Stuckman. A global search method for optimizing nonlinear systems.
             Systems, Man and Cybernetics, IEEE Transactions on, 18(6):965 –977,
             nov/dec 1988.

[SWR04]   M. Serbay, C. Wree, and W. Rosenkranz. Comparison of six different
             RZ-DQPSK transmitter set-ups regarding their tolerance towards fibre
             impairments in 8x40Gb/s WDM-systems. In *Advanced Modulation For-
             mats, 2004 IEEE/LEOS Workshop on*, pages 9 – 10, july 2004.

[SX07]   B. Spinnler and C. Xie. Performance assessment of DQPSK using pseudo-
             random quaternary sequences. *Optical Communication (ECOC), 2007
             33rd European Conference and Ehxibition of*, pages 1 –2, sept. 2007.

[Tel10]   Telegeography Research. *Global Bandwidth Research Service*, 2010.

[TSGS00]   G. A. Thomas, B. I. Shraiman, P. F. Glodis, and M. J. Stephen. Towards
             the clarity limit in optical fibre. *Nature*, 404:262, 2000.

[vdB08]   D. van den Borne. *Robust optical transmission systems*. PhD thesis,
             Technische Universiteit Eindhoven, Eindhoven, The Netherlands, March
             2008.

[vdBDF+07]   D. van den Borne, T. Duthel, C.R.S. Fludger, E.D. Schmidt, T. Wuth,
             C. Schulien, E. Gottwald, G.D. Khoe, and H. de Waardt. Coherent
             equalization versus direct detection for 111-Gb/s ethernet transport. In
             IEEE/LEOS Summer Topical Meetings, 2007 Digest of the, pages 11 –12,
             july 2007.

[vdBJK+06]   D. van den Borne, S.L. Jansen, G.D. Khoe, H. de Waardt, and
             E. Gottwald. Line optimization in long-haul transmission systems with
             42.8-Gbit/s RZ-DQPSK modulation. In *Optical Fiber Communication
             Conference, 2006 and the 2006 National Fiber Optic Engineers Confer-
             ence. OFC 2006*, page 3 pp., march 2006.

[vdBKdWG07] D. van den Borne, G.D. Khoe, H. de Waardt, and E. Gottwald. Bit pattern dependence in optical DQPSK modulation. *Electronics Letters*, 43(22), 25 2007.

[Vor07] S. Vorbeck. *Systementwurf von optischen Übertragungsstrecken mit 160 Gbit/s Kanaldatenrate*. PhD thesis, Universität Dortmund, Dortmund, Germany, August 2007.

[WBO+09] H. Wernz, S. Bayer, B.E. Olsson, M. Camera, H. Griesser, C. Furst, B. Koch, V. Mirvoda, A. Hidayat, and R. Noe. 112 Gb/s PolMux RZ-DQPSK with fast polarization tracking based on interference control. In *Optical Fiber Communication - incudes post deadline papers, 2009. OFC 2009. Conference on*, pages 1 –3, march 2009.

[WE06] P.J. Winzer and R.-J. Essiambre. Advanced optical modulation formats. *Proceedings of the IEEE*, 94(5):952 –985, may 2006.

[WEG+04] L.K. Wickham, R.-J. Essiambre, A.H. Gnauck, P.J. Winzer, and A.R. Chraplyvy. Bit pattern length dependence of intrachannel nonlinearities in pseudolinear transmission. *Photonics Technology Letters, IEEE*, 16(6):1591 –1593, june 2004.

[WLR02] C. Wree, J. Leibrich, and W. Rosenkranz. RZ-DQPSK format with high spectral efficiency and high robustness towards fiber nonlinearities. In *Optical Communication, 2002. ECOC 2002. 28th European Conference on*, volume 4, pages 1 –2, sept. 2002.

[WPSL01] P.J. Winzer, M. Pfennigbauer, M.M. Strasser, and W.R. Leeb. Optimum filter bandwidths for optically preamplified NRZ receivers. *Lightwave Technology, Journal of*, 19(9):1263 –1273, sep 2001.

[WSR03] C. Wree, M. Serbay, and W. Rosenkranz. Towards 1.6 b/s/Hz spectral efficiency by strong optical filtering of RZ-DQPSK. In *Optical Communication. ECOC 2003. 29th European Conference on*, 2003.

[Xia08] C. Xia. *Advanced electronic distortion equalization for high speed optical SMF and MMF communications*. PhD thesis, Christian-Albrechts-Universität zu Kiel, Kiel, Germany, February 2008.

[YFP79] A. Yariv, D. Fekete, and D. Pepper. Compensation for channel dispersion by non-linear optical phase conjugation. *Optics Letters*, 4, no. 2, 1979.

[ZLL+01] Y. Zhu, W.S. Lee, P. Lobb, C. Scahill, D. Watley, S. Savory, C. Fludger, B. Shaw, and A. Hadjifotiou. Polarisation-channel-interleaved carrier-suppressed RZ ETDM/DWDM transmission at 40 Gbit/s with 0.8 bit/s/Hz spectral efficiency. In *Optical Communication, 2001. ECOC '01. 27th European Conference on*, volume 1, pages 54 – 55 vol.1, 2001.